UNIVERSIDADE DA BEIRA INTERIOR
Engenharia

Integrated Multi-functional Morphing Aircraft Technologies

Pedro Daniel da Rocha Santos

Tese para obtenção do Grau de Doutor em
Engenharia Aeronáutica
(3º ciclo de estudos)

Orientador: Professor Doutor Pedro Vieira Gamboa
Coorientador: Professor Doutor José Miguel Silva

Covilhã, abril de 2018

Abstract

In the past years, the development of morphing wing technologies has received a great deal of interest from the scientific community. These technologies potentially enable an increase in aircraft efficiency by changing the wing shape, thus allowing the aircraft to fly near its optimal performance point at different flight conditions. This thesis explores the development, analysis, building and integration of two new functional Variable-Span Wing (VSW) concepts to be applied in Remotely Piloted Aircraft Systems (RPAS). Additional studies are performed to synthesize the mass of such morphing concepts and to develop mass prediction models.

The VSW concept is composed of one fixed rectangular inboard part, inboard fixed wing (IFW), and a moving rectangular outboard part: outboard moving wing (OMW). An aerodynamic shape optimization code is used to solve a drag minimization problem to determine the optimal values of wingspan for various speeds of the vehicle's flight envelope. It was concluded that, at low speeds, the original wing has slightly better performance than the VSW and for speeds higher than 25 m/s the opposite occurs, due to the reduction in wing area and consequently the total wing drag. A structural Finite Element Model (FEM) of the VSW is developed, where the interface between wing parts is modelled. Deflections and stresses resulting from static aerodynamic loading conditions showed that the wing is suitable for flight. Flutter critical speed is studied. FEM is used to compute the VSW mode shapes and frequencies of free vibration, considering a rigid or the real flexible interface, showing that the effect of rigidity loss in the interface between the IFW and the OMW, has a negative impact on the critical flutter speed.

A full-scale prototype is built using composite materials and an electro-mechanical actuation system is developed using a rack and pinion driven by two servomotors. Bench tests, performed to evaluate the wing and its actuation mechanism under load, showed that the system can perform the required extension/retraction cycles and is suitable to be installed on a RPAS airframe, which has been modified and instrumented to serve as test bed for evaluating the prototype in-flight. Two sets of flight tests are performed: aerodynamic and energy characterization. The former aims at determining the lift-to-drag ratio for different airspeeds and the latter to measure the propulsive and manoeuvring energy when performing a prescribed mission. In the aerodynamic testing, in-flight evaluation of the RPAS fitted with the VSW demonstrates full flight capability and shows improvements produced by the VSW over a conventional fixed wing for speeds above 19 m/s. At low speeds, the original wing has slightly better lift-to-drag ratio than the VSW. Contrarily, at 30 m/s, the VSW in minimum span configuration is 35% better than the original fixed wing. In the other performed test, it is concluded that the VSW fitted RPAS has less overall energy consumption despite the increased vehicle weight. The energy reduction occurs only in the high speed condition but it is so marked that it offsets the increase in energy during takeoff, climb and loiter phases.

Following the work on the first VSW prototype, a new telescopic wing that allows the integration of other morphing strategies is developed, within the CHANGE EU project. The wing adopted span change, leading and trailing edge camber changes. A modular design philosophy, based on a wing-box like structure, is implemented, such that the individual systems can be separately developed and then integrated. The structure is sized for strength and stiffness using FEM, based on flight loads derived from the mission requirements. A partial span, full-sized cross-section prototype is built to validate the structural performance and the actuation

mechanism capability and durability. The wing is built using composite materials and an electro-mechanical actuation system with an oil filled nylon rack and pinion is developed to actuate it. The structural static testing shows similar trends when compared with numerical predictions. The actuation mechanism is characterized in terms of actuation speed and specific energy consumption and it was concluded that it functioned within its designed specifications. A full-scale prototype is later built by the consortium and the leading and trailing edge concepts from the different partners integrated in a single wing. Wind tunnel tests confirmed that the wing can withstand the aerodynamic loading. Flight tests are performed by TEKEVER, showing that the modular concept works reliably.

From the previous works, it is inferred that morphing concepts are promising and feasible methodologies but present an undesired mass increase due to their inherent complexity. On the other hand, mass prediction methods to aid the design of morphing wings at the conceptual design phase are rare. Therefore, a mass model of a VSW with a trailing edge device is proposed. The structural mass prediction is based on a parametric study. A minimum mass optimization problem with stiffness and strength constraints is implemented and solved, being the design variables structural thicknesses and widths, using a parametric FEM of the wing. The study is done for a conventional fixed wing and the VSW, which are then combined to ascertain the VSW mass increment, i.e., the mass penalization of the adopted morphing concept. Polynomials are found to produce good approximations of the wing mass. Additionally, the effects of various VSW design parameters in the structural mass are discussed. On one hand, it was found that the span and chord have the highest impact in the wing mass. On the other hand, the VSW to fixed wing ratio proved that the influence of span variation ratio in the wing mass is not trivial. It is found that the mass increase does not grow proportionally with span variation ratio increase and that for each combination of span and chord, exists a span variation ratio that minimizes the mass penalty. Using the VSW to fixed wing ratio function, the mass model is derived. To ascertain its accuracy, a case study is performed, which demonstrated prediction errors below 10%. Although the mass model results are encouraging, more case studies are necessary to prove its applicability over a wide range of VSWs.

The work performed successfully demonstrated that VSW concepts can achieve considerable geometry changes which, in turn, translate into considerable aerodynamic gains, despite the increased weight. They influence all aspects of the wing design, from the structural side to the actuation mechanisms. The parametric study summarizes the mass penalties of such concepts, being successful at demonstrating that the mass penalty is not straightforward and that a careful selection of span, chord and variable-span ratio can minimize the mass increase.

Keywords

Morphing Aircraft, Morphing Wing, Telescopic Wing, Variable-span Wing, Remotely Piloted Aircraft System, Optimization, Structural Analysis, Finite Element Model, Composite Material Structure, Flight Testing, Parametric Study, Multivariable Polynomial Fitting, Mass Model

Resumo Alargado

Nos últimos anos, o desenvolvimento de asas adaptativas tem sido alvo de um grande interesse por parte da comunidade científica. Nesta tese explora-se o desenvolvimento, análise, construção e integração de dois novos conceitos de Asas de Envergadura Variável (VSWs) funcionais a serem aplicados em Sistemas de Aeronaves Pilotadas Remotamente (RPASs). Estudos adicionais são levados a cabo para sintetizar a massa desses conceitos e desenvolver modelos de previsão de massa.

O conceito da VSW é constituído por uma parte interna retangular fixa, Asa Fixa Interna (IFW), e por uma parte externa retangular móvel, Asa Móvel Externa (OMW). Um código de otimização aerodinâmica é utilizado para minimizar a resistência ao avanço, determinando os valores ótimos de envergadura para várias velocidades de voo do veículo. Concluiu-se que, a baixas velocidades, a asa original apresenta um desempenho ligeiramente melhor que a VSW, enquanto que a velocidades superiores a 25 m/s, a VSW apresenta um desempenho melhor devido à redução da área das asas e, consequentemente, à redução da resistência total das asas. Para levar a cabo um estudo estrutural, foi desenvolvido um Modelo de Elementos Finitos (FEM) estrutural da VSW, no qual se modelou a interface entre a IFW/OMW. As deflexões e tensões resultantes dos carregamentos aerodinâmicos estáticos mostraram que a asa é capaz de suportar as cargas em voo. A velocidade de *flutter* é também investigada, sendo o FEM utilizado para calcular as formas dos modos de vibração da VSW e respetivas frequências de vibração livre. Considerou-se uma interface colada ou flexível, confirmando-se que o efeito da perda de rigidez na interface IFW/OMW, tem um impacto negativo sobre a velocidade de *flutter*.

Um protótipo da VSW é construído, utilizando materiais compósitos, e um sistema de atuação eletromecânico é desenvolvido usando um sistema de pinhão e cremalheira movido por dois servomotores. Os testes de bancada, realizados para avaliar a asa e o mecanismo de atuação, mostraram que o sistema é capaz de realizar a extensão/retração da asa, sendo adequado para ser instalado num RPAS. Este RPAS foi modificado e instrumentado para servir de banco de ensaio para avaliação do protótipo em voo. São realizados dois conjuntos de testes de voo: caracterização aerodinâmica e energética. O primeiro incide na determinação da razão de planeio para diferentes velocidades e o segundo é levado a cabo para determinar a energia propulsiva e de manobra ao executar uma missão típica. Nos testes aerodinâmicos ficou comprovado que o RPAS equipado com a VSW é capaz de uma normal operação e ainda que mostra melhorias sobre uma asa fixa convencional para velocidades acima de 19 m/s. A velocidades mais reduzidas, a asa original tem um desempenho ligeiramente melhor do que a VSW. Por outro lado, a 30 m/s, a VSW na configuração de envergadura mínima é 35% melhor do que a asa fixa original. No outro ensaio realizado, conclui-se que o RPAS de envergadura variável tem menos consumo de energia global, apesar do aumento de peso do veículo. A redução de energia ocorre apenas na fase de cruzeiro de alta velocidade, mas foi tão acentuada que compensou o aumento da energia durante as fases de descolagem, subida e espera.

Na sequência do trabalho anterior e no âmbito do projeto europeu CHANGE, é desenvolvida uma nova VSW que permite a integração de outras estratégias adaptativas. A nova asa adotou a mudança de envergadura, e a mudança de curvatura nos bordos de ataque e de fuga. Esta adotou uma filosofia de projeto modular, baseada numa caixa de torção, permitindo o desenvolvimento das diferentes tecnologias adaptativas separadamente. A estrutura é di-

mensionada para resistência e rigidez usando FEM, com base em cargas de voo derivadas dos requisitos da missão. Um primeiro protótipo é construído para validar o desempenho estrutural e a funcionalidade do mecanismo de atuação. A asa é construída usando materiais compósitos e utiliza um sistema de pinhão e cremalheira e um servomotor, para variar a envergadura. Testes estruturais estáticos mostram que as deflexões corroboram as previsões numéricas. O mecanismo de atuação é caracterizado em termos de velocidade de atuação e consumo de energia específica, concluindo-se que funciona dentro do previsto. O segundo protótipo é construído pelo consórcio e os conceitos de bordo de ataque e de fuga são integrados. Testes em túnel de vento confirmaram que a asa suporta o carregamento aerodinâmico. Os testes de voo, realizados pela TEKEVER, mostram que o conceito modular funciona de forma fiável.

Baseado nos trabalhos anteriores, conclui-se que os conceitos adaptativos são promissores e viáveis, mas apresentam um aumento de massa indesejável devido à sua inerente complexidade. Por outro lado, os métodos de previsão de massa para auxiliar o projeto de asas adaptativas na fase de projeto conceitual são raros. Deste modo, um modelo de massa da VSW com um dispositivo de borda de fuga é proposto. A previsão de massa estrutural é baseada num estudo paramétrico. Um problema de minimização de massa com constrangimentos de rigidez e resistência é implementado e resolvido, sendo as variáveis de projeto espessuras e larguras estruturais. Para o levar a cabo, um FEM paramétrico da VSW é desenvolvido. O estudo é feito para uma asa fixa convencional e para a VSW, os quais são combinados para determinar o incremento de massa da VSW. Aproximações polinomiais das massas da asa são produzidas, mostrando serem capazes de produzir uma adequada representação. Adicionalmente, são discutidos os efeitos dos vários parâmetros de design da VSW na massa estrutural. Por um lado, verificou-se que a envergadura e a corda têm o maior impacto na massa da asa. Por outro lado, a razão de massas da VSW e da asa fixa provou que a influência da razão de variação de envergadura na massa das asas não é trivial. Verifica-se que o aumento de massa não cresce proporcionalmente com o aumento da razão de variação de envergadura e que para um dado conjunto de envergadura e corda existe uma razão de variação de envergadura que minimiza o aumento de massa. O modelo de massa é derivado usando a aproximação polinomial da razão da VSW com a asa fixa. Para verificar a precisão do modelo, é realizado um caso de estudo que demonstrou erros de previsão abaixo dos 10%. Embora os resultados do modelo de massa sejam encorajadores, mais casos de estudo são necessários para provar a sua aplicabilidade a uma ampla gama de VSW.

O trabalho realizado demonstrou com sucesso que os conceitos de VSW podem alcançar consideráveis mudanças de geometria, que se traduzem em ganhos aerodinâmicos consideráveis, apesar do aumento de peso. Estes influenciam todos os aspetos do projeto da asa, desde a parte estrutural até aos mecanismos de atuação. O estudo paramétrico tentou resumir a penalização de massa de tais conceitos, sendo bem sucedido em demonstrar que esta penalização não é simples e que uma seleção cuidadosa de envergadura, corda e razão de variação de envergadura pode minimizar o aumento de peso.

Palavras-chave

Aeronave Adaptativa, Asa Adaptativa, Asa de Envergadura Variável, Sistemas Aéreos Não Tripulados, Otimização, Análise Estrutural, Modelo de Elementos Finitos, Ensaio em Voo, Estudo Paramétrico, Aproximação Polinomial Multivariável, Modelo de Massa

Contents

List of Figures

List of Tables

List of Symbols

Alphanumeric

A	area [m^2]
$A_{hh}, A_{h\theta}, A_{\theta h}, A_{\theta\theta}$	generalized incremental aerodynamic loads
AR	aspect ratio
b	wingspan [m]
c	wing/aerofoil chord [m]
c_a	wing aerodynamic chord [m]
C_d	aerofoil drag coefficient
C_D	wing drag coefficient
C_{D0}	zero-lift drag coefficient
c_{flap}, c_{tip}	flap and tip chords [m]
$\overline{c}_{flap}$	nondimensionalized version c_{flap} with respect to local chord
C_h, C_θ	viscous damping coefficients
c_i	mean chord at location i [m]
C_l	aerofoil lift coefficient
C_L	wing lift coefficient
$dC_l/d\alpha$ or C_{l_α}	aerofoil lift curve slope
$dC_L/d\alpha$ or C_{L_α}	wing lift curve slope
$C_{l,max}$	maximum aerofoil lift coefficient
$C_{L,max}$	maximum wing lift coefficient
$C_{L,min}$	minimum wing lift coefficient
C_m	aerofoil pitching moment coefficient about the quarter chord
C_M	wing pitching moment coefficient
C_P	propeller power coefficient
C_T	propeller thrust coefficient
D	drag [N]
d_b	base circle diameter [mm]
E_1, E_2, E_3	longitudinal elastic modulus parallel, perpendicular and interlaminar direction of the fibre [GPa]
e.a.	elastic axis
EI	bending stiffness [N·m^2]
$E_{vsw,elec}$	total energy used by the servomotor [J]
$E_{vsw,force}$	work of the force to move the OMW [J]
$F_{cu1}, F_{cu2}, F_{cu3}$	compressive strength parallel, perpendicular and interlaminar direction of the fibre [MPa]
F_H, F_V	horizontal and vertical forces [N]
$F_{tu1}, F_{tu2}, F_{tu3}$	tensile strength parallel, perpendicular and interlaminar direction of the fibre [MPa]
$F_{vsw,avg}$	average force to actuate the OMW [N]
g	gravitational acceleration constant [m/s^2]
G_{12}, G_{23}, G_{13}	shear modulus in the three principal directions [GPa]
g_D	damping coefficient

GJ	torsional stiffness [N·m^2]
H_{rack}	height of rack pitch line [mm]
I	electrical current [A]
i_θ	moment of inertia about the e.a. per unit width [kg·m]
I_θ	total moment of inertia about the e.a. [kg·m^2]
J	propeller advance ratio
K_1	lift-dependent drag factor
K_2	lift squared-dependent drag factor
$k_{act,type}$	VSW actuation system constant: 0 performance; 1 performance/control
k_{flap}	flap mass estimation constant
K_g	aeroplane gust alleviation factor
K_h	total stiffness in bending [N/m]
K_θ	total stiffness in rotation [N·m/rad]
l	length [m]
L	lift [N]
l_{var}	variable-span moving length [m]
$\bar{l}_{var}$	nondimensionalized version of l_{var} with respect to semi-span
m	mass [kg]
$\overline{m}$	wing mass per unit width [kg/m]
M	wing mass [kg] or wing pitching moment [N·m]
Ma	Mach number
M_{gear}	gear/rack module [mm]
n	load factor
N	propeller rotational velocity [rot/s]
N_t	number of teeth in gear
p	roll rate [rad/s]
P	power [W] or pressure [Pa]
P_d	pitch circle diameter [mm]
$P_{elec,avg}$	servomotor electric average power [W]
q	pitch rate [rad/s]
Q	propeller torque [N·m]
Q_h, Q_θ	generalized incremental aerodynamic loads
r	yaw rate [rad/s]
R	electrical resistance [Ω]
R_{air}	specific air gas constant [J·kg^{-1}·K^{-1}]
Re	Reynolds number
S	wing area [m^2]
S_{12}, S_{23}, S_{13}	shear strength in the three principal directions [MPa]
s_{OMW}	OMW displacement [m]
$\overline{SR}_{TW}$	ratio of failed elements using the inverse of *Tsai-Wu* strength ratio index failure criterion
s_θ	static mass moment about the e.a. per unit width [kg]
S_θ	static mass moment about the e.a. [kg·m]
t	thickness [m] or time [s]
T	propeller thrust [N]
t/c	aerofoil relative thickness
t_{cycle}	servomotor operating time [s]

t_f	final time instant [s]
t_i	initial time instant [s]
t_{lam}	laminate thickness [m]
u, v, w	body axis velocities in x, y and z directions [m/s]
U	electrical voltage [V]
V	speed or velocity [m/s]
V_C, V_D	design cruise and dive speeds [m/s]
V_f	flutter speed [m/s]
$V_{g,C}, V_{g,D}$	vertical gust speeds for cruise and dive conditions [m/s]
W	weight [N]
w_{sc}	spar cap width [m]
w_{tip}	tip deflection [m]
$\overline{x}_1, \overline{x}_2$	ratios of the fore and aft spar positions to the chord length of the VSW
X_a, Y_a, Z_a	total aerodynamic force components in x, y and z directions [N]
x_α, y_α	distances of the angle of attack sensor from the CG [m]
x_β, z_β	distances of the angle of sideslip sensor from the CG [m]
x_{cg}	chordwise position of the centre of gravity [m]
x_e	chordwise position of the e.a. [m]
X_T, Y_T, Z_T	total thrust force components in x, y and z directions [N]
$\overline{y}$	geometric centroid in the y direction [m]
Y	sideforce [N]
y_i	lateral position at location i [m]

Greek Letters

α	angle of attack [rad] or [deg]
α_{gear}	pressure angle [deg]
α_m, α_c	measured and corrected angles of attack [rad] or [deg]
β	sideslip angle [rad] or [deg]
β_m, β_c	measured and corrected angles of sideslip [rad] or [deg]
δ	thrust setting
Δy_i	strips of width at location i
η_p	propeller efficiency
η_{vsw}	actuator system electro-mechanical efficiency
Γ	dihedral angle [rad] or [deg]
Λ	wing sweep [rad] or [deg]
λ	wing taper ratio [rad] or [deg]
μ_g	aeroplane mass ratio
$\nu_{12}, \nu_{23}, \nu_{13}$	Poisson's ratios in the three principal directions
ω	frequency [rad/s]
$\Omega_{flap,act}$	flap actuation system mass density
ω_h	uncoupled natural frequency in bending [rad/s]
ω_θ	uncoupled natural frequency in torsion [rad/s]
ϕ	bank angle [rad] or [deg]
ψ	heading [rad] or [deg]
ρ	density [kg/m^3]
τ	wing lift curve slope correction due to non-elliptical wing shape

θ	pitch angle [rad] or [deg]
θ_{tip}	tip rotation [deg]

Subscripts

act	actuation
atm	atmospheric
avg	average
blw	baseline wing
cb	climb
cg	centre of gravity
exp	exposed
fus	fuselage
fw	fixed wing
lam	laminate
max	maximum
mot	motor
prop	propeller
ref	reference
req	required
sc	spar cap
str	structural
tk	thickness
var	variable
vsw or VSW	variable-span wing
VSW/fw	variable-span wing to fixed wing ratio
wb	wing-box

List of Acronyms

AC Alternating Current
AdaR Adaptive Aspect Ratio
AFW Active Flexible Wing
AGL Height above Ground Level
AHRS Attitude and Heading Reference System
AMSL Altitude above Mean Sea Level
AOA Angle of Attack
AOS Angle of Sideslip
APA Anisotropic Piezoelectric Actuators
APDL ANSYS® Parametric Design Language
API Application Programming Interface
AUAV Additive Unmanned Aerial Vehicle
BEC Battery Eliminator Circuit
CA Commercial Aviation
CAD Computer-Aided Design
CAM Computer Aided Manufacturing
CFD Computational Fluid Dynamics
CFRP Carbon Fibre Reinforced Polymer
CG Centre of Gravity
CNC Computer Numerical Control
DOE Design of Experiments
EASA European Aviation Safety Agency
EKF Extended Kalman Filter
EPS Expanded Polystyrene
ERR Error Reduction Ratio
ESC Electronic Speed Controller
FBW Fly-By-Wire
FEM Finite Element Model
FHSS Frequency Hopping Spread Spectrum
FPV First-Person View
GA General Aviation
GCS Ground Control Station
GFRP Glass Fibre Reinforced Polymer
GUI Graphical User Interface
HM High Modulus
HS High Strength
HUD Head-Up Display
IFW Inboard Fixed Wing

ISA International Standard Atmosphere
LE Leading Edge
LiPo Lithium-ion Polymer
LoS Line-of-Sight
LRS Long-Range System
MAC Mean Aerodynamic Chord
MALE Medium Altitude Long Endurance
MIT Massachusetts Institute of technology
MPC Multipoint Constraint
MTOW Maximum Takeoff Weight
NI National Instruments
NiMh Nickel–Metal Hydride
NTP Normal Temperature and Pressure
OMW Outboard Moving Wing
PPM Pulse-Position Modulation
PTFE Polytetrafluoroethylene
PVC Polyvinyl Chloride
PWM Pulse-Width Modulation
PXI PCI eXtensions for Instrumentation
RAMP Range Amplified MultiPoint
RC Radio Control
ROC Rate Of Climb
RPAS Remotely Piloted Aircraft System
RPM Rotation(s) Per Minute
RSSI Receiver Signal Strength Indication
RTL Return To Launch
RX Receiver
SDK Software Development Kit
SERR Sum of Error Reduction Ratio
SMA Shape Memory Alloy
SMP Shape Memory Polymer
SQP Sequential Quadratic Programming
SR Strength Ratio
TE Trailing Edge
TRL Technology Readiness Level
TX Transmitter
UAV Unmanned Aerial Vehicle
VII Viscous Inviscid Interaction
VLM Vortex Lattice Method
VMC Visual Meteorological Conditions
VSW Variable-span Wing
XPS Extruded Polystyrene

Legal Mentions

This thesis and the associated research were made possible by the financial support of the Portuguese Science Foundation (FCT - Fundação para a Ciência e Tecnologia) through the PhD Grant SFRH/BD/90159/2012.

The author acknowledges LAETA/AeroG for supporting this thesis.

This thesis and the associated research was partially funded by the European Community's Seventh Framework Programme (FP7) under the Grant Agreement 314139. The CHANGE project (Combined morphing assessment software using flight envelope data and mission based morphing prototype wing development) was a Level 1 project funded under the topic AAT.2012.1.1-2. involving 9 partners. The project started on the 1st of August 2012, and ended in December 2015, lasting for a total of 40 months.

Acknowledgements

I wish to acknowledge my supervisor, Professor Pedro Vieira Gamboa, for the guidance, trust and open mindedness that allowed me to feel the joy in my research. His broad scientific perspective allied to his understanding of human motivations proved to be valuable for pointing out to me the necessary changes in the direction of my research. A heartfelt thank you to you for your academic input but most importantly for your continuous friendship and encouragement, over the last few years.

I also wish to thank Dr Yifan Zhao at University of Cranfield, United Kingdom, for his collaboration in the polynomial approximations.

I would like to extend a special thanks to my friend and former colleague Joaquim Sousa. Joaquim worked tirelessly on the Olharapo instrumentation and VSW prototype with me and was an enormous help. Joaquim did an incredible amount of work in testing out the concept and he was very patient with all the required design iterations. I would also want to thank the contributions by João Felício and Lino Miguel to various aspects of the development of the VSW concept, in particular manufacturing.

I am also indebted to everyone that shared their time with me in the last few years, for the good times, the valuable ideas, the provoking discussions and so much more: Pedro Albuquerque, Luís Cândido, Alexandre Nunes, Diogo Sousa, Pedro Alves, Paulo Neves, Pedro Moutinho, Afonso Rodrigues and Alexandre Duarte.

I thank my parents, Agostinho and Ermelinda Santos, and also my grandmother Alexandrina, for their continued and unconditional support throughout my academic career and all other aspects of my life. They have always been a driving influence in my life and I appreciate them so much for the path they have set me on. Without them, none of this would have been possible.

I would like to express my sincere gratitude to Sara Zorro for her love and patience, especially in those moments when my thoughts were focussed on nothing but work. Without her I would not been able to conclude my work.

xxx

Patience and perseverance have a magical effect before which difficulties disappear and obstacles vanish into air.

John Quincy Adams - 6th President of the United States of America (1825-29)

Chapter 1

Introduction

1.1 Background and Motivation

The search for increased efficiency has been one of the greatest motivators of technological development. Therefore, activities that consume more resources or depend on scarcer resources are under more pressure to achieve more without sacrificing those resources. On the other hand, due to the use of the planet resources, human activities have an impact on the environment. During the last century, the impacts of human activity have been studied, leading to an increasing awareness of its effects. This in turn lead to an increased social pressure to mitigate the negative impacts of the modern way of life. The transportation industry is a natural target, due to its reliance on fossil fuels and its emissions of pollutant gases. These economic and environmental challenges, and the ever increasing public awareness, drive companies and unite countries in search for more efficient ways to reach their goals.

Breakthroughs in many fields have provided evolutionary improvements in aircraft performance. Newer aircraft generations are able to achieve reductions in operational cost of nearly a factor of three since the Boeing 707. This has been accomplished through improvements in aerodynamics, structures and materials, control systems and primarily using new propulsion technology [1]. Aeroplanes are now fabricated using materials with higher specific strength and stiffness ratios, being possible to achieve lighter airframe structures. High-bypass ratio turbofan engines are now a standard in commercial aviation. Both mentioned aspects are just an example of the technologies that increased range and reduced fuel consumptions in commercial aviation (CA). Despite the high levels of optimization and innovation in the aviation industry, all modern commercial planes configurations virtually share the same general features for three or four decades ago [2]. Therefore, no radical changes to aircraft's configuration have been made, as can be seen in Fig.1.1. Boeing 707 first flight was in 1957 whereas the Airbus A340 was in 1991. More than three decades separate the two aircraft, but the configurations look alike.

Due to the heterogeneous nature of aircraft operation, one significant limitation persists: one aircraft must perform largely dissimilar missions phases, ranging from taxi, takeoff, climb and cruise to the descent and landing. The operating conditions are also highly variable, with different altitudes and air temperatures. In classical aircraft design, the baseline design provides optimal performance for the most important flight phase, e.g. cruise for commercial airliners. In order to satisfy additional constraints posed by other flight phases, the baseline is modified and augmented by discrete mechanisms. Consequently, the final design is generally a compromise between several sub-optimal aerodynamic shapes. Therefore, it is, in principle, impossible for a single, fixed design to perform optimally across the various missions. This suggests that an aircraft able to significantly change its shape throughout the flight, could operate more efficiently during all flight stages.

One possible answer to that problem is morphing. The word morphing has its root in the Greek words morphology and metamorphosis. Morphology is a branch of biology which studies

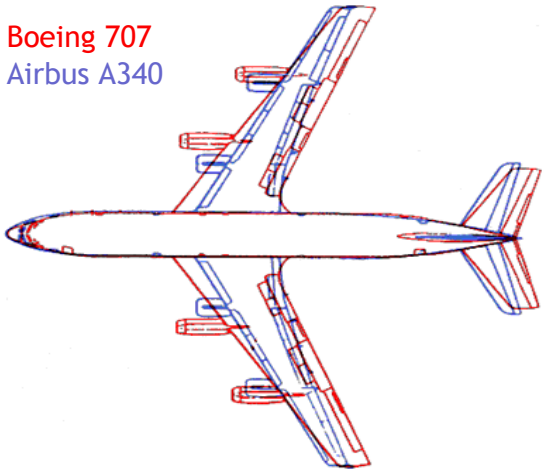

Figure 1.1: Comparison between the planform configuration of Boeing 707 and Airbus A340 (adapted from [2]).

the shape and structure of an organism while metamorphosis is synonymous of transformation [3], which is associated to biological transformation, involving a conspicuous and relatively abrupt change in the animal's body structure. This association to biology is not unexpected, since morphing aircraft quite often resemble or include features of birds and insects. Therefore, biologically inspired technology is frequent in morphing aircraft studies.

The deconstruction of the word morphing gives some clues about its definition. However, we are a long way from an exact definition or an agreement between the researchers about the type or the extent of the geometrical changes necessary to qualify an aircraft for the title morphing [4]. According to Weisshaar [5], morphing is a technology, or set of technologies, that allows air vehicles to alter their characteristics to achieve improved flight performance and control authority, or to complete tasks that are not possible without this technology. The NATO RTO Technical Team on morphing vehicles suggested that morphing is the real-time adaptation to enable multi-point optimised performance [6]. A more detailed definition was provided by the DARPA Morphing Aircraft Structures (MAS) program. According to Seigler [7], the MAS program defined the morphing aircraft as a multi-role platform that changes its state substantially to adapt to changing mission environments, provides superior system capability not possible without reconfiguration, and uses a design that integrates innovative combinations of advanced materials, actuators, flow controllers, and mechanisms to achieve the state change.

The majority of the authors accept that morphing does not include systems that are only able to adopt a few discrete positions and are only intended for use in specific circumstances (as is the case with traditional moving parts on aircraft, such as retractable landing-gears, flaps, spoilers and slats) [4]. However, some authors consider these conventional systems a form of discrete morphing. Since the purpose of morphing is to improve the performance and/or extend the capabilities of an aircraft, the definition does not include the control surfaces (e.g. ailerons, elevators, rudder) whose primary function is to command the aircraft's attitude.

Shape changes have been used to modify the aerodynamic characteristics of aircraft since the early days of flight. Probably the first and most renowned example is wing warping, i.e., twist motion of the wings, to achieve roll control. The Wright Brothers designed this mechanism in 1899 and employed it subsequently in all their designs, most notably during their first successful flight demonstrating a coordinated turning manoeuvre in 1905 [8].

In the past years the development of morphing wing technologies has received a great deal of interest from the scientific community. These technologies potentially enable an increase in aircraft efficiency by changing the wing shape thus allowing the aircraft to fly near its optimal performance point at different flight conditions. Joshi et al.[9] clearly demonstrated the advantages of such technologies in expanding the flight envelope of a fixed geometry aircraft, so that new multi-role missions could be performed. They used the Firebee Unmanned Aerial Vehicle (UAV) as the base design and then ran two distinct optimizations for each of the important flight stages or manoeuvres. The first optimization consisted in obtaining the optimum aerofoil for each flight condition while the second aimed at determining the most suitable wing planform for the same condition. The morphing strategies were effectively compared using a *spider plot*, which is presented in Fig.1.2.

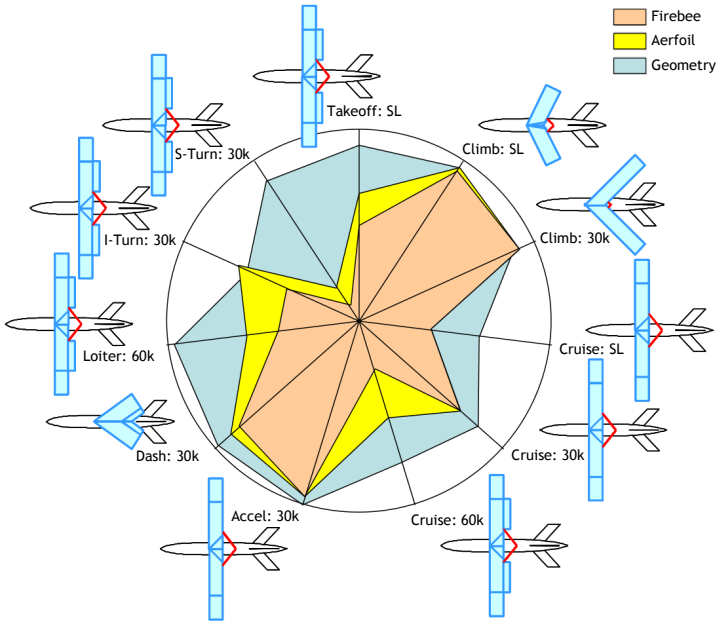

Figure 1.2: *Spider plot* comparing predicted performance of the fixed-geometry Firebee, a morphing aerofoil Firebee and a morphing planform Firebee (adapted from [9]).

In the plot, the fixed geometry Firebee appears as the innermost area, demonstrating worse overall performance. Since it was designed as a high speed target UAV, it excels at climbing and high speed flight, but shows poorer performance at high altitudes, particularly in the ability to perform a sustained turn at 60000 ft above sea level. Moving outward from the centre of the plot, one can see an aircraft with the UAV's wing planform, but the aerofoil can morph to a shape better suited to each performance point flight condition. This aerofoil morphing provides some notable improvements in performance, particularly in the phases of flight for which the original Firebee is not well suited. The outermost shaded area represents the performance of a Firebee sized aircraft with a wing capable of changing span, chord and sweep angle. This planform morphing significantly improves the aircraft performance over that provided by morphing the aerofoil alone.

The presented case study provides some valuable information about the benefits that can be attained using morphing aircraft technologies. Additionally, it shows that morphing can assume a variety of shapes, from aerofoil variation to planform shape changes. The use of unnamed aerial vehicles (UAV) or remotely piloted aircraft systems (RPAS) is not incidental, since there is a broad consensus that current morphing technology has not reached the maturity

required to be adopted by major aircraft manufacturers, as many concepts have a technology readiness level (TRL) that is still too low. Another topic that has not been completely clarified is the role of the aircraft in which the morphing technology is supposed to be introduced. In fact, considering the broad definition of morphing aircraft, in which large shape changes take place, a multi-role aircraft is more likely to benefit from these technologies, due to the high dissimilar flight phases that need to be accomplished.

The increase in structural and actuation mass can be a serious problem in morphing structures. Skillen and Crossley [10] demonstrated that the mechanisms can account for a considerable portion of the mass increase and are highly dependent of the wing geometry. Moreover, the development of a morphing wing requires the availability of materials and solutions that guarantee the necessary deformation of the structure while maintaining structural integrity and load-bearing capability. The intricate mechanisms used in morphing structures are often heavy, which reduces, or potently completely negate, the performance increase of the morphing aircraft. Part of this mass penalty is determined by the required actuators and associated batteries, which are mainly driven by the required actuation force and energy. The force and energy requirements of such concepts are other factors that need to be understood, in order to develop light and energy efficient solutions. Breuker et al.[11] focused on two underexposed influences on these: flight condition at which morphing should take place and the order of the morphing manoeuvres, i.e., morphing scheduling. Their work proved that proper flight conditions and adequate morphing schedule can reduce energy consumption and/or effectively reduce the actuator weight. The latter is due to the reduced actuation system requirements (e.g. force and/or speed). Moreover, the results showed that there is not necessarily one optimal flight condition or morphing schedule and a trade-off needs to be made.

From what have been said, it can be inferred that the current challenges of morphing vehicle design are the additional weight and complexity, the power consumption of the required distributed actuation concepts and the development of structural mechanization concepts. Additionally, there is a strong need to understand the scalability of morphing wing concepts to achieve sufficient structural stiffness [12].

1.2 Morphing Aircraft Technologies

Research and development is being made on new concepts that challenge current design philosophies: morphing aircraft. As said before, a morphing aircraft is defined as having the capability to perform significant controlled shape changes during flight, with the purpose of increasing efficiency, versatility and/or mission performance. Contrary to traditional aircraft that are designed as a compromise of various performance needs, a single morphing aircraft can excel at numerous tasks [13]. Due to the potential for improving aircraft performance and, consequently reducing costs and environmental footprint, morphing is currently the subject of thorough studies, covering different aircraft components and using different materials and systems. The wing is the major aerodynamic element of an aircraft and, therefore is the optimum candidate for morphing. Over the past few decades, numerous adaptative designs have been proposed, being applied to different geometrical parameters of the wing. Morphing technologies can be classified in terms of shape parameters (what to morph), performance benefits (why morph), and enabling technologies (how to morph) [14]. Barbarino et al.[15] compiled over 150

morphing concepts (for fixed wing and rotary wing applications) classified according to shape parameters. Figure 1.3 shows the classification of morphing strategies followed by the cited author.

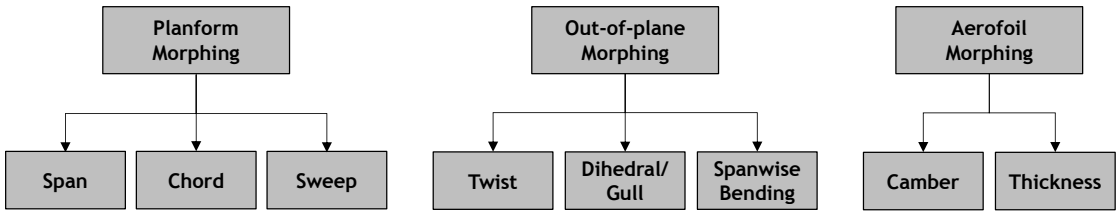

Figure 1.3: Morphing wing technologies organized in categories (adapted from [15]).

These technologies can be divided into three different categories according to the type of geometric transformation implemented: planform changes, out-of-plane transformations and aerofoil adjustments. Planform changes include variations of the wing's chord, sweep and span. Regarding the out-of-plane transformations, it includes twist, dihedral and spanwise bending. Finally, aerofoil adjustments include camber and thickness as the main geometric transformations.

In the next sections, examples of such morphing technologies are given, with a special emphasis on span varying wings and focusing only on technologies applied to fixed wing aircraft. For each morphing category an explanation of the potential benefits is also given. Note that, this is not an exhaustive survey and is intended to contextualize and provide the reader with a broader view of the state-of-the-art of past and present technologies.

1.2.1 Span Variation

This type of morphing belongs to the planform changes of the wing and implies that the aircraft has different wingspans throughout the flight. As a result of a wingspan increase, the aspect ratio and wing area increases and decreases the spanwise lift distribution, when considering a constant lift. In this way, the induced drag of this wing decreases and consequently the efficiency and range of the vehicle increases. Therefore, the increase in span is beneficial at low speed flight, since the induced drag is dominant, namely during takeoff and landing flight phases. A smaller span is beneficial at higher speeds due to the wetted area reduction. This, in turn, reduces the aircraft friction drag. However, the in-flight span variation can considerably change the wing-root bending moment due to the longer span [16].

Different methodologies have been applied to achieve span variation. Probably the most successful methodology is the telescopic concept. In this methodology, the movable part is rigid and slides inside or outside a central fixed wing. Other methodologies rely on the use of elastomeric skins, in which the skin stretches and retracts to maintain the aerodynamic shape of an internal span changing structure. Additionally, deployable inflatable wings have been used with some success.

1.2.1.1 Telescopic Wings

The first variable-span wing was realized using a telescopic type concept in 1931 by the Russian Ivan Makhonine on the MAK-10 aircraft. This system was based on a telescopic mechanism where the outer panels moved along the wingspan within the central panels of the wing. Using a pneumatic actuation, the wingspan increased up to 62% of its original size, from 13 m to 21 m, thus causing a 57% increase in its area. This aircraft served as the first proof of concept. With the support of the French government, the concept evolved into a new aircraft, the MAK-101, which was capable of reaching 375 km/h with the wings retracted. By the end World War II, Makhonine's work culminated in his last project, the MAK-123, which flew for the first time in 1947. This aircraft was very peculiar because, in addition to having telescopic wings, it had space for four occupants in a tandem arrangement. The aircraft, shown in Fig.1.4, did not show any undesirable characteristics and its operating system worked reliably, proving the feasibility of such concept [17].

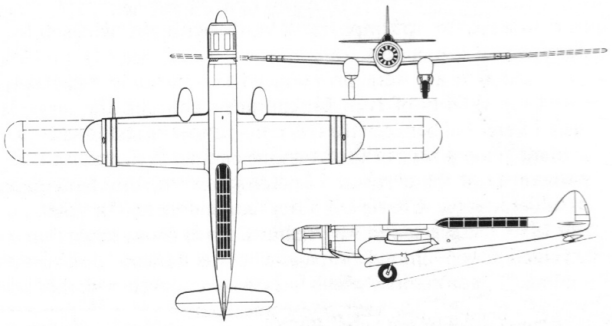

Figure 1.4: Planform view of the MAK-123 aircraft [17].

The Akaflieg Stuttgart FS-29 experimental high performance sailplane, developed 44 years later, in 1972, used telescopic wings to optimise both low speed thermalling and high speed penetration performance without the added induced drag of camber and area changing flaps (Fig.1.5(a)). The wing of the glider consisted of a fixed central section and a movable external part that slides on the outside. The actuating mechanism consisted of a pilot operated crank, which was connected to a worm screw. A nut connected to the moving part transformed the rotation movement into translation, thus changing the span. In the retracted configuration the wingspan was 13.3 m, being the corresponding area 8.56 m^2. For the extended wing configuration the wingspan was 19 m, with an area of 12.65 m^2 [18]. The sailplane was built using a combination of Carbon Fibre Reinforced Polymer (CFRP), Glass Fibre Reinforced Polymer (GFRP), Polyvinyl Chloride (PVC) foam and steel and aluminium alloys.

In 1997, Gevers Aircraft Inc. introduced a new concept of aircraft with a variable-span wing, to be used on a six-seat amphibious aircraft. The wing was composed of a fixed central section and two extendible outer sections, using an overlapping extension spar system. The central section was optimized for high speeds (low drag and high stiffness) and the completely retractable high-lift section was optimized for low speed, i.e., takeoff and landing. When in the minimum wingspan configuration of 7.87 m, cruising speeds above 450 km/h could be achieved. The aircraft stall speed was approximately 100 km/h in the maximum span configuration of 15.24 m [19].

Arrison et al.[20], modified a model aeroplane purchased in kit, so that it could accommodate a telescopic wing. They chose a flying wing model, Delta Vortex RC, which after in-

clusion of the telescopic wing was renamed BetaMax. In Fig.1.5(b) it is possible to visualize the original and the modified version of this model aeroplane. The wing actuating mechanism consisted of a pinion coupled to a servomotor, and two racks, each one connected to one of the wings. This system allowed the original model aeroplane to increase its span from 1.105 m to 1.359 m. The data collected from the flight testing campaign was not conclusive, because they did not perform the same type of manoeuvres for both versions. However, a numerical study conducted for both configurations predicted an increase in range of 19%.

(a) (b)

Figure 1.5: (a) FS-29 on display at the Deutsches Museum Flugwerft Schleißheim (photo by Ingo Warnecke) [18] and (b) Delta Vortex RC model aeroplane and its modified version with telescopic wings [20].

Within the framework of the DARPA-funded Morphing Aircraft Structures (MAS) program, Aerovisions Inc. developed an Unmanned Morphing Aerial Attack Vehicle (UMAAV). This vehicle consisted of several sliding mechanisms, in which the wingspan was inversely proportional to the cruise speed, and allowed for several operating conditions from loiter to high speed attack, as shown in Fig.1.6. A first configuration with wings fully extended (Fig.1.6(a))) is used during the loiter periods. A second intermediate configuration (Fig.1.6(b))) allows fast cruising and the last configuration (Fig.1.6(c)) is used for high speed attacks [21].

(a) (b) (c)

Figure 1.6: UMAAV in three configurations: (a) loiter, (b) fast cruise and (c) high speed dash [21].

Blondeau et al.[22] designed and fabricated a three-segmented telescopic wing for an UAV. The wing could undergo a 114% change in the aspect ratio, while supporting aerodynamic loads. They used hollow fibreglass shells to preserve the spanwise aerofoil geometry and ensure compact storage and deployment of the telescopic wing. To reduce the weight, they replaced the wing spars with pneumatic actuators that could support the aerodynamic loads on the wing. Their telescopic spar design consisted of three concentric circular aluminium tubes of decreasing diameter and increasing length, connected by ceramic linear bearings, and actuated by a pressure differential. The wing prototype can be seen in Fig.1.7(a). After wind tunnel testing, they found that for the smaller span configuration (0.20 m), the maximum efficiency exceeded

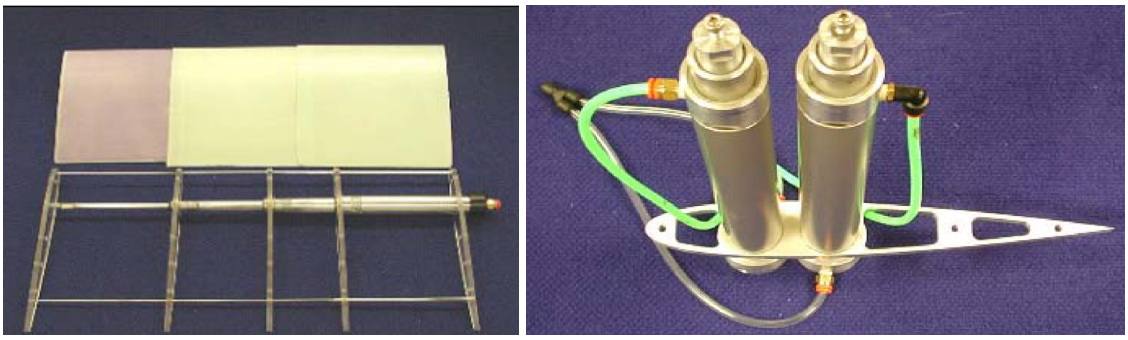

(a) (b)

Figure 1.7: Pneumatic telescopic wing prototype: (a) prototype with a single pneumatic actuator [22] and (b) double pneumatic actuator [23].

by 15% the efficiency of a fixed wing with the same dimensions. Such an event was explained by a lower friction drag and a greater flexibility of the telescopic wing, which tends to change the characteristics of the flow, thus increasing the angle of attack at the tip. For the larger wing configuration (0.38 m), the wing achieved aerodynamic efficiencies between 9 and 10, about 25% less than its rigid fixed wing counterpart, due to the fact that the telescopic wing had a low torsional stiffness, being observed a tip rotation of up to 5°. In a further development, Blondeau and Pines [23] adopted two identical telescopic spars instead of one, mechanically coupled by ribs, to prevent wing twist and fluttering. The new prototype could undergo a 230% change in aspect ratio and discontinuities between wing segments were reduced giving less parasitic drag. In its maximum span configuration, the telescopic wing achieved lift-to-drag ratios as high as 16, which were similar to the ones obtained using a solid foam-core wing. However, the authors did not explore the mass penalties of using pneumatic actuator, both in the actuator itself and the necessity of a pressurized air source.

Neal et al.[24] designed and demonstrated a variable-planform aircraft capable of large wing planform changes in span and sweep, using a telescopic pneumatic actuator. The aspect ratio could change up to 131% through combined span and sweep, while wing area could change by 31%. Wind tunnel results showed that only three planform geometries were required to maintain minimum drag over a large range of lift coefficients. In a further development, Neal et al.[25] redesigned the vehicle to implement a variable-geometry tail and increased the strength of the structure and mechanisms. This vehicle, called the Adaptive Planform Vehicle Experiment (APVE), used pneumatic actuators to control the span of the wing, resist the air loads and support the twist mechanism. Twist was accomplished by rotary pneumatic actuators and wing sweep was controlled by lead-screw actuators which were non-backdrivable (Fig.1.8). The wing skin was mould compliant with adequate stiffness to allow twisting while bearing the loads. Vortex Lattice Method (VLM) analysis and experimental results showed similar trends on the lift curve slope and aerodynamic centre, caused by morphing the vehicle. Overall, the advancements of the APVE are the combination of multiple morphing degrees of freedom and the ability to precisely control the morphing rate for transient aerodynamic experimentation and flight control testing.

More recently, researchers from the MIT laboratory in Lincoln, Michael Stern and Eli Cohen [26], developed an Additive Unmanned Aerial Vehicle (AUAV) with the purpose of collecting meteorological data. All the UAV components were manufactured using additive manufacturing process or 3D printing. The wing is composed of a fixed central part and two movable parts,

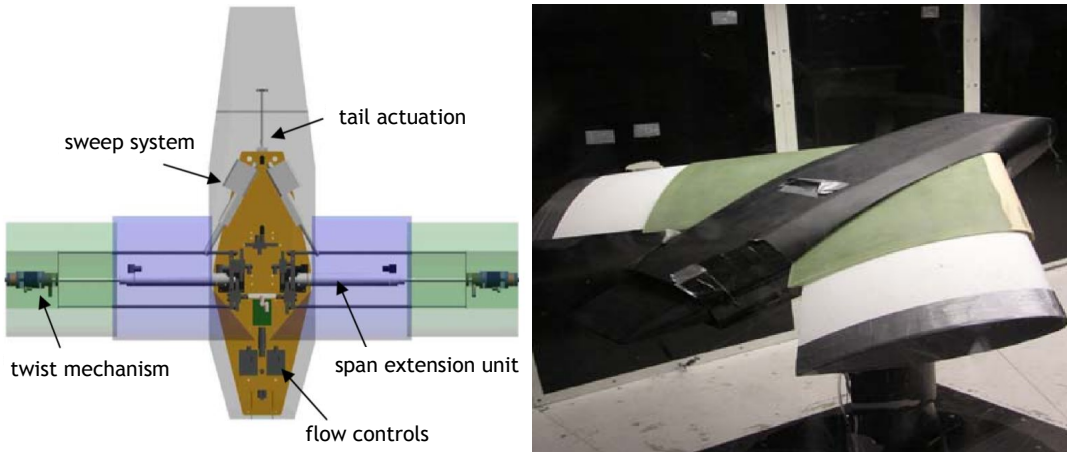

Figure 1.8: APVE: (a) overview of internal vehicle structure and (b) experimental model mounted in the wing tunnel [25].

that slide inside the interior of the fixed portion, using a system of rack and pinion actuated by a direct current (DC) motor. In a fully extended wing configuration, the wingspan measures 2.032 m with an equivalent area of 0.325 m^2. In a fully retracted configuration, the wingspan is 1.422 m and the wing area is 0.236 m^2, which equates to an area reduction of 27%. In Fig.1.9 it is possible to observe the developed prototype during a flight demonstration. No performance or flight testing data was provided.

Figure 1.9: AUAV during a demonstration flight [26].

1.2.1.2 Non-telescopic Wings

Joo et al.[27] and Bharti et al.[28] explored scissor-like mechanisms as a way to achieve span morphing mechanisms. The former explored the optimal placement of actuators on the scissor-like mechanism. The latter focused on developing an internal mechanism of a wing that can produce sweep and span changes. A prototype was built using a tendon-actuated compliant cellular truss made of diamond or hexagonal unit cells, allowing 55% span increase. Johnson et al.[29] went further and related optimal actuator placement on energy efficiency of morphing wings, using diamond-shaped cells. A finite element model was developed, considering an elastic skin, actuator and aerodynamic loads, and a two-stage optimization was used to optimize

actuator position and placement for different constraints and loadings.

More recently, Ajaj et al.[30] developed a variable-span wing using a similar principle: a zigzag wing-box concept. This system allows the wingspan to be varied by 44% (22% extension and 22% retraction). The zigzag wing-box consists of a rigid part and a morphing part, as seen in Fig.1.10. The rigid part is a semi-monocoque construction that transfers the aerodynamic loads from the morphing part to the fuselage. The morphing part consists of various morphing partitions where in each partition there are two spars each consisting of two beams hinged together. Each morphing partition is covered by flexible skin and is bounded by two ribs through which the spars are connected. The ribs transfer the loads between the spars of adjacent morphing partitions and serve as the main structure to which the flexible skins are to be attached. They integrated such concept in the wing of a medium altitude long endurance (MALE) UAV to enhance its operational performance and provide roll control. They performed an equivalent modelling and preliminary sizing to assess its feasibility and quantify its potential benefits. It was concluded that, despite the concept being heavier than the conventional wing-box, it can still provide an endurance benefit of up to 5.5%. However, no actual prototype was built to corroborate the weight estimation and the challenges of building such spar concept were not addressed, since these types of structures present some technical challenges related with the detailed actuation and the necessity of robust compliant skins.

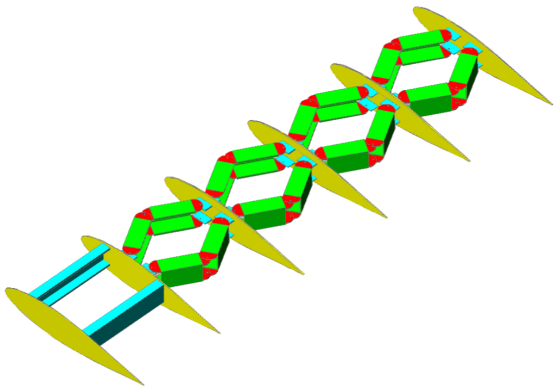

Figure 1.10: The Zigzag wing-box concept [30].

Gamboa et al.[31] designed a wing section capable of independent changes of span and chord by the use of extendible ribs and spars. They compared the performance achievable with such a morphing wing, in terms of minimum drag, to a traditional fixed wing at different flight speeds (15-50 m/s). An aero-structural analysis was performed, considering a mechanism that could expand in the spanwise direction, keeping the ribs evenly distributed, and increasing the chord using the ribs. The mechanism allowed a 50% increase in span and chord in various span stations, allowing taper variation. The skin was assumed to be rubber, wrapped as a sleeve around the wing internal mechanism and structure, with some pre-tension. The computational results for drag performance of the mechanism covered with an ideal skin able to comply perfectly with the expected shape changes, and the results of the mechanism covered with the actual elastomeric skin model were compared to an optimum fixed wing performance. The ideal skin model outperformed the fixed wing at all speeds except for speeds around the fixed wing's optimum design speed. The actual skin model showed increased drag compared to the fixed wing at all speeds due to skin's out-of-plane displacements. The final design was also heavy due to the servomotors, transmission components, and other equipments. Additionally, the torque requirements for the chord expansion mechanism were prohibitive. Gamboa et

al.[32] proposed new structural designs for chord and span extension, but no prototype results are available.

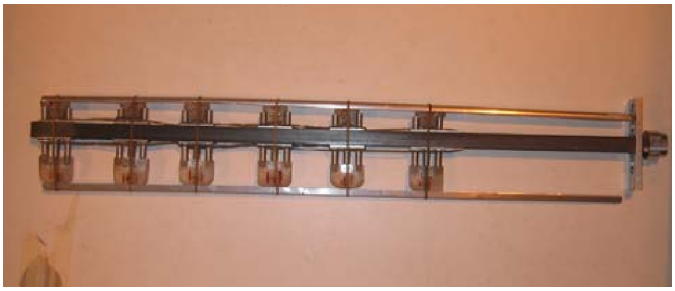

Figure 1.11: Complete assembly of the final span/chord morphing wing mechanism prototype [31].

Vocke et al.[33] explored the development of a continuous morphing structure, capable of increasing efficiency in several flight regimes. They developed a skin consisting of an elastomeric matrix composite and a support honeycomb substructure with zero Poisson's coefficient. The elastomeric composite was bonded to the substructure using an industrial silicone adhesive. The developed prototype was able to increase its wingspan by 100%, while retaining a constant chord during the actuation process. Thorough wind tunnel testing was conducted where various airspeeds, angles of attack (AOA) and span positions were tested. During the wind tunnel testing, the maximum out-of-plane displacement of the wing was analysed using imaging processing. The maximum computed displacement was 0.5 mm, which, as expected, occurred between ribs. This result was sufficient to conclude that an aerodynamically viable surface was maintained during all the tested conditions. Figure 1.12(a) shows the internal honeycomb substructure, Fig.1.12(b) the final prototype in the minimum span configuration and Fig.1.12(c) in maximum span configuration.

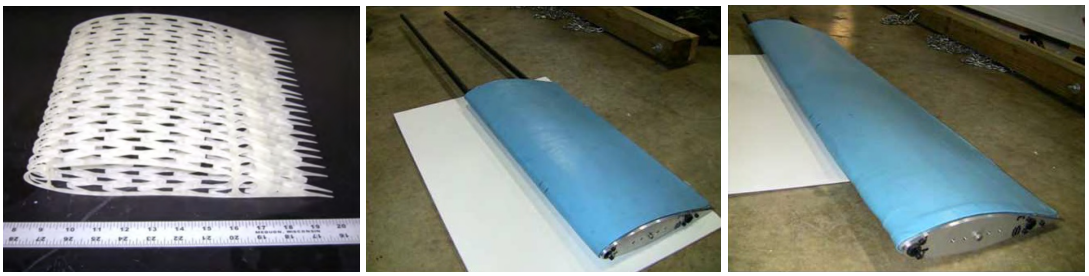

(a) (b) (c)

Figure 1.12: Continuous morphing structure: (a) internal support substructure using a zero Poisson honeycomb, and final prototype in (b) minimum span and (c) maximum span configuration [33].

Woods et al [34], developed a conceptual compliant skinned wing called Adaptive Aspect Ratio (AdAR). The AdAR concept combined four technologies to create a wing capable of 100% span change: a compliant skin made from elastomeric matrix composite (EMC), a telescopic rectangular box spar, sliding ribs, and a strap drive actuation system. Due to the change in length required of the skin surface, it becomes necessary to use hyper elastic materials to enable the large strains required for this compliance. In order to provide an effective interface between the compliant skin, which strains continuously along its length, and the telescopic spar, which morphs length in a much more discrete manner, the AdAR wing concept incorporated sliding ribs. The strap drive system is a tension driven actuation system which connects the inner

moving portion of the telescopic spar to the outer fixed portion, using a high strength fabric strap. The telescoping box beam, sliding ribs and the strap drive actuations system are clearly visible in Fig.1.13. No actual prototype was built and aerodynamic data were not provided by the authors.

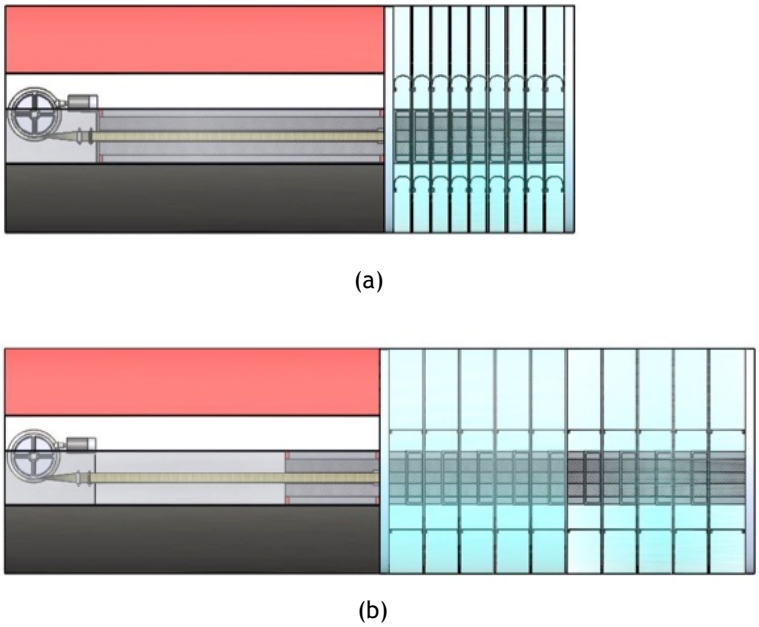

Figure 1.13: AdAR concept: (a) retracted and (b) fully extended [34].

Cadogan et al. performed in-depth studies on inflatable deployable wings, from an extensive literature review [35], to the use of wing warping to provide roll on inflatable wings [36]. In another study [37], the inflatable concept was investigated to allow compact packaging, easy transportation and aspect ratio change. The aspect ratio variation was considered for packed systems which were air dropped or gun launched, and for bigger vehicles requiring changes in aspect ratio to increase endurance. The study evaluated several materials such as unsupported films, film bladders supported by textile restraints and coated fabrics (Fig.1.14(a)). The "bumpy" surfaces, resulting of the inflatable cell arrangement improved aerodynamics for low Reynolds numbers (Re<500000), with the possibility of a covering being added if required. The work included several technology studies about camber morphing (wing warping) using embedded devices, aspect ratio morphing, concealment through structural materials development and system durability. For wing warping, Shape Memory Alloys (SMA) and servo actuated systems were considered (see Fig.1.14(b)). A combined servomotor and SMA mechanism was developed, being able to achieve quick response times with significant wing deflection – closer to that of a wing flap arrangement at the trailing edge. Both configurations, SMA and servo mechanism, were flight tested.

1.2.1.3 Related Studies

Bae et al.[38] performed both static aerodynamic and aeroelastic studies on the wing of a long-range cruise missile and highlighted some of the benefits and challenges associated with the design of a morphing wing capable of span variation. The morphing wing decreased the total drag by approximately 25%, while increasing the range by approximately 30%. The

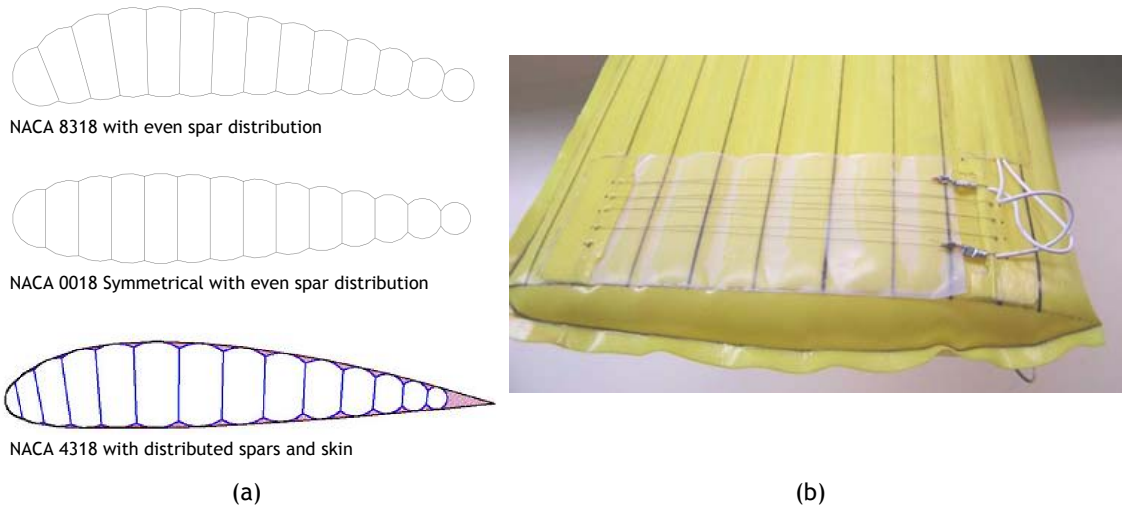

Figure 1.14: Inflatable wings: (a) distinct cross-sectional methodologies [35] and (b) SMA wires used to perform wing warping [37].

aeroelastic analysis showed that the flexibility of the morphing wing structure increased as the wingspan increased. At a given flight condition, the displacement from the aerodynamic loads was much larger than that of the conventional wing. Static aeroelastic considerations showed that a variable-span wing requires increased bending stiffness because the bending displacement is more significant than twist.

Vale et al.[39] performed an aero-structural design and analysis study of a telescopic wing with a conformal camber morphing capability. First, an aerodynamic analysis of a telescopic wing was performed, using a high and low speed aerofoil. The data obtained from these analyses was used to determine the optimum polar curves for drag reduction at different speeds. This information in turn provided the background for devising an optimal morphing strategy for drag reduction assuming that the telescopic wing aerofoil has the capability to step morph between the high and low speed aerofoils. A conformal camber morphing concept was then introduced, based on a non-uniform thickness distribution along the chord of the wing shell section that deforms from a symmetrical aerofoil shape into a cambered aerofoil shape under actuation. Finally, a comparison study was made between the performance of an aircraft equipped with the developed morphing wing and the performance of the same aircraft equipped with an optimized fixed wing for a cruise speed of 30 m/s and weight of 100 N. It was concluded that the morphing wing generally outperforms the optimum fixed wing with the exception of a 10% reduction in rate of climb and 4% drag penalty at 30 m/s cruise speed.

The benefits of span increase in a small UAV for loiter and attack missions were studied by Leylek et al.[40]. The aircraft dynamics were simulated using a six degree of freedom model and a *Monte Carlo* trade study was run with uncertainties and randomized missions to compare four different configurations. In this study, they concluded that, although morphing span improves performance, it was not significant to justify the increased complexity.

Lesieutre et al.[41] studied the capability of a two-dimensional span changing compliant cellular truss structure, in different aircraft weight classes. At Radio Control (RC) model scale, approximately 0.5-5 kg, the wing structure is capable of an 85% decrease in the planform area with a structural weight of 2.9% of the gross weight. As the gross weight of the aircraft increases, the achievable span reduction decreases while the structural weight fraction increases. For 50

and 500 kg aircraft, the decrease in planform area is 74% and 48%, respectively. At 50 kg, the wing structure comprises 7.4% of the gross weight, while at 500 kg, this increases to 8.9%. Therefore, it is possible to conclude that the benefit of span morphing (with the proposed structural concept) increases with gross weight but structural morphing capability decreases with gross weight, suggesting that for a given structural paradigm, there is a gross weight for which morphing is most advantageous and applicable.

Ajaj et al.[42] performed a comparison between the use of ailerons and the asymmetrical extension of a telescopic wing for roll controlling the UAV Herti from BAE systems. After aerodynamic simulations, they found that the maximum extension required to guarantee the same moment created by the 10° deflection in the ailerons was 36.4% of the half-wingspan. They verified that the rolling moment coefficient varies parabolically with the extension of the wingspan. They also found that with higher wing loading, the rolling sensitivity increased, i.e., less wingspan variation is necessary to create the same rolling moment. Therefore, for the same asymmetrical variation of span, an increase in the AOA, causes an increase in rolling moment coefficient.

Kryvokhatko and Sukhov [43] developed a small aeroplane model to investigate the effect of span variation on lift-to-drag ratio. The telescopic wing model was developed using two inserts at the ends of an inboard fixed wing (Fig.1.15). The model had a span of 1.85 m, being each insert 0.4 m long. The chord of fixed portion of the wing was 0.11 m (t/c=0.12), and the inserts portion 0.095 m (t/c=8.7). The wind tunnel study was conducted using a six component aerodynamic balance. They also visually investigated the presence of a vortex at the chord discontinuity between the fixed and moving wings. They concluded that increasing the span effectively reduces the induced drag, for the same lift coefficient. More importantly, they could not find a vortex in the chord discontinuity, even at high AOA (about 10°). Thus, they concluded that if the chord ratio of the variable wing to the fixed wing is above or equal to 0.86, then the joint vortex is less intense than a tip vortex at least by a factor of ten. Thus, the former has a negligible impact on induced drag.

Figure 1.15: Wind tunnel model used by Kryvokhatko and Sukhov [43].

Beaverstock et al.[44] proposed a low-fidelity framework to capture the effects of span morphing on flight performance and flight dynamics. A UAV with 25 kg, with a straight, rectangular, unswept wing was used to demonstrate the tool and results were presented for both symmetric and asymmetric span retraction. The span retraction was performed using the outboard 50% of the main wing, with up to 50% allowable span retraction. The study was performed for a loiter mission (55 km/h) and a high speed cruise (75-110 km/h). Span retraction was used to optimise the configuration performance and also to perform coordinated turns. Loiter results were presented for lateral coordinated turns, being the UAV trimmed using either rudder or

span retraction. It was concluded that the maximum trim error occurs when the roll and inertia dynamics are matched. They found that span retraction generally decreases both short period damping and Dutch roll damping. Additionally, loiter results suggested that the trim inputs required for a trim strategy using the rudder varied greatly from that using span retraction in a lateral coordinated turn and that when using a strategy that includes both span retraction and rudder control, the trimmed inputs were dominated by the span retraction parameter.

In a further development, Beaverstock et al.[45] investigated the effect of span and camber morphing on the mission performance of a UAV with the same characteristics. They optimized range between two speeds using various fixed wing and morphing wing strategies. Among other mission parameters, they investigated the maximum allowable span retraction and the influence of weight penalty on mission performance. They concluded that span morphing strategy with optimised fixed camber at the root can deliver up to 25% improvement in aerodynamic efficiency over a fixed camber and fixed span wing, for an allowable 50% retraction in a speed range of 50–115 km/h. Reducing the allowable retraction to 25% reduced the improvement to 8%–10%. On the other hand, the improvements in the efficiency achieved through camber morphing were more sensitive to the speed range in the mission, decreasing rapidly by changing the speed range, where span morphing appears more robust for an increase in speed range beyond the optimum. Span morphing, at the optimal mission speed range, with 25% allowable retraction, can allow up to a 12% increase in mass before no performance advantage was observed, whereas the camber morphing only allowed up to 3%. This conclusion is valuable to provide the designer with a mass budget that guarantees the improvements in mission performance.

1.2.2 Camber Variation

Camber morphing belongs to the aerofoil morphing, representing the effective curvature of an aerofoil. Thus, the term camber change refers to the alteration of the aerofoil curvature using active or passive actuation. The motivation to change the aerofoil camber lies in its effect in terms of lift and drag. The need for wing curvature change arises from the possibility, in the subsonic regime, to adjust continuously the aerofoil geometry at different flight conditions, thus increasing the lift-to-drag ratio [46]. Camber morphing can be used to change the pressure distribution. Potential benefits from camber morphing in this respect include replacing conventional flaps or control surfaces to remove the discontinuous interface between the main surface and the flap or control surface.

There are many methods that can be implemented to vary the camber. The wing camber can change either on specific parts (leading or trailing edge) or in a global manner, effectively changing the wing to act as an unique control surface. The choice of actuators can be conventional (servomotor, hydraulic and pneumatic) or solid-state “smart” materials (piezoelectrics and shape memory alloys).

1.2.2.1 Conventional Actuation

An active camber variation concept, that is continuous along the wing span, was investigated by Politecnico di Milano, by using the rotating rib concept applied to the trailing and leading edges of the wing [47]. They replaced the rigid connection between the control surface

skin and its ribs with discrete linear slides, allowing the skin to slide over the rib contour, allowing the control surface skin to have a continuous varying deflection along the span (Fig.1.16). Conventional hydraulic actuation was used. Numerical studies indicated that induced drag could be reduced between 6% and 15% on a commercial aeroplane.

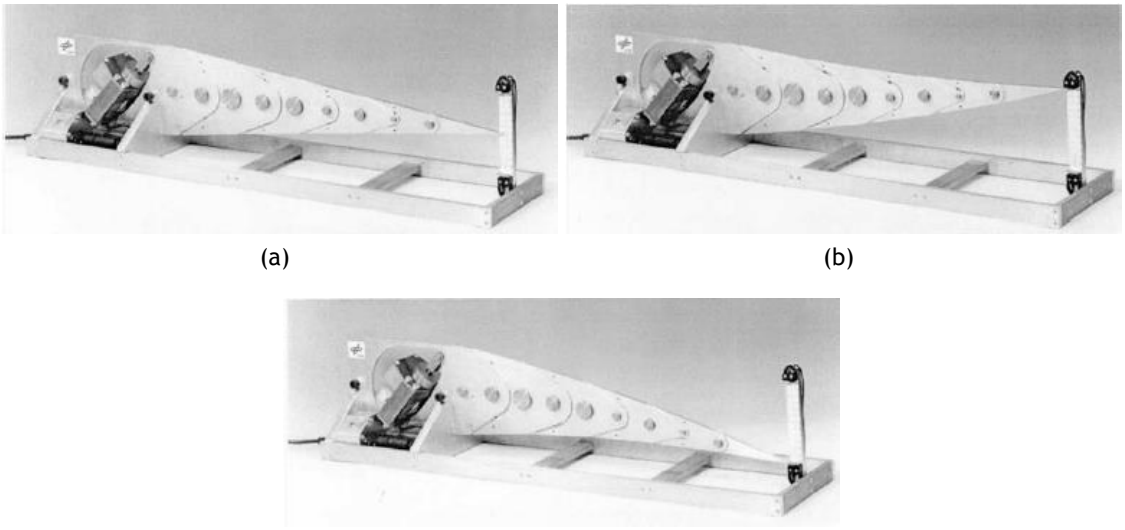

(a) (b)

(c)

Figure 1.16: Active adjustable rib in: (a) neutral position, (b) total upper and (c) total lower deflection [47].

Kota et al.[48], from Flexsys Inc., developed a functional, seamless, hinge-free morphing trailing edge, named the Mission Adaptive Compliant Wing (MACW). This wing used a variable-camber trailing edge in conjunction with a natural laminar flow aerofoil. The wing was flight tested at full-scale dynamic pressure, full-scale Mach number, and reduced-scale Reynolds numbers on the Scaled Composites White Knight aircraft. Data collected from flight testing revealed that laminar flow was maintained over approximately 60% of the aerofoil chord for the majority of lift range, allowing an increase in endurance by at least 15%. In a further development, a compliant structure was developed to enable a seamless transition between the fixed and flapped portions of the wing. The main purpose of this region was to reduce noise associated with the turbulent airflow generated by the discontinuous surfaces at the flap ends when the high lift flaps were deployed. This system was integrated in the MACW to form a seamless flap, named the FlexFoil control surface. This system was later integrated in a Gulfstream III business aircraft, replacing the primary trailing edge wing flaps (Fig.1.17). The test flights were performed in partnership with NASA and the Air Force Research Laboratory (AFRL), demonstrating full functionality and the possibility to reduce fuel consumption and decrease aircraft noise during takeoffs and landings [49].

Sahin et al.[50] developed an open trailing edge camber changing mechanism to be applied in an UAV wing. The morphing flap was made using aluminium sheets, being each section of the morphing surface driven by two servomotors actuators (Fig.1.18(a)). The symmetric actuation of the servomotors created a camber variation and an asymmetric actuation created a wing twist. The vehicle was successfully flown, demonstrating the effectiveness of the flap to perform roll control.

Woods et al.[51] introduced a novel aerofoil morphing structure known as the Fishbone

Figure 1.17: FlexFoil control surface installed in a Gulfstream III business aircraft [49].

Active Camber (FishBAC). This design employs a biologically inspired compliant structure to create large, continuous changes in aerofoil camber and section aerodynamic properties. The structure consists of a thin chordwise bending beam spine with stringers branching off to connect it to a pre-tensioned Elastomeric Matrix Composite (EMC) skin surface. Actuators mounted in the D-box spar induce bending moments on the spine through an antagonistic pair of tendons in a manner similar to natural musculature systems. A prototype section was built to explore specific aspects of the structural geometry, and demonstrated that it is capable of large camber changes (see Fig.1.18(b)) with low actuation effort.

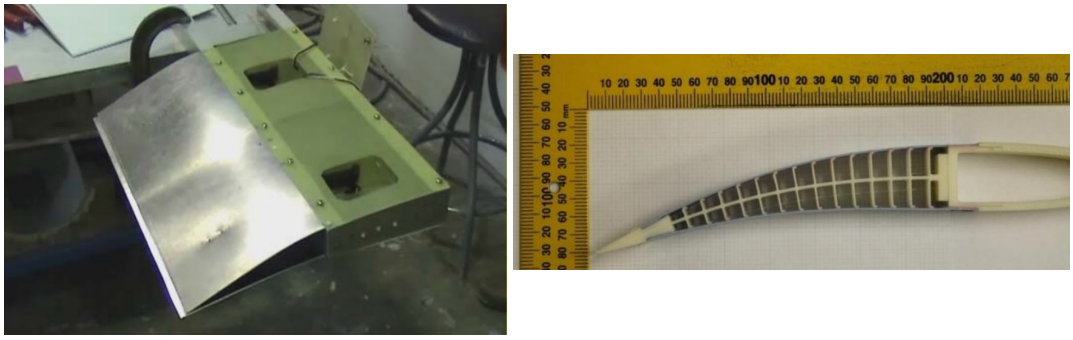

(a) (b)

Figure 1.18: (a) Aluminium morphing control surface [50] and (b) Fishbone Active Camber prototype deflected downwards [51].

Gaspari et al.[52] described a two-level approach for the optimal design of morphing aerofoils. The first level was responsible to create an optimal aerofoil shape that is a compromise between aerodynamic efficiency and the energy required for skin deformation. The second level defined the internal structure configuration, using topology optimization. This tool was based on a genetic algorithm that created a compliant structure able to match the optimal aerofoil shapes obtained in the first level (Fig.1.19). In a further development [53, 54, 55], this morphing concept was applied to the leading and trailing edge of a typical regional aircraft. A scaled wind tunnel model was designed and built for validating the concept. The first phase of the wind tunnel experiment was used to assess the predicted and the actual morphing shape, which corroborated the design and sizing of the actuator. The second phase was devoted to the aerodynamic assessment by means of the $C_L - \alpha$ curve determination, demonstrating the potential benefits of the leading/trailing edge morphing surfaces in increasing the maximum lift coefficient.

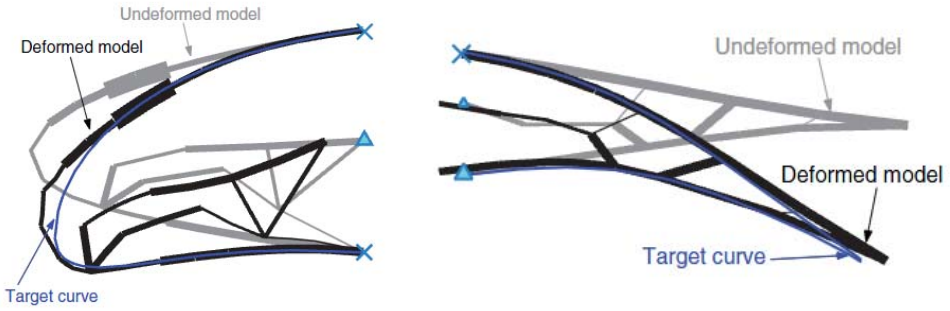

Figure 1.19: Compliant mechanism used to match optimal aerofoils shapes: (a) leading edge and (b) trailing edge [52].

Radestock et al.[56] developed a compliant skin/actuator mechanism to morph between two different aerofoils: NACA 2510 and NACA 6510. Geometric analysis concluded that both aerofoils could not be morphed into each other, by simple changing the camber. Therefore, a skin tailoring was implemented to achieve compliance between the two shapes. This optimization delivered the skin thickness at evenly distributed positions along the skin, a stringer position and the deflection at the stringer position. Then, a kinematic actuator was designed using topology optimization. The actuator was manufactured using fused deposition modelling. The load originating the shape change was created by a servomotor and introduced to the skin using an omega stringer. Wind tunnel testing showed complete functionality of the prototype.

Werter et al.[57] developed a combined twist and camber morphing, applied to the leading and trailing edge. By cutting the wing skin at both the leading and trailing edge close to the spar, a slot is obtained, which allows the skin to be actuated. The skin was actuated in the chordwise direction and since freedom of movement exists in the spanwise direction, a combination of twist and camber morphing can be obtained. Activating two actuators at different span positions equally results in camber, while differential actuation between the two actuators results in twist. The leading edge (LE) actuation is based on servo-actuators and a sliding mechanism supported by a ball linkage system. In the case of the trailing edge (TE), the sliding mechanism chosen used a straight guide system due to lack of space (height) for ball linkages. The skin was made out of pre-impregnated glass fibre. A proof of concept was developed and a demonstrator wing was built to fit a 25 kg UAV. Wind tunnel tests were carried out at a airspeed of 15 m/s and 28 m/s. Comparison between numerical simulations and experimental results showed good agreement and the concept showed merit for camber and twist morphing.

Integrated in the framework of SARISTU European research project, Pecora et al.[58] developed a novel architecture enabling wing trailing edge camber morphing to be applied in a large aircraft (EASA CS-25). They replaced the conventional monolithic box arrangement with a multi-box solution characterized by conventional spars and segmented adaptive ribs. Single-degree-of-freedom mechanisms, driven by load-bearing electro-mechanical actuators, were implemented to change the wing trailing edge shape by controlling the adaptive ribs individually. A compliant multi-material skin was used to accommodate the large deformation induced by ribs kinematics. Relying upon Finite Element Model (FEM), the morphing structure was proven to be compliant with EASA CS-25 requirements in terms of stress levels at limit and ultimate load conditions.

Koreanschi et al.[59, 60] developed a wing tip demonstrator equipped with an adaptive aileron and an adaptative upper surface (Fig.1.20). A genetic algorithm was applied for improving the aerodynamic performances, through delayed boundary layer transition of this wing, using the upper surface morphing and aileron deflection. The optimization was performed for 16 flight cases. The displacements computed with the optimization were reproduced during the wind tunnel tests, in order to match the upper surface shape and thus, allow a comparison of the optimized and experimental results. Wind tunnel testing showed full functionality of the demonstrator and the possibility to delay transition using these concepts. The results showed that the optimization overestimated the aerodynamic benefits.

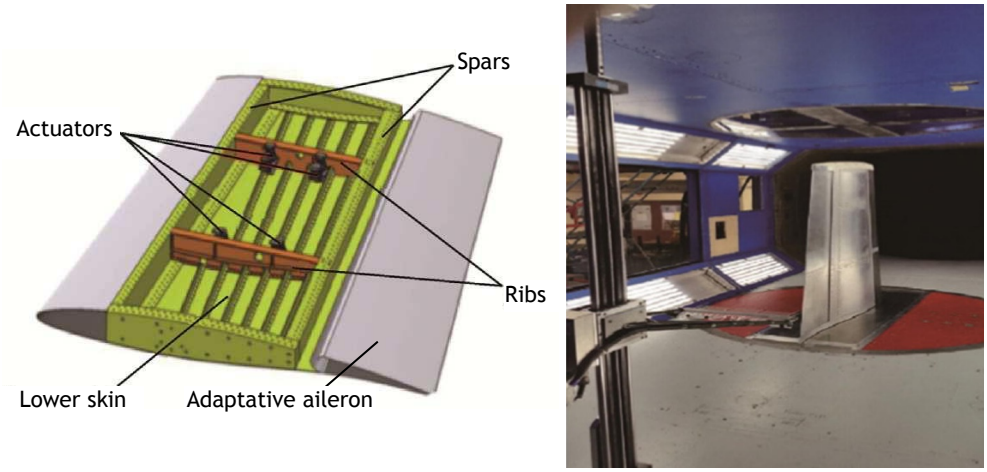

(a) (b)

Figure 1.20: Combined flexible upper skin/aileron: (a) structural elements (upper surface not shown) and (b) wing model setup [59].

1.2.2.2 Piezoelectric Actuation

Piezoelectric materials respond to mechanical force by generating an electric charge or voltage. This phenomenon is called the direct piezoelectric effect. On the other hand, when an electric field is applied to the piezoelectric, mechanical stress or strain is induced, being this phenomenon called the converse piezoelectric effect [61]. These materials have high frequency bandwidth and can therefore be applied in high frequency actuation and sensing. However, the displacements of such devices are small, generally in the μm scale.

Barrett et al.[62] employed piezoelectric elements along with elastic elements to magnify control deflections and forces of an aerodynamic surface, called post-buckled precompression (PBP) concept. A proof-of-concept empennage assembly and actuator were fabricated using the principles of PBP actuation. Quasi-static bench testing demonstrated deflections higher than $\pm 6^\circ$ at rates as high as 15 Hz. Additionally, the PBP actuator was shown to reduce the part count with respect to conventional servo actuators by one order of magnitude. In a subsequent work, Vos et al.[63] conducted a research to improve the PBP concept for aerodynamic applications. The actuator was mounted between the end of a tapered D-box spar, located at 40% chord position, and a trailing-edge stiffener. Axial precompression was generated in the piezoelectric elements by an elastic skin which covered the outside of the wing. The prototype demonstrated trailing-edge deflections of $\pm 3.1^\circ$, with a maximum frequency of 34 Hz. Wind tunnel and flight

testing showed that the PBP concept was capable of increasing the roll control authority of a small UAV (1.4 m span).

Piezoelectric Macro Fiber Composites (MFC) were extensively tested for camber control. Bilgen et al.[64] presented an application of MFC actuators on a 0.76 m wingspan morphing wing UAV. Two MFC actuators were bonded to the wings in an elevator/aileron (elevon) configuration and the camber of the wings was changed asymmetrically, using a voltage excitation. Sufficient roll control authority was proved in the wind tunnel as well as during the flight tests. The MFC power electronics were powered by an 11.1 V Lithium-ion Polymer (LiPo) battery, consuming only 3 W during peak operation. In another application, Paradie et al.[65] used MFC as actuators for roll control of an UAV wing with a thin profile. The design and optimization were based on a fully coupled structural fluid dynamics model that implemented constraints from available materials and manufacturing. A scaled prototype wing was manufactured. The computational models were validated with static and preliminary dynamic tests of the wing prototype, showing good agreement. Dynamic tests were also performed on a sandwich wing of the same size with conventional aileron control for comparison. The morphing wing showed lower rolling moment but it was sufficient for the intended application.

In a further evolution, Bilgen et al.[66] presented a completely servoless remotely piloted aircraft (Fig.1.21). MFC actuators were used to create variable-camber, continuous, piezocomposite wings, instead of the traditional servomotor controlled, discrete control surfaces. Wind tunnel tests and theoretical models were used to analyse the aerodynamic characteristics of the aircraft, providing a foundation for future MFC actuated control surfaces design.

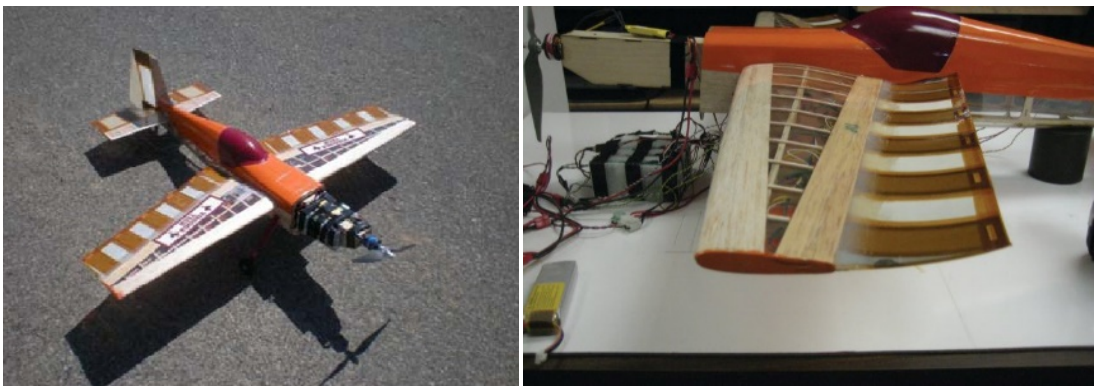

(a) (b)

Figure 1.21: Servoless remotely piloted aeroplane: (a) general view and (b) close view of aileron MFC actuators [66].

1.2.2.3 Shape Memory Alloy Actuation

Shape Memory Alloys (SMAs) belong to a class of shape memory materials (SMMs), which have the ability to “memorise” or retain their previous form when subjected to certain stimulus such as thermomechanical or magnetic variations [67]. Due to their generally good electric conductivity, they are usually heated using Joule effect. SMAs are used in low frequency applications, due to the time needed for heating and cooling cycles.

Elzey et al.[68] proposed a bio-inspired, fully reversing, shape morphing structural actuator. The actuator was comprised of a cellular flexible core sandwiched between shape memory

alloy face sheets. The heating of either SMA elements causes contraction of that face and resulted in a corresponding curvature change of the actuator. The core design was based on an assembly of modular elements that were able to rotate relative to one another. A prototype shape morphing panel was developed, in which vertebrate actuators were incorporated as ribs.

Alasty et al.[69] studied the effect of a variable shape wing applied to a small sized (less than one meter of wingspan) and ultra-light aircraft, focusing on aerodynamic efficiency and flight control. SMAs were used in detriment of traditional actuators, due to their high strength, low weight, and reduced dimensions. The aeroplane structure was made with balsa wood and nylon sticks. The wings were composed by two parts: a rigid frontal element, and a deformable rear element. SMA actuators were used in pairs in an antagonistic configuration, i.e., each wire acted in opposition to another. The wing shape variations were obtained using FEA and then imported to a Computational Fluid Dynamics (CFD) software to compute the aerodynamic coefficients. Simulation results demonstrated an effective improvement on manoeuvrability of the plane, when compared to the conventional models.

Seow et al.[70] studied the feasibility to control a wing flap using shape memory alloy. Two key issues were addressed: how to use SMA to effectively actuate the wing flap and how to improve the actuation frequency once the initial conceptual design proves to be feasible. A wing prototype was designed and fabricated, and the actuation of the flap was demonstrated, achieving an actuation angle of 5.2°. A second prototype achieved 15° deflection (Fig.1.22). Flexible skins were also explored and tested. Finally, the controllability of the prototype was investigated, including the measurement of power consumption, and the dependence of heating and cooling time on wire diameter. The results showed that better actuation rate could be achieved using small diameter SMA.

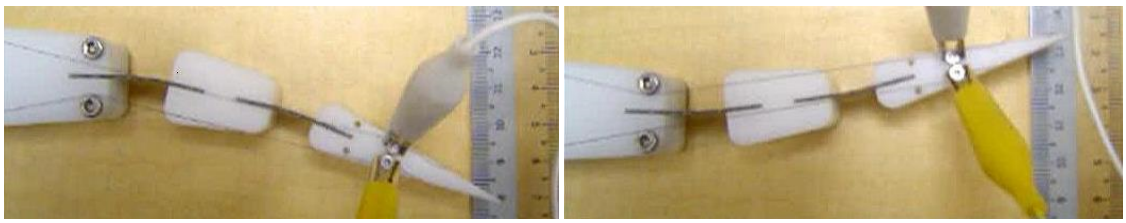

(a) (b)

Figure 1.22: Wing flap using shape memory alloy: (a) maximum upward deflection and (b) maximum downward deflection [70].

Abdullah et al.[71] used SMAs to alter the shape of an aerofoil, in order to increase the lift-to-drag ratio of an UAV. A flexible skin was used to allow the variable camber control surface to maintain a smooth surface. The aerodynamic effect of camber location and magnitude were analysed using a two-dimensional panel method. The authors found that shifting the location of maximum camber thickness from 10% to 50% of the chord, and increasing the camber from 1% to 5%, maximized lift-to-drag for low AOA. Therefore, the wing should use this range to permit multiple flight conditions with increased efficiency. This study focused on cruise efficiency rather than control, and thus the low response time of the SMA actuators did not pose a problem.

Barbarino et al.[72] studied the possibility of replacing a split flap on a full scale wing of a civil regional transport aircraft, by a hingeless, smooth morphed flap. An actuator was developed and tested, based on a SMA ribbon, capable of a net rotation of 5°. Then, a flap

bay, based on a compliant rib built as a series repetition of the SMA actuator, was designed and experimentally tested using static loads. The flap bay was 0.3 m wide, with two morphing ribs collocated at its edges (Fig.1.23). An aero-thermo-mechanical simulation within a FE approach was adopted to estimate the behaviour and performance of the compliant rib. Good numerical-experimental correlation was found for the unloaded case, while some fatigue issues emerged in presence of static loading.

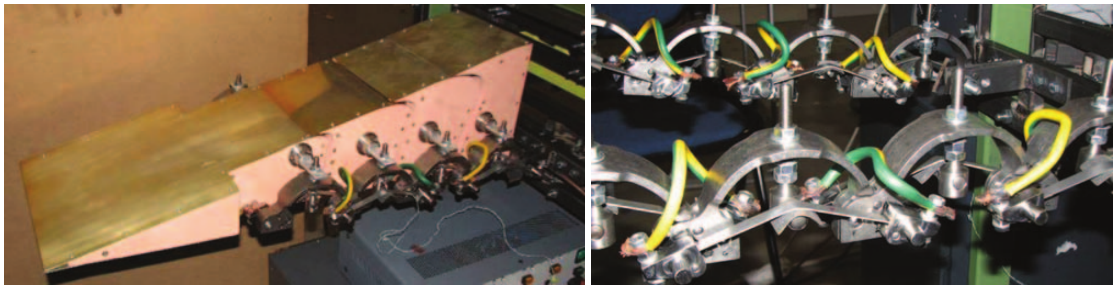

(a) (b)

Figure 1.23: Shape memory alloy ribbon actuator: (a) fully assembled demonstrator and (b) detail of the SMA ribbons [72].

Pecora et al.[73] studied another concept to substitute the conventional flap of a regional aircraft. The design assessment of an innovative flap architecture for a variable-camber trailing edge was described. The authors proposed an architecture that assures high deformability while keeping good load-sustaining capabilities. The trailing-edge structure was conceived as a set of interconnected morphing wing ribs moved by actuators embedded within the rib structure and based on SMA. Preliminary testing demonstrated structural feasibility of the morphing architecture. However, several issues were identified, mainly due to SMAs heating-cooling cycles and difficulties with elastomeric skins, necessary to provide a smooth shape.

1.2.3 Chord Variation

The chord variation belongs to the planform morphing and can be used to increase wing performance by changing its area, as well as the taper ratio and aspect ratio [16]. Both taper and aspect ratio variation can be used to minimize the wing induced drag. There is very limited investigation on chord variation on fixed wing aeroplanes, due to the smaller potential benefits (when compared with other strategies) and large challenges involved.

Probably the first aircraft to allow chord variation was the Baksaev LIG-7, developed in the Soviet Union in 1937 [5]. For takeoff and landing, six telescopic chord wing sections were extended from the fuselage to 2/3 of the wingspan, as can be seen in Fig.1.24. Each wing section, 0.5 m wide, was made of plywood, with a support rib on the inboard side and a light frame on the outboard side. The telescoping wing sections were retracted and extended by tensioned steel wires, operated manually from the cockpit. All retractable sections were completely hidden inside the fuselage when retracted. The morphing impact on performance was not significant, despite an area increase of around 44%, since the wing contributed only 20% of total drag.

Recent works of chord morphing were performed by Perkins et al.[74] and used dynamic modulus foam (DMF) to alter chord length, being able to achieve an 80% increase in lift. DMF

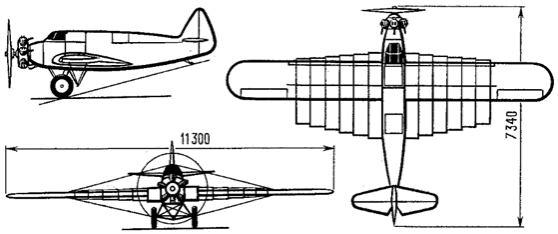

Figure 1.24: Bakshaev RK LIG-7 planform view.

foam is a lightweight form of shape memory polymer (SMP). An SMP was proposed for the skin, to accommodate large strains, and temperature activation was implemented using thin nichrome wires embedded in the skin. The prototype wing section demonstrated the chord extension upon heating, but it was not able to return to its original shape upon cooling, due to the low recovery stress of SMPs.

Reed et al.[75] used an interpenetrating rib mechanisms actuated with miniature DC motors and threaded screws. Partial rib structures that could slide through a central slotted box and alter the chordwise position of the leading and trailing edges were used. A flexible honeycomb structure kept the aerofoil shape during the chord variation. The system proved to be feasible, but the high added weight and complexity of the design were strong disadvantages, along with difficulties to smoothly actuate the mechanism.

The already discussed work of Gamboa et al.[32] provides an example of a morphing wing that can vary its chord. However, the use of an elastomeric skin proved to be problematic, due to out-of-plane displacements, and the associated significant aerodynamic penalty. The mechanism also proved to have a high weight penalty and hight actuation torque.

1.2.4 Sweep Variation

The reasons to use wing sweep are varied but it is most often used to delay the onset of shock waves and accompanying aerodynamic drag increase, caused by compressibility effects in transonic speeds. This is due to the decrease of the component of the airstream perpendicular to the wing [16]. It is also used to avoid the impingement of the shock waves with the wing tips, i.e., keep the aircraft inside the Mach cone at supersonic speeds. Aft-swept wings are more common in modern aeroplanes, although forward-swept wing designs offer aerodynamic performance improvements over the former, namely higher lift-to-drag ratios, lower trim drag, and better stall/spin characteristics. However, forward-swept wings have unfavourable static aeroelastic characteristics, namely, static divergence, requiring sufficient stiffness, and consequently, a wing mass penalty, to ensure adequate divergence speed margins [76]. Sweep variation is categorized in the planform change of the wing.

Full-scale development of variable-geometry wings began in Germany during World War II with the Messerschmitt P-1101, which had preset wing sweep (the sweep angle was set on the ground). The first swing-wing aircraft, the Bell X-5, flew in 1951 and was adapted from the P-1101, with a variable-sweep mechanism actuated by a jackscrew assembly [77]. Swing-wings became viable in the mid-1950s when the NASA Langley Research Centre developed a system with pivots outboard of the fuselage [78]. The first production aircraft with swing wing capability was the F-111, which entered service in 1967. Later, variable sweep angle was used

in the F-14 Tomcat and B-1 Lancer, among others.

The already mentioned work by Neal et al.[24] provided a sweeping mechanism for their shape morphing UAV that was actuated using two electromechanical, lead-screw actuators via a three-bar linkage. Later [25], the sweep actuator was redesigned to include new direct-drive sweep actuators with a higher load capacity and added rotating sweep supports to transmit reaction torques from the twist actuation and normal wing loads.

Probably the most successful sweep varying concept was developed by NextGen Aeronautics [79, 80, 81]. They designed and built an UAV, called the MFX-1, also known as the BatWing, with a wing that could undergo significant sweep changes during flight. An electric motor was used to deform an endoskeleton wing-box structure that was covered with an elastomeric skin with out-of-plane stiffeners. The wing was capable of five distinct configurations during flight, with an aspect ratio variation of 200%, a span variation of 40%, and wing area variation of 70%. Wing sweep and wing area could be controlled independently using four-bar linkages, revolute joints and slider mechanisms. The skin could strain by over 100%, while resisting the aerodynamic loading. The MFX-1 UAV was successfully flight tested in 2006. A larger version was developed in 2007, named MFX-2, and demonstrated a 40% change in wing area, a 73% change in span, and a 177% change in aspect ratio. Figure 1.25 shows the MFX-1 in high-lift and loiter configurations.

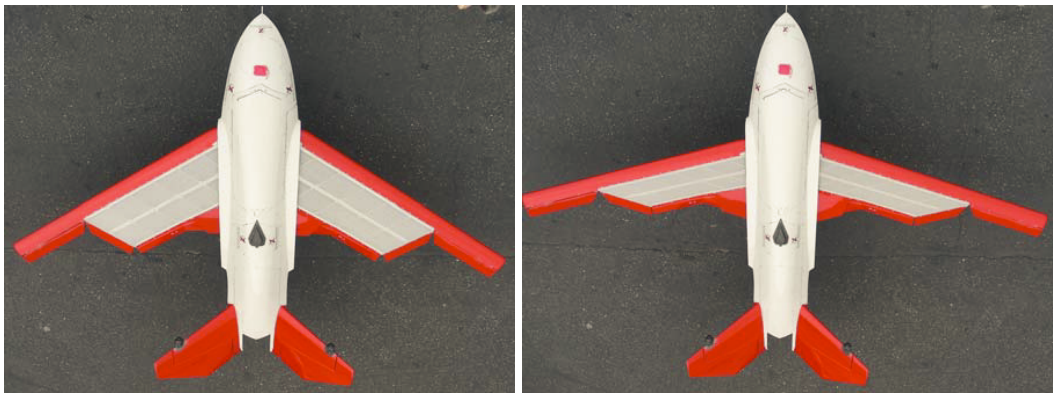

(a) (b)

Figure 1.25: NextGen MFX-1 in two extreme configurations: (a) high-lift and (b) loiter [80].

Using shape memory alloys, Sofla et al.[4] proposed a wing that changes its shape by actuating the wing-box. Prototypes were developed and showed excellent and smooth movement under representative loads. Aerodynamic analysis was conducted to evaluate the effect of reconfigured wing shape on the lift and drag coefficients.

Based on the work of Lentik et al.[82], who studied the way swifts control their glide performance, a bioinspired morphing-wing Micro Aerial Vehicle (MAV) was developed, named RoboSwift. Its morphing wing was based on discrete feather-like elements inspired by swift birds, which were able to fold backwards, thereby changing its wing sweep and aspect ratio [83] (Fig.1.26). However, no aerodynamic data is available in the literature to support the benefits of such configuration.

More recently, Di Luca et al.[84] described a novel morphing wing design composed of artificial feathers that can rapidly modify its geometry to fulfil different aerodynamic requirements: fully deployed configuration for manoeuvrability (Fig.1.27(a)) and folded configuration

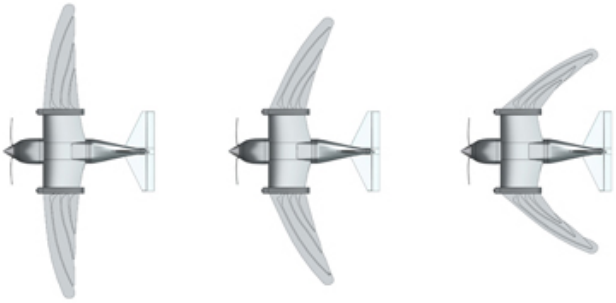

Figure 1.26: Top view of the RoboSwift MAV wing from unswept to sweptback position [83].

for low drag at high speeds (Fig.1.27(c)). They showed that asymmetric folding of the wings can be used for roll control (Fig.1.27(b)). The wing is capable of 41% area reduction. Aerodynamic performance of the morphing wing was studied in simulations, in wind tunnel measurements and validated inflight with a small drone. It was found that, in the fully deployed configuration, the wing had a 32% higher lift coefficient. On the other hand, when fully folded, the wing reduced the minimum drag coefficient by more than 40%.

(a) (b) (c)

Figure 1.27: Extreme configurations of the feather-like wing: (a) fully extended, (b) asymmetric and (c) fully folded [84].

1.2.5 Twist Variation

As mentioned earlier in the present chapter, varying the twist distribution of the wing to enhance flight performance and control authority of the air vehicle can be regarded as the oldest form of morphing. The Wright Brothers employed the wing warping technique to change the twist of a flexible wing and provide roll control for their first flying machine [8]. Nowadays, aircraft wings use twist to change the lift distribution along the span. On one hand, it can be used to avoid tip stall, by reducing the tip effective AOA. In this way, the stall happens first near the root, maintaining the roll control of the aeroplane [16]. To achieve this, the wing sections at the tip of the wing are rotated downwards relative to the root section, creating a “wash-out”. When the wing twist causes the wing tip aerofoil sections to operate at higher AOA it is referred as “wash-in”. On the other hand, it can be used to alleviate the bending moment and substitute roll control surfaces, such as ailerons. Twist can also be created by asymmetrically cambering the wing leading and trailing edges. This approach is not discussed here, since technologies to change camber were already discussed in section 1.2.2. Twist variation belongs to the out-of-plane morphing category.

Active Aeroelastic Structures (AASs) are being actively studied for aeronautical applications due to their potential to improve drag performance, as well as roll control and loads alleviation. They allow significant performance and control improvements by manipulating the aerodynamic shape of a lifting surface by changing its internal structure, without the need for radical wing configuration change, which normally use complex and heavy actuators. The Active Flexible Wing (AFW) program, started in the late 1980s [85], pioneered in the use of such concept. Rockwell International exploited wing flexibility to reduce structural weight and prevent roll control problems (aileron reversal) for high-performance fighter aircraft at large dynamic pressures. The former program was followed by the Active Aeroelastic Wing (AAW) research program, where the methodology was implemented and tested using a modified F/A-18 fighter, named X-53, to demonstrate its feasibility [86, 87] (Fig.1.28). The X-53 wing skin panels were replaced with thinner and more flexible skin panels. The leading edge flap was split into separate inboard and outboard segments, and additional actuators were added to operate the outboard leading edge flaps separately from the inboard leading edge surfaces. Trailing edge control surfaces and leading edge flaps were used to control the aeroelastic twist of the wing and to achieve the required rolling moment. Flight testing demonstrated that high rate rolls were possible within the structural limits of the aircraft [88].

Figure 1.28: X-53 configured F/A-18 fighter from the Active Aeroelastic Wing (AAW) program during flight.

The active aeroelastic aircraft structures research project developed an All-Moving Vertical Tail (AMVT) with a variable torsional stiffness attachment. The AMVT concept provided a smaller and lighter fin while maintaining stability and control effectiveness at a wide range of airspeeds [89]. In this design, a single attachment existed and could be adjusted in the chordwise direction relative to the position of the centre of pressure. In the scope of the same project, Amprikidis and Cooper [90, 91] investigated two AAS concepts that modified the static aeroelastic twist of the wing by modifying its internal structure. The first concept exploited the chordwise translation of an intermediate spar in a three-spar wing-box to vary its torsional stiffness and the position of the shear centre (Fig.1.29(a)). The second concept used rotating spars to vary the torsional and bending stiffnesses and the shear centre position (Fig.1.29(b)). Prototypes of the concepts were built and tested in a wind tunnel to examine their behaviour under aerodynamic loading. The experimental results were found to show good agreement with static and dynamic aeroelastic behaviour predictions from FEM.

Vos et al.[92] proposed a new concept for actively controlling the wing twist. The concept relied on inducing warping deformation of the wing skin, which was split at the trailing edge to create an open-section aerofoil. An internal screw mechanism was used near the trailing edge, so that the load-carrying capability of the wing was maintained while allowing the introduction of warping displacement between the lower and upper wing skins at the trailing edge. A

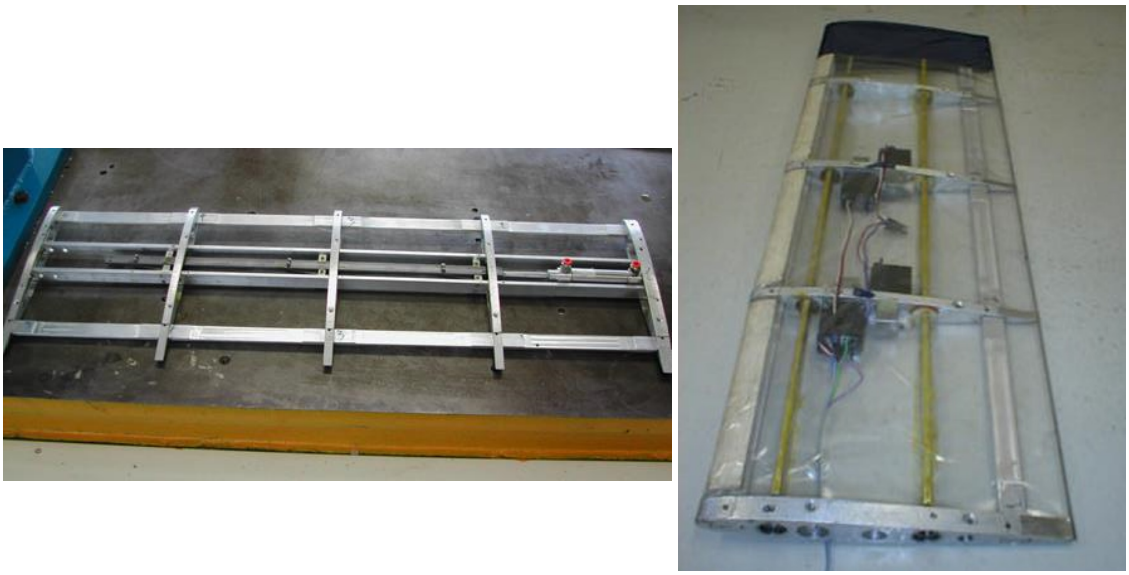

(a) (b)

Figure 1.29: Adaptive internal structures prototypes: (a) moving spar with pneumatic actuation and (b) rotating spar with servomotor actuation [91].

demonstration wing was built based on a NACA 23012 with a span of 0.68 m and a chord length of 0.235 m, being capable of a maximum twist of 27°. Wind tunnel tests showed that twist could change the lift coefficient by as much as 0.7. In general, it was demonstrated that at lower angles of attack, a more positive twist resulted in a higher lift-to-drag ratio.

Ajaj et al.[93] investigated the Adaptive Torsion Structure (ATS) concept to control the static aeroelastic stiffness of the wing. Their concept had a wing-box with two spars, where the webs of the spars could translate inward to vary the torsional stiffness and the position of the shear centre. This allowed the external aerodynamic flow to induce aeroelastic twist deformation on the wing, which could be used to enhance the performance or control authority of the vehicle. Preliminary numerical results indicated that significant increases in tip twists and lift force could be achieved by moving the front spar web. However, this was also associated with large reductions in divergence speed and large increases in actuation energy and forces.

Piezoelectric actuators have been used in a variety of wing twist concepts with limited success. Sahoo and Cesnik [94] investigated the use of high authority Anisotropic Piezoelectric Actuators (APA) to induce wing warping and achieve roll controllability for the next generation of Unmanned Combat Air Vehicle (UCAV). A numerical study was performed using the Boeing X-45A-based UCAV model and it was concluded that these actuators do not have sufficient control authority. Similar results were obtained by Cesnik and Brown [95] for the use of APA to induce wing warping actuation for roll control of the joined-wing Sensorcraft. Detrick and Washington [96] developed two concepts for morphing wings for MAVs. The first design split the supporting ribs and achieved wing twist using levers and a piezoelectric actuator. This design had limitations because the wing skin was attached directly to the ribs and so stiffened the wing. The second concept used one piece ribs interconnected by a truss structure, being the wing twist accomplished by changing the length of the truss structure members. The ribs had rollers in contact with the skin to allow sliding, and so avoid stiffening the wing. Aerodynamic and structural numerical studies showed that wing twisting is a viable form of roll control. However, no actual prototype was built to prove the feasibility of the concept.

SMAs have been used with success to control wing incidence (rigid motion) and torsion distribution. Barrett et al.[97] introduced the pitch active SMA wing UAV with a 2 m span, to demonstrate that a SMA flight control system could generate substantially higher control moments than a conventional actuator system. An SMA based actuator was used to cause rigid-body rotation of the wings, effectively changing its incidence. Flight testing demonstrated that roll rates were increased by nearly fourfold. Sofla et al.[98] used antagonistic flexural cells to create a two-way SMA flexural actuators using a one-way shape memory effect. The cells provided four distinct positions for each segment of the actuator, and two of the positions required no external energy to be maintained. These actuators could control the twist of wing sections if incorporated as ribs and actuated asymmetrically. Lv et al.[99] developed an SMA torsion actuator, using NiTi wires and a thin-walled tube for an adaptive wing demonstration system. The incidence of the wing could be changed continuously up to 15° in 1 s. Then, a novel smart wing rib using this actuation was developed, allowing swing angles of up to 10°.

1.2.6 Dihedral/Gull Variation

Variable dihedral/gull wings are interesting morphing concepts due to their ability to enhance aircraft performance and flight control. A variable dihedral wing enables the control of the aerodynamic span, replacement of conventional control surfaces, agility and flight characteristics enhancement, induced drag reduction (by altering the vorticity distribution) and stall characteristics improvement [16]. Folding wings and variable cant and toe angle winglets are two morphing concepts that vary the dihedral angle to obtain advantages in different flight conditions. This type of technology is integrated in the out-of-plane morphing category. The IS-1 fighter, designed by Nikitin-Shevchenko in 1932, was one of the first applications of variable dihedral wings, and was capable of out-of-plane morphing from a biplane to a monoplane, to operate at high speed.

As part of the MAS program, Lockheed Martin developed the folding wing (Z-wing), a concept that enabled span length, aspect ratio, and effective sweep angle to be varied [100, 101]. The folding wing design incorporated hinged joints at two spanwise stations permitting rigid body motion of the wing sections, in order to allow high dash speed, using the folded configuration and to increase endurance, in the unfolded configuration. Elastomeric skins covered the seams between wing panels, providing smooth shape changes (Fig.1.30). A half vehicle model was developed for wind tunnel testing, using CFD and FE analyses. The wind tunnel tests were performed for a Mach range of 0.2 to 0.9. Experimental data was correlated with the CFD and FE results [102]. Aeroelastic characteristics were investigated and no instabilities were found although several unexpected aeroelastic phenomenon were observed [103]. These were mainly due to the high wing mass and the lack of stiffness in the attachments to the wind tunnel. Overall, the concept was feasible, but the high prototype mass negated the potential aerodynamic benefits.

Shelton et al.[104] investigated the possible benefits of active multiple winglets applied in an UAV. It was concluded that the use of actively controlled winglets can enhance the low-speed performance and manoeuvrability of the vehicle and can increase range and endurance by up to 40%.

Manzo [105] investigated a Hyper-Elliptical Cambered Span (HECS) wing. He divided the wing in articulated panels at different span positions, to achieve out-of-plane shapes, using a

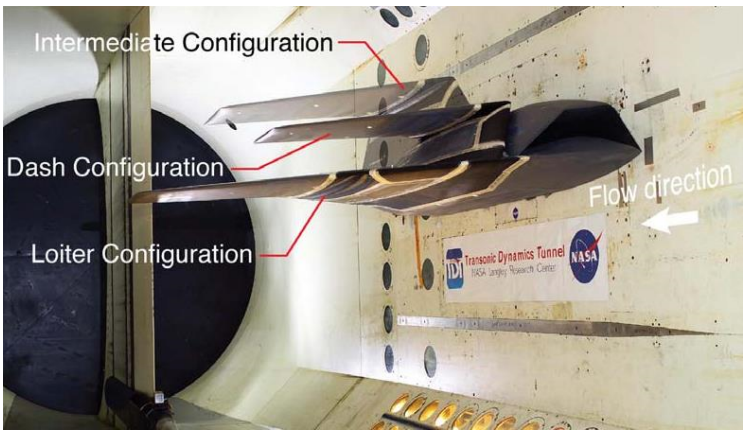

Figure 1.30: Multiple exposure photograph of Lockheed Martin Z-wing wind tunnel model during a morphing sequence [102].

network of coordinated tendons and spools. In this design, SMA-based tendons internal to the wing actuate differently towards the tip. This was achieved using a number of varying radii spools along the span, that generated proportional motion changes according to the desired relative angle change between each wing section. The wing prototype with its mechanism is shown in Fig.1.31. Wind tunnel testing showed that the planar HECS wing had a better lift-to-drag ratio than an elliptical wing, but the nonplanar HECS wing did not perform as well as the planar one.

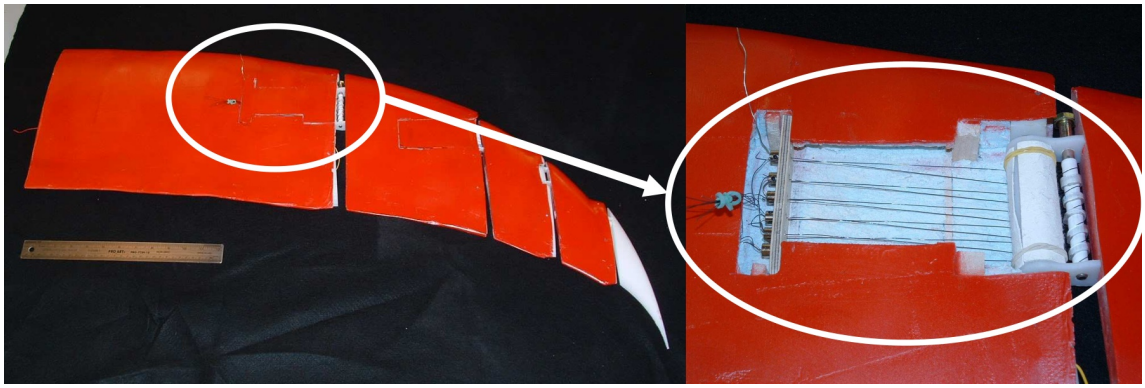

Figure 1.31: HECS wing with tendon and spool actuation [105].

Several studies were carried out on variable cant winglets applied to flying wings. Bourdin et al.[106] performed computational and experimental studies on a commercially available flying swept wing, which was modified to allow dihedral angle variation of both outboard wing portions. These were used for roll control with proverse yaw. VLM results were compared with the wind tunnel testing results, being found a reasonable similarity. They also concluded that the studied devices coupled the longitudinal and lateral control dynamics due to the effects on pitching moment. Therefore, some form of pitching moment control was required for stable flying. In a subsequent study [107], they added another pair of variable cant winglets to attempt to control the aircraft solely with wingtip (Fig.1.32). Computations with a VLM and wind tunnel tests demonstrated the viability of the concept for coordinated turns, with individual and/or combined wing-tip deflections producing multi-axis and coupled control moments.

Falcão et al.[108] designed and tested a morphing wingtip mechanism based on a servo-actuated articulated winglet, that was able to rotate about the vertical and longitudinal axes,

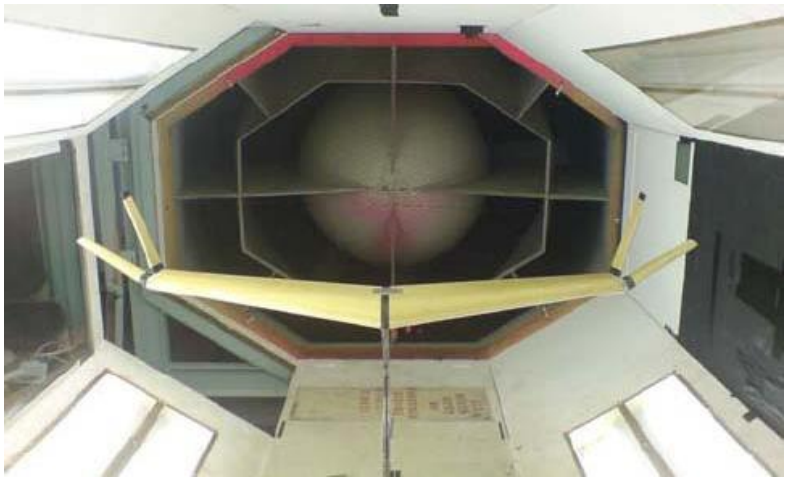

Figure 1.32: Flying wing with multiple variable cant winglets during wind tunnel testing [107].

thus, allowing the control of toe and cant angles, respectively. A multidisciplinary design optimization procedure was performed in order to determine the ideal wingtip configuration for five scenarios: maximum endurance, maximum range, minimum stall speed, minimum turn radius and maximum speed. When compared with a fixed winglet optimized for maximum range, the morphing winglet improved significantly the stall speed (10.7% reduction) and marginally the drag in cruise and maximum speeds (2.6% and 4.0% reductions, respectively).

Han et al.[109] investigated the aerodynamic performance of a self-contained morphing winglet for an UAV that mimics the wing-tip feathers of gliding birds. A smart soft composite (SSC), formed of SMA wires and glass fibres within a soft polymeric matrix, was used to fabricate the morphing winglets. They were implemented at both wing tips of a WASP 4/7-scale UAV, and the aerodynamic characteristics were investigated using wind tunnel testing. Improvements to the lift-to-drag ratio of 5.8% were seen, when compared with the flat wing geometry for AOA greater than 5°.

1.3 Mass Estimation of Morphing Wings

Mass control, namely the process by which the lightest possible aeroplane is derived within the constraints of the design criteria [110], is an essential part of the design process of any aerospace vehicle. Accurate estimations of aircraft mass are vital in the early stages of an aircraft design process. They drive all the major choices in configuration and layout as well as being the main foundation of performance predictions. Mass estimation in aircraft design is very challenging due to the high number of variables involved in the creation of an accurate mass model, the numerous relationships between them and the high degree of uncertainty associated with the problem itself.

Morphing wing technologies require the concurrent development of design and optimization strategies to expedite overall development of these systems. The development of robust morphing wing sizing codes to be used during conceptual design tasks is of major importance, since it enables studies of the operational benefits and provide a methodological basis for future morphing aircraft sizing codes. However, such tools need accurate mass predictions for the major components, including the morphing wings. Therefore, morphing technologies will

only be considered in new aircraft development, if mass predictions with sufficient accuracy are available.

Most of the existing mass estimation models available in the literature can be classified into two main categories: semi-empirical and finite element [111]. Semi-empirical models are based on data from similar existing aircraft. Therefore the robustness of these models depends on the similarities: size, configuration, and technology (systems, structural efficiency, and materials), between the aircraft under study and the aircraft that have been used in the derivation process of these models [112]. In the case of morphing wings, little information is currently available to substantiate such a wing mass prediction and thus, the sizing results would be unfounded. On the other hand, FEMs are not suitable to be used during the conceptual and preliminary design phases, since they require detailed knowledge of the internal geometry and aerodynamics that are usually not available early in the design process [113]. Therefore, it is desirable to formulate a model based on FEM analyses, to capture the structural trends, but without the complexity posed by these methods.

Various studies have been performed in mass models for conceptual design of conventional wings. Some developed wing mass estimation models for commercial and transport aircraft [111, 114] and others for more unconventional configurations, such as nonplannar configurations [115, 112, 116] or high speed transport [117]. However, very few studies have focused on morphing wings.

Frommer and Crossley [118] used a technique called *photo-morphing*. In this technique, the reference wing mass is computed using a mass model developed for conventional wings, the so called basic mass. Then, this value is corrected for actuation system mass, using the maximum variation in unique planform area, multiplied by an actuator specific (in relation to area) mass constant. Figure 1.33(a) provides an illustration of the unique area method. The light coloured area is the non-unique area, shared by both planforms, while the dark area is the area unique to each of the two planforms. This metric is indicative of the wing planform that needs to be moved when changing from one shape to another. Although the *photo-morphing* is simple to implement, it is very limiting, since there may be no skin materials or actuation strategy to achieve some of the shape changes represented. Additionally, the actuator specific mass constant is difficult or even impossible to derive for some morphing systems.

Probably, the most significant study was performed by Skillen and Crossley [10, 101], where they developed a wing mass model, considering the variation of span, chord and sweep. FEM analyses, based on equivalent box-beam models or shell type structures, were used to estimate the mass for a sufficient number of combinations and then a least square regression was used to approximate the wing mass. Validation examples were provided for chord and variable sweep morphing wings (Fig.1.33(b)). No details about the span variation methodology were given. The shape variation considered clearly required the use of high strainable skins, but they were not formally addressed in the FEM, potently resulting in erroneous mass estimations. Moreover, the actuation system was modelled using simplified hydraulic actuators, not being considered other types of actuators that could yield better results, specially for small sized RPASs.

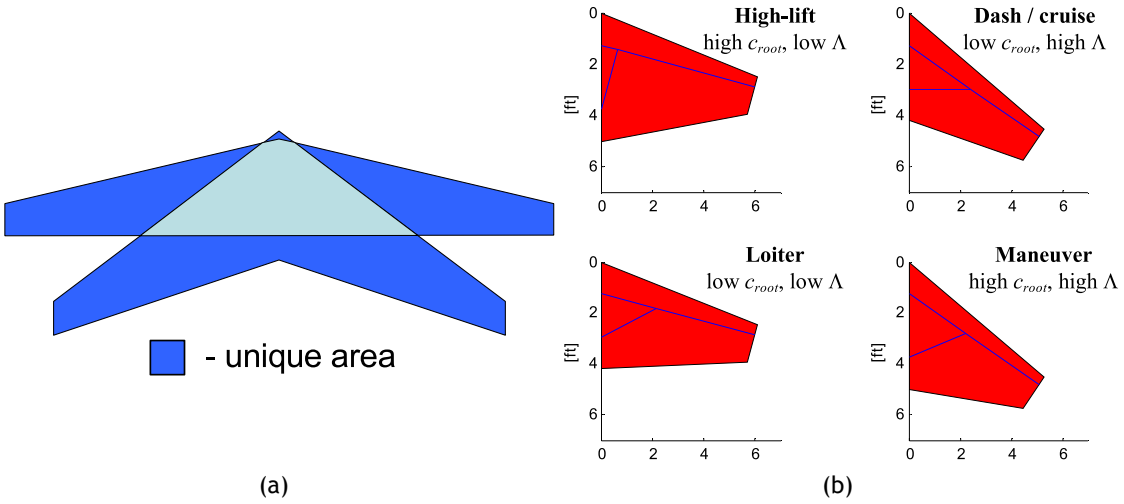

Figure 1.33: (a) Unique area method considered by Frommer and Crossley [118] and (b) morphing wing configurations considered by Skillen and Crossley [10].

1.4 Thesis Objectives, Outline and Contributions

From what has been said so far, it is clear that the current work focus on morphing aircraft technologies. In more detail, two variable-span morphing wings are studied from the conceptual idea, to prototype construction and ground and flight testing. The current work uses Remotely Piloted Aerial Systems (RPAS) as test beds to flight test the newly developed technologies. It is interesting to notice that practically no study in the literature provides flight performance results of the concepts presented, therefore this work not only summarises the design and development of a new telescopic wing but also provides flight data on the VSW performance, as well as comparisons with a conventional fixed wing. These vehicles serve a dual purpose: provide design requirements and constraints and allow flight testing to be carried out. Of particular interest is also the impact of morphing on the wing mass. In fact, from what has been presented in the previous section, methods to predict wing mass of morphing wings are limited and scarce. Therefore, the current work also focus in the development of mass models that synthesize the potential mass penalties of variable-span concepts, to be used in the conceptual design phases. The influence of the geometrical and inertial parameters on the wing mass is also addressed.

A special emphasis is given to flight testing and practicability of the proposed concepts. In fact, many devices were developed and tested in laboratory, but only some had merit to be tested in wind tunnel and very few have been actually flight tested. Hence, the benefits and penalties of morphing technologies applied in an actual aeroplane are still relatively unknown. The use of RPAS is crucial to the success of the present work, since they are used to validate the benefits of such systems, including the quantification of the benefits and penalties, when compared to conventional fixed wings. In fact, alongside morphing technologies, the development of RPASs has undergone a major expansion in recent years, being an excellent platform for testing new concepts of morphing wings [119]. They present numerous advantages (when compared with manned aeroplanes) such as low development and operating costs, no flight crew is required and, since they are subjected to low aerodynamic loads, the use of these technologies is potentiated. Thus, RPASs provide an ideal platform for further development and raising the

Technology Readiness Level (TRL) of new technologies.

The present chapter has introduced the basic definitions and provided an overview of the latest developments in aircraft morphing technologies. An overview of mass models for the estimation of morphing wing mass was also presented, where recent works were shown and the need for more advanced mass estimation methods for morphing wings was justified.

Chapter 2 focus on the idealization, development and ground testing of a wing capable of varying its span: a Variable-Span Wing - VSW. The variable-span concept is described, to familiarize the reader with the general concept and with the used terminology. Then, the aerodynamic and structural design of the VSW is described. An aeroelastic study is also conducted, focusing on the estimation of flutter speed, considering the effects of interface between fixed and moving wing parts. Later in the chapter, the prototype construction is explained, with an emphasis on the manufacturing techniques and actuation mechanism sizing and integration. Finally, the full-scale prototype is subjected to a ground evaluation, focusing on the structural elements and the actuation system.

In chapter 3, the wing developed in the previous chapter is integrated in a RPAS with the purpose of performing in-flight concept evaluation, i.e., experimental flight testing. In the beginning of the chapter, the modifications made to the RPAS to fit the VSW and to allow safe flight testing are presented. Subsequently, the necessary instrumentation to characterize the VSW is introduced and described. In the second part of the chapter, the experimental flight testing of the RPAS, fitted with a conventional fixed wing and the VSW is explained. Two sets of flight tests are performed: aerodynamic and energy characterization. The former aims at determining the lift-to-drag ratio for different airspeeds and the latter to measure the propulsive and manoeuvring energy when performing a typical mission.

The work presented in Chapter 4 is build upon the knowledge gained from the previous chapters. In fact, it is recognized that the VSW developed and flight tested in chapters 2 and 3 is limiting in terms of other morphing strategies. Therefore, chapter 4 is devoted to the idealization, development, building and testing of a new telescopic wing concept that allows the integration of other morphing strategies. The new wing is developed within the CHANGE (Combined morpHing Assessment software usiNG flight Envelope data and mission based morphing prototype wing development) project. Beyond the span change capability, the wing adopts leading edge (LE) and trailing edge (TE) camber changes. A modular design, based on a wing-box like structure, is selected, allowing the systems producing span change and LE and TE change, to be separately developed and then integrated into the overall wing. This structure is sized for strength and stiffness using FEM analysis. A partial span, full-sized cross-section of the wing-box is built to allow the definition of an optimal manufacturing procedure and to perform bench testing. In the end of the chapter, the full-scale prototype developed by the consortium is presented, along with the wind tunnel and flight testing performed.

Chapter 5 focus on the the mass study of a VSW and methods to predict it. The studies of the previous chapters highlighted that morphing concepts present an undesired mass increase due to their inherent complexity both in the load carrying structure and in the actuations systems. This can potentially limit or even negate any performance benefits, depending on the intended flight mission and/or aeroplane type. However, mass estimation of morphing wings is difficult and very little is known about the impact of wingspan or wingspan maximum variation, among others, on the mass of the load carrying structure. Therefore, chapter 5 synthesizes the effects of various VSW design parameters on the structural mass, with the final purpose of cre-

ating a mass model. Different geometrical and inertial parameters are considered in this study, being: wingspan, wing chord, span variation ratio, flap chord ratio and aeroplane weight. A minimum mass optimization problem with stiffness and strength constraints is implemented and solved for a sufficient number of combinations of the mentioned parameters, being the design variables structural thicknesses and widths. A parametric structural finite element model of the wing is built and solved in ANSYS® APDL. Using the data collected with the parametric study, a mass function is created by fitting a polynomial function to the data. Later in the chapter, the developed function is used to derive a mass model, by adding the mass contributions of the actuation system and morphing flap. Finally, the model is applied to a selection of telescopic morphing wings and the results are compared to ascertain its applicability and accuracy.

Each of the described chapters has a short introduction and concluding sections.

Finally, chapter 6 summarises all the work presented throughout the thesis and its most important results. The main contributions of this thesis to the state of the art in adaptive aircraft systems are also enumerated. Future work and recommendations are also discussed.

One of the primary purposes of a thesis is the dissemination of new findings, i.e., the contributions to the state of the art. Clearly, the most important contribution of the current work to the state of the art is the complete design cycle of variable-span wings and the search to quantify the benefits and shortcomings arising from such technologies, in true operational conditions. In fact, as far as the author is aware, there is not any other VSW that is in actual operation. In that sense, the current work effectively raises the TRL of variable-span wings and associated technologies. As a result of this work, several works have been published (Appendix B).

In order to achieve that high level goal and due to the fact that the design and implementation of such VSW concepts is not a straightforward task, it will require the development of new procedures and techniques to support it. These are adjunct to the main goal of this thesis and range from flight testing methodologies and computational methods, to building techniques and systems integration. However, they constitute considerable developments with application to this and different areas of research. These include: the development of parametric finite element models and a comparison of numerical results with full-scale prototype models; the development of testing procedures applied to VSWs for bench testing and, more importantly, for flight testing; systematization of structural methodologies and building procedures; identification of key requirements of the RPAS test beds, to maximize flight testing safety and success, i.e., preservation of the vehicle's structural integrity and the extraction of meaningful data; a systematic analysis of the effects of major geometrical and inertial parameters, on the mass of VSWs concepts, thus greatly extending the studies currently found in the literature; and derivation of a multivariable polynomial approximation model, to be used as the foundation for the creation of a mass model of VSWs.

Chapter 2

Variable-span Wing Development

2.1 Chapter Overview

In the previous chapter the motivation of this work has been set out and the main goal has been established, namely the design, study and flight testing of variable-span adaptative morphing wings, applied to Remotely Piloted Aerial Systems (RPAS). In this chapter, the first steps taken in this endeavour are presented. More particularly, this chapter focus on the development and ground testing of a wing capable of varying its span: a variable-span wing (VSW). All the steps that culminated in the ground testing of the prototype are described in detail.

Parallel to the project of the variable-span wing, a RPAS platform, called Olharapo, has been developed in the Department of Aerospace Sciences with the purpose of studying, testing and validating new wing concepts. The VSW was developed having in mind future flight testing. Thus, this RPAS serves as a test bed for the developed wing. These types of vehicle were chosen since they have numerous advantages for testing new concepts, such as low development and operating costs, no flight crew is required and, since they are subjected to low aerodynamic loads, the use of morphing technologies is potentiated. Hence, maximum span and chord (for example) was selected to fit Olharapo RPAS. Additionally, an effort was made to keep the wing mass to a minimum, in order to reduce any detrimental impacts of the increased weight in the vehicle's performance.

The chapter begins with a brief description and history of the development of the RPAS test platform, in order to contextualize the whole project. Then, the variable-span concept is described, to familiarize the reader with the general concept of such wing configuration and with the used terminology. Subsequently, all the design steps are described, starting with the aerodynamic design optimization. The aerodynamic design uses a design tool aimed at improving the VSW overall performance (drag $\times$ speed integral) relative to the performance obtained with a conventional fixed wing, in the design speed range of the Olharapo RPAS.

A structural numerical analysis of the VSW was performed using finite element analysis, in order to study the effect of the interface between the inboard fixed part and the outboard moving part of the wing, due to its sliding characteristics. An analysis of the deflections and stresses under aerodynamic flight loads is presented to assess the suitability of the wing for future flight tests. Additionally, an aeroelastic study of the variable-span wing was conducted. The study focus on the estimation of flutter critical speed and the effects arising due to the interface between fixed and moving wing parts (flexible or bonded). The critical flutter speed was computed using the typical section in aeroelasticity with unsteady linearised potential theory together with the three-dimensional lifting surface strip theory approximation for lifting surfaces with high aspect ratio.

After performing the numerical studies, a prototype of the variable-span wing was designed and built for ground evaluation and to pursue flight testing. The manufacturing tech-

niques used to build the wing are presented in detail, as well as the actuation mechanism sizing and its integration in the wing.

Finally, the full-scale prototype was subjected to a thorough ground evaluation. The ground evaluation focused on the structural elements and the actuation system. The static testing is compared with the numerical predictions. The actuation system testing includes actuation time and system efficiency.

2.2 RPAS Platform

The RPAS testing platform is called Olharapo. The name comes from a set of figures that were represented in the animations of EXPO 98, called "Olharapos". Generally speaking, the original purpose of the project was to provide students of the Aeronautical Engineering course at the University of Beira Interior (UBI) an experience of the development cycle of an aircraft. The motto of the project was: design, manufacture and test. The students had available a combination of natural materials: balsa wood, plywood, basswood; and composite materials: Carbon Fibre Reinforced Polymer (CFRP) and Glass Fibre Reinforced Polymer (GFRP), as well as diverse Polyvinyl Chloride (PVC) and Extruded Polystyrene (XPS) foams.

In the following sections, a brief history of the Olharapo RPAS is presented. The main structural features, propulsion system and the rational behind the adopted configurations is explored.

2.2.1 Olharapo 1

Olharapo 1 development was based on a set of design requirements. The main requirements were an endurance of one hour, electric motorization, Maximum Takeoff Weight (MTOW) of 60 N, video surveillance capability and autonomously flying capability.

To answer those requirements, a RPAS was designed and built. The vehicle has a tricycle fixed landing gear and upward V-tail. The wing planform is rectangular, uses the SG6042 aerofoil and has no twist. The wing is integrated in the fuselage in a high wing configuration. Additionally, the vehicle has the particularity of the propeller being positioned at the beginning of the tail boom, as shown in Fig.2.1.

Figure 2.1: Olharapo 1 in Covilhã municipality airfield.

Olharapo 1 fuselage was conceived only to receive a conventional wing, since the centre portion of the wing is an integral part of the fuselage. The propulsive system is constituted by a brushless inrunner electric motor, powered by a lithium polymer battery in a 3s configuration (three batteries in series). The electric motor was installed inside the fuselage, 5 cm behind the wing. Due to installation reasons a shaft and two gears were used: one connected directly to the motor and the other attached to the propeller. This configuration proved to be problematic. The main problems were related to cooling and efficiency. The latter was due to gearing system and the former due to insufficient cooling duct area and also due to the use of an inrunner motor.

The first version of Olharapo is known has Olharapo 1. In Fig.2.2(a) it is possible to see a planform view of the RPAS and in Fig.2.2(b) the RPAS during a flight in Covilhã airfield.

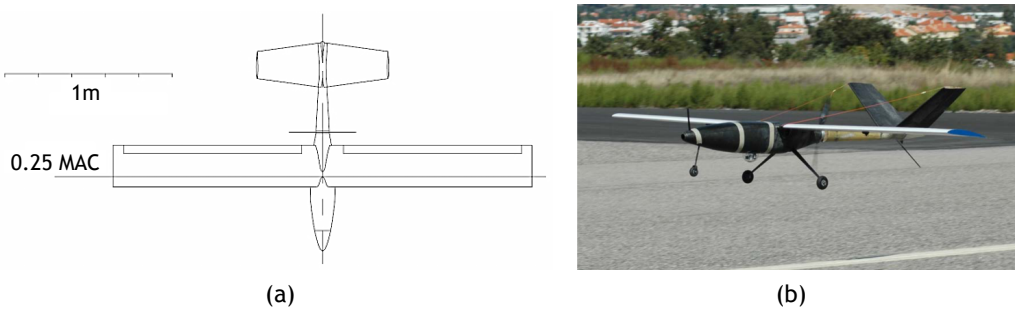

(a) (b)

Figure 2.2: Olharapo 1 RPAS: (a) planform view and (b) inflight photo.

2.2.2 Olharapo 2

Olharapo 2 is an evolution of the first Olharapo. It shares the same key requirements and consequently, the same key features. However, some crucial modifications were introduced or extended:

- The width of the fuselage was increased due to space requirements for the installation of an autonomous navigation systems and more batteries to extend endurance;
- The fuselage was equipped with a wing fastening system that allows the installation of different wings (following the interest shown by the research unit in testing new wing concepts);
- A new propulsive system was developed using a transmission shaft from the electric motor to the propeller, which is now located behind the tail boom (due to the poor efficiency of the previous system).

The high wing configuration was maintained, since the dihedral effect using this configuration is higher, when compared with the other wing positioning possibilities. On one hand, the lateral stability is fundamental in an experimental aircraft, especially when it comes to the development of new wing concepts. On the other hand, for operational reasons there is a need to assemble and disassemble the wings from the fuselage. Hence, this configuration allowed for easier access to the wing zone. The new fuselage incorporates a newly developed form of wing fastening. This system allows distinct wings to be integrated without the need to modify the fuselage. This system is composed by a central wing structure, that can be detached from

the fuselage. This central part was developed for each wing. Hence, the fuselage is generic, from a wing structure point of view.

The Olharapo fuselage was built using a semi-monocoque type structure, being constituted by two main assemblies: the main fuselage and the tail boom. The main fuselage is composed by an external skin made with carbon fibre reinforced polymer (epoxy resin), reinforced with plywood frames near the areas of the frontal landing gear, the main landing gear and the fuselage/wing joint. The electric motor is located inside the fuselage, near the interface between the fuselage and the tail boom. In the interface area between the two main assemblies, two frames are used to screw them together. The tail boom structure is similar to the fuselage: carbon/epoxy skin and plywood frames. There are three frames in the tail boom, being the first one positioned in the interface of the fuselage to the tail boom. The second one is positioned in the middle of the tail boom and is used to support a radial ball-bearing. This ball-bearing adds a middle support to the transmission shaft, preventing the buckling of the mentioned component. The third one is positioned in the tip of the tail boom and is used to support the motor shaft. It has an embedded bearing to reduce the friction during the shaft rotation. The tail boom has two empennage sockets, due to the the upward V-tail configuration that Olharapo has. These empennage sockets are tilted 30° relative to the horizontal plane, and have an incidence of -3° relative to the fuselage centre line. The combined overall length of the fuselage and tail boom is 1.54 m.

In the new version of the RPAS, the propulsive system differs from the previous version in that the propeller is positioned at the aft end of the tail boom. The transmission between the propeller and the electric motor is done using a shaft that passes through the tail boom. It is powered using a brushless outrunner electric motor and a pusher two or three-bladed fixed pitch propeller, that provides an installed electrical power that ranges from 400 W to 600 W. The pusher propeller configuration is very convenient since the wing is in a position where the flow is not disturbed by the propwash. Additionally, this configuration allows for an increase in payload volume and also provides an unobstructed frontal visual field. This is specially important when a surveillance camera is used. In order to protect the propeller from the ground impact, a tail skid was installed at the rear of the tail boom. Figure 2.3 shows the fuselage tail boom along with the transmission shaft coupled to the electric motor. Note that in the figure the tail boom has an H-tail installed and not the original V-tail. This new tail was developed due to controllability reasons and it is subject of analysis in the the next chapter.

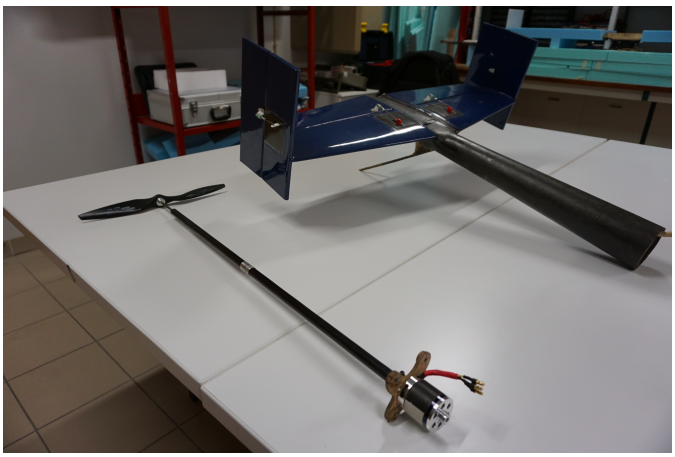

Figure 2.3: Olharapo 2 motor transmission shaft and tail boom side by side (H-tail installed).

The RPAS uses a tricycle landing gear, which consists of two wheels behind the Centre of Gravity (CG) and a directional auxiliary wheel in front of the CG. The latter is operated by a servomotor. Both main landing gear and frontal landing gear are fixed. The combination of the tricycle landing gear and the pusher propeller (installed in the end of the tail boom) forces a reduced angle between the main landing gear and the tail boom skid and consequently a lower rotation angle, forcing a greater takeoff distance and a higher landing speed.

Olharapo uses a conventional fixed rectangular wing, built using soft and hard woods. The fixed wing has a constant chord of 0.25 m and a planform area of 0.625 m^2. The aerofoil used is the SG6042, a low speed aerofoil with a good compromise between maximum lift coefficient and geometry simplicity. The main wing spar is made of pine wood, while the skin and ribs are made of balsa wood. The skin is finished using an iron-on covering film (polypropylene), which ensures a smooth and airtight surface. The wing has an incidence of 4° relative to the fuselage centre line.

The takeoff weight of the vehicle is around 60 N and the typical cruise speed varies from 18 m/s to 25 m/s, with a stall speed of 11 m/s and a maximum speed of about 40 m/s. The main specifications of Olharapo 2 are identified in Table 2.1 and Fig.2.4 shows the complete RPAS in Covilhã airfield.

Table 2.1: Main specifications of Olharapo 2 RPAS platform.

Specification	Value
Wingspan	2.50 m
Wing chord	0.25 m
Wing thickness	10% max (SG6042)
Wing planform	rectangular
Empennage configuration	Upward V-tail (30°)
Empennage aerofoil	NACA 0009
Fuselage length	1.54 m
MTOW	60 N
Payload weight	15 N
Operational range	5-20 km LoS
Operational altitude	up to 2000 m
Stall speed	11 m/s ≈ 40 km/s
Typical cruise speed	18-25 m/s ≈ 65-90 km/s
Maximum speed	40 m/s ≈ 144 km/h
Electric motor	Hyperion ZS-3025-10 (775KV) - 1150 Watts Max
Power source	Lithium-ion Polymer 3s1p 10Ah

Figure 2.4: Olharapo 2 parked in Covilhã municipality airfield.

2.3 Variable-span Wing Concept

The variable-span wing, VSW, is, as the name implies, a wing that is capable of changing its span during flight. In the fist chapter, the merit of the two different approaches to change the span has been discussed: a telescopic methodology, in which the movable part is rigid and slides inside or outside a central wing, and using elastomeric skins, in which the skin stretches and retracts to maintain the aerodynamic shape of an internal span changing structure. Both concepts have advantages and disadvantages. The elastomeric skin concept requires high actuation forces to maintain the aerodynamic shape. The aerodynamic surface is also affected due to the out-of-plane displacements of the skin and consequently aerofoil modification. On the other hand, the telescopic concept severely limits the internal available space and adds some structural duplication, which translates in an increased weight.

In the current work a telescopic concept VSW was selected. The wing does not exhibit any dihedral or any sweep and is made of one rectangular inboard part, inboard fixed wing (IFW), and a rectangular outboard part: outboard moving wing (OMW). The OMW is actuated by an electromechanical mechanism, consisting of a servomotor, a pinion and a rack. The pinion is driven by the servomotor installed at the centre of the wing assembly and pushes/pulls the rack which is attached to the OMW to make it slide inside the IFW. The maximum span length was set to the same value as in the original wing of the recipient RPAS: 2.5 m. For this total span, it was estimated that both inboard and outboard wing parts would have a length of 0.625 m and that 0.1 m of minimum wing overlapping would allow sufficient wing stiffness in the fully extended configuration. Knowing these dimensions and fuselage width one was able to estimate the IFW and OMW lengths. The sketch of the overall system was developed in a CAD/CAM tool and is illustrated in Fig.2.5 where the main components are highlighted.

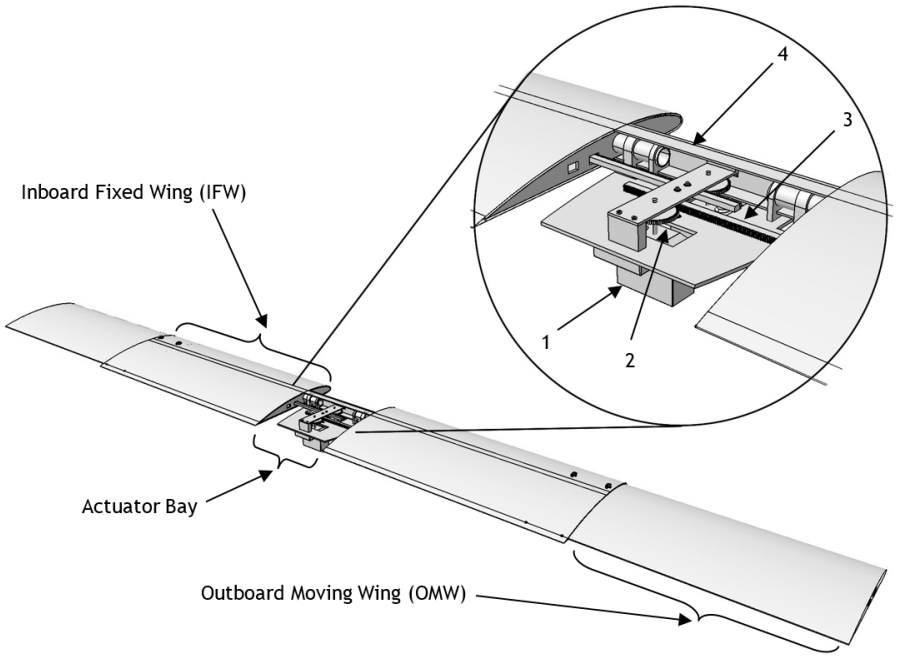

Figure 2.5: General CAD view of the Variable-Span Wing (VSW) showing its main components and detail of the actuator bay: 1) servomotor, 2) transmission pinion, 3) transmission rack, and 4) pultruded unidirectional carbon spar.

Designing the VSW structure requires a compromise between aerodynamic function, geometric compatibility and internal space necessary for actuators and related components. It was decided that the most convenient solution to match the IFW aerofoil to the OMW aerofoil was to create an aerofoil for the fixed part from an outward offset of the moving part aerofoil in order to achieve the lowest possible discontinuity between wing sections. Figure 2.6 presents all the nomenclature of the geometrical characteristics of the telescopic wing and Table 2.2 describes them and indicate their specific values.

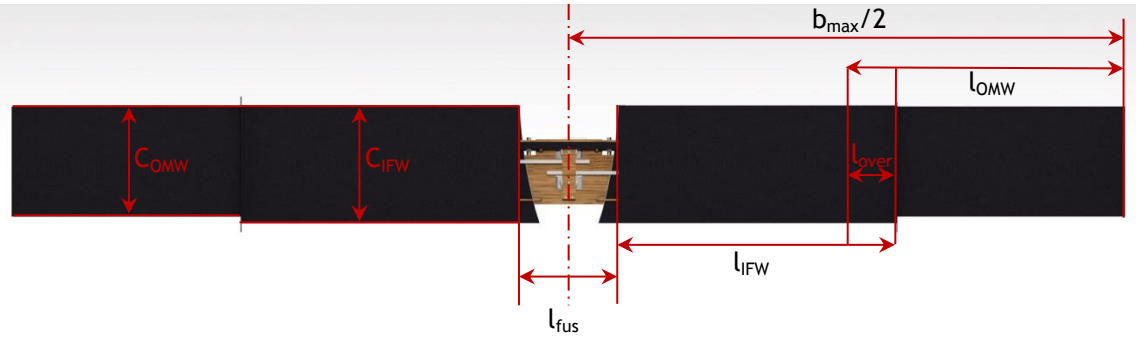

Figure 2.6: Planform view of the Variable-Span Wing (VSW) highlighting the main parameters nomenclature.

Table 2.2: Main parameters and dimensions of the Variable-Span Wing (VSW).

Parameter	Description	Dimension
$b_{max}/2$	Semi-span in maximum span configuration	1.250 m
l_{fus}	Fuselage width	0.220 m
l_{IFW}	Inboard fixed wing length	0.600 m
l_{OMW}	Outboard moving wing length	0.625 m
l_{over}	IFW/OMW minimum overlap	0.100 m
c_{IFW}	Inboard fixed wing chord	0.265 m
c_{OMW}	Outboard moving wing chord	0.25 m

2.4 Aerodynamic Optimisation

The main topic of this section is the aerodynamic design of the wing that can perform in-flight span variations. Olharapo 2 RPAS fitted with the VSW should be capable of operating in the same range of speeds as with the original fixed wing, from a stall speed of about 11 m/s to the maximum speed of 40 m/s, with similar performance at low speed but better performance at high speed.

The size of the VSW was obtained through a computational constrained aerodynamic shape optimization aimed at determining the span values that minimize its drag for a given speed range. The geometric constrains imposed on the wing design optimization were dictated by component fitting, manufacturing simplicity and mechanism functionality considerations. A description of the optimization procedure and its results are given below, but more detailed information can be sought in [120].

2.4.1 Aerodynamic Analysis and Optimisation

Medium-fidelity aerodynamic analysis algorithms were implemented and integrated with other aerodynamic analysis programs and optimization algorithms in order to assemble the wing aerodynamic shape optimization tool.

The aerodynamic analysis implemented in the code is done in two steps [13]. First, the two-dimensional (2D) aerodynamic coefficients as functions of angle of attack (AOA) and Reynolds number (Re) at specified wing sections across the span of the wing are obtained using the solver of the XFOIL code [121]. Then, a non-linear VLM is used to obtain the lift distribution and the induced drag. The VLM algorithm implemented is based on the steady linear VLM from [122] and is coupled with an iterative decambering approach [123]. In calculating the total lift of the vehicle it was assumed that only wing and horizontal tail contribute to lift. The tailplane lift was calculated such that the pitching moment about the CG (assumed at wing quarter chord position) is zero. Therefore, for a negative wing pitching moment, typical of positive cambered aerofoils, the wing lift must be greater than the weight to compensate for the negative tail lift. This affects not only the induced drag of the wing but also the parasite drag since it flies at a higher AOA.

In this tool, empirical weight information for the wing, the tailplane and the vertical tail was introduced to allow for the variations in aerofoil relative thickness, wing area, aspect ratio and taper ratio. The weight formulation is based in [124] and is described in [13].

The gradients of the objective function and constraints are computed using forward finite-differences. The constrained aerodynamic shape optimization was carried out with the Sequential Quadratic Programming (SQP) constrained optimization algorithm of FFSQP3.7 [125]. SQP has been shown to produce good results in [126].

2.4.2 Aerodynamic Shape Optimization

The objective of the optimization problem was to determine the wingspan that minimizes the drag, D, of the wing, at International Standard Atmosphere (ISA) conditions. This is done from a speed of 15 m/s to a speed of 35 m/s keeping lift, L, equal to the aircraft weight, W, at all speeds and subject to geometric constraints imposed by the limitations of the maximum and minimum span values, component fitting (IFW and OMW aerofoil compatibility), and mechanism functionality considerations (OMW travel).

The VSW planform geometry is illustrated in a schematic form in Fig.2.7. Taking into account fuselage dimensions and the geometric characteristics of the wing, four wing sections were defined from the root to the tip for the optimization problem, as shown in Fig.2.7, where the lateral position of station 4 is the only one allowed to vary during the optimization process. The positions of sections 2 and 3 are automatically defined given the highest value of the position of section 4 (maximum semi-span) in such a way that the OMW when fully retracted fits completely inside the IFW (between fuselage side and section 3 and when fully extended maintains a 0.1 m overlap with the IFW for structural reasons. The maximum wing span is 2.5 m, the same value as in the original fixed wing.

The most convenient solution to match the IFW aerofoil to the OMW aerofoil was to create an aerofoil for the fixed part from a given outward offset of the moving part aerofoil in order

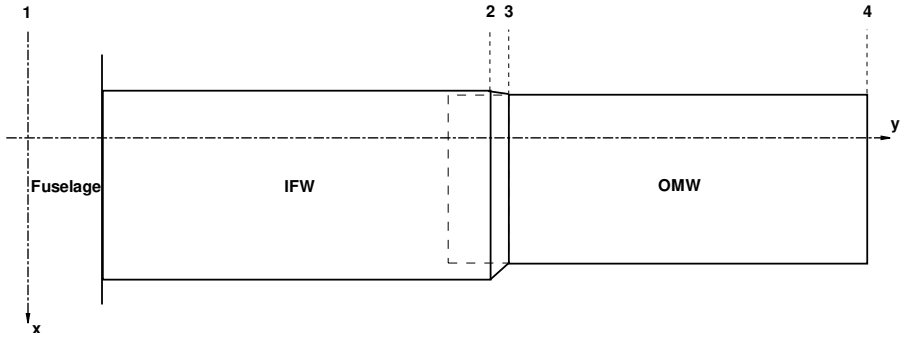

Figure 2.7: Variable-span wing aerodynamic optimization planform.

to achieve the lowest possible discontinuity between wing sections. This solution would result in a small geometric conflict between aerofoils, in which the trailing edge of the moving wing would intersect the lower surface of the fixed wing. Therefore, it was necessary to perform a slight modification in the original aerofoil (SG6042), straightening the lower surface through a tangent from the lowest point to the trailing edge, resulting in a slightly less efficient aerofoil. In the present case the aerofoils were kept constant along each part of the wing. The aerofoil geometries are shown in Fig.2.8. The relative thickness of the SG6042 aerofoil is 10% whereas that of the modified aerofoil is 10.03%.

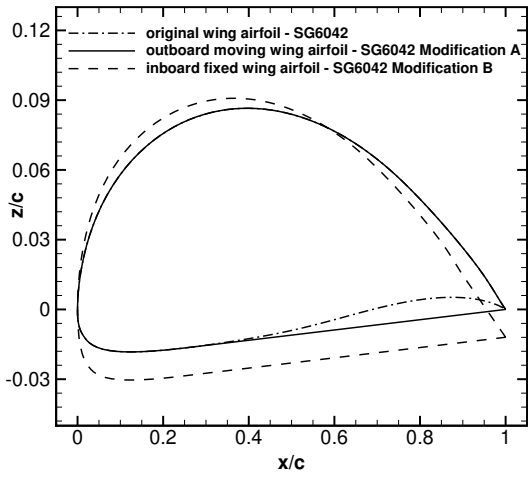

Figure 2.8: Comparison between original SG 6042 aerofoil and modified fixed and moving wing aerofoils.

In the optimization problem, the OMW chord length was fixed and equal to 0.25 m and no stall speed constraint was imposed. The optimization statement is shown below, for two sets of design variables, span, b, and angle of attack, α, where the angles are in degrees.

$$\text{Minimize: } f = \int_{V_i}^{V_f} D(\alpha, b, V) dV \tag{2.1}$$

$$\begin{aligned} & L(\alpha, b, V) = W \\ \text{Subjected to: } & -5 < \alpha \leq 20 \\ & 1.475 < b \leq 2.5 \end{aligned} \tag{2.2}$$

In the objective function of Eq.(2.1), the integral between the initial and final speed val-

ues, V_i and V_f, respectively, was calculated using Simpson's Rule where drag, D, was computed at five different speeds: 15 m/s, 20 m/s, 25 m/s, 30 m/s, and 35 m/s. For each one of these speed values there are two design variables, AOA and span, totalling 10 design variables for this optimization problem.

2.4.3 Results

For the fully extended wing, the increase in wing weight was computed as 3.6 N, using the weight equations in [120], resulting in a takeoff aircraft weight of 63.6 N. For the OMW fixed chord of 0.25 m, the IFW chord resulted in a value of 0.282 m from an offset of 3 mm around the OMW aerofoil. Based on the aerodynamic shape optimization results, the plots of Fig.2.9 were obtained for the VSW and the fixed wing.

Figure 2.9(c) shows that the VSW has better performance than the original wing only at speeds above 25 m/s, indicating that the present design allows better performance at the higher speed end of the envelope. At 30 m/s the VSW has about 10% less drag than the original one. At a speed of 40 m/s the drag reduction increases drastically to 28%. At low speeds, the original wing outperforms the new wing, although presenting only slightly better results. The original wing was designed for low speeds, and near the design point it was expected to have better performance than the new wing because of the higher relative thickness of the aerofoil in the IFW and because of the less efficient aerofoil resulting from the lower surface simplification of the SG6042 aerofoil. Therefore, the new wing presents a slightly higher total drag at low speeds when it is fully extended, which is only compensated at higher speeds, when the wingspan starts to decrease. For example, one can see that above 20 m/s a major span reduction takes place (see Fig.2.9(b)), when the new wing performance surpasses the original wing, until the minimum span of 1.475 m is reached at a speed of 35 m/s. Stall speed increased too, from 10.75 m/s in the original wing to 11.5 m/s in the new wing. The increased weight of the wing had an important effect in the wing performance at low speeds. Lift-to-drag ratio of the VSW is slightly reduced below 19 m/s, then is maintained up to 23 m/s but is greatly increased at higher speeds (see Fig.2.9(d)). Clearly, the increased drag below 25 m/s seen in Fig.2.9(c) is due to the increased weight of the VSW.

Fuselage drag was not considered in this study but clearly the smaller variation in AOA of the VSW may result in reduced fuselage pressure drag allowing further benefits in the aircraft overall drag curve. In the range 17.5 m/s to 30 m/s the variation in AOA of the VSW is only around 2° whilst that of the original wing is 4.5°(see Fig.2.9(a)). Clearly, the planned aerodynamic flight tests (subject of the next chapter) are going to help to substantiate this statement, since total aeroplane drag is going to be determined.

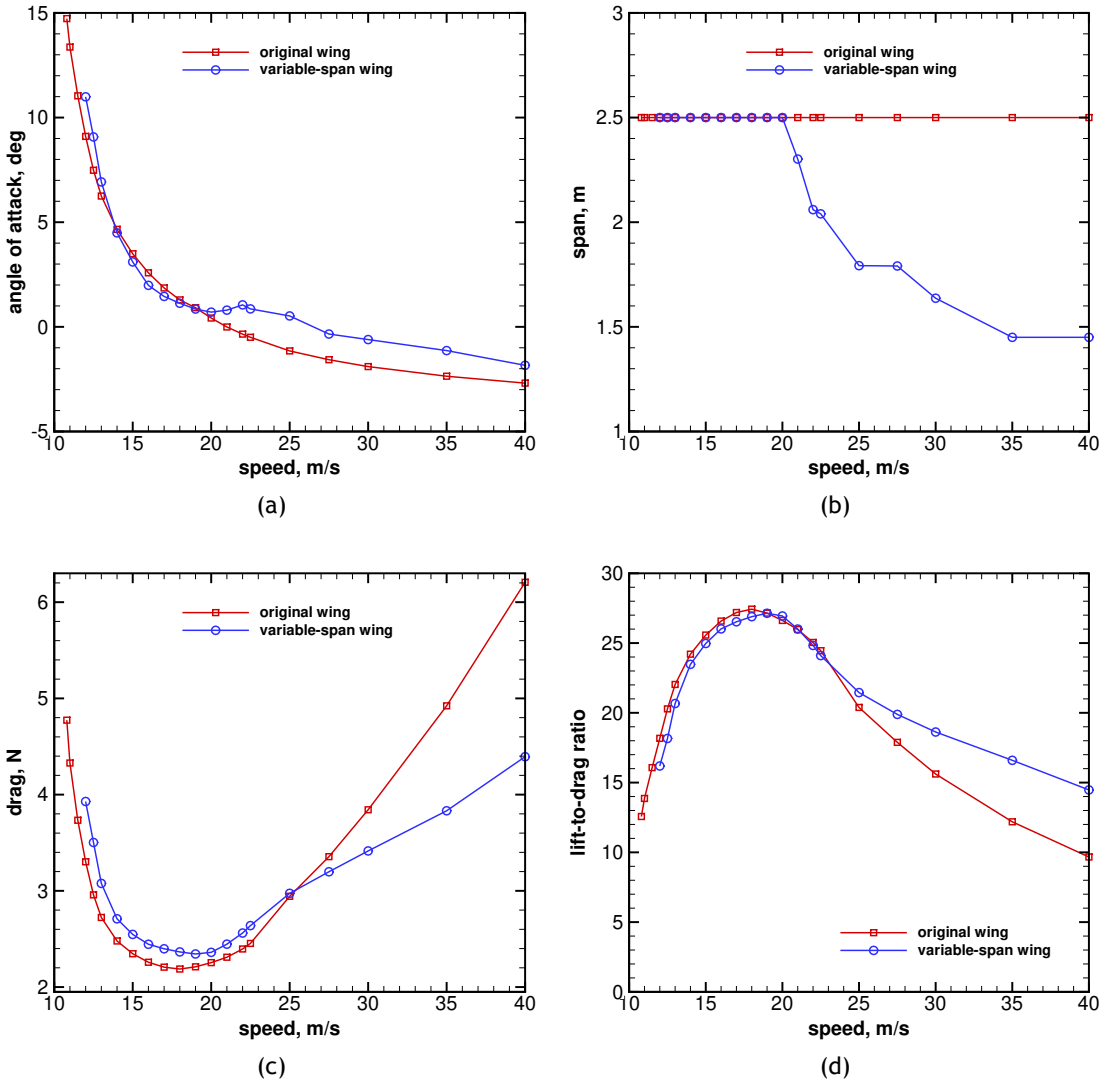

Figure 2.9: Numerical results comparison between original and variable-span wing: (a) angle-of-attack, (b) span variation, (c) wing drag, and (d) lift-to-drag ratio as a function of speed.

2.5 Structural Design

The structural components of the wing were developed with a combination of composite materials and hard and soft wood which provide good general strength and stiffness. The sizing of the structure was performed using structural analysis models based on FEM considering limit material stresses and required structural stiffness. A description of the structural analysis and their results is given in the following sections. Additionally, an aeroelastic study of VSW was performed. The study concentrated on the flutter critical speed estimation and more specifically on the effects arising due to the interface between fixed and moving wing parts.

2.5.1 Structural Concept

The IFW uses a monocoque type of structure with a sandwich skin of carbon/foam/carbon which is required to both provide the correct shape and resist shear loads. The PVC foam core

was incorporated between the carbon fibre layers to allow embedding of the main spar and to give adequate stiffness to the skin. All fibre fabric layers are plain weave oriented at 0° along the wing span.

The structural configuration used in the moving wing part is very conventional: the wing is composed of ten thin balsa wood ribs, a carbon fibre/epoxy skin and a I-section spar consisting of pultruded carbon spar caps with balsa wood spar web. The main spar confers sufficient bending stiffness while the ribs provide the correct wing shape. The ribs were bonded to the skin and spar with epoxy glue.

The cross-sections of the wing are represented in Fig.2.10 clearly showing the different structural layouts adopted for the inboard and outboard parts of the wing as necessary to allow the motion of the OMW inside the IFW. The circular tubes in the OMW are present to allow the span actuation system components (racks) to move inside it, and although they have no special structural function they contribute to the stiffness of the OMW both in bending and in torsion.

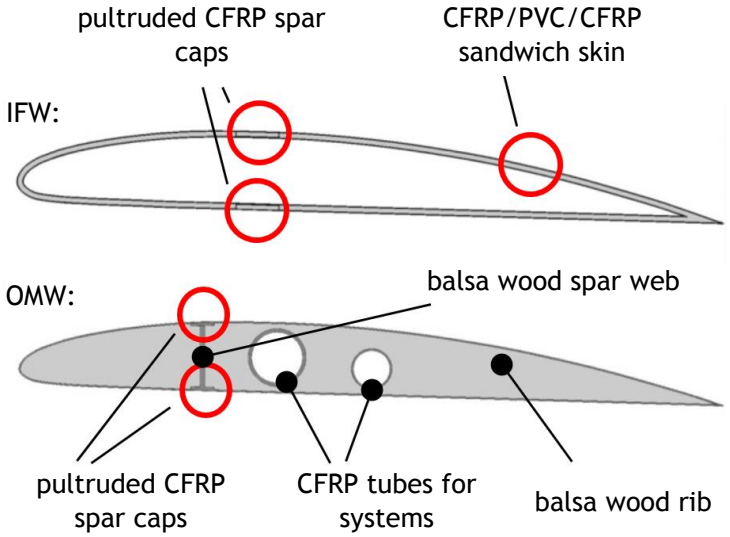

Figure 2.10: Variable-span wing cross-sections for IFW (top) and OMW (bottom).

2.5.2 Materials

As stated before, the variable-span wing was made with a combination of four materials: woven carbon/epoxy composite, PVC foam (Airex® C70.55), unidirectional carbon-fibre with epoxy and balsa wood. The material properties of the PVC foam - Airex® C70.55 and the pultruded carbon/epoxy elements were obtained from the manufacturer's datasheet [127, 128]. The balsa wood properties were obtained from the *Wood handbook: wood as an engineering material* [129].

The woven carbon/epoxy composite tensile moduli and ultimate strength properties were obtained experimentally following ASTM D3039/D3039M [130]. This standard contains guidelines to determine the ultimate tensile strength of the composite and the longitudinal elastic modulus. Five rectangular carbon/epoxy specimens were hand laminated with a fibre orientation of 0°/90° balanced and symmetric, for which the specified dimensions were 25 mm in width,

250 mm in length and 1.1 mm in thickness. The specimens were tested in a Shimadzu® universal testing machine up to rupture, with a test speed of 2 mm/min and with the data being recorded in the form of a load/strain curve. The maximum registered load was used to determine the ultimate tensile strength of the specimens and from the stress-strain curve's slope the elastic moduli, E_1 and E_2, were computed. Since the skin material had identical fibre fractions at 0° and 90° both longitudinal elastic moduli were assumed to be the same. The results were statistically analysed revealing the sample average, the sample standard deviation and the sample coefficient of variation. The remaining properties (e.g shear modulus, ultimate compressive strength) were estimated using the literature [131].

The properties of the different materials used in the VSW structure are summarized in Table 2.3. The pultruded carbon-fibre, woven carbon/epoxy and balsa wood were formulated as orthotropic materials and the PVC foam was considered to be an isotropic material. Note that subscripts 1 and 2 denote the direction of the fibre and perpendicular to the fibre, respectively (where applicable) and subscript 3, denotes the out-of-plane or interlaminar direction, which was assumed to have the same properties as the perpendicular direction (where applicable), with the exception of balsa wood, where all properties were extracted from [129].

Table 2.3: Material properties used in the variable-span wing structural design.

property	woven carbon/epoxy	pultruded carbon/epoxy	balsa wood	PVC foam (Airex®C70.55)
ρ, kg/m^3	1500	1600	160	60
E_1, GPa	46	105	1.28	0.045
E_2, GPa	46	7.5	0.0192	-
E_3, GPa	46	7.5	0.0589	-
G_{12}, GPa	3.25	3.75	0.02484	0.022
G_{23}, GPa	3.25	3.75	0.02116	-
ν_{12}	0.1	0.3	0.488	0.0227
ν_{23}	0.1	0.3	0.231	-
F_{tu1}, MPa	600	1500	19.9	1.3
F_{tu2}, MPa	600	50	0.299	-
F_{tu3}, MPa	600	50	0.915	-
F_{cu1}, MPa	570	1200	12.1	0.9
F_{cu2}, MPa	570	250	0.182	-
F_{cu3}, MPa	570	250	0.557	-
S_{12}, MPa	90	70	1.07	0.85
S_{23}, MPa	90	70	1.07	-

2.5.3 Loading

The VSW was loaded at 25% chord position with an elliptic distribution, induced by aerodynamic loading with varying load factor. More particularly, two loading factors were considered, 4G and 6G, corresponding to total lift forces of 120 N and 180 N, respectively, on a single wing for a takeoff weight of 60 N.

The VSW model was tested with two additional loading cases: bending with a concentrated load of 5 N applied at 35% of the OMW tip chord and torsion with a couple of 1.1 N·m at the IFW tip chord. These two loading cases were used to ascertain numerical model and developed prototype similarity. Thus, results for these two loading conditions are described later

in this chapter, being compared with experimental deflection results, obtained from the wing prototype (section 2.7.1).

2.5.4 Static Analysis

2.5.4.1 Finite Element Model

The numerical model of the VSW wing was developed in ANSYS® Mechanical using the ANSYS Parametric Design Language (APDL) [132] with shell and beam elements according to the model shown in Fig.2.10. An APDL script was written to handle geometry creation, material definition, section properties and meshing.

The IFW was discretized using SHELL181 elements. The sandwich skin was modelled with three layers built as offset surfaces from the aerofoil contour according to its own thickness. These three layers constitute the carbon/epoxy faces and PVC sandwich. In the locations of the embedded spar, the PVC foam layer was replaced with unidirectional pultruded carbon/epoxy elements. Likewise, the OMW skins, ribs, I-shaped spar web and circular spar were discretized using SHELL181 type elements. The OMW I-spar cap is discretized using BEAM188 elements.

The SHELL181 element is suitable for analysing thin to moderately-thick shell structures. It is a four-node element with six degrees of freedom at each node: translations in the x, y and z directions, and rotations about the x, y and z axes. This type of element is well-suited for linear, large rotation, and/or large strain nonlinear applications. Additionally, the change in shell thickness is taken into account in nonlinear analyses. The BEAM188 is suitable for analysing slender to moderately thick beam structures. The element is a linear, quadratic, or cubic two-node beam element in 3D. BEAM188 has six degrees of freedom at each node. These include translations in the x, y and z directions and rotations about the x, y and z axes. This element is well-suited for linear, large rotation, and/or large strain nonlinear applications.

The peculiar structure used by the VSW, required the use of contact elements, in order to correctly model the interface. This contact in the overlap surface between the IFW and the OMW was modelled with a shell to shell contact using TARGE170 (target element for 3D geometries) and CONTA173 (contact element for 3D shells without mid side nodes). Since the distinction between the contact and target surfaces is not clear in the interface, a symmetric contact (or "two-pass contact") was created. In this type of contact, each surface is designated to be both a target and a contact surface. Then, two sets of contact pairs between the contacting surfaces are generated. The symmetric contact is less efficient than asymmetric contact. One other reason to use this type of contact in this particular situation was to reduce penetration between contact surfaces. The contact elements' behaviour was considered standard when the simulation of the flexible contact on the interface was desired. Otherwise, it was considered bonded when a rigid contact interface is intended.

The wing was considered to be built-in at the root. Additionally, the centre portion of the innermost rib of the OMW was constrained along the y axis to simulate the constraint imposed by the rack and pinion actuator mechanism and thus avoid outward sliding of the OMW. The performed solution was a static analysis with large deflections effects activated. Thus, the solution was always non-linear, independently on the contact formulation (standard/bonded).

Figure 2.11 shows the different assemblies that make up the FEM as well as the complete wing model.

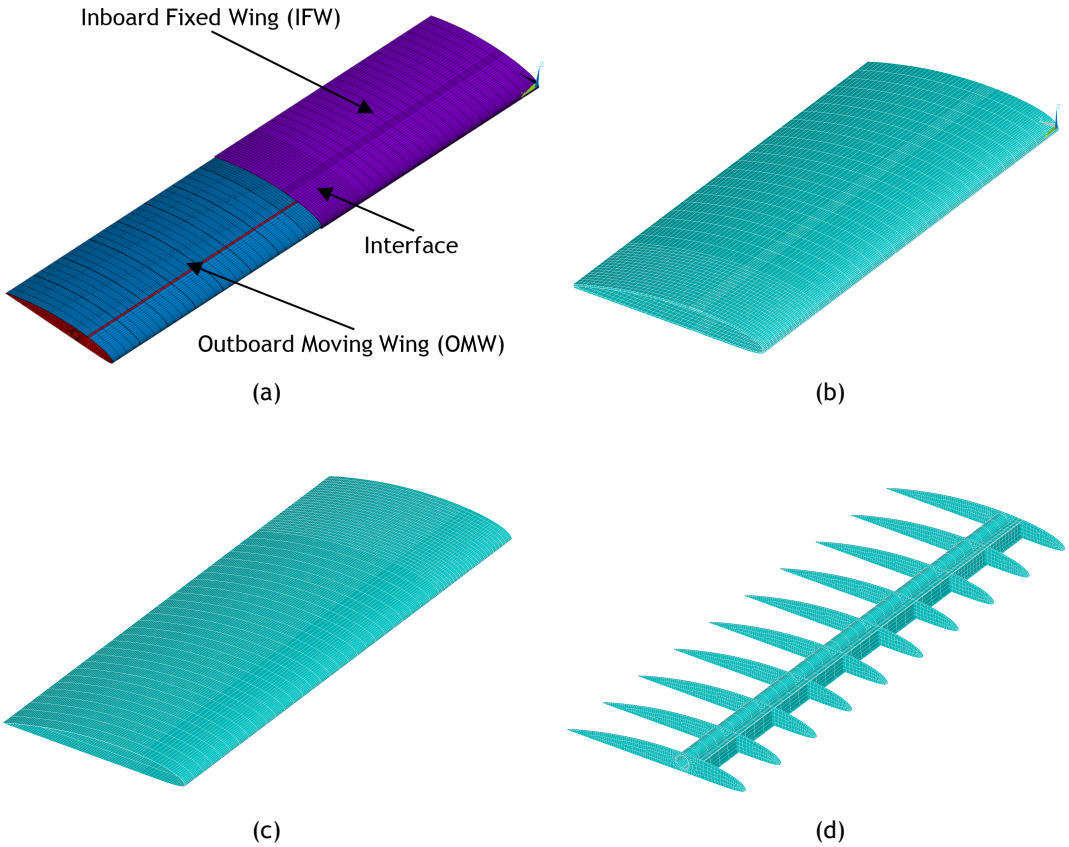

Figure 2.11: Variable-span wing model in ANSYS® Mechanical APDL: (a) complete finite element model, (b) IFW layered shell, (c) OMW shell and (d) OMW ribs, I-beam and circular spar.

2.5.4.2 Mesh Convergence Study

A convergence analysis of the finite element model was carried out to assess the sensitivity of the maximum tip deflection as a function of the number of elements in the grid. Several grids were created and a static analysis was performed using the aerodynamic elliptic loading in cruise flight condition (1G condition), distributed along the span at 25% chord line. During this study, the contact between the IFW and OMW was considered to be bonded.

The refinement of the mesh was done by changing the size of the elements (in both chord-wise and spanwise direction) in the finite element software. Figure 2.12 shows the convergence of the maximum wing tip deflection for several grids. It is possible to conclude that the solution is for practical reasons stabilized for a grid with about 31000 elements. In fact, the deflection variation is well below 1%. Therefore, the finite element model with 31000 elements was selected for the following analyses.

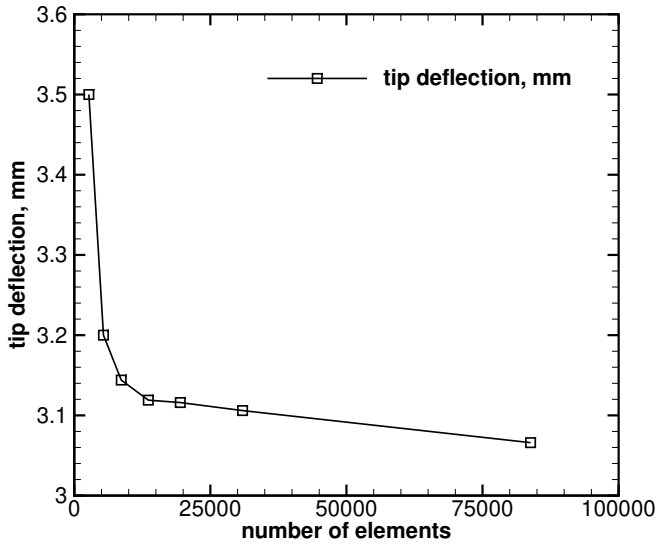

Figure 2.12: Maximum tip deflection obtained using different numbers of elements.

2.5.4.3 Results

The wing deflection induced by aerodynamic loading with varying load factor was studied for the proposed VSW. As mentioned before, two loading factors were considered, 4G and 6G, corresponding to total lift forces of 120 N and 180 N. The vertical deflections obtained in this study are shown in Fig.2.13 and 2.14.

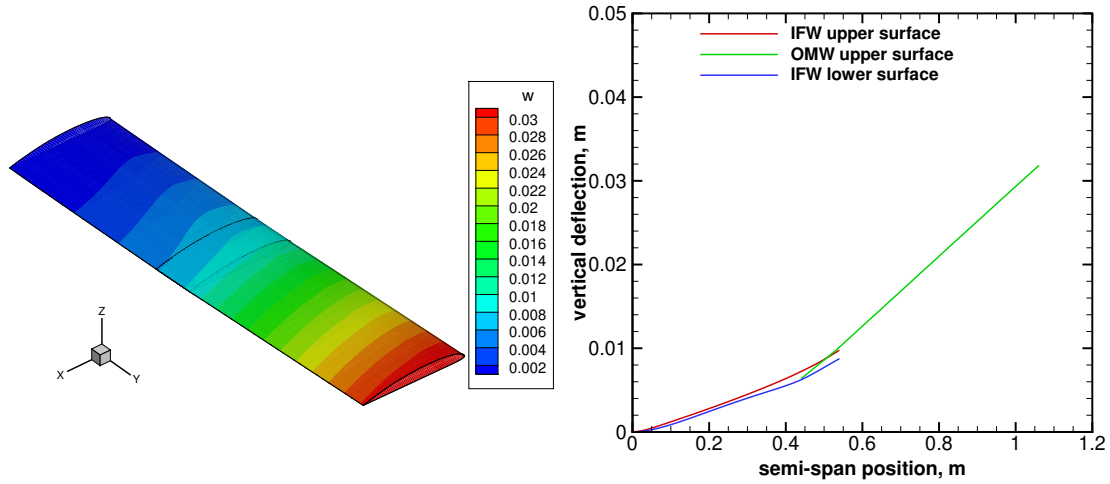

(a) (b)

Figure 2.13: Deflections of the variable-span wing due to aerodynamic elliptic loading of 4G: (a) vertical deflection distribution (in m) and (b) vertical deflection along span at 35% chord line.

From Fig.2.13(b) and 2.14(b), the widening of the wing aerofoil thickness at the IFW tip due to the moment transmitted from the OMW is clearly seen. The tip deflection varies from 0.032 m at the 4G condition to 0.048 m at the 6G load case, corresponding to relative deflections with respect to half-span of 2.6% and 3.8%, respectively. These values are well below the maximum relative deflection of 10% typically allowed in wing designs at limit load, but necessary to allow the seamless motion of the OMW under high loads.

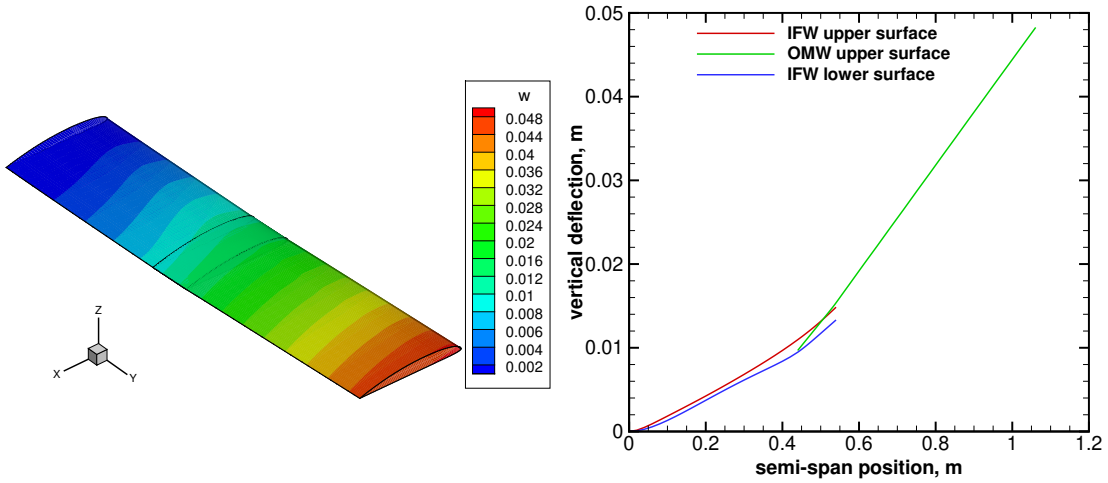

(a) (b)

Figure 2.14: Deflections of the variable-span wing due to aerodynamic elliptic loading of 6G: (a) vertical deflection distribution (in m) and (b) vertical deflection along span at 35% chord line.

For the maximum load factor case, the maximum stress index distribution, from the maximum strength criteria [133], was obtained to visualize high stress concentration areas which may require further attention in the structural elements design and to identify oversized areas that can be subject of weight reductions for increased structural efficiency. This is shown in Fig.2.15.

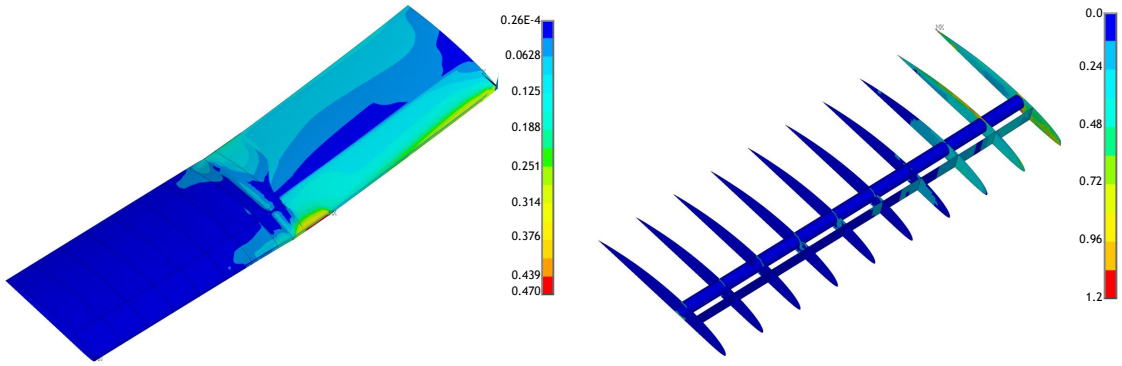

(a) (b)

Figure 2.15: Maximum stress index distribution of the variable-span wing structure due to an aerodynamic load of 6G (180 N): (a) IFW and OMW skin and (b) OMW spars and ribs (inboard section in the right side).

As expected, two highly stressed regions stand out in Fig.2.15: the OMW leading edge skin in the IFW/OMW overlap region and upper and lower rib area on the second and first ribs of the OMW in the same IFW/OMW interface region. The maximum stress index reaches values near 1.0 in these balsa ribs. When the OMW deflects under load, the bending moment transmitted from the OMW to the IFW should produce a linear reaction force distribution over the 0.1 m overlap distance, should the structure be completely rigid. However, the effect observed in Fig.2.15(b), where the upper and lower skins slightly move apart at the IFW tip chord, makes this reaction distribution to be non-linear and have peak values at the overlap extremities (OMW root chord and IFW tip chord). This effect overloads the lower part of the first OMW rib and the upper part of the second OMW rib due to the vertical compressive reaction that was exerted on them by

the IFW sandwich skin. The maximum stress index observed on the leading edge of the IFW in the interface area is close to 0.5, therefore, not critical; although this results from bending of the leading edge skin as the upper and lower IFW skin move apart in the interface.

Overall, the wing structure exhibits adequate strength requiring, though, three improvements to make it more efficient: (a) increasing the thickness of the first two balsa ribs of the OMW to reduce the stress levels; (b) stiffening the rib contour at the tip of the IFW to reduce the aerofoil section deformation; and (c) reducing the weight of the OMW towards the tip.

2.5.5 Flutter Speed Analysis

Aeroelastic instabilities are within the factors that most restrict the flight envelope of aircraft. The simultaneous presence of aerodynamic, inertia, and elastic forces makes it an interdisciplinary problem that has been studied since the early days of aviation. The most dangerous aeroelastic phenomenon is flutter, when aerodynamic lifting surfaces suffer a self-excited oscillation that may often be destructive, since the structure absorbs energy from the flow and leads to large amplitude oscillations of the lifting body. Due to its catastrophic nature, it is imperative that the occurrence of flutter on lifting surfaces is avoided to prevent failure of the structure, due to large deformation from occurring. On the other hand, the reduction of structural stiffness that may be required to allow the geometric changes is also an important factor in producing instabilities at lower flight speeds. For these reasons, an aeroelastic analysis of the VSW was performed. The analysis was divided into two main parts: (1) calculation of mode shapes and frequencies of natural vibration and (2) computation of flutter critical speed and considerations about the aeroelastic behaviour of the wing in particular the effects arising due to interfaces between fixed and moving wing parts.

2.5.5.1 Aeroelastic Model Theory

The flutter study uses complex determinant analysis to determine the combination of airspeed and frequency for which the neutrally damped motion is sustained. The computational analysis of this phenomenon requires the following steps: (a) building the structural model and performing a modal analysis; (b) generating strip section data (inertia, elastic); (c) computing aerodynamic coefficients; and, finally, (d) solving the flutter determinant. An explanation of the first and second steps is given later. The third and fourth steps are briefly described in the following paragraphs.

The typical section using unsteady linearised potential theory together with the strip theory aerodynamic simplification was used to estimate the aeroelastic characteristics of a straight, high aspect ratio wing. Such section is depicted in Fig.2.16, along with the main parameters necessary to characterize its dynamic motion. The determination of the aerodynamic forces acting on an aerofoil moving in an unsteady motion about its initial state of equilibrium is complex. At any instant in time, the change in the aerofoil position results in a change in the circulation around the aerofoil which causes a change in the vortex shed from its trailing edge. This vortex shedding produces vertical velocities on the aerofoil and affects the incremental non-stationary aerodynamic loads on the lifting section. At the critical point of dynamic instability, the motion of such a system is a pure harmonic oscillation. From this fact, a formulation to compute the incremental non-stationary aerodynamic loads has been established which presents the exact

solution at the critical instability condition. The linearised incremental lift and moment acting on a two-dimensional aerofoil performing a simple harmonic motion in two degrees of freedom (aerofoil vertical displacement and aerofoil rotation) has been obtained by other authors [134, 135].

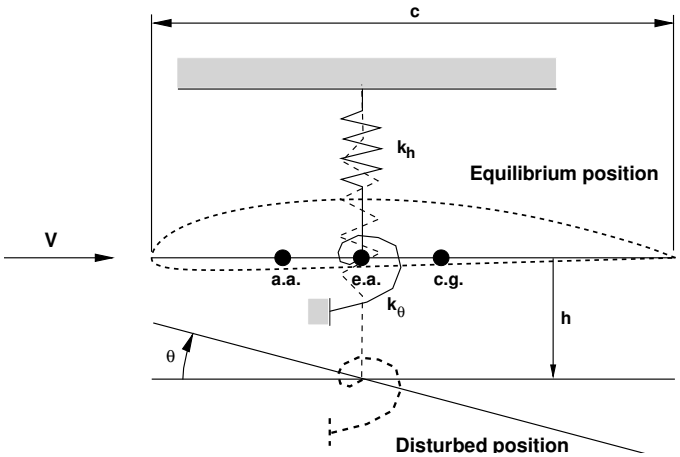

Figure 2.16: Typical section of the aeroelastic lifting surface.

The typical section theory was extended for the computation of the aeroelastic stability of a three-dimensional lifting surface at low speeds with no considerable mass concentration areas using the strip theory aerodynamic simplification [136]. The strip theory approximation for lifting surfaces of high aspect ratio consists in dividing the lifting surface in chordwise small strips of finite width and assuming that at each strip the flow is two-dimensional and does not interact with the flow of other strips.

Consider a lifting surface divided into strips of width Δy_i, mean chord c_i and lateral position y_i. For each strip of the wing the mass per unit width, $\overline{m}$, the moment of inertia about the elastic axis (e.a.) per unit width, i_θ, the static mass moment about the e.a. per unit width, s_θ, the bending stiffness, EI, and the torsional stiffness, GJ, are known quantities. The Lagrange equations of motion of the complete wing are

$$\begin{aligned} M\ddot{h} + S_\theta\ddot{\theta} + C_h\dot{h} + K_h h &= Q_h \\ I_\theta\ddot{\theta} + S_\theta\ddot{h} + C_\theta\dot{\theta} + K_\theta\theta &= Q_\theta \end{aligned} \tag{2.3}$$

where M is the total mass of the wing, S_θ is the total static mass about the elastic axis, I_θ is the total moment of inertia about the e.a., K_h is the total stiffness in bending and K_θ is the total stiffness in rotation. These quantities can be computed from

$$\begin{aligned} M &= \int_0^{b/2} \overline{m}(y)[f_h(y)]^2 dy \\ S_\theta &= \int_0^{b/2} s_\theta(y) f_h(y) f_\theta(y) dy \\ I_\theta &= \int_0^{b/2} i_\theta(y)[f_\theta(y)]^2 dy \\ K_h &= \int_0^{b/2} EI(y)\left[\frac{\partial^2}{\partial y^2} f_h(y)\right]^2 dy \\ K_\theta &= \int_0^{b/2} GJ(y)\left[\frac{\partial^2}{\partial y^2} f_\theta(y)\right]^2 dy \end{aligned} \tag{2.4}$$

where $f_h(y)$ and $f_\theta(y)$ are the assumed shapes of the first uncoupled bending and torsion modes of vibration, respectively, normalized to unit values at the wing tip.

In Eq.(2.3), C_h and C_θ are the viscous damping coefficients, which are assumed zero in this work, and Q_h and Q_θ are the generalized incremental aerodynamic loads given by

$$\left\{ \begin{array}{c} Q_h \\ Q_\theta \end{array} \right\} = \pi\rho\omega^2 \begin{bmatrix} A_{hh} & A_{h\theta} \\ A_{\theta h} & A_{\theta\theta} \end{bmatrix} \times \left[\begin{array}{c} \underline{h} \\ \underline{\theta} \end{array} \right] \tag{2.5}$$

where ω is the coupled frequency of vibration of the system and the elements A_{hh}, $A_{h\theta}$, $A_{\theta h}$ and $A_{\theta\theta}$ are functions of the wing chord and wing span sizes, the elastic axis position, the normalized bending and torsion mode shapes and the complex unsteady aerodynamic coefficients [136] that are functions of the reduced frequency

$$k = \frac{\omega c}{2V} \tag{2.6}$$

where c is taken as the wing chord at $2/3$ of the semi-span and V is the flow velocity. The integrals of Eq.(2.4) are calculated from the root to the tip, where the semi-span is represented by $b/2$, by applying a sum through all the strips considered.

Because the oscillation is harmonic at the critical condition, the solution of the equations of motion can be written in the form

$$\underline{h} = h_0 e^{i\omega t} \quad ; \quad \underline{\theta} = \theta_0 e^{i\omega t} \tag{2.7}$$

which on substitution into Eqs.(2.3) leads to the final system of equations representing the vibration of the wing as

$$\begin{bmatrix} \overline{A}_{hh} - \Omega_h Z & \overline{A}_{h\theta} \\ \overline{A}_{\theta h} & \overline{A}_{\theta\theta} - Z \end{bmatrix} \left\{ \begin{array}{c} h_0 \\ \theta_0 \end{array} \right\} = \left\{ \begin{array}{c} 0 \\ 0 \end{array} \right\} \tag{2.8}$$

where $\overline{A}_{hh}$, $\overline{A}_{h\theta}$, $\overline{A}_{\theta h}$ and $\overline{A}_{\theta\theta}$ are functions of M, S_θ, I_θ, the air density and the A elements of Eq.(2.5) [136] and

$$\begin{gathered} Z = X - iY \quad \text{with} \quad X = \left(\frac{\omega_\theta}{\omega}\right)^2 \quad ; \quad Y = g_D X \\ \Omega_h = \left(\frac{\omega_h}{\omega_\theta}\right)^2 \end{gathered} \tag{2.9}$$

where ω_h and ω_θ are the uncoupled natural frequencies in bending and in torsion, respectively, and g_D is the damping coefficient.

For the nontrivial solution of Eq.(2.8), its determinant must be zero, thus

$$\Delta = \begin{vmatrix} \overline{A}_{hh} - \Omega_h Z & \overline{A}_{h\theta} \\ \overline{A}_{\theta h} & \overline{A}_{\theta\theta} - Z \end{vmatrix} = 0 \tag{2.10}$$

The flutter boundary is provided when the value of damping is equal to zero. A technique of reduced frequency sweeps is used. The sweeping starts from zero reduced frequency of the unsteady aerodynamic forces with an increment up to a maximum selected value. Eq.(2.10) is solved for Z and its real and imaginary parts, X and Y, respectively, are extracted. The

frequency, damping and speed are then obtained from Eqs.(2.9) and (2.6) in the form

$$\omega = \frac{\omega_\theta}{\sqrt{X}} \quad ; \quad g_D = \frac{Y}{Z} \quad ; \quad V = \frac{\omega c}{2k} \tag{2.11}$$

Then, the curves of $V - g_D$ and $V - \omega$ can be plotted.

The determinant of Eq.(2.10) is a second order polynomial in Z. Therefore, two values of ω and g_D are obtained for each k selected, being the flutter curve the one for which g_D becomes zero at a lower value of $1/k$. At this point, where the system is neutrally damped, the critical flutter condition is obtained as

$$\omega_f = \frac{\omega_\theta}{\sqrt{X}} \quad ; \quad V_f = \frac{\omega_f c}{2k} \tag{2.12}$$

The uncoupled natural frequencies of vibration can be either calculated from the results of Eq.(2.4) with

$$\omega_h = \sqrt{\frac{K_h}{M}} \quad ; \quad \omega_\theta = \sqrt{\frac{K_\theta}{I_\theta}} \tag{2.13}$$

or from a modal analysis. In the present study, the modal analysis was used.

2.5.5.2 Finite Element Model

The finite-element model is similar to the one used to perform the static analysis (see section 2.5.4.1). However, in the current study the finite element model was used to perform a modal analysis. Due to the presence of nonlinearities in the structure, a traditional linear modal analysis was not possible. Therefore, the modal analysis was based on a "Linear Perturbation Analysis" [133]. This methodology uses a prior nonlinear preloaded structural status. The modal analysis can then be performed using this preloaded structure. Therefore, the linear perturbation analysis procedure was designed to solve a linear problem from this preloaded case, being the effects from the previous static analysis included. This is important to make the contacts assume realistic positions. In fact, before the loading is applied to the model, all contacts are open or in near-open positions. Upon loading application, the contacts are solved and contact elements change the status (where appropriate) to closed.

2.5.5.3 Mesh Convergence Study

The first step to estimate the flutter speed was to perform a modal analysis. The linear perturbation modal analysis [133] was performed using at the initial state a static wing deformation induced by the aerodynamic loading in cruise flight condition (1G condition).

A convergence analysis for a free vibration analysis of the developed finite element model was carried out with several grid sizes. During this study, the contact between the IFW and OMW was considered to be rigidly bonded. The refinement of the mesh was done by changing the elements size (in both chordwise and spanwise direction) in the FE software. Figure 2.17 shows the convergence of the first six modal frequencies for several mesh sizes. It is possible to conclude that the first four modal frequencies show a stabilized result for a mesh with 31000 elements. Therefore, the results achieved in the following analysis are obtained for a mesh with

this number of elements. Note that the convergence occurs for a number of elements similar to that of the static loading convergence study (section 2.5.4.2).

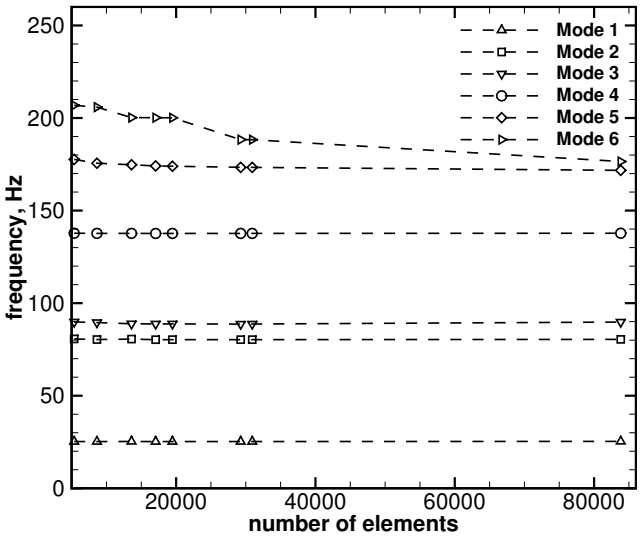

Figure 2.17: First six modal frequencies obtained using different number of elements.

2.5.5.4 Results

Due to the flexible nature of the interface between the two parts of the wing, two situations were analysed: one corresponding to the flexible interface that exists in the proposed wing and another with an hypothetical interface that is assumed to be much stiffer. The latter represents a stiffener placed around the tip of the IFW section in the shape of a wing fence. The effect of this rigid interface is to prevent the sandwich skin to bend thus reducing the amount of rotation in bending which the outer wing part experiences.

Mode Shapes and Natural Frequencies

The first four mode shapes obtained are shown in Fig.2.18. Essentially, the mode shapes are similar irrespective of the interface between the IFW and the OMW (flexible or rigidly bonded). The first two modes are practically pure bending modes, particularly in the wing with the rigid interface. The third mode in both types of interface is a pure torsion mode. The fourth mode is a bending mode in the horizontal x-y plane. In the second mode, an increase in the bending curvature is observed at the IFW/OMW interface region where the wing is less rigid in bending. The difference in the two types of interface has little effect on the torsion mode because, unlike in the bending case, the torsion motion does not make the upper and lower skins move slightly apart at the interface thus restricting the amplitude of the deflection.

Regarding the natural vibration frequencies the large difference in the two types of interface occurs between the bending modes (mode 1, mode 2 and mode 4). In the first torsion mode (mode 3) there is only a reduction of 3.6% due to the less rigid interface. Table 2.4 summarizes the frequencies of the first four mode shapes in the two interface cases.

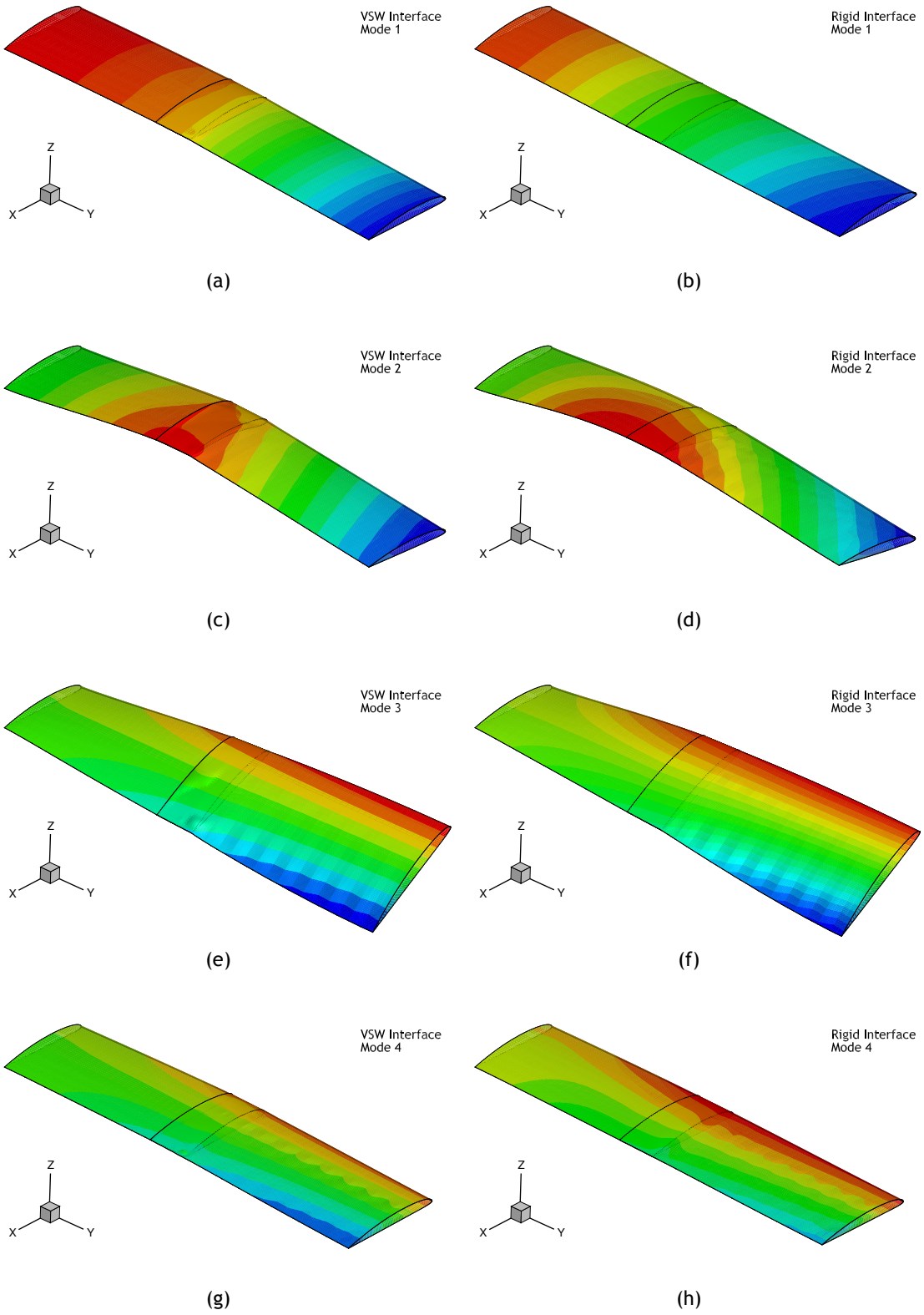

Figure 2.18: First four mode shapes of natural vibration of the wing fully extended (a), (c), (e), (g) with elastic VSW interface (19.9 Hz, 57.9 Hz, 85.5 Hz and 107.3 Hz) and (b), (d), (f), (h) with rigid interface (25.2 Hz, 80.3 Hz, 88.7 Hz and 137.7 Hz).

Table 2.4: First four natural vibration frequencies in Hz (or rad/s).

Mode	VSW interface	Rigid interface
1st	17.93 (112.7)	25.24 (158.6)
2nd	57.94 (364.1)	80.28 (504.1)
3rd	85.49 (537.2)	88.72 (557.4)
4th	107.33 (674.4)	137.67 (865.0)

From the data obtained by the numerical modal analysis, vertical deflections and rotations of and about the elastic axis were extracted to produce two-dimensional, beam-like, bending and torsion modes. Figure 2.19 illustrates the first and third mode shapes scaled to unit value at the wing tip. There is a noticeable effect from the different modelling of the interface on the bending mode. The curvature at the VSW interface is increased owing to the reduced stiffness implemented in this region in the numerical model (see section 2.5.4.3). On the other hand, the torsion behaviour is hardly altered, fact that can also be observed from the natural vibration frequencies. These mode shape curves in Fig.2.19 are used in the flutter model to estimate the flutter critical speed and frequency for the two types of interface.

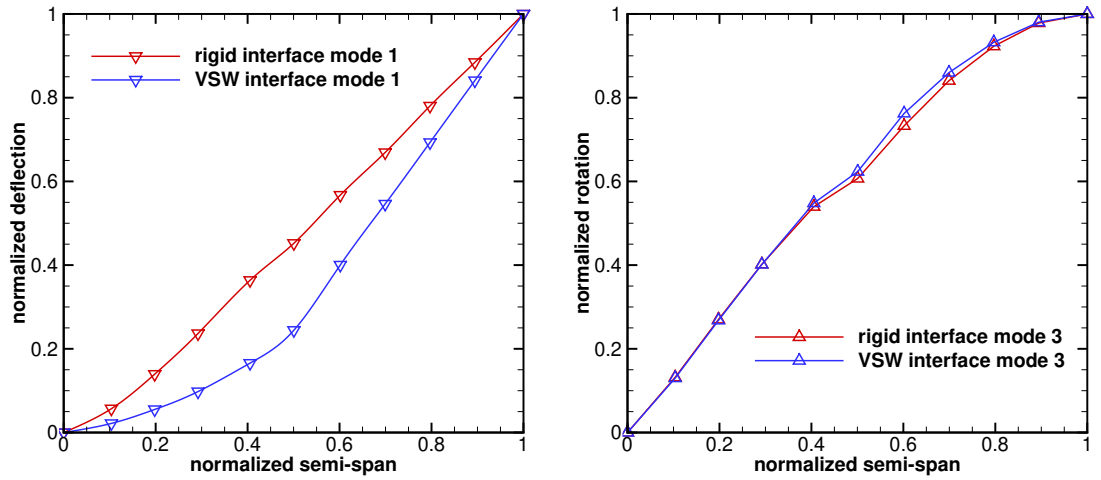

Figure 2.19: Mode shapes at the elastic axis for both types of interface: (a) bending $f_h(y)$ and (b) torsion $f_\theta(y)$.

Flutter Speed

The flutter analysis was performed for sea level standard conditions where the air density is greatest and the flutter critical speed will be lowest.

Some parameters of the wing sections were required to be available in order to perform the flutter analysis, namely: local chord, c; chordwise position of the e.a., x_e; chordwise position of the centre of gravity, x_{cg}; wing mass per unit width, $\overline{m}$; moment of inertia about the e.a. per unit width, i_θ; and static mass moment about the e.a. per unit width, s_θ. These parameters are shown in Table 2.5 for the three different sections available in the wing, namely the IFW, the OMW and the interface of the two. The elastic axis position on the chord was estimated

from the numerical FEM by applying a pure force couple at the tip of the wing and observing the line along the span that does not suffer any vertical displacement. The mass properties and centre of gravity position were obtained through calculations. Calculation of the static mass moment and mass moment of inertia follow by taking the moment of the mass about the elastic centre and by multiplying the mass by the squared distance to the e.a., respectively. A total of ten segments along the span were used to represent the wing's varying characteristics and the local parameter values for each segment were interpolated as required. The natural uncoupled frequencies are those obtained from the modal analysis.

Table 2.5: Variable-span wing section properties.

Parameter	IFW section	Interface	OMW section
c, m	0.266	0.266	0.245
x_e/c	0.371	0.368	0.365
x_{cg}/c	0.464	0.455	0.445
$\overline{m}$, kg/m	0.613	1.030	0.417
s_θ, kg	15.16×10^{-3}	23.61×10^{-3}	8.10×10^{-3}
i_θ, kg·m	0.375×10^{-3}	0.541×10^{-3}	0.158×10^{-3}

Figure 2.20(a) represents the $V - g_D$ diagram for the wing with different interface rigidity. Positive and negative damping values are representative of unstable and stable conditions, respectively. As we can see, flutter occurs when the speed curve intersects the zero damping line. This means that at this velocity, if the structure suffers an excitation, the aerodynamic flow will no longer damp the structural vibration. One is then able to determine the flutter frequency of the model using the plot of $V - \omega$ from Fig.2.20(b) and picking off the frequency value of the unstable mode at the flutter velocity value. The slope of the damping versus speed curve as it passes through flutter velocity can be thought of as a qualitative measure of how violently the oscillations would occur during accelerated flight.

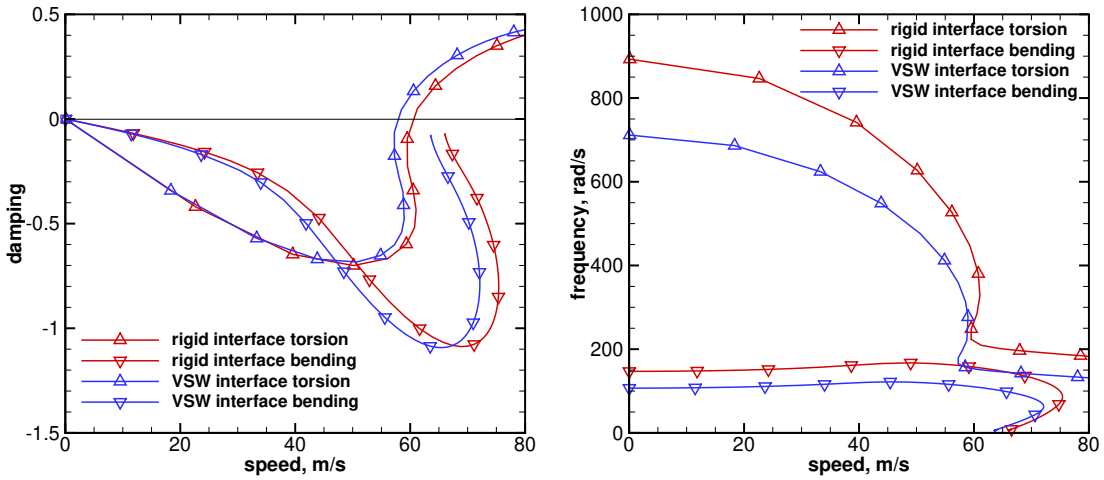

(a) (b)

Figure 2.20: Damping and frequency results for the two types of wing interface: (a) $V - g_D$ diagram and (b) $V - \omega$ diagram.

The first bending mode (mode 1) and the first torsion mode (mode 3) were used to compute the flutter critical speed since these are the uncoupled natural modes with the lowest

frequencies. The critical mode, as seen from Fig.2.20(a), is the torsion mode because its damping becomes zero before that of the bending mode. Typically, this is the case in aircraft lifting surfaces. As expected, the effect of a less rigid interface between the OMW and the IFW is to reduce the flutter critical speed. Even though not so significant, the reduction in the bending natural frequency results in a decrease of 4.2% in V_f from 60.36 m/s for the wing with the rigid interface to 57.81 m/s for the VSW interface. The flutter critical frequency of the rigid interface wing is 33.95 Hz (213.4 rad/s) whilst the flutter frequency of the VSW interface is 25.48 Hz (160.1 rad/s), as observed from Fig.2.20(b).

The normal cruise speed of the RPAS ranges from 20 m/s to 35 m/s and the intended maximum speed for the variable-span wing is 40 m/s (see section 2.4). From the results obtained in this study, a speed margin of 44.5% ensures safe operations of the VSW during the flight tests programme.

2.5.6 Final Design

In summary, the final IFW structure uses a sandwich skin with the following layers (from inside out): a layer of 48 g/m^2 glass/epoxy, a layer of 185 g/m^2 carbon/epoxy, a layer of 2 mm porous PVC foam (55 kg/m^3), a layer of 185 g/m^2 carbon/epoxy, and finally another layer of 48 g/m^2 glass/epoxy. All fibre fabric layers are plain weave oriented at 0° along the wing span. The glass layers do not have a structural role, and thus were not included in the FEM analysis, but are added to reduce the porosity of the carbon/epoxy layers. The complete assembled skin has a thickness of 2.5 mm, which creates a fairly acceptable small discontinuity between the IFW and the OMW. Spar caps inside the IFW are composed of rectangular beams made of pultruded carbon fibre with a cross-section of 16 mm $\times$ 1.7 mm. For greater strength and stiffness, the spar extends along the complete IFW span of 1.475 m.

The structure of the OMW is: ten 2 mm thick balsa wood ribs, a 240 g/m^2 carbon fibre/epoxy skin and a I-section spar consisting of 8 mm $\times$ 0.8 mm pultruded carbon spar caps with a 1.5 mm balsa wood spar web. The main spar confers sufficient bending stiffness while the ribs provide the correct wing shape.

2.6 Prototype Development

A full-scale prototype was built to allow the pursuit of several ground tests and experimental flight testing. The manufacturing techniques used to build the wing are presented below. Additionally, the actuation mechanism sizing and integration in the wing are described.

2.6.1 Preliminary Considerations about the Manufacturing Process

For a suitable lamination and good surface quality, the hand-layup and vacuum bagging lamination approach was chosen, since this technique allows a lightweight structure to be obtained with low cost and reduced complexity. In fact, this procedure allowed draining much of the excess resin, prevented air bubbles to be trapped in the carbon layer and enabled a satisfactory surface finish. Briefly, this method consisted of laying up the carbon/epoxy in the

mould previously protected with wax to work as a releasing agent. Then, a layer of peel-ply was placed, whose function was to provide an ideal finishing for future bonding. Next, the release film was applied and a layer of breather cloth was added. This set was involved with a plastic film, which after sealed with a vacuum joint, made it airtight. Finally, a vacuum pump was connected to the sealed film in order to remove air from its interior.

The cure process was performed under controlled temperature conditions in two steps: cure and post-cure. The resin used was the Sicomin® SR1500 with SD2503 hardener, which is suitable for long curing times [137]. The first step required curing for 24 hours at 20°C. After this phase, a post-cure of 24 hours at 40°C was done. A higher temperature post-cure would reduce the manufacturing time but would risk damaging the tooling used. This procedure was used for all composite fabrications that have been undertaken. The curing and post-curing processes were properly controlled so that the mechanical properties of the composite parts could be known with confidence.

2.6.2 Outboard Moving Wing (OMW)

As described before, the wing is composed of ten 2 mm thick balsa wood ribs, a 240 g/m^2 carbon fibre/epoxy skin and a 22 mm carbon circular tube spar. The ribs were perforated in order to attach both the circular spar and a rack-guide tube. To prevent the transmission rack from getting stuck when crossing the other wing ribs, a rack-guide tube was made from epoxy impregnated carbon fibre. This carbon fibre tube was bonded to the ribs in the same way as the circular spar. Two stringers of pultruded carbon fibre were added (in the zone of the circular spar) under the skin and supported by a 1.5 mm thick balsa wood web. The set of two carbon stringers and the balsa web formed an I-beam as illustrated in Fig.2.21. This modification substantially increased the bending strength and stiffness with minimal gain in weight (about a 3% increase in this component's weight). A small jig was built to ensure the intended shape was obtained after bonding all the constitutive elements. All the structural components were bonded to the skin and spar with epoxy glue. Figure 2.21 shows the building of the OMW.

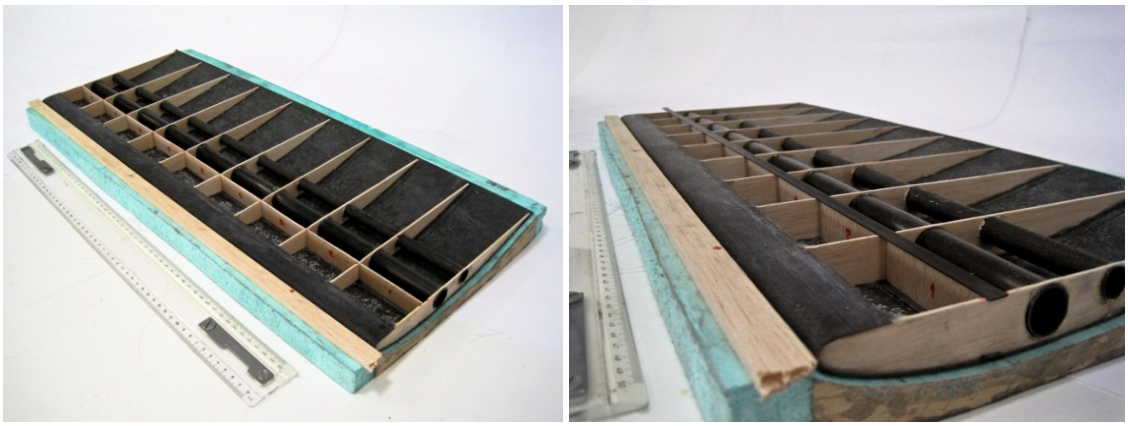

(a) (b)

Figure 2.21: Construction of the OMW showing all elements in place with (a) the balsa web and (b) the carbon flange, except for the lower skin.

2.6.3 Inboard Fixed Wing (IFW)

The need to have a hollow wing to allow the OMW to slide inside it, required a different design approach for the IFW. In the OMW, the main circular spar conferred sufficient bending stiffness while the ribs provided the correct wing shape. In the IFW the skin is required to both provide the correct shape and resist shear loads. Bending strength was achieved with a main spar configuration made of spar caps embedded in the skin sandwich.

The IFW was made using the positive mould used to obtain the OMW negative mould. This allowed an inside out construction of the sandwich skin guaranteeing the smallest space between wing parts to avoid any undesirable slack. From inside out, the load carrying thick skin was built with a layer of 48 g/m^2 glass/epoxy, a layer of 185 g/m^2 carbon/epoxy, a layer of 2 mm porous PVC foam - Airex® C70.55 (55 kg/m^3), a layer of 185 g/m^2 carbon/epoxy, and finally another layer of 48 g/m^2 glass/epoxy. The PVC foam core was incorporated between the carbon fibre layers to allow embedding of the main spar and to give adequate stiffness to the skin. All fibre fabric layers were plain weave (carbon fibre with 50% warp 1K HS and 50% weft 1K HS and E glass fibre with 56% warp EC5 11 and 44% weft EC5 11) oriented at 0° along the wing span. The glass layers were added to reduce the porosity of the carbon/epoxy layers and to allow surface sanding after curing to improve its finishing without damaging the structural carbon/epoxy layer. The complete assembled skin has a thickness of 2.5 mm, which originated a fairly acceptable small discontinuity between IFW and OMW.

The spar of the IFW is composed by two rectangular beams made of pultruded carbon fibre with a cross-section of 8 mm × 1.8 mm. For greater strength and stiffness of both sides of the IFW, the spar spans the complete fixed wing length of 1.475 m.

The PVC foam was shaped in order to make it compliant to the IFW inner carbon skin. This was accomplished using hot water and pressure against the master mould. The hot water facilitated a uniform heat distribution across the length of the fold, resulting in a uniform and constant curvature. Figure 2.22(a) shows the PVC foam portions and Fig.2.22(b) shows the IFW before the lamination of the outer layer.

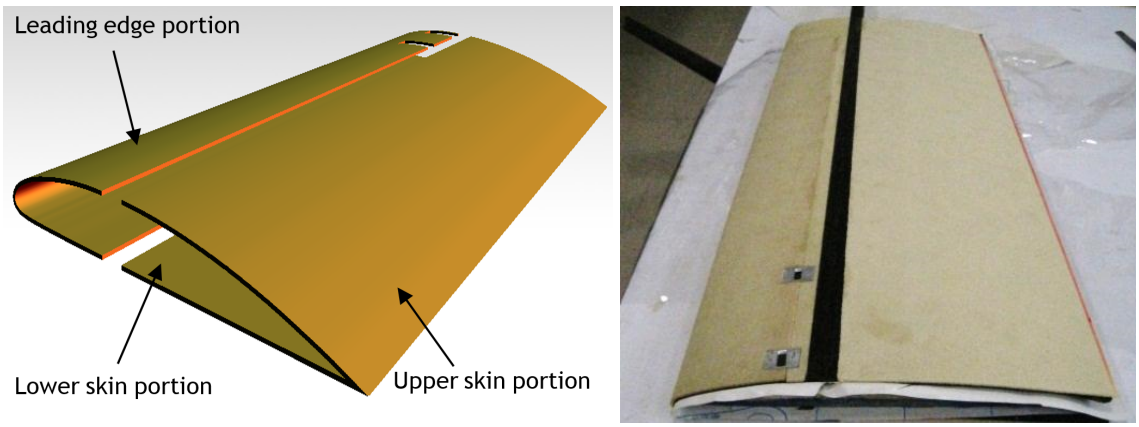

Figure 2.22: Construction detail of the IFW: (a) PVC foam core and (b) lower carbon fibre skin with foam and pultruded carbon fibre spar on top.

2.6.4 Actuation Mechanism

The VSW actuation mechanism was designed to allow in-flight extensions and retractions of the wing, in order to adapt the span to the flight regime and to perform roll and turn manoeuvres without the use of ailerons. An electro-mechanical system was chosen as the most plausible way to achieve what was proposed. Two types of actuators were considered as possible candidates: DC-motor based servomotor and an open-loop stepper motor. To create the linear movement, a rack and pinion system and a leading-screw mechanism were considered.

2.6.4.1 Electro-mechanical Actuator

Two types of actuators configurations were considered: DC-motor based servomotor and an open-loop stepper motor. A servomotor is a rotary actuator that allows for precise control of angular position, functioning in closed-loop. It consists of typically a DC brushed motor and a gearbox coupled to a sensor for position feedback. It also requires a servo drive to complete the system. The drive uses the feedback sensor to precisely control the angular position of the motor. Servomotors are better at delivering high speed and high torque and are able to maintain their torque rating at high speed, up to 90% of the rated torque is available from a servo at high speed. On the other hand, stepper motors have a large number of poles, generated either by a permanent magnet or an electric current. Since each pole offers a natural stopping point for the motor shaft, the greater number of poles allows a stepper motor to move accurately and precisely between each pole. Therefore, stepper motors are usually operated without any position feedback, i.e., in an open-loop configuration. With a stepper motor, a single drive pulse will move the motor shaft one step, from one pole to the next. Since the step size of a given motor is fixed to a certain amount of angular rotation, moving to a precise position is simply a matter of sending the right number of pulses. Stepper motors lose a significant amount of their torque as they approach their maximum driver speed. Typically, a loss of 80% of the rated torque at 90% of the maximum speed is to be expected.

Since the actuation system is also used to perform roll control, where speed and accuracy are important, the servomotor actuator was chosen. The selection of the servomotors followed a series of prerequisites regarding availability, high speed, high torque, low weight and robustness. Given the latter requirement, a servomotor that uses metal gears was necessary. This also facilitates further modifications. The selected servomotor was the HiTec® HS-805MG.

This servomotor, being fast for control surface actuation (429 °/s), was not fast enough for this particular application, where the deployment of the OMW should be fast enough for roll control. Due to actuation bay size constrains, the maximum diameter of the actuation pinion is 36 mm, which corresponds to a perimeter of 113.1 mm. Therefore, a total of 4.6 turns would be required (1672.6°) for a full deployment, taking approximately 4.2 seconds, with a maximum force of 134.5 N. This would not be an acceptable situation due to roll control authority requirements.

Further examination of the servomotor, revealed that a ratio of 0.385 exists between the first and second gear stages of the servo. Therefore, an angular speed and torque of 1111°/s and 0.93 N·m, respectively, is obtained in the second gear stage. Thus, using the shaft of the second gear stage of the servo for actuation allowed an ideal complete deployment of 1.5 seconds (with no load) with a force of 51.97 N available to move the OMW. This was suited for the considered

application. In order to couple the pinion to the second gear stage shaft, it was necessary to modify the servomotor. The solution was to use a steel shaft, lathe machined, that fitted inside the spur gear recess of the second stage. The 6 mm diameter shaft was made in a single piece, and is supported by two ball bearings, improving its alignment with the centre of the original shaft and supporting the radial forces applied during the actuation process. The pinion was attached to the shaft using a M2 screw. The steel shaft was glued and pinned (using two steel pins) to the second stage of the servomotor, in order to resist the torsion moment. The feedback potentiometer of the servo was removed and an external potentiometer was installed with a nylon pinion designed to provide the correct travel for the OMW motion. This was done to make the feedback system less complex and increase the resolution. The new potentiometer is capable of performing 10 turns (3600°). In Fig.2.25 it is possible to see the actuation pinion and the feedback potentiometer reduction pinion.

2.6.4.2 Rack and Pinion Transmission

To create the linear movement, a rack and pinion system and a leading-screw mechanism were considered. However, the leading-screw mechanism was rapidly discarded due to its high weight and low actuation speed. Thus, the rack and pinion system was the ideal compromise. The rack and pinion system is responsible for the push/pull of the OMW. To select the material and size of the rack several factors were addressed: weight, availability and size. Two options were considered: a rack made of reinforced plastic or a rack made of aluminium. The aluminium rack would eventually be chosen due to difficulties in sourcing a compatible rack made of plastic. Theoretical buckling calculations revealed that a section of 3 mm $\times$ 3 mm was sufficient for an ideal static application. Nevertheless, given that the rack is a critical element of the control system and operates in a very dynamic environment, subject to vibrations, a section of 9 mm $\times$ 5 mm was adopted. The rack is 0.8 m long, which is enough to span the wing length of 0.625 m and the stroke needed of 0.525 m. The material selected for the pinion was bronze due to its reduced friction coefficient. The maximum diameter of the pinion is (36 mm), due to space constrains of the actuation bay. This diameter is called the pitch circle diameter, P_d. Figure 2.23 clarifies the main rack and pinion parameters and Table 2.6 defines the nomenclature.

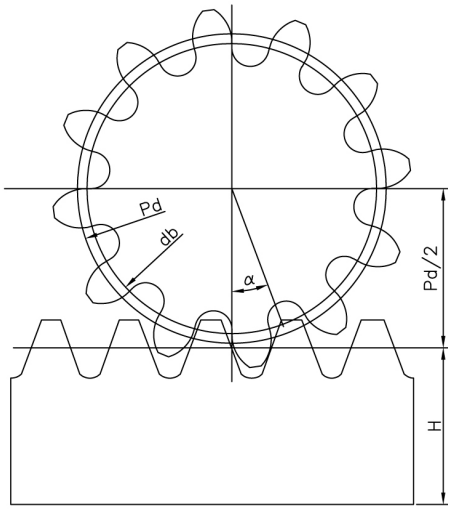

Figure 2.23: Rack and pinion nomenclature schematic.

Table 2.6: Rack and pinion nomenclature description.

Description	Symbol
Module	M_{gear}
Pressure Angle	α_{gear}
Number of Teeth	N_t
Height of Rack Pitch Line	H_{rack}
Pitch Circle Diameter	P_d
Base Circle Diameter	d_b

In order to determine the number of teeth of the pinion, the module, M_{gear}, should be defined. The module indicates the tooth size and is the length in mm of the pitch circle diameter per tooth. Thus, it is the ratio of the pitch circle diameter, P_d of the gear pinion divided by the number of teeth, N_t. Hence

$$M_{gear} = \frac{P_d}{N_t} \text{ or } N_t = \frac{P_d}{M_{gear}} \tag{2.14}$$

For gears and racks to mesh (compatibility between teeth), their modules must be equal. Due to the circle diameter and to maintain smoothness, a modulus of 1 mm was selected. Using Eq.(2.14) one determines that the pinion has 36 teeth. The standard pressure angle, α_{gear} of 20° was chosen in order to ensure optimal load distribution across the racks and pinions teeth. Figure 2.24(a) shows a close view of the rack and pinion and Fig.2.24(b) shows the two racks attached to the OMWs.

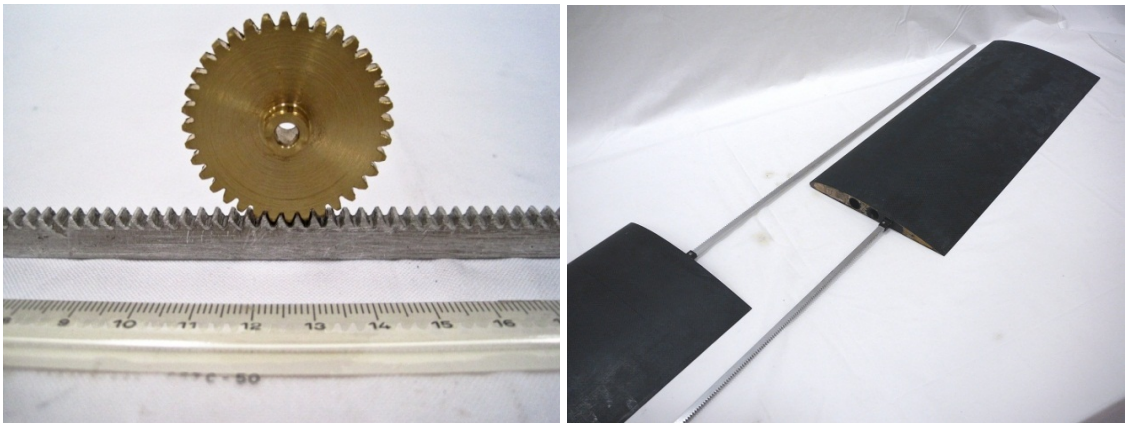

(a) (b)

Figure 2.24: VSW transmission elements: (a) close view of rack and pinion and (b) racks attached to the OMWs.

The developed system uses a pinion and rack made with metallic materials. However, in the future lighter materials (e.g. nylon) and advanced manufacturing techniques, should be sourced and tested, respectively, due to its potential to lighten up the system.

2.6.5 Central Structure of the Wing

After the actuation system was developed, a platform capable of supporting the servos and effectively transmitting the forces to the VSW moving parts, subjected to geometric constraints dictated by the fuselage size of the RPAS, was built. Considering all this, the result was a main support board made of 3 mm thick plywood, supported by two 6 mm thick lugs of the same material bonded to the wing tube and spars as seen in Fig.2.25. In this figure, the upper board (6) supports the pinion's shafts and the rack's guiding rollers at the top. The function of the rollers is to align and maintain the racks in contact with the corresponding pinions' teeth. In order to reduce friction to an acceptable minimum, ball bearings were placed in all contact holes between shafts and supporting wooded structure. The rollers were lathe machined from a 10 mm aluminium circular rod.

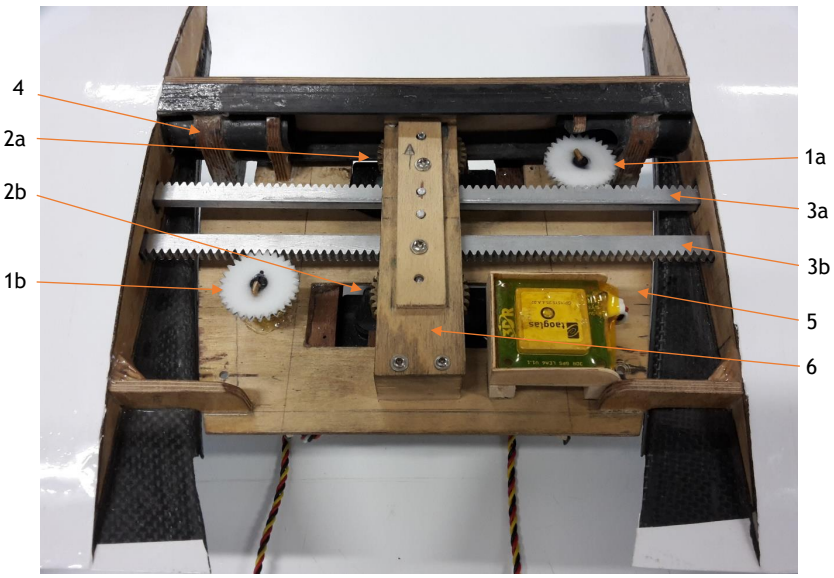

Figure 2.25: VSW actuation bay (subscript “a” refers to the left wing and “b” to the right wing): (1) feedback potentiometer, (2) servo actuators with pinions, (3) actuation racks, (4) wing-fuselage connection, (5) main support board and (6) upper support board.

2.6.6 Variable-span Wing Mass

All components were weighed to evaluate the difference in mass between the conventional wing and the telescopic wing. Table 2.7 summarizes the mass of the main components.

Table 2.7: Mass of the components and major assemblies of the telescopic wing.

Assembly	Quantity	Component	Mass, kg
OMW	20	Balsa ribs	0.02
	2	Carbon tubular spar	0.108
	2	Guide tube	0.029
	2	Skin	0.142
	2	Rack	0.171
	Subtotal		0.471
IFW	2	Plywood Ribs	0.025
	2	Unidirectional carbon/epoxy	0.115
	2	Shells + foam	0.57
	3	Wing/fuselage fairings	0.07
	Subtotal		0.852
Actuation bay	1	Board	0.084
	2	Modified servomotor	0.4
	1	Fuselage linkages	0.005
	4	Board support	0.008
	1	Upper support	0.009
	2	Pinion	0.09
	Subtotal		0.596
Total mass of VSW			1.846
Fixed wing mass			1.295

The wing’s total mass, including the actuation mechanisms, is around 1.85 kg, as opposed

to 1.3 kg of the originally wings developed for the Olharapo RPAS (with the original flight control system of servos and cables and the wing supporting part that attaches to the fuselage). This is an increase of about 0.55 kg: 42% of wing mass or 9% of total vehicle mass. This value represents 0.18 kg more than the 0.37 kg first estimated with a preliminary wing prototype and assumed in the aerodynamic optimization of the wing (section 2.4). The increased mass is mainly due to the selected servos which had to be more powerful and hence larger than initially anticipated and to the heavier rack and pinion transmission. This negative mass margin should be, in the future, reduced through actuating system optimization and by improving construction techniques.

2.7 Ground Testing

The developed variable-span wing was subjected to bench testing, in order to evaluate the performance of the overall system. Two distinct types of tests were conducted: structural and actuator system testing.

2.7.1 Static Tests

The structural static tests were performed with the objective of evaluating the strength and stiffness of the VSW. These tests also helped the validation of the structural finite element model. More specifically, the wing tip deflection was measured when subjected to different loads representing a range of flight load factors. The flight loads were simulated by placing sand bags on the upper surface of the wing. For simplicity, the wing load distribution was considered constant in the IFW and triangular in the OMW portion. Load factors between approximately 0G and 4.5G were applied. Furthermore, all the sand bags were distributed along the main wing spar in order to avoid unnecessary torsion of the telescopic wing assembly. The tip deflection was determined by reading off a scale placed behind the wing tip. Figure 2.26 shows the assembly used to carry out the tests and the loads used to represent the different load factors.

The variation in tip deflection with increasing load factor is in-line with the numerical predictions. As expected, the increase in load factor led to a considerable increase in the wing tip vertical deflection. Furthermore, a slight slope discontinuity was observed at the position where the movable wing enters the fixed wing, particularly at higher load factors. However, the OMW proved to be quite stiff. The overlap of 100 mm between both wing parts resisted the bending loads by deforming the aerofoil contour shape, effectively increasing the aerofoil thickness, situation also modelled in the FEM. This localized bending produced a small gap between the IFW upper skin and the OMW upper skin which became more apparent at higher load factors, reaching a value close to 2 mm under a 4.5G load (Fig.2.27).

The variation in tip deflection with increasing load factor is shown in Table 2.8. It should be noted that for load factors of 3.5G and 4.5G, the tip deflection was about 39 mm and 55 mm, respectively, showing an overall good stiffness in bending. The deflections reached these values, in part, due to the lack of skin stiffness at the interface of the OMW with the IFW.

To ascertain numerical model and developed prototype similarity, experimental deflection results of the wing prototype are used. In the experiment, the VSW with the span fully

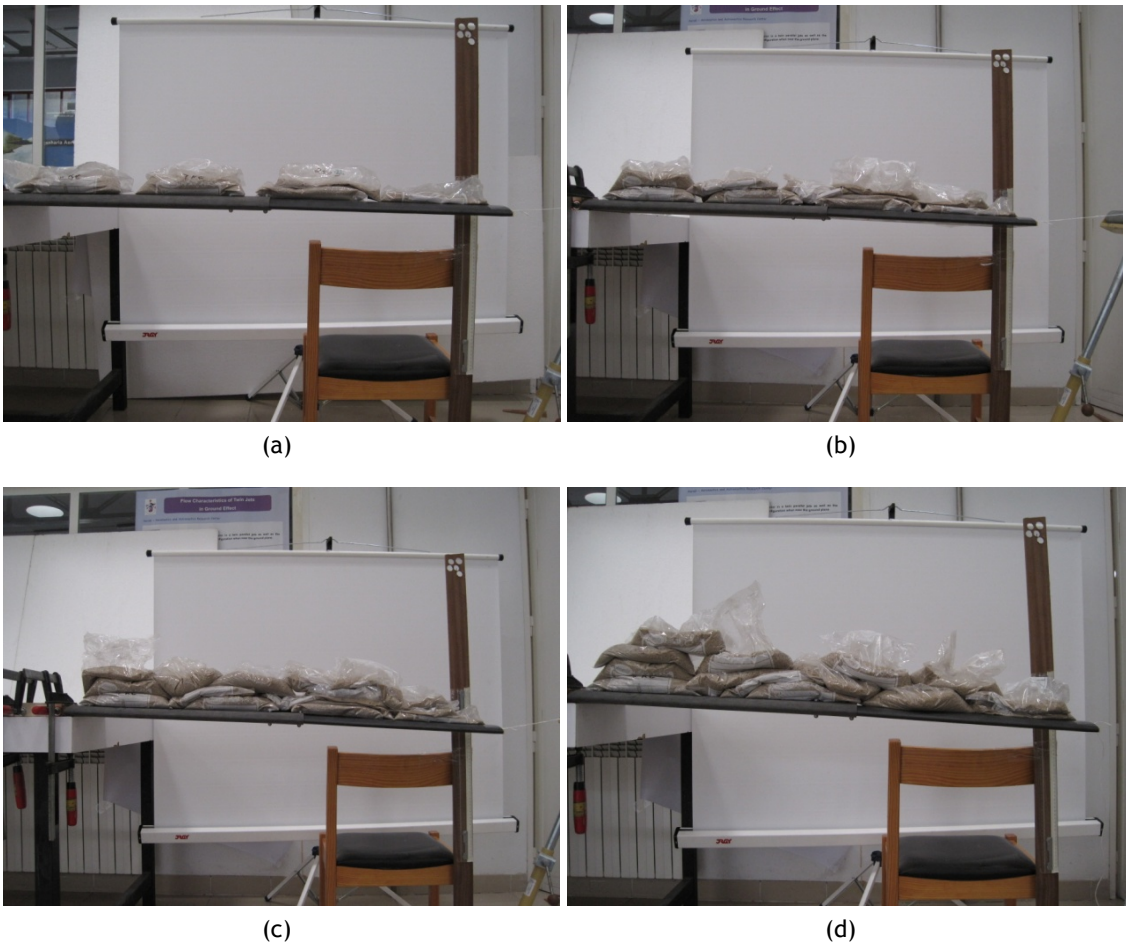

(a) (b)

(c) (d)

Figure 2.26: Variable-span wing loaded at: (a) 1G – 3 kgf, (b) 2G – 6 kgf, (c) 3.5G – 10.5 kgf, and (d) 4.5G – 13.5 kgf.

Figure 2.27: Gap between the IFW upper skin and the OMW upper skin when the wing is fully loaded.

Table 2.8: Variable-span wing tip vertical deflection as a function of load factor.

load factor	0	1	2	3.5	4.5
tip deflection, mm	0	6	18	39	55

extended was clamped at its root and was statically tested with two loading cases: (a) bending with a concentrated load of 5 N applied at 35% of the OMW tip chord and (b) torsion with a couple of 1.1 N·m at the IFW tip chord. For the former loading case, both experimental and numerical deflections were evaluated at constant 35% chord position along the wingspan. In the other loading case, the deflections were evaluated along the IFW tip chord. The results from the numerical study and the experimental tests are shown in Fig.2.28.

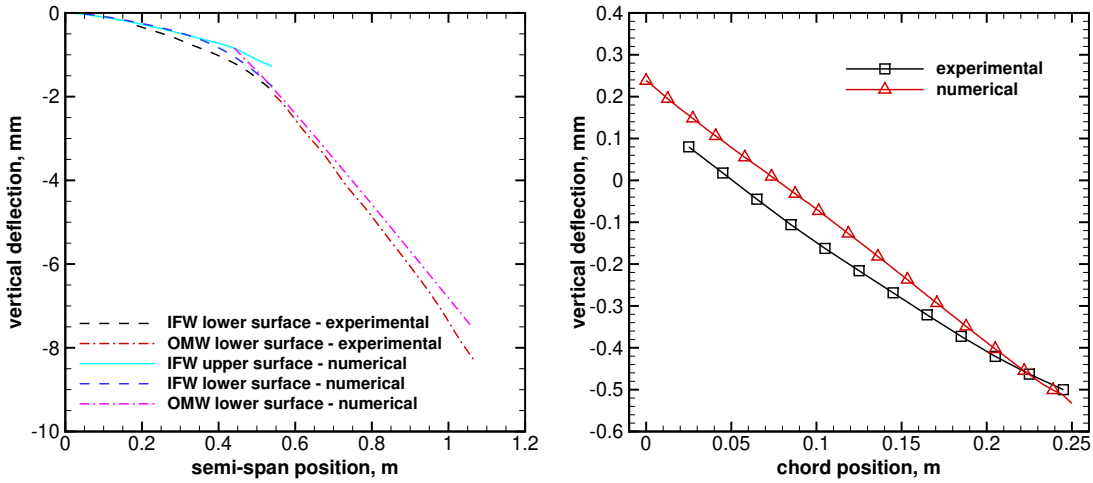

Figure 2.28: Static deflections of the variable-span wing: (a) bending along span due to tip load and (b) torsion due to tip couple on IFW tip chord.

Observing Fig.2.28(a), which presents the vertical deflection along the span due to tip load, it is clear that a general good agreement exists between experimental and numerical data. It is important to note the change of slope of the deflected shape at the OMW/IFW interface. In fact, the IFW aerofoil contour in the proximity of the interface expands in the thickness direction and a small gap appears on the top side of the IFW, resulting in the slope discontinuity observed in this region. The interface in the numerical model appears to be slightly stiffer, since the maximum deflection is underestimated. It is also noticeable the high stiffness of the OMW, evidenced by the linear deflection of this component. Regarding the torsion due to the tip couple (Fig.2.28(b)), it is possible to conclude that the torsion angle is similar in both the numerical and the experimental situations. This indicates that the torsional stiffness of the FEM is correct. From both tests, it becomes evident that the developed FEM represents with good approximation the elastic characteristics of the prototype VSW.

2.7.2 Actuation System Tests

The actuation system was subjected to a series of tests aimed at measuring its performance. In particular, two types of tests were performed: extension/retraction actuation speed and servo-actuator energy efficiency.

2.7.2.1 Testing Methodology

Extension/Retraction Time

This test aimed at measuring the telescopic wing extension and retraction times for various load factors. The approach used during the structural bending tests, where weights were placed over the OMW, was not appropriate in this case, because this part of the wing was required to slide inside the IFW during the actuation sequence. For this reason, instead of loading the OMW with the triangular load distribution an equivalent concentrated force was placed at the wing tip. The equivalent concentrated force was calculated in such a way that it caused the same bending moment in the interface of the OMW/IFW, when compared with the triangular load distribution. Figure 2.29 illustrates the relationship between the load factor and the equivalent concentrated load at the wing tip.

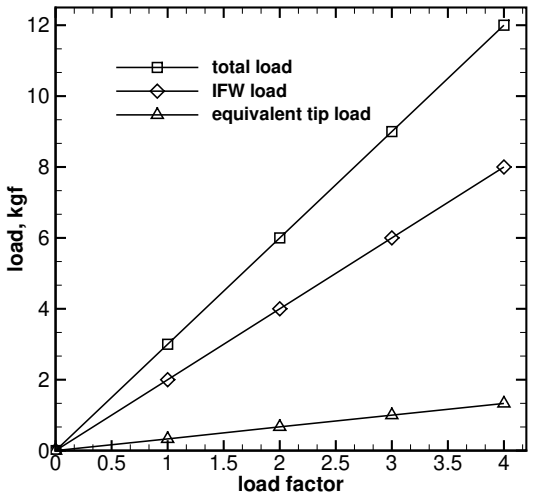

Figure 2.29: IFW load, equivalent wing tip load and total load as function of the load factor.

Full cycle times (extension followed by retraction) were measured using a digital stopwatch. This procedure leads to small errors due to operator reaction time. In future work it is suggested that the whole process is automated to avoid these errors.

Actuation System Efficiency

To determine the servomotor actuation system efficiency, η_{vsw} two separate tests were performed. These tests were: (a) evaluating the average power used by the servomotor, $P_{elec,avg}$, and (b) evaluating the average force necessary to move the OMW, $F_{vsw,avg}$. Both tests were carried out for various load factors, ranging from 0G to 4G.

In order to carry out the first test (a), an e-logger V3 from Eagle Tree Systems® was used to determine the power consumed by the servomotor. This device measured the values of current and voltage, over a prescribed period of time, with a frequency of 10 Hz. In order to ensure a point of comparison between the various load factors, a proportional radio controller (RC) system, Multiplex® Royal EVO9, was used to control the VSW servomotor. The test run function was used, in which the servo is automatically controlled, by selecting a period time. Thus, using this procedure manual command inputs are avoided, which could compromise the test

process. After conceiving the test assembly, shown in Fig.2.30, actuation system current and voltage were obtained for various load factors and then averaged. Using the averaged current and voltage, the average power used by the servomotor, $P_{elec,avg}$ was determined.

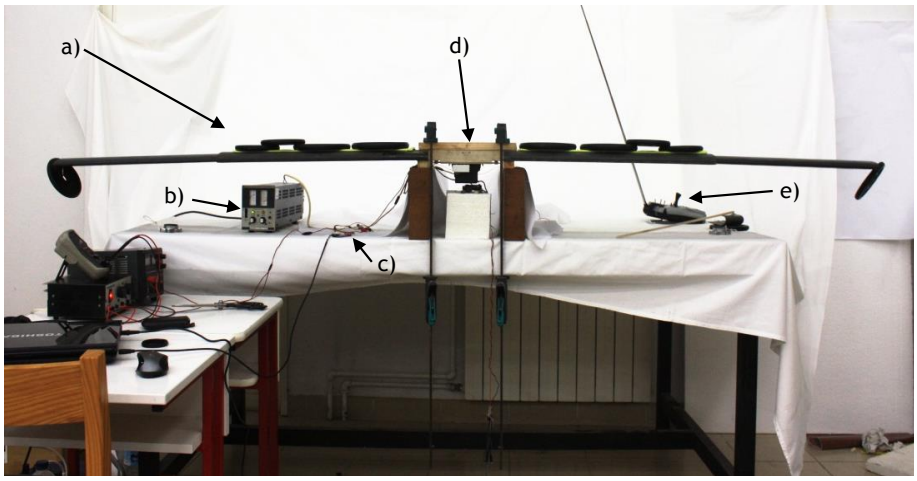

Figure 2.30: Test assembly for the power consumption determination, highlighting the different equipments employed during the test: (a) VSW, (b) power source, (c) e-logger V3, (d) servomotor assembly and (e) RC transmitter.

The total energy used by the servomotor, $E_{vsw,elec}$, is readily computed from the average of the servomotor electric power and the servomotor operating time (needed to complete a full-cycle), t_{cycle} (known from the "extension/retraction time" test). Thus

$$E_{vsw,elec} = P_{elec,avg}\, t_{cycle} \tag{2.15}$$

In the second test (b), the average actuation force and total deployment distance were measured, in order to obtain the useful work. The force was measured during the actuation cycle using a load cell. The load cell was an in-line force measuring S-beam shaped, capable of measuring both compression and traction loads. In more detail, one VSW servomotor was removed from the actuation bay and used to pull the load cell, that was connected on the OMW wing tip. Thus, the actuation point is now in the OMW tip and not the root. This was done in order to have enough space to mount the load cell. The same rack and pinion were used to actuate the wing. The connection between the load cell and the OMW tip was done using an aluminium rod that was permitted to rotate, in order to compensate for the different wing-tip deflections with varying load factor. To ensure a stable, low friction motion, the load cell and rack assembly were mounted along a linear guide, correctly aligned with the VSW. The cell signal was registered using a Picoscope2000 from Pico Technology® and later converted into force using the load cell calibration curve, in a software developed in FORTRAN programming language. After computing the force variation, the average force to actuate the wing, $F_{vsw,avg}$ was calculated. Various cycles were performed in order to increase the accuracy of the results. The assembly used in this test is shown in Fig.2.31.

In order to compute actuator system mechanism efficiency, η_{vsw}, the work of the force used to move the variable-span wing is divided by the energy used by the servomotor. Thus

$$\eta_{vsw} = \frac{E_{vsw,force}}{E_{vsw,elec}} \tag{2.16}$$

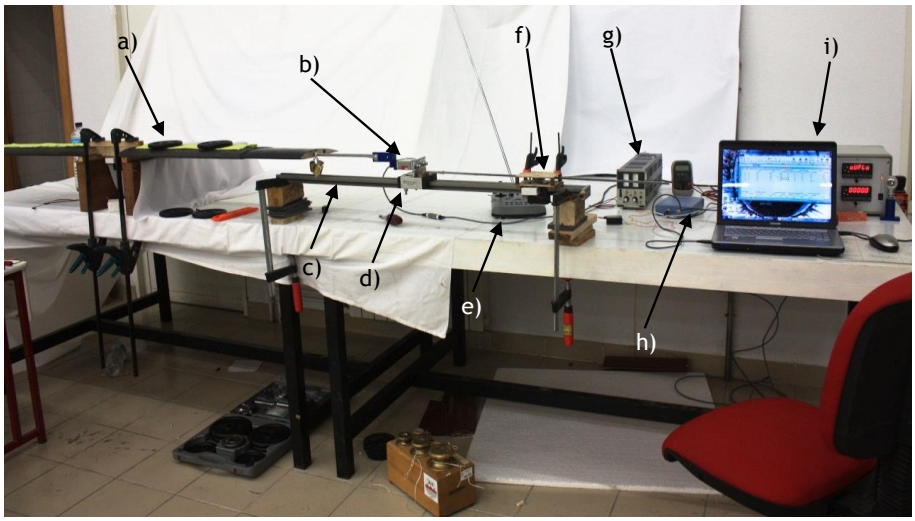

Figure 2.31: Test assembly for the mean force determination, highlighting the different equipments used during the test: (a) VSW, (b) S-beam load cell, (c) linear guide, (d) linear bearing, (e) RC transmitter, (f) servomotor assembly, (g) power source, (h) Picoscope2000 and (i) laptop with Pico Technology® software.

where $E_{vsw,force}$ is the work of the force used to move the VSW. It is computed by multiplying the average actuation force, $F_{vsw,avg}$ by the OMW displacement (for an extension/retraction cycle), s_{OMW}. Thus

$$E_{vsw,force} = F_{vsw,avg}\, s_{OMW} \tag{2.17}$$

2.7.2.2 Results

Extension/Retraction Time

Table 2.9 shows the half-cycle (extension or retraction) actuation times of the VSW with increasing load factor. Referring to Table 2.9, it becomes clear that the time of retraction/extension increased as load factor was raised. This was already expected, since increasing the load factor increases the friction force between wing parts and hence the servomotor had more difficulty in overcoming the increased force.

Table 2.9: Half-cycle actuation times of the VSW using the HiTec® HS-805MG servos.

load factor	0	1	2	3	4
time, s	1.8	2.0	2.3	2.5	3.0

Actuator System Efficiency

The data from the actuator servomotor power and the actuation force tests was compiled and the system efficiency was computed for a full actuation cycle (extension followed by retraction). These calculations were applied for all the tested load factors. A summary of the test results and respective calculations can be found in Table 2.10.

Table 2.10: Servo-actuator efficiency for a variable-span full-cycle actuation.

load factor	$P_{elec,avg}$, W	$E_{vsw,elec}$, J	$F_{vsw,avg}$, N	$E_{vsw,force}$, J	η_{vsw}
0	2.34	8.42	4.81	4.33	0.51
1	3.76	15.04	6.62	5.96	0.40
2	5.79	26.63	9.73	8.76	0.33
3	7.60	38.00	13.27	11.94	0.31
4	9.49	56.94	17.25	15.53	0.27

From Table 2.10, one can see the expected increase in power consumption due to the higher wing loading and the consequent friction increase. On the other hand, it is also seen that, as load factor increases, the efficiency decreases. The explanation for that lies in the servomotor, since the high current drain imposed by the high torque output, reduces its efficiency. The major energy loss is due to heat. In fact, during high load factor tests, a cooling system had to be setup in order to avoid servomotor damage. This heat generation is due to the brushed DC motor used in the servomotor actuator. One other factor that could also contribute to this efficiency reduction, are small construction imperfections that were more apparent when the VSW worked under higher load factors. Another aspect that could have influenced negatively the force measurements, and consequently the efficiency results, are the linear bearings and load cell (and respective linkage), since they introduced more inertia to the system, effectively increasing the actuation time. This was more noticeable during the deceleration followed by acceleration that occurs when the extension is completed and the retraction is initiated and vice-versa.

During these experimental measurements, some peculiarities occurred that should be highlighted. Due to the large size of the servos, they absorb large amounts of current causing significant input voltage drops. This voltage reduction had a negative influence in the available torque. This behaviour was improved substantially by replacing the original power cables with ones of higher cross-section area.

One should note that the obtained efficiencies are inline with typical values from the literature for DC-based servomotors. However, there are servomotor architectures that are capable of delivering better efficiency. The key to the high-efficiency of these devices lies in the use of coreless electric motors.

2.8 Concluding Remarks

A fully functional VSW system was developed covering areas from aerodynamic optimization and structural design, to composite prototyping manufacturing and actuator and structural testing.

The aerodynamic design optimization allowed the sizing of a VSW which reduces the drag $\times$ speed integral in the design speed range of the vehicle. At low speeds, it was found that the original wing has slightly better performance than the VSW, due to the performance reduction of the modified SG6042 aerofoil, the higher relative thickness ratio of the IFW aerofoil and the increased vehicle weight. However, this performance trend inverted beyond 25 m/s, in the speed range where retraction of the OMW occurs, which reduced the wing area and, consequently,

the total wing drag. For example, at 35 m/s the drag of the VSW was reduced by 22% from the original fixed wing.

A structural FEM of the VSW was developed with ANSYS® Mechanical APDL, in order to study the effect of the interface between the inboard fixed part and the outboard moving part of the wing, due to its unconventional characteristics. Static aerodynamic loading conditions were analysed for various flight load factors. Deflections and stresses resulting from the load distributions applied showed that the structure of the wing is suitable for the flight loads which will be experienced during normal operation. Even though structural tests revealed some discrepancies between the experimental and the FEM deflections, the trends and magnitudes were similar. The differences were mainly due to the modelling of the interface between IFW and OMW, the uncertainty in material properties and also due to manufacturing imperfections of the prototype wing. Nevertheless the design was generally confirmed in the loading tests.

An aeroelastic study of the VSW was also performed. The study focused on the flutter critical speed estimation because of the effects arising due to the interface between fixed and moving wing parts (flexible or bonded). The same FEM was used to compute the VSW mode shapes and frequencies of free vibration, considering a rigid or the real flexible interface. It was concluded that the effect of rigidity loss in the interface between the IFW and the OMW, had a negative impact on the critical flutter speed. Nevertheless, the flutter analysis undertaken allowed to conclude that the flight speed envelope required for the RPAS under consideration is still viable for the proposed structural design of the VSW concept.

A full-scale prototype was implemented using a combination of hard and soft wood, CFRP, GFRP and PVC foam, in order to allow the pursuit of several ground and future flight validation and evaluation tests. The manufacturing techniques used to build the wing were presented in detail, as well as, the actuation mechanism sizing and its integration in the wing.

The full-scale prototype was subjected to a thorough ground evaluation. The ground evaluation focused on the structural elements and the actuation system. The static bending testing demonstrated that the wing can withstand loads up to 4.5G at its maximum wingspan configuration. However, some lack of rigidity was identified in the interface of IFW/OMW. This could be mitigated (a) by increasing the skin stiffness at the IFW tip with an internal stiff rib (between sandwich facings) or with an external lighter rib similar to an end plate around the perimeter of the aerofoil; and (b) by decreasing the friction force between the wings with enhanced surface finishing. Should the external plate rib, at the tip of the IFW, be used it could also reduce the potential negative effect of aerodynamic chord discontinuity while stiffening the assembly. The experimental testing also served to validate the FEM. This study showed that FEM simulations were inline with the experimental deflections of the VSW subjected to the selected loading conditions. The actuation system testing revealed satisfactory performance of the VSW. The low measured deployment time provided a good indication that the RPAS could be roll controlled with this actuation system by asymmetrically deploying the wings. The system efficiency was also evaluated. The results of this test showed that the maximum efficiency was around 51% for the 0G load case and decreases to about 27% at the 4G condition. Several factors may have contributed to the low system efficiency result, specially noticed at high loading conditions. The most significant were the thermal losses in the DC motor. These could be enhanced by using a coreless based servomotor architecture. This type of servomotors should be considered in the future. To a lesser degree, the imperfections in construction, systems' gears and rack and pinion set, were responsible for reducing the systems' efficiency.

Chapter 3

Variable-span Wing Flight Performance

3.1 Chapter Overview

In the previous chapter, the VSW was developed and ground tested, and it was concluded that it was suitable to be installed on Olharapo 2 RPAS for in-flight concept evaluation.

In the first part of the chapter, the modifications made to RPAS Olharapo to fit the VSW and to allow a safe flight testing are presented. Additionally, the RPAS was equipped with the necessary instrumentation to characterize such new wing concept, mainly with flight data acquisition, real-time telemetry, first-person view capabilities and long range piloting control. A thorough description of the added instrumentation is done, highlighting its purposes and functionalities.

In the second part of the chapter, the main focus is on the experimental flight testing of the RPAS, fitted with a conventional fixed wing and the newly developed VSW. Essentially, two sets of flight tests were performed: aerodynamic and energy characterization. The former aimed at determining the lift-to-drag ratio for different airspeeds. The latter was performed to measure the propulsive and manoeuvring energy when performing a typical mission. The mission was chosen in such a way that the multi-role capability of the VSW could stand out. The methodology and experimental procedure used to perform both tests is described. Then, flight testing results are presented for both sets of flight tests. The results are compared for both sets of flight tests and conclusions about the benefits of the use of the morphing wing concept are addressed.

3.2 RPAS Integration and Instrumentation

In the first part of this section, the necessary modifications to integrate the VSW in Olharapo 2 RPAS, are described. These modifications were made in order to allow flight testing to be carried out, without compromising the safety of the vehicle. The alterations range from the development of the wing/fuselage connection to modification of the empennage configuration.

In the second part of the section, the instrumentation necessary to characterize the new wing concept is described. The instrumentation ranges from an autopilot system with real-time telemetry to first-person view capabilities and long range piloting control.

3.2.1 RPAS Modifications

The RPAS presented in the beginning of the past chapter (section 2.2), serves as a test bed to the newly developed VSW. As presented before, Olharapo 2 uses an upward V-tail em-

pennage configuration. This configuration was found to be inadequate because it did not meet the requirements for the first flight tests with the telescopic wing, being subsequently changed to an H-tail. Therefore, Olharapo 2 has two tail configurations, being the RPAS denominated Olharapo 2V or Olharapo 2H, when a V-tail or H-tail is used, respectively.

Wing-fuselage Connection

In order to allow the fitting of the VSW to Olharapo 2 fuselage, a connection was developed. Four points of attachment (two on each side) were used: one main pair to transfer the bending and the other pair to transfer the torsion moment. The main attachment points use an aluminium tube and a wooden connection that is located in the lower part of the actuator bay, directly below the the VSW spars. The bonding was done using epoxy and reinforced using carbon-fibre. The other attachment point is located about 70% of the IFW chord. An inverted L-shaped CFRP part was bonded to the inside of the fuselage with a blind-nut on the horizontal part. A pair of holes were then drilled on the actuator bay platform to allow bolts to be inserted, which in turn, bolt into the two blind-nuts. Figure 3.1 illustrates the mechanism adopted to fix VSW to the fuselage.

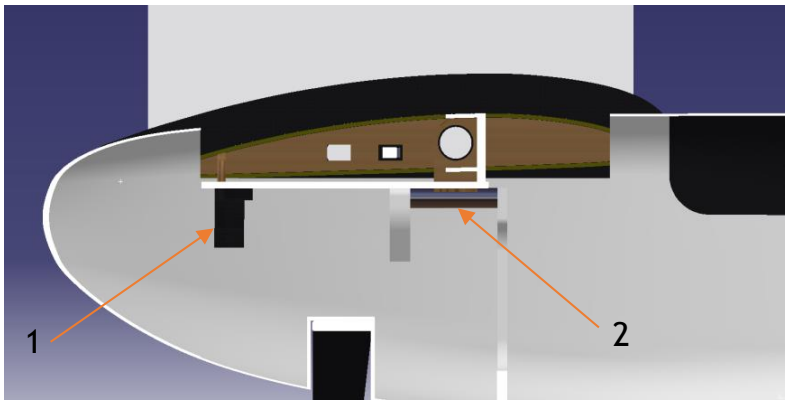

Figure 3.1: CAD longitudinal cut view of the telescopic wing and the RPAS showing: (1) L-point of attachment and (2) aluminium tube.

Wing Fairings

Two sets of fairings were built to streamline the wing fuselage connection. In the wing upper surface, a removable fairing covering the entire wing central portion was used. Regarding the wing lower surface, the better solution was to bond two fairings near the root of the IFWs. These fairing go from the leading to the trailing edge, between the wing flange and the fuselage side. Both fairings were built using CFRP. Figure 3.2(a) shows the fairings of the upper surface and Fig.3.2(b) the fairings of the lower surface.

Tail Modification

The original V-tail of Olharapo 2V proved to be inadequate because it did not meet the requirements for the first flight tests with the telescopic wing, which required the use of the empennage as a way to control aircraft roll. This requirement was not fulfilled because upwards

(a) (b)

Figure 3.2: Variable-span wing fairings: (a) upper surface cover and (b) lower surface.

V-tails suffer from a phenomenon known as adverse roll-yaw coupling, i.e., the created rolling moment opposes the desired yaw direction. Therefore, it is very difficult, if not impossible to control the RPAS banking angle using only the tail control surfaces. For this reason, it was necessary to find a solution that offered the best compromise between functionality, necessary modifications and construction difficulty. The best compromise was found to be the construction of an H-tail. It is characterized by having an horizontal empennage and two vertical surfaces, which are positioned in the tips of the horizontal empennage. This configuration did not require any modifications to the tail boom. The H-tail allows the RPAS to perform safe roll manoeuvres with rudder and elevon deflections (asymmetrical deflection of the elevators) without the need for aileron actuation. This can be seen as a precaution measure that guarantees roll manoeuvres in the case of VSW asymmetrical wing inadequate control authority or deployment failure. In addition, the vertical empennage of the H-tail are more effective than in the previous configuration because they are attached at the end of the horizontal empennage and they have a larger wetted area. The major drawback of this setup was the added weight.

The horizontal empennage uses a NACA0009 profile and has a span of 0.77 m, being the root chord 0.245 m and the tip chord 0.165 m. The vertical portions of the empennage are constituted by two rectangular flat plates. It has a chord of 0.175 m, a thickness of 10 mm and a height of 0.255 m. The H-tail was built with a combination of natural materials and composite materials. The skins and ribs were made with balsa wood and plywood. The main spar is C-shaped and was made using CFRP. The spar caps were reinforced with pultruded unidirectional carbon fibre and the spar web was reinforced with basswood near the root and the remaining portion filled with balsa wood.

The built H-tail (except covering film and servomotor assembly) can be seen in Fig.3.3(a) and the H-tail installed in RPAS tail boom in Fig.3.3(b).

Wing Tips

During the first flight tests of Olharapo 2H using the fixed wing and H-tail, it was found that the aircraft was stable laterally, but this was still not sufficient to properly control the bank angle without using ailerons. Therefore, it was decided to increase the lateral area above the CG in order to further increase the lateral stability. To achieve this, two wing endplates

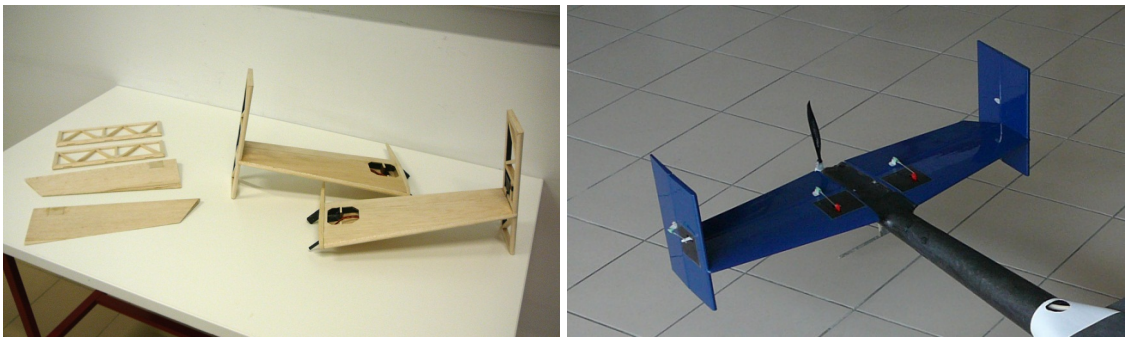

(a) (b)

Figure 3.3: Olharapo 2 RPAS H-tail: (a) assembly before being covered with iron-on plastic film and (b) installed in the tail boom.

were built and glued to both wing tips. These endplates were added to both wings (conventional/telescopic) in order to keep the two wings comparable. With this small modification the RPAS bank angle was now fully controllable without using the ailerons. However, this modification made the RPAS more sensitive to the wind, which in turn made the piloting more challenging, specially during the landing phase.

Figure 3.4(a) illustrates Olharapo 2H fitted with a conventional fixed wing while Fig.3.4(b) shows the RPAS prototype fitted with the VSW. Both wings are equipped with the developed endplates.

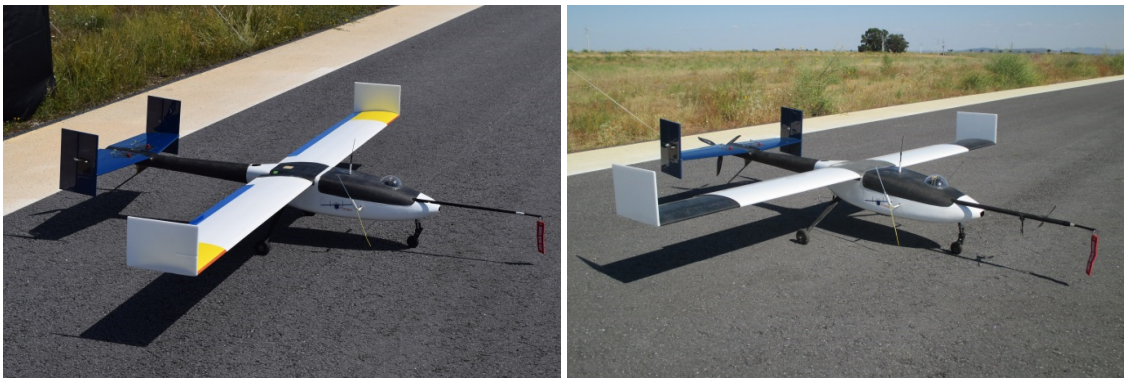

(a) (b)

Figure 3.4: Olharapo 2H RPAS parked in Castelo Branco municipality airfield: (a) conventional fixed wing and (b) variable-span wing.

3.2.2 Instrumentation

In order to perform flight tests with Olharapo 2H RPAS and collect complete and meaningful data, a myriad of equipment was necessary, both in the air and on the ground. The basic necessary components are: a First-Person View (FPV) system, a long range control system, an autopilot system and a bidirectional telemetry radio link. Additionally, the power monitoring subsystem plays an important role, since it allows the pilot to fly within the available flight energy. These systems are described below.

3.2.2.1 Autopilot System

The core of the RPAS instrumentation is the *Pixhawk* autopilot (see Fig.3.5(a)). *Pixhawk* is a fully-featured autopilot system developed by the PX4 open-hardware project. It features a 32bit ARM Cortex M4 and sensor technology from STMicroelectronics® and a NuttX real-time operating system. It has also dual gyroscope and dual accelerometer (STMicroelectronics® L3GD20 3-axis 16-bit gyroscope, STMicroelectronics® LSM303D 3-axis 14-bit accelerometer/magnetometer and Invensense® MPU 6000 3-axis accelerometer/gyroscope). To perform navigation, the *Pixhawk* also uses an Ublox® LEA-6H GPS. The autopilot allows full logging of the various flight parameters and sensor data at 50 Hz (or faster) to a micro SD-card. This greatly facilitates inflight data logging and further data processing.

In order to measure the Angle of Attack (AOA), α, and the Angle of Sideslip (AOS), β, of the RPAS, an alpha-beta probe was built. The probe is made up of two very low friction magnetic encoders whose output gives a voltage that is proportional to the angle of rotation. Each encoder shaft is connected to one vane in order to allow the encoders to adjust to the surrounding flowfield. The probe is also featured with a pitot-static tube to measure airspeed connected to a Measurement Specialties® 4525DO differential pressure sensor with 6.9 MPa measurement range (maximum airspeed of about 100 m/s). Figure 3.5(b) shows the assembled alpha-beta probe.

(a) (b)

Figure 3.5: (a) *Pixhawk* autopilot general view and (b) alpha-beta probe with pitot-static tube.

Software

The *Pixhawk* autopilot can run two different flight software: the PX4 native flight control stack and the APM.Plane flight control stack. The latter was chosen given the higher maturity level of the code and also because of the previous team experience in its operation. Since the hardware has available rate gyroscopes, accelerometers, magnetometers, GPS, airspeed and barometric pressure measurements, it is essential to fuse all data to build an Attitude and Heading Reference System (AHRS). This is used to provide attitude information of the RPAS, including heading, pitch, yaw and roll angles. In order to fuse all data reliably an Extended Kalman Filter (EKF) algorithm is used in APM.Plane. The employed algorithm in the software estimates a total of 22 states. More information can be found in [138].

3.2.2.2 First-person View System

The First-Person View (FPV) system is crucial to the RPAS safe operation since it provides real-time video feed, allowing the pilot to have good situational awareness. This system comprises the airborne components and the Ground Control Station (GCS).

The airborne main components are an analogue video camera with pan and tilt motion, a microphone, an On-screen Display (OSD) that overlays all the relevant data for piloting purposes on the video signal before being broadcasted, and a transmitter that feeds the video signal to the GCS. The airborne components can be powered up using the main flight battery or using an auxiliary systems battery. Additional care should be taken when powering from the main flight battery, in order to avoid noise on the video signal coming from the brushless motor. To avoid this, a LC filter, consisting of a capacitor and inductor ferrite ring, is used in series with the flight battery. If an auxiliary battery is used to power the FPV system, the LC filter is no longer needed. The pan and tilt support is made of laser cut birch plywood and is actuated by two micro servos that are responsible for the pan and tilt motion. It is installed in the frontal area of Olharapo access hatch, protected by an optical grade clear plastic dome. Figure 3.6 shows the FPV camera and the pan/tilt plywood support.

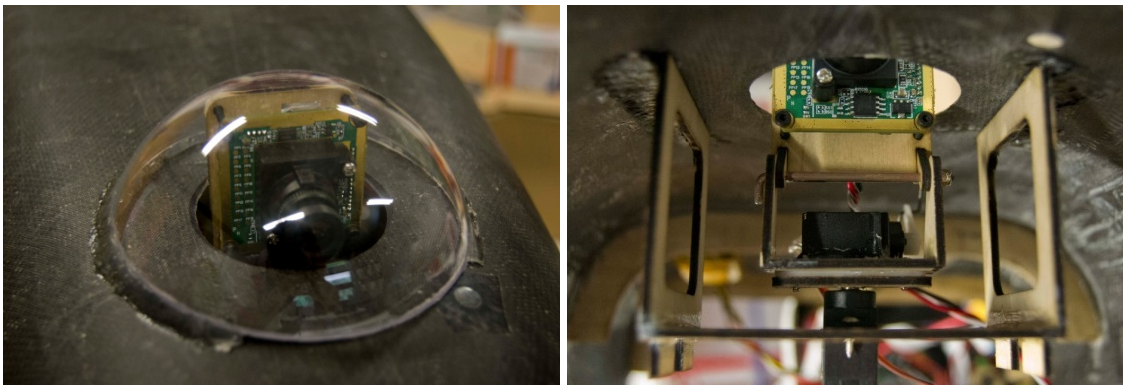

(a) (b)

Figure 3.6: Olharapo FPV components installed in the fuselage access hatch: (a) camera and (b) pan/tilt structure.

The video transmitter has 600 mW (28 dBi) of radiated power and is equipped with a skew planar wheel antenna. It is a low directivity circular polarized antenna with a near isotropic radiation pattern. Circular polarized antennas are desirable in FPV since they have two distinct advantages: multipath interference is rejected, and polarization is not lost when the aircraft is banked during a turn. Figure 3.7 shows the GCS video with all the piloting related information overlaid.

The components of the GCS are two 1.3 GHz analogue video receivers and respective diversity controller, a 12.1" LCD screen, a digital video recorder that records the flight real-time video feed to a memory card, two battery voltage checkers, a power module that distributes the power to all the ground station equipment and contains a video buffer that ensures a clean video signal to all connected devices and finally two Lithium-ion Polymer (LiPo) batteries that power all the ground station's equipment.

There are two identical video receivers, one being connected to a skew planar wheel and another to a heliaxial high directivity (11 dBi) antenna. The latter allows very long range

Figure 3.7: Video feed with overlaid information: 1) remaining flight battery, 2) flight battery voltage, 3) electric motor current, 4) airspeed, 5) groundspeed, 6) vertical speed, 7) number of GPS satellites, 8) predicted gliding distance, 9) GPS latitude and 10) longitude, 11) roll angle, 12) home direction, 13) compass, 14) total flight distance, 15) MSL altitude, 16) flight time, 17) radio control RSSI, 18) home height, 19) distance to takeoff point, 20) pitch angle, 21) wind speed and direction, 22) trajectory angle.

flights whilst the former allows closer range flights. This is due to the different directivity of the antennas. The signal received from each receiver is fed into a diversity controller whose function is to select the best video signal. This guarantees that the pilot is always using the best available video feed. The video display screen has the particularity of always showing a video signal despite the signal intensity or quality. This is of utmost importance because in the eventuality of video signal degradation, the screen continues to show the noisy video feed, providing sufficient eye clues for the pilot to carry on the flight safely. The two LiPo battery power sources are able to provide power for more than 12 hours of continuous operation. The GCS is shown in Fig.3.8 with the two different video receiver antennas.

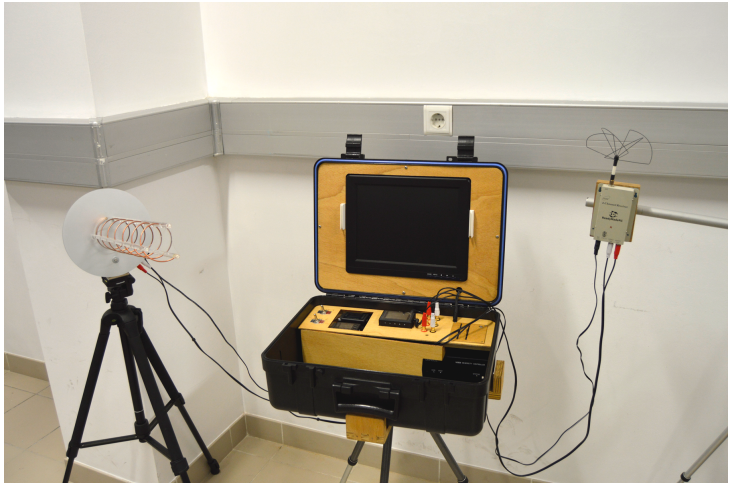

Figure 3.8: Complete ground control station showing the LCD monitor, the two video receivers with the heliaxial high directivity antenna (left) and the skew planar wheel antenna (right).

3.2.2.3 Long Range Control System

To increase the flying range of the RPAS, a reliable and long range radio control link was required. This allowed flight testing to be more flexible, since non-Line of Sight (non-LoS) flights can be executed safely[1]. This system is constituted by three key elements: radio control (RC) system, long range transmitter and long range receiver.

The long-range TX/RX used is the *Thomas Scherrer* Long Range System (TSLRS). This LRS has been used since 2008 in the most diverse applications both civil and military with very good results. It operates on the UHF band (433 MHz to 440 MHz) and has three selectable power outputs: 0.5 W, 1 W and 2 W. It also supports Frequency Hopping Spread Spectrum (FHSS), to avoid interference from other emitters in the same band.

On the air side, the LRS receiver main features are: diversity (two independent receiving antennas), 12 output channels via standard pin connectors or Pulse Position Modulation (PPM) output and Receiver Signal Strength Indication (RSSI) output, used to monitor the signal strength. The PPM output dramatically reduced the wiring between the receiver and the autopilot to just only two cables: the RSSI and the PPM out. The diversity feature of the receiver allowed the receiving antennas to be placed in different RPAS location. Thus, increasing receiving quality and enhancing link reliability.

The RC used is a Multiplex® Royal SX 16. The radio has 16 channels outputs and allows highly flexible programming features (e.g free channel assignments, five point servo curves, free mixer outputs). It was connected to the transmission module through the PPM external port of the RC system.

Figure 3.9(a) shows the LRS transmitter module connected to the RC transmitter and Fig.3.9(b) shows the LRS receiver with its dipole antennas.

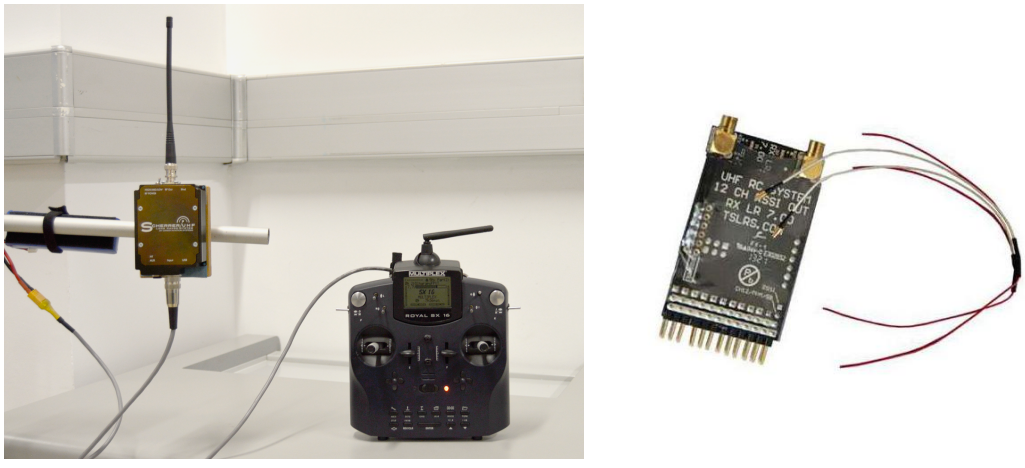

(a) (b)

Figure 3.9: Complete long range radio control system showing: (a) the RC transmitter and LRS transmitter and (b) LRS diversity receiver with dipole antennas.

[1]Non-LoS is from the pilot point of view and not from an electromagnetic point of view. Radio frequency line of sight is defined by "Fresnel Zones" which are ellipse shaped areas between any two radios. The primary Fresnel zone is required to be at least 60% clear of any obstruction to ensure the highest performance of the wireless link.

3.2.2.4 Telemetry Ground Station

The telemetry ground station is constituted by a laptop with a GCS software and a 2.4 GHz Range Amplified MultiPoint (RAMP) module (model RM024) from Laird Technologies® with an L-com® 2.4 GHz 8 dBi Linear Patch Antenna. Both can be seen in Fig.3.10. In the RPAS side, a similar transceiver is installed but with a standard 2 dBi dipole to ensure near isotropic signal radiation. The maximum radiated power of the transceivers is 125 mW (21 dBm). Both modules support the FHSS technology, in order to ensure a reliable link in all situations. RAMP modules provide the ideal solution for machine-to-machine applications, whose need is to transmit serial data over long distances, wirelessly, with the highest degree of reliability.

The laptop used is a Toshiba® Portégé R600 12.1" ultraportable. The main particularity is that it uses a transflective LCD display that allows the backlight to be completely turned-off and use direct light, such as the sun, to light up the screen. It also has a long lasting battery (more than 6 hours). Both features are very important during field operation, because direct sun exposure is very likely to be present and the access to a power outlet is difficult and limited.

Figure 3.10: Telemetry ground control station showing the laptop with a GCS software and RM024 transceiver connected to the L-com® Linear Patch Antenna.

There are a myriad of GCS software packages that enable the user to monitor and control the RPAS in-flight. In the current application, two software solutions are used: Ardupilot Mission Planner and MAVProxy.

MAVProxy is a highly flexible, fully-functioning and open-source GCS for RPASs. It is designed to be minimalist, portable and extendible. The light-weight design means it can run on small netbooks. It is a command-line, console based application that supports loadable modules to extend its base features. These modules provide a basic Graphical User Interface (GUI), moving maps, joysticks, antenna trackers, among others. It also allows the real time plotting of RPAS relayed telemetry data, like attitude information and sensor information. This feature is very useful because it streamlines the testing process using graphic plots, instead of only relying on numeric data (or later plotting of the data). This software runs on Windows and Linux based operative systems. The software can be seen in Fig.3.11(a) with the command line (left), the console module (upper right) and map module (lower right) activated.

The Ardupilot Mission Planner is an open source autopilot software where the autopilot can be tuned and the missions can be programmed. It is only compatible with Windows based operative systems. Mission Planner can be used as a configuration utility or as a dynamic control

supplement for the autonomous vehicle. It enables the user to setup, configure, and tune the vehicle using a graphic interface and also to monitor the vehicle's status while in operation. Other features include the real-time planning of autonomous missions with simple point-and-click on supported maps (Google maps or other). The head-up display (HUD) is particularly useful to assist the pilot during flight. It provides essential information about RPAS attitude, speed and battery status. A screenshot of the software application during execution can be seen in Fig.3.11(b).

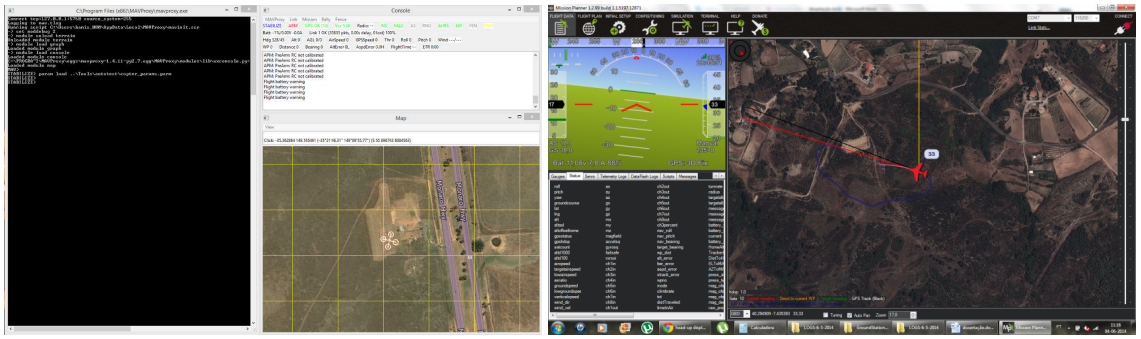

(a) (b)

Figure 3.11: Ground control station software solution: (a) MAVProvy and (b) Ardupilot Mission Planer.

When using the autopilot to perform autonomous flight, it is necessary to define way-points. Both software interfaces with Google® Maps (or other mapping service) to facilitate waypoints positioning and mission planning. The waypoints are then transferred to the *Pixhawk* autopilot controller which ensures that the RPAS will follow the pre-set mission. There are also other flight modes that can be selected, namely, *Stabilize*, *Fly-By-Wire* (FBW) and *Return To Launch* (RTL). The *stabilize* and FBW modes are augmented stability flight modes, being the autopilot responsible for holding the vehicle's attitude and in the case of FBW, attitude, altitude and airspeed. The RTL mode is very useful because it provides a way to automatically return to the takeoff site, increasing safety in case of video signal loss or long range radio control system interference.

3.2.2.5 RPAS Power System and Installation

In order to power all RPAS systems, a well structured and redundant battery configuration is necessary. The RPAS platform uses three distinct battery sources, being two primary and one used has a backup.

The electric motor and autopilot are both powered via a 11.1 V SLS APL LiPo battery with 10 Ah of capacity, which provides a flight time of approximately 40 minutes. This constitutes the flight battery. The battery is connected to a "Power Module", which distributes the power to the Electronic Speed Controller (ESC) and steps-down the voltage to 5.1 V, so that it can be fed to the autopilot. It also has a voltage and current sensor that is used to monitor the flight battery status.

The second battery used, a 11.1 V Hyperion LiPo with 5 Ah of capacity, is responsible for powering up the servomotors and the FPV system. This battery is denominated the control systems battery. The servomotor voltage is regulated to 5.5 V using a high-power switching

regulator (8 A maximum continuous current). The regulator is connected to the power rail of the autopilot, which distributes the power to all servos. When the RPAS is being flown with the VSW, there is an additional high power regulator, responsible for providing energy to the two wing servos.

The third battery is a backup 8 cell NiMh Panasonic® Eneloop battery in a 4s2p configuration (4.8 V nominal voltage and 4 Ah of capacity). It powers the autopilot, long-range system, FPV system and servos in case of control systems battery failure. This battery is protected from the control systems battery using a high current *Schottky* diode. This diode type has a low forward voltage drop and a fast switching action.

Note that in the case of flight battery failure, all systems would be operational with exception of the propulsive system. The RPAS can then perform a gliding flight to a safe landing site, provided sufficient altitude is available.

Figure 3.12 shows the various components used in Olharapo 2H. The *Pixhawk* autopilot was mounted as close as possible to the CG. The remaining components were fitted in such a way to allow proper CG centring and also to limit interferences between sensitive components (long range receiver) and high power sources (electric motor and electronic speed controller).

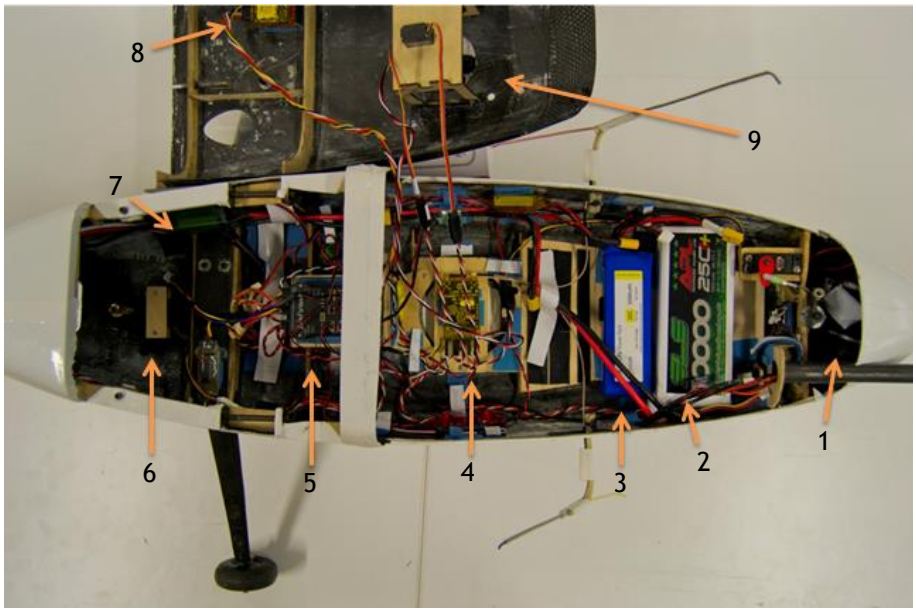

Figure 3.12: General view of RPAS systems: (1) NiMh backup battery, (2) electric motor battery (LiPo 3S 10 Ah), (3) control systems battery (LiPo 3S 5 Ah), (4) long range receiver, (5) *Pixhawk* autopilot, (6) real time video transmitter, (7) motor electronic speed controller, (8) telemetry transceiver, (9) First Person View (FPV) camera.

3.2.2.6 Power Monitoring

Inflight power monitoring and recording is of utmost importance both for flight safety and systems testing. The power relevant parameters were sent in real-time to the GCS and also recorded in-flight to be further processed. Real-time monitoring of the propulsion battery and instruments battery is critical to the pilot. In fact, the pilot in possession of this information

can better assess the mission progress, take adequate actions to safeguard the RPAS and decide when to land.

In particular, the recorded parameters are: electric motor voltage and current, rudder and elevator actuation servos voltage and current and wing actuation servos voltage and current. Since all the data is recorded, electric current and voltage can be numerically integrated using Simpson's rule (or other numerical integration scheme) to compute energy consumption of the various sub-systems (e.g. electric motor, servomotor actuators and video feed).

3.3 Methodology to Determine Aerodynamic Efficiency

The main purpose of the aerodynamic efficiency flight testing was to provide aerodynamic data to compare a conventional fixed wing with the designed VSW. In particular, the obtained aerodynamic data was the lift-to-drag ratio, as a function of airspeed. In this section, the mathematical model and experimental procedure used to compute the lift-to-drag ratio is described.

3.3.1 Flight Mechanics

3.3.1.1 Reference Systems

There are numerous reference systems used in aerospace applications. In this work, it is important to describe four reference systems: the topodetic, the vehicle carried vertical, body and wind. The topodetic or earth fixed reference is considered to be fixed in space with the orientations of the axes: x is directed north, y axis to east and z axis down. The vehicle carried vertical axis system is used to define the attitude of the aeroplane using the Euler angles: pitch angle, θ, bank angle, ϕ and heading, ψ. This reference system is obtained by a translation of the topodetic axis system to the vehicle centre of gravity. The body axis system has its origin coincident with the vehicle's centre of gravity. In a symmetric aeroplane x and z axes are in the plane of symmetry. The positive direction of the body axis angular velocities: roll rate, p, pitch rate, q and yaw rate, r (about x, y and z, respectively) and the body axis velocities: u, v and w (in x, y and z direction, respectively) are shown in Figure 3.13. This reference system and the vehicle carried vertical are related through the Euler angles (pitch, roll and heading). Figure 3.13 also shows the relationship between wind axis and body axis.

From Figure 3.13 the components of the airspeed vector, V, in the body axes, u, v and w, can be extracted. These are

$$\begin{aligned} u &= V\cos(\alpha)\cos(\beta) \\ v &= V\sin(\beta) \\ w &= V\sin(\alpha)\cos(\beta) \end{aligned} \tag{3.1}$$

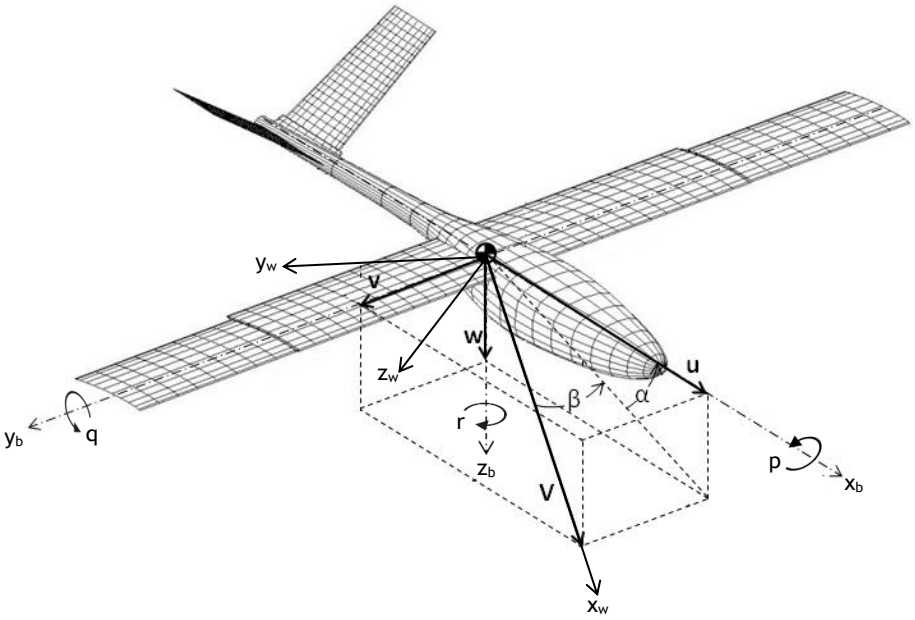

Figure 3.13: Relationship between body axis and wind axis.

3.3.1.2 Euler Equations of Motion

After defining the reference axes system, the equations of motion for an aeroplane that is assumed to be rigid can be derived into Eq.(3.2). The equations are shown here with no further derivation. More details can be found in [139] and [140].

$$\begin{aligned} \dot{u} &= \frac{(X_T + X_a)}{m} - g\sin(\theta) - qw + rv \\ \dot{v} &= \frac{(Y_T + Y_a)}{m} + g\sin(\phi)\cos(\theta) - ru + pw \\ \dot{w} &= \frac{(Z_T + Z_a)}{m} + g\cos(\phi)\cos(\theta) + qu - pv \end{aligned} \tag{3.2}$$

where X_a, Y_a and Z_a are the total aerodynamic force components in each direction given by

$$\begin{aligned} X_a &= -D\cos(\alpha)\cos(\beta) - Y\cos(\alpha)\sin(\beta) + L\sin(\alpha) \\ Y_a &= -D\sin(\beta) + Y\cos(\beta) \\ Z_a &= -D\sin(\alpha)\cos(\beta) - Y\sin(\alpha)\sin(\beta) - L\cos(\alpha) \end{aligned} \tag{3.3}$$

being L, D and Y the lift, drag and sideforce, respectively. The thrust vector is defined as

$$[T] = \begin{bmatrix} X_T \\ Y_T \\ Z_T \end{bmatrix} \tag{3.4}$$

where X_T, Y_T and Z_T are the total thrust force components along the x, y and z body axes. In this particular case these were zero because a gliding flight with the electric motor turned off was considered. The presented system of linear equations was solved with respect to lift (L), drag (D) and aerodynamic lateral force (Y), and the lift-to-drag ratio was obtained by dividing L by D.

3.3.1.3 Sensor Corrections

Since not all sensors were located near the vehicle CG, it was necessary to apply corrections. Of particular interest is the AOA and AOS corrections, since the sensors used to measure these quantities are moderately displaced from the RPAS CG, in order to reduce aerodynamic interference from the vehicles' body. From [139] the corrections are found to be

$$\alpha_c = \alpha_m - \frac{qx_\alpha - py_\alpha}{V} \tag{3.5}$$

$$\beta_c = \beta_m - \frac{rx_\beta - pz_\beta}{V} \tag{3.6}$$

being α_m and β_m the measured values of AOA and AOS, α_c and β_c the corrected values of AOA and AOS, x_α and y_α the x and y distances of the AOA sensor from the CG and x_β and z_β the x and z distances of the AOS sensor from the CG.

3.3.1.4 Drag Polar Representation

In order to compute the drag polar, lift and drag coefficients should be calculated. Lift coefficient can be directly calculated from its definition and using the flight path angle to calculate the component of the weight during the glide. Thus

$$C_L = \frac{W\cos(\gamma)}{0.5\rho V^2 S_{ref}} \tag{3.7}$$

where γ is the flight path angle, W the RPAS weight, ρ_{air} the air density and S_{ref} the reference wing area (of the fixed wing). The flight path angle can be computed from

$$\gamma = \arctan\left(\frac{1}{L/D}\right) \tag{3.8}$$

Finally, the drag coefficient is calculated noting that

$$C_D = \frac{C_L}{L/D} \tag{3.9}$$

3.3.2 Flight Performance

The aerodynamic efficiency was assessed using gliding flights. Each flight consisted of a series of power-off descents at different airspeeds that were achieved by simply changing the elevator trim position. It should be mentioned that the flight tests were performed using a folding propeller and with the electric motor brake activated. This was of utmost importance, in order to eliminate the propeller windmill, which would inadvertently increase drag and, consequently, reduce the L/D.

3.3.2.1 Experimental Procedure

A typical flight path for data acquisition started with an initial climb until the RPAS reached a certain altitude. The altitude to reach was highly dependent on the speed condi-

tion that would be analysed, since the sink rate greatly increases with vehicle's speed. Then, the electric motor was turned off and motor brake was automatically activated, allowing the propeller blades to retract. This eliminated windmill and reduced propeller drag. As the gliding flight was initiated, the elevator trim was set to establish the airspeed. The dynamics of the RPAS and the wind characteristics determined the time it takes to converge. This can clearly be seen in Fig.3.14 as a damped sinusoidal motion. The RPAS was then allowed to lose altitude until a predefined minimum and throttle was restored, in order to regain the altitude. This cycle was repeated until the energy stored in the battery was not sufficient to perform more flight cycles, thus proceeding to the landing stage.

A sample of the collected flight testing data is shown in Fig.3.14. It is possible to observe the variation of absolute altitude (AGL), angle of attack (α), pitch angle (θ) and airspeed, during a typical gliding flight in good weather conditions.

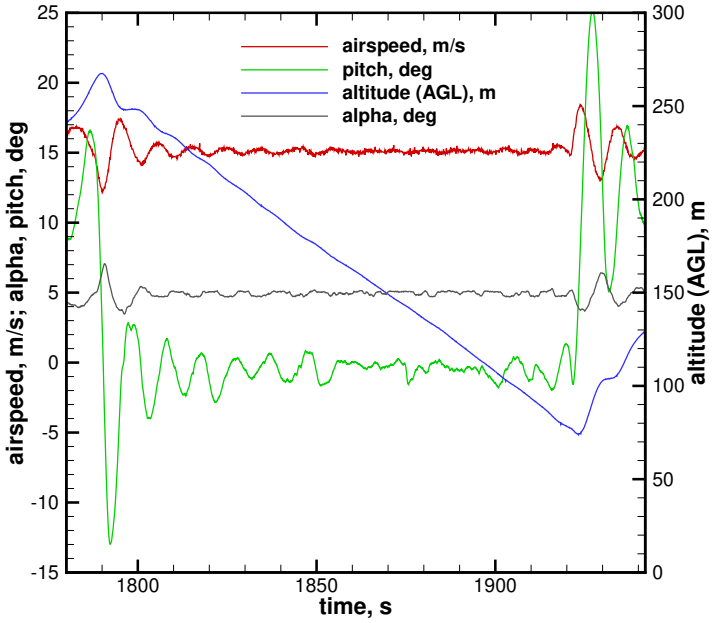

Figure 3.14: Typical recorded data from a gliding flight in good weather conditions.

3.3.2.2 Data Post-processing

All flight tests were recorded on-board to a micro SD-card in a binary format, allowing later processing of the data. A Python script was developed to convert the stored binary logs to text based files that could be loaded in Tecplot® graphing software. This allowed visual post-processing of the data on-the-fly, as well as easy generation of high quality plots, as shown in Fig.3.14.

In order to compute the L/D and ultimately the drag polars for each RPAS configuration, a FORTRAN software that implements the algorithm described in section 3.3.1 was developed. The program uses a methodical procedure composed by the following steps:

1. Identification of the gliding flights starting and finishing instants, based on flight log analysis (airspeed and altitude data);
2. Correction of AOA and AOS due to their offset position as given by Eqs.(3.5) and (3.6);

3. Computation of L, D and L/D by the solution of Eq.(3.2) for each instant during the glide;
4. Computation of average L/D during the entire glide;
5. Computation of averages of all values of interest during the glide: α, β, γ and ρ_{atm};
6. Computation of C_L and C_D using Eqs.(3.7) and (3.9);
7. Storage of all data to the corresponding database (fixed wing or VSW as a function of span position);
8. Repeat steps 2 to 7 until all flights are computed.

The C_L and C_D curves for each studied case (fixed wing, VSW fully extended and VSW fully retracted) were approximated with a parabola using the least square method, in order to obtain the asymmetric quadratic drag polar of the form

$$C_D = C_{D0} + K_1 C_L + K_2 C_L^2 \tag{3.10}$$

3.4 Methodology to Determine Mission Energy

In this section, the experimental evaluation of the energy requirements when performing a typical mission is explained. Olharapo RPAS was fitted with either a VSW or a conventional fixed wing and the propulsion and manoeuvring power was accessed.

3.4.1 Mission Profile

The main purpose of the mission definition is to provide a given mission to compare the energy consumption of the RPAS fitted with a conventional fixed wing and with the VSW. It was defined in such a way that the multi-role capability of the VSW could stand out. The proposed mission profile is shown in Fig.3.15. This is only a sample mission and, as such, other mission profiles could be studied to better understand the benefits of the VSW.

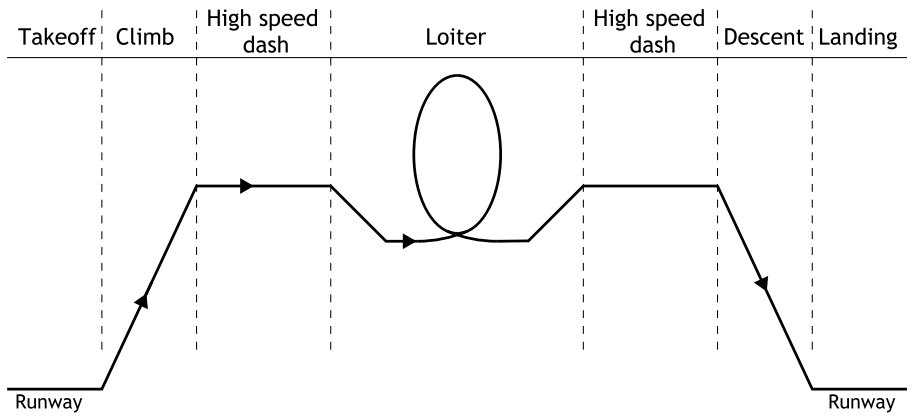

Figure 3.15: Mission profile: (1) takeoff; (2) climb; (3) short range high speed dash; (4) loiter; (5) short range high speed dash; (6) descent and (7) landing.

Referring to Fig.3.15, the flight phases are:

1. Takeoff - Takeoff from airfield. Typical distance is 100 m.
2. Climb - Fast climb to 300 m above ground level (AGL) with an airspeed of 16 m/s. The time to climb is around 2 minutes.
3. Short range high speed dash - Short range high speed dash performed at 300 m (AGL) with an airspeed of 25 m/s and a duration of 5 minutes. This flight phase should be performed in a downwind condition.
4. Loiter - Long duration loiter at 300 m (AGL) with an airspeed of 17 m/s and a duration of 10 minutes.
5. Short range high speed dash - similar to flight phase 3) with the exception that it should be performed in upwind conditions.
6. Descent - Fast descent to landing site. The descent is performed in 1.5 minutes.
7. Landing - Landing at the airfield. Typical time to stop is around 10 seconds (no active breaking).

This mission was chosen having in mind the flight envelope of Olharapo 2H RPAS. In the takeoff phase, the RPAS nominally needed 100 m to initiate the rotation phase. Additionally, the high speed dash was performed with the wing fully retracted in the case of the VSW configuration, since it is the configuration with less drag. A total of two actuation cycles were needed (retraction and extension). Regarding the descent and landing, the propulsion power was considered to be zero, since during the descent the aircraft was gliding and after the touchdown there was no active braking, neither aerodynamic (thrust reversers or spoilers) nor wheel brakes.

3.4.2 Level Flight Propulsion Performance

The selected propeller was a 13”$\times$12” 2-bladed Aero-naut® CAMcarbon Power-Prop. This propeller was selected in order to allow the vehicle to achieve and sustain velocities in the high speed range of the envelope, during levelled flight. This propeller presents a slightly thickened profile, yet still relatively thin, resulting in a low-drag section and a very good torsional stiffness, combined with low weight. It is made of carbon fibre reinforced material. The motor used was a Hyperion ZS3025-10 and the ESC was a Castle Creations® Phoenix Ice 75A. A battery pack of three LiPo elements used in series was employed, giving a rated voltage of 11.1 V to the motor.

In order to compute the propulsion power for level flight, a series of sequential calculations were performed. These are:

1. Propeller performance characterization using experimental wind tunnel testing;
2. Propeller curves approximation using polynomial functions;
3. Electric motor and propeller coupling to compute battery power, given aircraft’s drag polars.

3.4.2.1 Propeller Characterization

Curves for power coefficient, C_P, and for propulsive efficiency, η_{prop}, as functions of advance ratio, J, and propeller rotational speed, N, were obtained from wind tunnel propeller testing.

The propeller test bench used was assembled inside the test section of the wind tunnel installed in the Aerodynamics and Propulsion Laboratory of University of Beira Interior. It is an open type wind tunnel from the French manufacturer EReME. It has a variable speed Alternating Current (AC) motor with a rated power of 15 kW at 970 Rotations Per Minute (RPM). Directly linked to the motor shaft is a sucking axial fan with 1.2 m of diameter. The wind tunnel test section has a width of 0.8 m, a height of 0.8 m and a length of 1.5 m. The maximum velocity inside the test section in normal temperature and pressure conditions (NTP) is around 30 m/s. The settling chamber has a cross section of 2 m$\times$2 m and is fitted with a stainless steel honeycomb. The diffuser has a square inlet section of 0.8 m$\times$0.8 m and an outlet circular section of 1.2 m.

A propeller thrust balance was developed using a T-shaped pendulum concept. The pendulum is pivoted about two flexural pivots while being constrained by a load cell outside of the tunnel in an area above the test volume. The flexural pivots were chosen over standard bearings, since they greatly reduce the adverse tendencies that bearings are prone to, when used in static applications, namely stiction and hysteresis. The pendulum was designed in order to have the thrust vector located at the centre of the test section. One of the key features of this concept is the possibility to adjust the position of the load cell along the upper arm of the pendulum. Thus, it becomes possible to use the full range of the load cell for different intervals of propeller's produced thrust [141].

The thrust load cell used is the FN3148 manufactured by FGP Sensors®, having a maximum capacity of $\pm$100 N (positive in tension or negative in compression). The torque produced by the propeller is measured using the RTS-100 or RTS-200 reaction torque cell made by Transducer Techniques® according to the torque level of the propeller being tested. Both thrust and torque load cells are connected to a high-precision strain gauge converter DSCH from Mantracourt®. To measure the propeller rotation speed, a photo-reflector is used to count the number of revolutions of the output shaft [141].

Figure 3.16 shows the balance concept, where it is possible to see the thrust and torque load cell positioning, propeller and electric motor. Additionally, the two drilled rails, that allow the sensitivity of the thrust cell to be adjusted, can also be seen.

The freestream velocity was measured with a differential pressure transducer, an absolute pressure transducer, and a thermocouple. The measuring mechanism uses two static pressure ports, one at the tunnel settling section (section 1 - P_1, A_1) and another at the entrance of the test volume (section 2 - P_2, A_2). The determination of the flow velocity in the test section is given by:

$$V_2 = \sqrt{\frac{2(P_1 - P_2)}{\rho_{air}\left[1 - (\frac{A_2}{A_1})^2\right]}} \tag{3.11}$$

A software based in NI LabVIEW® was developed to perform and automate all the data

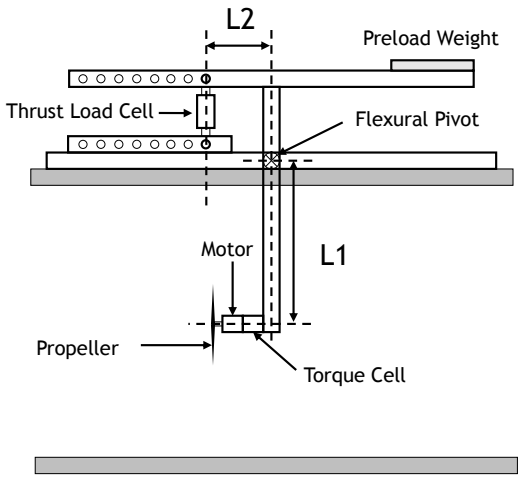

Figure 3.16: T-shaped pendulum thrust balance concept with all its components [141].

acquisition and data reduction. The propeller rotational speed and wind tunnel freestream velocity are set using PID controllers. It is possible to perform two types of tests: static and dynamic. For static performance tests, the propeller thrust and torque are measured along with the local atmospheric pressure and temperature at different RPMs. For the dynamic performance tests (with freestream speed), the propeller rotational speed is set to a desired value and the wind tunnel's freestream velocity is increased from 4 m/s to 28 m/s in 1 m/s increments. At each measured freestream velocity, the propeller thrust and torque were measured along with the ambient pressure and temperature. The test is finished if the torque value becomes close to zero, because the propeller is entering the windmill brake state.

Once the data was collected, the data reduction subroutine is executed. The collected data is systematically reduced and stored. Variables can be divided into two categories, namely measured and calculated variables. The measured variables are directly obtained from the measurement instruments. Physical measurements of thrust, T_{prop}, torque, Q_{prop}, rotational speed, N, atmospheric pressures, P_{abs}, and temperature, T_{atm} are gathered. From these quantities, propeller power, P_{prop}, and air density, ρ_{air}, are calculated according to

$$P_{prop} = 2\pi N Q_{prop} \tag{3.12}$$

$$\rho_{air} = \frac{P_{abs}}{R_{air} T_{atm}} \tag{3.13}$$

The above measured and calculated quantities are nondimensionalized in order to obtain the propeller performance characteristics. These quantities include the advance ratio, J, the thrust coefficient C_T, power coefficient, C_P, and propeller efficiency, η_{prop}. In the static case, since the advance ratio is zero, C_T and C_P are plotted against the propeller rotational speed. For the non-static case, the coefficients and the efficiency are plotted against the advance ratio. The definitions for the advance ratio, thrust and power coefficients, and propeller efficiency are given by

$$J = \frac{V}{N D_{prop}} \tag{3.14}$$

$$C_T = \frac{T_{prop}}{\rho_{air} N^2 D_{prop}^4} \tag{3.15}$$

$$C_P = \frac{P_{prop}}{\rho_{air} N^3 D_{prop}^5} \tag{3.16}$$

$$\eta_{prop} = J \frac{C_T}{C_P} \tag{3.17}$$

where, V is the freestream velocity (computed with Eq.(3.11)) and D_{prop} is the propeller diameter.

The described experimental setup was used to collect the data and the data reduction procedure to compute the propeller performance curves. Figure 3.17 shows the experimental data points for three different values of propeller rotational speed: 3000 RPM, 6000 RPM and 7000 RPM, for the 13"$\times$12" 2-bladed Aero-naut® CAMcarbon Power-Prop.

3.4.2.2 Propeller Curves Approximation

Based on the data collected and assuming a polynomial fit to the experimental points, analytical curves were obtained to calculate C_P and η_{prop} given any values of J and N within the range of the experimental data. The construction of these curves assumes a fixed non-dimensional shape based on other propeller's curves. For C_P a fourth order polynomial approximation is scaled by the power coefficient at zero advance ratio, C_{P0}, and the maximum advance ratio, J_{max}, (when the propeller becomes a windmill) and for η_{prop} a fifth order polynomial approximation is scaled by the maximum propulsive efficiency, $\eta_{prop,max}$, and J_{max}. Those parameters (C_{P0}, $\eta_{prop,max}$ and J_{max}) are functions of Reynolds number and thus propeller rotational speed. Thus, for a given rotational speed a set of C_{P0}, $\eta_{prop,max}$ and J_{max} values were obtained. Having these values, the curves $C_P(J, C_{P0}, J_{max})$ and $P(J, \eta_{prop,max}, J_{max})$ were created for each rotational speed, N, and the final curves $C_P(J, N, C_{P0}, J_{max})$ and $P(J, N, \eta_{prop,max}, J_{max})$ were obtained by linear interpolation of the former. Figure 3.17 illustrates the polynomial approximations and the experimental data points.

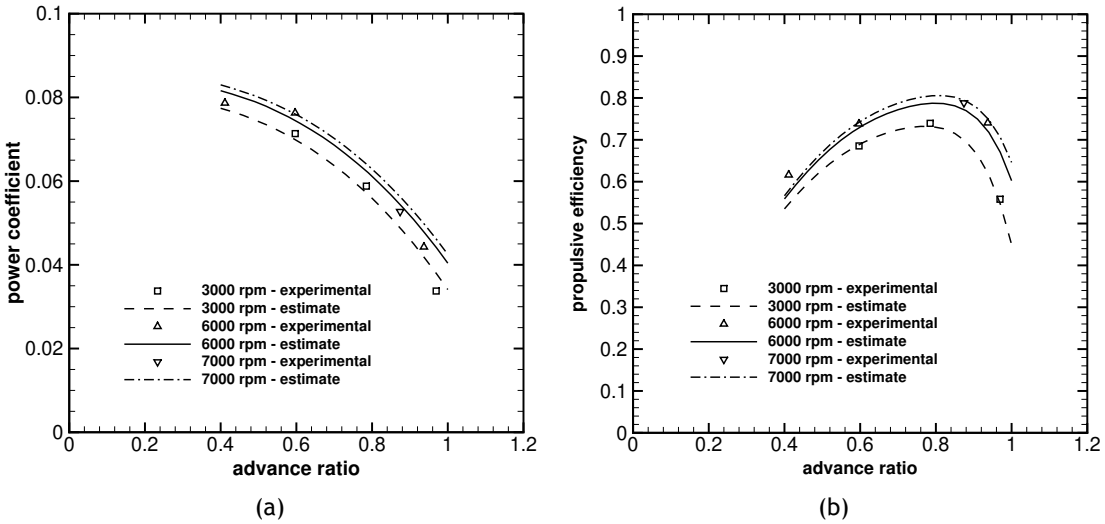

(a) (b)

Figure 3.17: Aero-naut® Power-Prop 13"$\times$12" 2-bladed propeller performance curves: (a) power coefficient and (b) propulsive efficiency, highlighting experimental and approximated data.

3.4.2.3 Propulsion Power

In order to evaluate the electric power consumption of the vehicle's propulsion system in different flight conditions, it is necessary to know the characteristics of the motor, the electronic speed controller (ESC), the battery, the propeller and the aerodynamic characteristics of the aircraft. Hence, the input constants are the idle voltage, $U_{bat,0}$, the internal resistance of the battery, R_{bat}, and that of the electronic speed controller, R_{ESC}. Additionally, since steady state conditions were considered, thrust has to equal drag or propulsive power has to equal required power. The airspeed, V, and air density, ρ_{air}, are derived from the mission profile.

An algorithm was used to couple the produced motor shaft power to the propeller power absorbed. Such algorithm is shown in Fig.3.18. The thrust setting, δ, and electrical current, I, are initially guessed and thereafter iterated. Finally, the required power, P_{req}, is the product of the aircraft drag, D, by its velocity, V, for the flight condition under study, which comes from the flight mechanics analysis and vehicle mission. Three iteration cycles have been built. One is optional and is only used if one wants to establish a maximum current and correct the thrust setting if this limit is exceeded. A second iteration cycle makes sure the electric current is corrected so that the electrical motor power, P_{mot}, equals the absorbed propeller power (P_{prop}/η_{prop}) which is a must since there is no slippage between the two. A last iteration corrects the thrust setting to ensure that the available propulsive power (P_{prop}) equals the required power, P_{req}. In the flowchart of Fig.3.18, η_{mot} refers to the motor efficiency and η_{prop} to the propeller's efficiency [142].

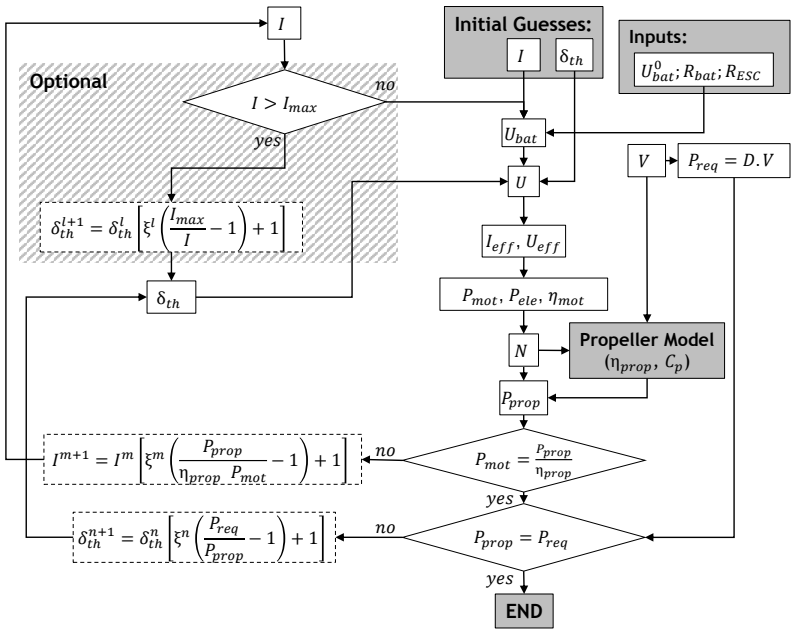

Figure 3.18: Propulsion model implementation for an electrical motor [142].

The implemented routine needs to know how the power coefficient, C_P, and propeller efficiency, η_{prop}, vary with the propeller advance ratio, J. The polynomial approximations computed using the experimental data were fed in the presented algorithm. Among other output parameters, one can obtain the battery voltage and current drawn and hence the battery power required by the propulsion system.

3.4.3 Takeoff and Climb Power

The takeoff energy was computed considering the total energy from the start of the acceleration until the wheels leave the ground. To account for small deviations in takeoff distance, the total takeoff energy was then divided by the takeoff distance, thus obtaining the takeoff energy per meter. This procedure was repeated for several flights and the results averaged. The takeoff distance was considered to be 100 m for both configurations.

The climb power of the RPAS was computed using experimental data. Several climbs were performed at the desired airspeed of 16 m/s and rate of climb of approximately 3.5 m/s and the propulsion power was recorded. The average power during the climb was then computed. Averaging was also performed across several climbs to compensate for airspeed variations. The effort was done for the RPAS equipped with the conventional wing and the VSW.

3.4.4 Control Actuation Power

The instrumentation available in the RPAS allows the energy of the various servo actuators to be quantified. Olharapo RPAS uses one servo for each control surface for reliability and robustness. In the fixed wing RPAS all the servos were recorded as a whole. From flight testing, it was concluded that the average power consumption does not change significantly (less than 5% variations) among the different flight phases. Thus, it was decided to compute an average power throughout the flight.

The VSW is servomotor actuated. Each wing can be actuated independently, thus providing roll control with asymmetric span deployment. However, this capability was not used in this study due to the complexity that it introduces in the energy quantification. In fact, due to the sliding nature of the VSW, the actuation energy is highly dependent on the load factor of the aeroplane. Thus, the VSW was only symmetrically actuated in level flight (in 1G conditions). The energy consumption can be divided into two contributions: a constant consumption and a cyclic consumption. The first one arises from the holding torque, necessary to maintain the OMW in place. The second contribution is the energy needed to move the OMW and arises from the friction between the IFW and the OMW. Several flight tests were performed with the power being logged. The data was later post-processed and the two contributions were computed.

3.5 Aerodynamic Efficiency Testing Results

A total of 45 test flights were performed, totalling about 30 hours of flight. All flights took place in Castelo Branco's airfield, Portugal, which has an altitude of 375 m above sea level.

The variable-span wing and fixed wing have different weights: 21.5 N and 13.5 N, respectively. Therefore, the CG position was carefully measured so that it was maintained at the same chord position for both wings. This allowed for a more direct comparison of the performance curves, since the lift-to-drag ratio (L/D) curve as a function of airspeed moves along the airspeed axis when changing the CG, due to trim adjustments. The takeoff weight of Olharapo

RPAS with the conventional wing was 54.5 N and with the VSW was 65.5 N and the CG was located at 28.6% and 28.9% of each wing chord, respectively. The VSW was tested in two different wingspan configurations: full wingspan (2.5 m) and minimum wingspan (1.55 m). It should be emphasized that the wing reference area used throughout the calculations was the conventional fixed wing area of 0.625 m^2.

3.5.1 Drag Polars

Figures 3.19 and 3.20 show the experimental data and the parabolic approximations for the RPAS fitted with the conventional wing, with the VSW in full-span configuration and minimum span configuration. Observing Fig.3.19, which shows both the experimental data and the parabolic approximation, it is visible that a strong correlation exists between the two, being the coefficient of determination (R^2) of 0.85. The equation of the approximation is

$$C_D = 0.0903 - 0.1652C_L + 0.1988C_L^2 \tag{3.18}$$

Observing Figure 3.20, which shows the drag polar of the VSW with full-span and minimum span, one can conclude that the experimental data and the parabolic approximation agrees well, being the coefficient of determination equal to 0.91 in both situations. The equations of the approximations are, for full-span and minimum span, respectively,

$$C_D = 0.1393 - 0.2873C_L + 0.2793C_L^2 \tag{3.19}$$

$$C_D = 0.0780 - 0.1282C_L + 0.2115C_L^2 \tag{3.20}$$

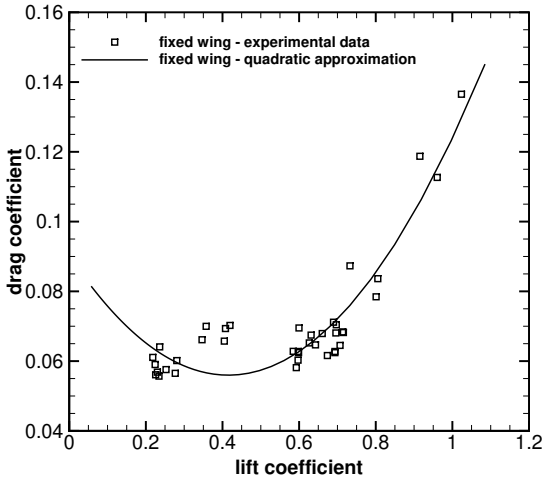

Figure 3.19: Drag polar of the RPAS fitted with the conventional wing.

3.5.2 Lift-to-drag Ratio

After computing the drag polar approximation for each test condition, the lift-to-drag ratio as a function of airspeed was recomputed using the parabolic curves at sea level conditions.

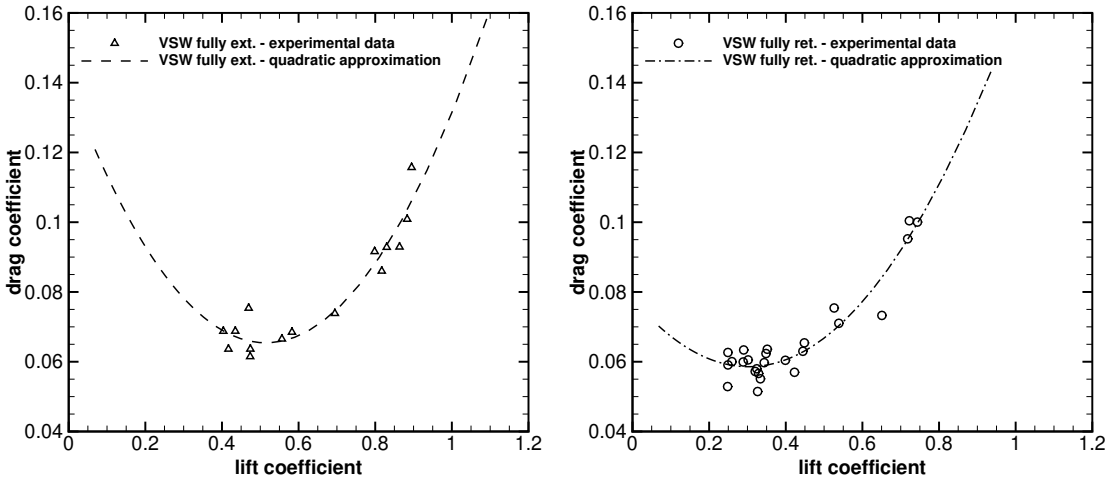

(a) (b)

Figure 3.20: Drag polars of the RPAS fitted with the VSW: (a) full-span and (b) minimum span configurations.

The results here presented are for the complete aircraft.

Considering Fig.3.21, it is visible that the maximum L/D occurs with the fixed wing at an airspeed of 14.6 m/s, with a value of 9.7. The maximum L/D with the VSW occurs with the maximum span, reaching a value of 9.3 at 15.6 m/s. Therefore, at low speed the VSW is less efficient than the conventional wing. This was to be expected due to mainly three aspects as discussed in section 2.4: less efficient aerofoil in OMW, thicker aerofoil in the IFW and chord discontinuity in the transition from the IFW to the OMW. The first two mentioned aspects are closely related, since the IFW aerofoil was generated as an offset of the OMW. In order to make this possible the OMW aerofoil was modified to have a flat lower surface, which in turn reduced the performance of the local aerofoil. Regarding the chord discontinuity, more induced drag due to trailing vortices generation is expected. However, as suggested in [43], if OMW to IFW chord ratio is above 0.86, then joint vortex intensity is at least ten times less intense than tip vortex. In the developed VSW, the chord ratio is 0.92, so the drag penalty arising from the chord discontinuity was small.

At higher speeds the fixed wing and the VSW with full-span show very similar characteristics. However, when the airspeed reaches 19 m/s the conventional wing becomes slightly better. This behaviour carries on up to the maximum measured speed of 30 m/s. The VSW with the minimum span has inferior performance at low speed, being the maximum L/D of 7.8 at 16.8 m/s. This was to be expected given the dramatic area reduction (40%). However, with the increase of the airspeed to 18.8 m/s, the benefits clearly start to be seen. At this airspeed L/D exceeds the one of the conventional wing. The benefit continues to increase, being the VSW in minimum span configuration 35% better than the original fixed wing at 30 m/s. The curve trends suggest that the benefit should continue to increase even further for higher speeds (as suggested by the numerical study in section 2.4).

Notice that, comparing Fig.2.9(d) (from section 2.4) with Fig.3.21, the former showing the numerical predictions for L/D of the wings alone and the latter showing the L/D curves obtained from the experimental data for the complete RPAS, one can see the same trends in both wings at similar airspeeds.

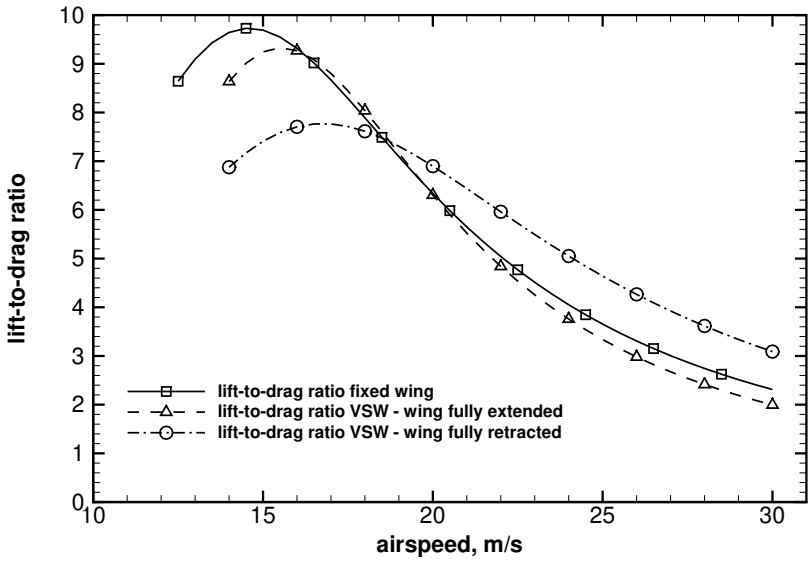

Figure 3.21: Lift-to-drag ratio over airspeed computed from the parabolic asymmetric polars for each RPAS configuration, at sea level conditions.

3.6 Mission Energy Results

3.6.1 Level Flight Propulsion Power

The power required for level flight can now be obtained using the aircraft's drag polars. These were computed in section 3.5 through parabolic curve fitting to the drag-lift data as functions of flight speed obtained during flight testing.

A second approach was also used in the present work. It consists in measuring the in-flight power drawn from the battery for various quasi-steady flight speeds and altitudes. Both approaches were used in this work, but due to intense wind conditions felt during the flight testing campaign only a few data points were really useful.

Figure 3.22 shows the electric power required for flight as a function of speed for the various wing configurations: fixed wing, VSW fully extended and VSW fully retracted. Now, with this plot, the overall electric power required for propulsion for a given airspeed can be readily obtained and energy consumptions of steady state level flight phases of the proposed mission may be computed for any of the three wings.

Apparently, the estimated curves approximate the experimental data points quite reasonably at high speeds but at lower speeds (below 17 m/s) it seems that the calculated powers are somewhat underestimated. On the other hand, recalling that the drag polar estimates were quite accurate at high lift coefficients, it may happen that the visible differences come mainly from experimental errors.

3.6.2 Takeoff Propulsion Power

Figures 3.23(a) and 3.23(b) shows altitude, airspeed, and propulsion battery voltage and current recorded during a takeoff with the fixed wing and VSW, respectively.

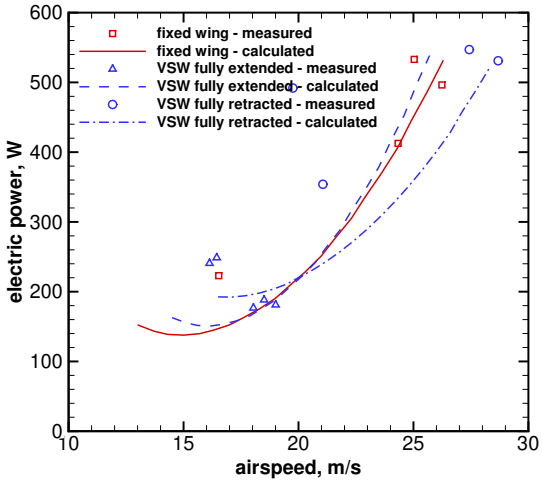

Figure 3.22: Experimental and estimated required electric power for level flight for all three studied wing configurations.

Observing Fig.3.23(a) one can see that takeoff starts at $t = 743\,s$ and the rotation happens 9 seconds later, approximately. The altitude remains constant during the acceleration phase, with the exception of a small reduction in altitude near the rotation. This is due to an aerodynamic effect in the barometer. Regarding Fig.3.23(b), which shows the takeoff with the VSW, it is possible to see that the takeoff starts at $t = 541.5\,s$ and rotation occurs 10.5 seconds later. Note that 1.5 extra seconds are necessary to achieve the same airspeed (≈20 m/s).

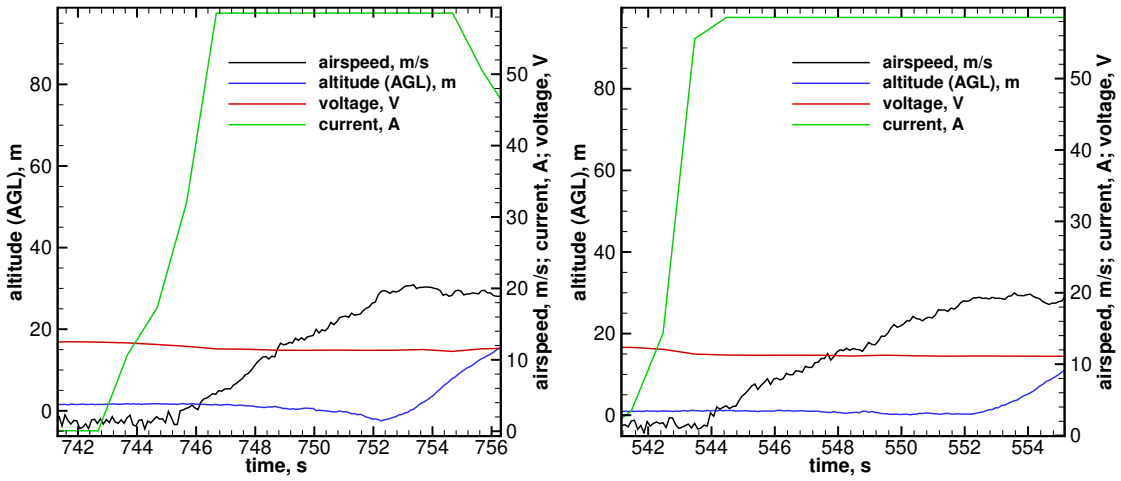

Figure 3.23: Olharapo 2H RPAS typical takeoff with the (a) fixed wing and (b) VSW.

The data discussed is just an example, since various takeoffs were recorded. For each takeoff the total energy was divided by the takeoff distance and later averaged for multiple takeoffs. Table 3.1 shows the specific propulsion energy for the takeoff phase.

Table 3.1: Specific propulsion energy of Olharapo 2H RPAS for the takeoff flight phase.

Specific Energy, J/m	RPAS Fixed wing	RPAS VSW
Takeoff	52.2	56.4

3.6.3 Climb Propulsion Power

Figures 3.24(a) and 3.24(b) shows altitude, airspeed, and propulsion battery voltage and current recorded during a typical climb with the fixed and variable-span wing, respectively. Regarding Fig.3.24(a), which shows a climb with the fixed wing, it is possible to see that the rate of climb (ROC) is about 3.5 m/s and the airspeed is approximately 16 m/s. Observing Fig.3.24(b), which shows a climb with the VSW, it is possible to see that a similar airspeed and ROC are achieved. However, the power required is higher, as evidenced by the higher current consumption (58/45 A).

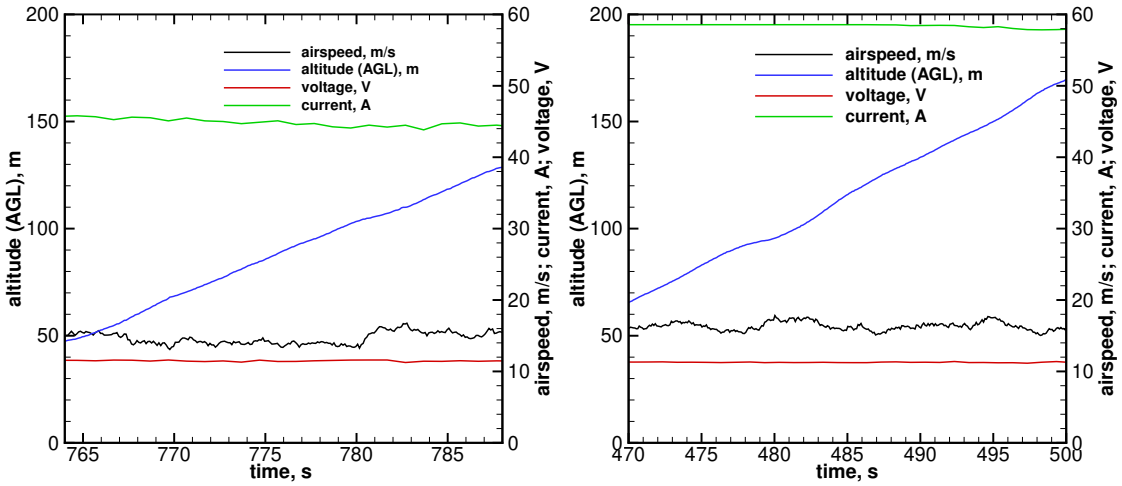

Figure 3.24: Olharapo 2H RPAS typical climb with the (a) fixed wing and (b) VSW.

The discussed climbs are just an example, since various climbs were recorded. Averaging was performed across several climbs to compensate for airspeed and ROC variations, in order to obtain a more reliable propulsion climb power.

3.6.4 Control Actuation Power

As explained before, in the fixed wing RPAS all the servomotors were recorded as a whole. In the VSW equipped RPAS the wing was only symmetrically actuated in level flight (in 1G conditions).

Figure 3.25(a) shows the recorded voltage, current and power during a fixed wing flight and Fig.3.25(b) shows the recorded voltage, current and power during a retraction and later extension movement of the wing. In Fig.3.25(a) it is possible to conclude that the power consumption of the servomotors changes significantly during the flight. However, the average is approximately constant throughout the flight. Figure 3.25(b) exemplifies a retraction ($t = 486.5\,s$) followed later by an extension ($t = 554\,s$). During the retraction or extension cycle, there is an increase in power demand. One can also see that the power consumption is not zero when the wing is in a fixed span position. This is due to the holding torque of the servomotor, required to prevent the OMW from moving. The analysis of this figure allows two distinct power terms two be clearly identified: VSW holding power and cycle power.

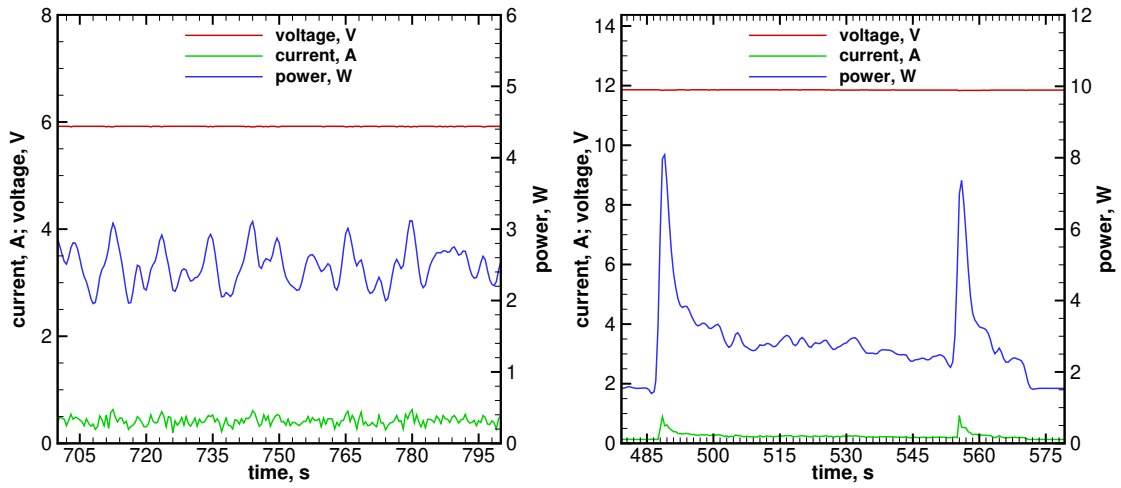

Figure 3.25: Olharapo 2H RPAS typical actuation power with the (a) fixed wing and (b) VSW.

The fixed wing equipped RPAS power consumption can be readily computed by averaging the power during flight. The VSW RPAS actuation was computed by summing three contributions: servo power (all except wing), VSW holding power and VSW cycle energy. Table 3.2 summarizes the power and energy terms for each wing configuration.

Table 3.2: Actuation energy of Olharapo 2H RPAS with the fixed wing and variable-span wing.

Fixed wing RPAS servo power	2.82 W
VSW RPAS servo power	2.17 W
VSW holding power	2.46 W
VSW cycle energy	477.9 J/cycle

3.6.5 Mission Analysis Results

From the drag polars of Figs.3.19 and 3.20 (from section 3.5), and considering the weight of each RPAS configuration, the lift-to-drag ratio (L/D) of the vehicle fitted with the conventional fixed wing and with the VSW was determined for the loiter and cruise airspeeds. Table 3.3 summarizes the lift-to-drag ratios that are important to the proposed mission (Fig.3.15).

Table 3.3: Lift-to-drag ratios of the RPAS for two airspeed conditions (loiter and high speed dash).

Speed, m/s	L/D - Fixed Wing	L/D - VSW Full Span	L/D - VSW Min Span
17	8.67	8.88	7.76
25	3.65	3.34	4.64

From the propulsion power, control actuation power and mission definition, it is possible to compute the energy for each flight mission phase. The data computed from the different disciplines is summarized in Tables 3.1, 3.2 and 3.4. Using the data from the mentioned tables, the energy for each flight mission phase can be readily computed. The computed data is shown in Table 3.5.

Table 3.4: Required power of Olharapo 2H RPAS in the various flight phases.

Required Electric Power, W	RPAS Fixed wing	RPAS VSW
Climb – 16 m/s	497.4	602.5
Loiter – 17 m/s	152.6	156
High Speed Dash – 25 m/s	452	363.8

Table 3.5: Energy required to perform each flight phase for the Olharapo 2H RPAS

	Conventional wing		Variable-span Wing	
	Propulsion, J	Actuation, J	Propulsion, J	Actuation, J
Takeoff	5,218	25	5,637	42
Climb	59,689	339	72,305	556
High Speed Dash	135,607	847	109,144	1,867
Loiter	91,547	1,693	93,620	2,778
High Speed Dash	135,607	847	109,144	1,867
Descent	0	254	0	417
Landing	0	28	0	46
	427,667	4,032	389,851	7,572
Total	431,699		397,423	

By looking at Table 3.5, which compares the energy required for each flight phase with the RPAS fitted with the fixed wing and the VSW, one immediately concludes that the VSW allows an energy reduction of around 8%. On the one hand, the energy consumption during takeoff, climb and loiter phase is higher than the RPAS fitted with the conventional wing. This is mainly due to three aspects: less efficient aerofoil of the VSW due to geometric compatibility requirements of the IFW/OMW, chord discontinuity in the transition from the IFW/OMW, and increased mass (1.12 kg). On the other hand, the short range high speed dash flight phase demonstrates a reduction in energy consumption with the VSW fitted RPAS, since the span retraction allows the wing area to reduce and adapt to the higher speed condition. This, in turn, reduces the parasite drag of the wing and also the trim drag (due to load alleviation in the horizontal stabilizer). Additionally, the flight phases where a higher gain in energy was necessary, the increased mass of the VSW was more penalizing. Therefore, takeoff and climb phases were the most affected, since in these phases the kinetic and potential energy variation, respectively, is maximum.

Regarding the actuators energy consumption, it is demonstrated, as expected, that the VSW servomotors require more energy to adapt the span during the flight. Furthermore, the high power servomotors have higher idle current to sustain the holding torque.

3.7 Concluding Remarks

In this chapter, the experimental flight testing of Olharapo 2H RPAS was described. Essentially, two sets of flight tests were performed: aerodynamic and energy characterization. The former aimed at determining the lift-to-drag ratio for different airspeeds. The latter was performed to measure the propulsive and manoeuvring energy when performing a prescribed mission.

In-flight concept evaluation of the RPAS fitted with the VSW demonstrated full flight

capability and showed improvements produced by the VSW over a conventional fixed wing for speeds above cruise speed. At low speeds, the original wing had slightly better performance than the VSW, due to the increased vehicle weight, chord discontinuity in the transition from the IFW to the OMW, less efficient aerofoil in OMW and thicker aerofoil in the IFW. The last two mentioned aspects are closely related, since the IFW aerofoil was generated as an outward offset of the OMW. In order to make this possible the OMW aerofoil was modified to have a flat lower surface, which in turn reduced the performance of the local aerofoil. Regarding the chord discontinuity, an increase in induced drag was to be expected due to trailing vortices generation. However, as suggested in [43], if OMW to IFW chord ratio is above 0.86, then joint vortex intensity is at least ten times less intense than tip vortex. In the developed VSW, the chord ratio is 0.92, so the drag penalty arising from the chord discontinuity is small. The performance trend was inverted beyond approximately 19 m/s, where the VSW in minimum span configuration is better than the conventional wing. At this airspeed the L/D exceeded the one of the conventional wing. The benefit continued to increase, being the VSW in minimum span configuration 35% better than the original fixed wing at 30 m/s.

The energy consumption was evaluated with the conventional fixed wing and the VSW given a prescribed mission. The mission was chosen in such a way that the multi-role capability of the VSW could be exercised. The power required for level flight was obtained by employing two distinct approaches: using the aircraft's drag polars and measuring the power drawn from the battery for various quasi-steady flight speeds and altitudes. The first method proved to be more accurate due to windy conditions experienced during the test flight campaign. The takeoff energy and climb power were both computed from experimental data. The control actuation system energy was characterized in-flight for both the conventional wing and variable-span wing, so that the actuation system energy consumption could be computed for the various flight phases. From the electric power values obtained for propulsion and control actuation and mission definition, the propulsion and actuation energy for each flight phase was calculated. It was concluded that the VSW fitted RPAS had less overall energy consumption despite the increased vehicle weight. The energy reduction occurred only in the high speed condition but was so marked that it offset the increase in energy during takeoff, climb and loiter phases.

The two analysed flight testing campaigns confirmed that the VSW concept here presented is an option to consider when extending the flight envelope and increasing the multi-task capability of a RPAS is required. Thus, the increased structural and power related weight and complexity introduced by the VSW are justified by the increased speed flight envelope. In principle, it is possible to design a VSW that extends the speed boundaries for lower and higher speeds relative to a fixed wing designed for a given main design speed.

Chapter 4

CHANGE Project

4.1 Chapter Overview

The knowledge gained from designing, building and flight testing the telescopic VSW, showed without doubt that variable-span morphing wings are promising and feasible concepts, in terms of extending aircraft flight envelope and/or increasing performance. However, the wing developed in chapters 2 and 3, is limiting in terms of other morphing strategies. The necessity to have a completely hollow inboard fixed wing and the geometric compatibility between the two wing elements, severely limits the hardware integration near the wing root and creates a barrier to the integration of other moving surfaces. Therefore, the topic of this chapter is the idealization, development and testing of a new telescopic wing concept that allow the integration of other morphing strategies.

The new morphing wing methodology capable of producing wing span changes for flight speed adaptation was developed within the CHANGE (Combined morpHing Assessment software usiNG flight Envelope data and mission based morphing prototype wing development) project under European Union 7th Framework Programme (EU FP7). The CHANGE project had two major goals: a) the development of a software that could predict the performance benefits of morphing wings and b) the development of a novel morphing system which integrates up to four different morphing mechanisms. This chapter focus on the latter. Four main flight phases: takeoff, high speed dash, loiter and landing were used to create four baseline wings, based on aerodynamic inputs. These baseline wings were the foundation of the project, and the morphing wing was developed to morph and replicate, to a certain degree, those four different wings.

The capabilities adopted for this wing were: span change, leading edge (LE) and trailing edge (TE) camber changes. The last two can produce combinations of positive and negative chordwise camber changes and even spanwise twist. A modular design philosophy was adopted for this wing such that the individual systems producing span change, LE or TE change could be separately developed and then integrated into the overall wing system. This approach facilitated the development of each required mechanism and made the integration of all components easier. The modular design is based on a wing-box like structure. This structure was sized for strength and stiffness using FEM, being the design procedure thoroughly described in the upcoming sections. Later, a partial span, full-sized cross-section prototype of the wing-box was developed, in order to define an optimal building procedure and to perform bench testing. Finally, the full-scale prototype was developed by the consortium, in order to pursuit wind tunnel testing and flight testing using a RPAS.

4.2 The CHANGE Project

CHANGE (Combined morpHing Assessment software usiNG flight Envelope data and mission based morphing prototype wing development) was a Collaborative Project financed under the Transport (including Aeronautics) theme of the Cooperation Programme of the 7th Framework Programme of the European Commission. The project started on the 1st of August 2012, and ended in December 2015, lasting for a total of 40 months. A total of nine partners participated in this project, based in four different European Member States and one European Associate Member State. The partners were: TEKEVER ASDS (Coordinator), German Aerospace Centre (Deutsches Zentrum für Luft-und Raumfahrt - DLR), Aircraft Research Association (ARA), University of Beira Interior (UBI), Cranfield University (CU), Swansea University (SU), INVENT GmbH, Middle East Technical University (METU) and Delft University of Technology (TUD)[143].

The CHANGE project had two major goals: the development of a morphing assessment software and the design and implementation of a morphing wing that combines more than one morphing concept.

The CHANGE project considered a variety of different morphing technologies, namely, span variation, camber variation, twist variation and variable sweep wings, and tried to gather them in a single wing that aimed to garner the performance increase of all the morphing systems. This would demonstrate the feasibility of combining morphing systems that target different wing improvements and which could in principle enable an aircraft to carry out flights with increased performance. In order to achieve this, the CHANGE project used a RPAS as its research baseline platform.

CHANGE had another objective, with a medium to long term impact, the development of a software tool that would compute the most efficient wing shape of a morphing wing solely by delivering the information of the type of flight that the aircraft would be flying in. Thus, it would be possible to know how to change the wing's shape to carry out flights with the highest performance possible. The development of the software was intended to be a stepping stone for an on-board autonomous software with control over the morphing actuators. However, this was outside the scope of CHANGE, which solely intended to change the shape of the aircraft's wing in accordance to the environmental inputs and flight envelope. The scope of project CHANGE is depicted in graphic form in Fig.4.1.

The software envisioned in project CHANGE would also have the capability to be applied to any other type of wing with any size and morphing technologies without the need to modify its core modules.

As seen throughout Chapters 2 and 3, morphing technologies are encouraging and show promising improvements in terms of performance. However, there is still some work to be done. As a consequence of this, the CHANGE project had established as its main goals to define a stepping stone to insert morphing technologies into air transport aircraft, enabling the aircraft to fly with increased performance during the length of their mission. In particular, the main lower level objectives of CHANGE were:

- Analyse the practicability and possibility of integration of various morphing techniques in one wing;
- Creation of a conceptual model to demonstrate the functionality of the morphing system,

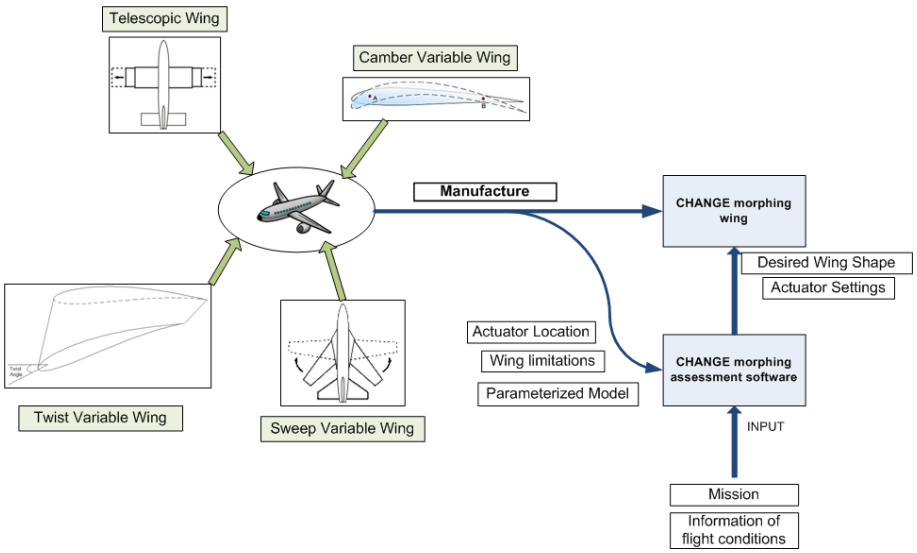

Figure 4.1: Scope of project CHANGE [143].

including its main advantages for performance increase and possible concerns;

- Design and development of a morphing prototype given four different performance driven missions;
- Validate the CHANGE morphing wing and morphing assessment software through wind tunnel and flight testing.

The CHANGE project contributions could be applicable not only to RPAS, but also to General Aviation (GA) and Commercial Aviation (CA) aircraft. In fact, morphing technologies applied in CA and GA aircraft may prove valuable in both increasing flight performance and decreasing overall fuel consumption. A morphing wing that can adapt to the best wing shape for a specific flight phase will allow aircraft to have better flight performance in non-optimal flight phases. The aircraft would be able to continue to fly with high performance during the cruise phase and at the same time, have the ability to operate at high performance in other flight phases including takeoff, landing, climb and descent. Increasing the performance throughout the flight will subsequently decrease the overall fuel consumption, hence decreasing CO_2 and NO_x emissions.

4.3 Mission Profile and Recipient RPAS

In this section, the mission profile and the recipient RPAS are described. The mission served to drive the aerodynamic design of the morphing wing, i.e., definition of flight phases airspeeds, and the recipient RPAS specifications served to define the general wing dimensions and the design maximum takeoff weight.

4.3.1 Recipient RPAS

The recipient platform of the morphing wing developed under the CHANGE project was a 25 kg RPAS, called DR5, developed by TEKEVER. The DR5 is part of the Demo Rays family, which

are platforms specifically conceived for testing, research and new product development. It was the platform chosen for use in CHANGE due to its high payload volume and weight, which are essential to eventually accommodate more power systems and additional instrumentation. Its main specifications are identified in Table 4.1.

Table 4.1: Main characteristics of TEKEVER's DR5 RPAS platform.

Specification	Value
Wingspan	3.60 m
Wing thickness	10% max (NACA 6510)
Mean wing chord	0.48 m
Length	2.4 m
MTOW	25 kgf
Payload weight	9 kgf
Operational range	5-20 km LoS
Operational altitude	up to 2000 m
Low speed	15.3 m/s - 55 km/s
Cruise (medium) speed	20.8 m/s - 75 km/s
Maximum speed	30.6 m/s - 110 km/h
Navigation	Autonomous or radio control

4.3.2 Mission Profile

The purpose of the flight mission carried out by the RPAS was to illustrate the real system capabilities and to validate the CHANGE morphing wing concept. It also served to drive the aerodynamic design of the morphing, i.e., definition of flight phases airspeeds. The wing prototype was flown using the DR5 platform, specified before, and was validated by performing several shape changes during the flight. The main objective is to perform simple tasks with the aircraft, in order to validate the capability to morph the wing during flight, and ascertain the capability to increase performance in flight. The defined mission is illustrated in Fig.4.2, in a schematic view and also viewed from above.

The mission starts with a takeoff, followed by a level high speed cruise. After some changes in altitude the RPAS performs a loiter, a return cruise and finally a descent and landing. Figure 4.2(a) shows a schematic of the established mission divided by mission phases. It was decided by the consortium that attitude adjustments were to be done only using the tail control surfaces and propulsive system. Therefore, the morphing system would not be tested as a means to control the attitude of the RPAS. In more detail the mission is composed by the following phases (referring to Fig.4.2):

- Takeoff - Takeoff from the airfield and subsequently a steady fast climb until an altitude of 1000 ft above ground level (AGL) is reached in order to proceed to W1 waypoint. Prior to the takeoff phase of the flight, the wing is set to the appropriate morphed state, which provides the greatest performance in this phase. The climb is performed at a fixed rate of climb, enduring around 3% of the total mission time.
- High speed levelled cruise - The climb phase ends at 1000 ft above ground level (AGL) and a levelled flight is maintained until waypoint W2. In this phase, the wing is in the high speed dash morphed phase, 30.6 m/s, in headwind conditions.

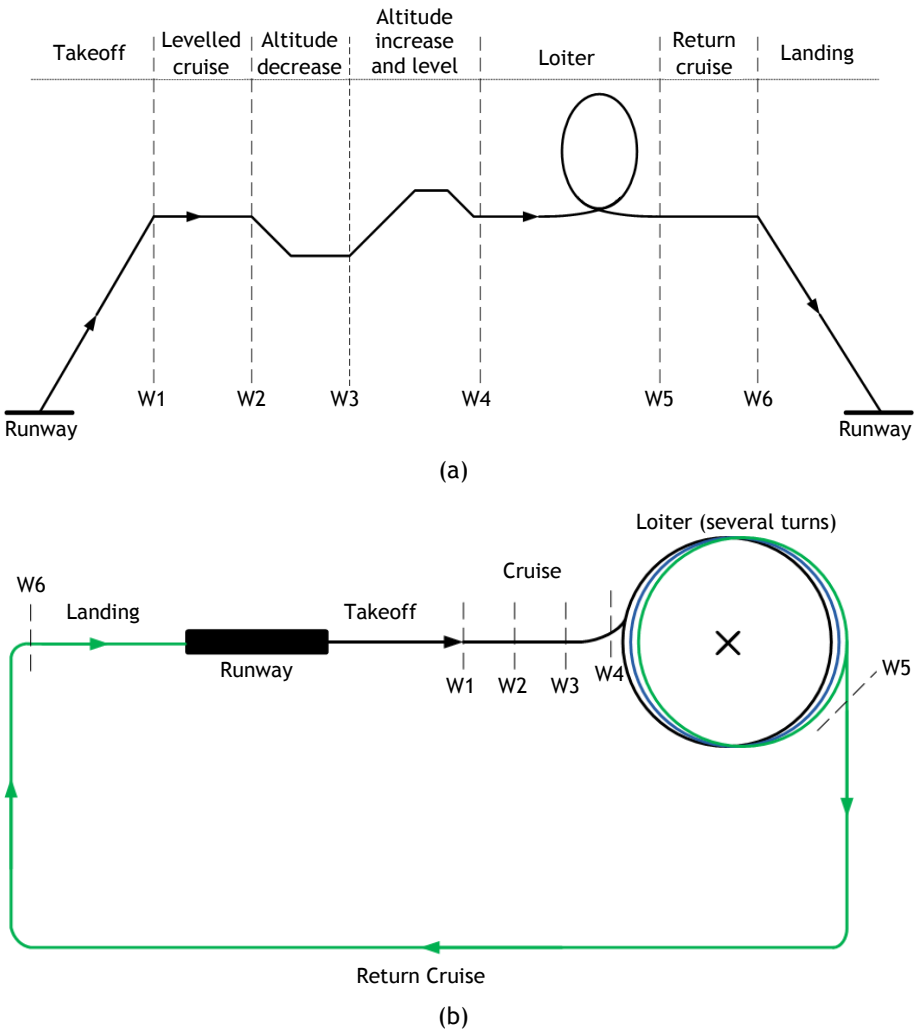

Figure 4.2: Mission profile used in CHANGE project: (a) schematic view and (b) viewed from above.

- Altitude decrease - After reaching waypoint W2, a decrease in altitude is performed. The aircraft continues in the defined new flight altitude until waypoint W3.

- Altitude increase and level - The altitude is increased until one established value. After this altitude is reached, the RPAS continues its levelled cruise flight. This increase and decrease of altitude are a part of the mission in order to demonstrate simple manoeuvre capability of the aircraft utilizing the morphed wing at the high speed state. The phases from W1 to W4 accounts for 7% of total mission time.

- Loiter - Waypoint W4 indicates the start of the loitering phase. The wing morphing surfaces are changed to the adequate position for this phase. The radius of the loiter manoeuvre is fixed at 200 m and the airspeed of this flight phase is 15.3 m/s. This phase accounts for 70% of the total mission time. When the loiter phase is concluded, the RPAS returns to the initial cruise altitude and airspeed, initiating the return cruise.

- Return Cruise - Between waypoints W5 and W6 the RPAS flies with tailwind at the same altitude (1000 ft) and speed (30.6 m/s) of the high speed levelled cruise, in order to return to the runway from where it has taken-off. This flight phase accounts for 17% of the total time defined for the mission.

- Landing - After W6 is reached, the RPAS initiates the descent to the runway with the appropriate heading. The wing changes its form to the adequate shape for the landing manoeuvre. This flight phase is performed in approximate 3% of the total time defined for the mission.

4.4 Baseline Wings Aerodynamic Design

The aerodynamic design was performed by ARA and is shown here due to its importance to the structural design (presented in the next section). A more detailed description of the aerodynamic design procedure used by ARA can be found in [144] and [145].

ARA developed an aerodynamic shape optimization tool to optimize the geometry of a conventional fixed wing for low drag given flight parameters. With this tool, four conventional fixed rectangular wings were designed, each suitable for one of the main design conditions, namely takeoff, loiter, high speed dash and landing. The mission profile and recipient RPAS specifications, drove the aerodynamic design.

4.4.1 Design Methodology

The baseline wings aerodynamic design was performed by ARA using a wing-twist design methodology. It is a design optimization process based on changing the wing-twist of the wing sections, in order to achieve the optimal loading distribution. The description of this methodology is presented in Fig.4.3.

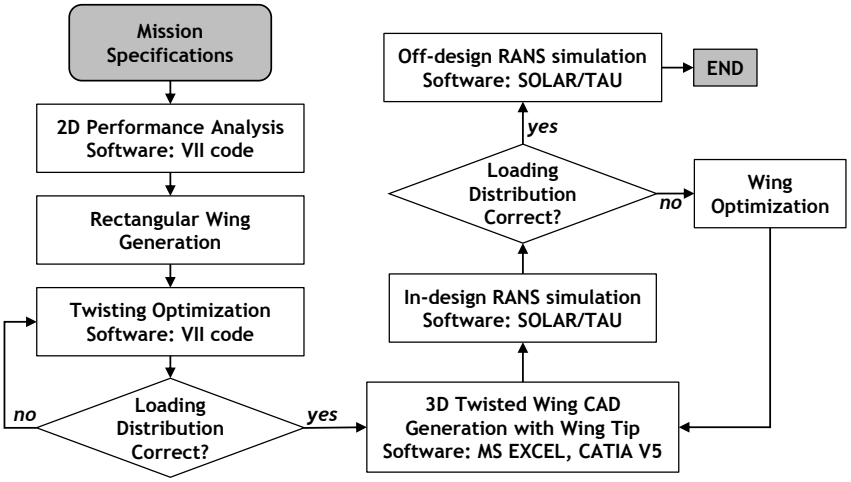

Figure 4.3: Baseline wings aerodynamic design methodology (adapted from [145]).

Referring to Fig.4.3, one can see that the first step was to define the flight phase. Additionally, geometrical and manufacturing limitations must be identified and defined in terms of achievable wing shape. The objective of the optimization process, i.e., maximum endurance, must also be defined at this stage. The second step was the selection of the baseline aerofoil. The software used to select the aerofoil at the design condition was the two-dimensional VII code. This code is used at ARA for the design and analysis of subsonic aerofoils and combines a

high-order panel method with an integral boundary layer method using a viscous-inviscid interaction technique. The selected aerofoil was then used to generate a simple untwisted rectangular wing. The rectangular wing was then divided along the spanwise direction into a predefined number of sections to perform the optimization process with the three-dimensional VII code. The number and the distance between sections were selected according to the complexity of the design. The wing twist was modified in an iterative process until the optimum loading distribution was achieved.

After completing the optimization process the Computer-aided design (CAD) model was generated with DS® CATIA V5 and a wing-tip was added to the design. The latter was added to improve the quality of the RANS results. The new CAD was used to perform a simulation with SOLAR/TAU at the design conditions [146, 147]. SOLAR/TAU is a software toolset developed by DLR and ARA to solve the RANS equations for aerospace applications. If the wing fulfils the design requirements, off-design simulations with SOLAR/TAU are performed to analyse stall characteristics and off-design performance. Both in-design and off-design RANS analysis were performed using the *Spalart-Allmaras* turbulence model. The result of the design process was a wing CAD model with aerodynamic parameters suitable for a specific flight phase.

4.4.2 Design Requirements

All wing designs were constrained to the same chord length, 0.6 m, and the same wingspan limits, 3-4 m, and the same family of aerofoils, NACA 4 digit aerofoils with at least 10% of thickness ratio, to allow all actuation systems to fit within the wing contour, as specified before. The mass of the RPAS was considered constant and equal to 25 kg.

ARA analysed the performance of several aerofoils in the NACA 4 digit aerofoil family, at the design conditions, in order to find the optimal candidate for each flight phase. The software used in this analysis was the two-dimensional VII code. Three aerofoils with different camber values provided the best performance: NACA 2510 for the high speed dash, NACA 3510 for takeoff and NACA 6510 for loiter and landing. All aerofoils trailing edge thicknesses were modified to be 4% of the chord (2.4 mm). The thickness of the trailing edge was chosen to be realistic in terms of manufacturing.

All baseline wings aerofoils were changed to a symmetric aerofoil in the proximity of the wing tip, in order to reduce local lift and consequently approximate better the elliptical loading distribution. Regarding the takeoff wing, the aerofoil was changed from the NACA 3510 to the symmetric NACA 0010. In the case of the high speed wing, it was changed from the baseline NACA 2510 to the NACA 0010. The loiter wing tip section uses the NACA 0010, instead of the baseline NACA 6510.

All wing designs were driven by the minimization of the total drag. In general terms, the total drag can be written as

$$D_{total} = D_{wave} + D_{profile} + D_{induced} \tag{4.1}$$

where, D_{wave} is the wave drag, $D_{profile}$ is the profile drag and D_{induce} is the induced drag.

The first component is zero because of the subsonic flow regime. The profile drag is the sum of form drag and skin friction drag and it is associated with losses in total pressure

and total temperature in the shear layer. The profile drag is the smallest component of the drag in the takeoff, loiter and landing flight phase whereas the induced drag is the dominant drag component. The minimum induced drag is achieved for an elliptical loading distribution. Additionally, the induced drag is inversely proportional to the wing aspect ratio (AR)

$$D_{induced} \propto \frac{1}{AR} \tag{4.2}$$

where $AR = b^2/S$ is the Aspect Ratio. In order to reduce the induced drag, the maximum allowable wingspan of 4 m was used in the design of takeoff, loiter and landing flight baseline wings. The minimum span was selected only for the high speed dash condition, in order to reduce the lift generated by the wing, and consequently, reduce the induced drag and friction drag.

Table 4.2 summarizes all the design parameters of the baseline wings.

Table 4.2: Baseline wings main design parameters.

Wing configuration	Span, m	Speed, km/h	Altitude, ft	Baseline aerofoil	RE	Design C_L
Takeoff	4	76.15	0	NACA 3510	858,013	0.3661
High speed	3	110	1000	NACA 2510	1,210,133	0.2454
Loiter	4	55	1000	NACA 6510	605,067	0.7361
Landing	4	56	1000	NACA 6510	524,567	0.9640

Observing Table 4.2, it is possible to see that the landing wing speed is similar to the loiter speed of 55 km/h. Therefore, ARA did not re-design the wing. The focus was in the reduction of the landing speed, i.e., increasing the target C_L. Note that, the landing speed was computed in order to be 25% higher than the stall speed of the wing.

4.4.3 Design Results

The described wing-twist methodology was applied for each baseline wing and the incidence distribution for each wing was computed. The in-design C_l and incidence distributions are presented, along with off-design $C_L - \alpha$ and $C_D - \alpha$ curves.

4.4.3.1 In-design conditions

Figure 4.4 presents the C_l and incidence distribution of the designed wing in takeoff, high speed dash, loiter and landing configurations.

The designed takeoff wing (Fig.4.4(a)) shows a positive incidence in the root of 0.52° and in the wing tip a negative incidence of -2.0°. The design angle of attack is 1.71° and the lift-to-drag ratio is 21.6. Regarding the high speed wing (Fig.4.4(b)), one can see that, in the wing root, the incidence is positive and has a value of 0.18° and in the wing tip it is negative and has a value of -2.0°. The design angle of attack is 1.59° and the corresponding lift-to-drag ratio is 17.94. The designed loiter wing, seen in Fig.4.4(c), has a root incidence of 1.9° and a wing tip incidence of -3.6°. The design angle of attack is 3.0° and the corresponding lift-to-drag ratio is 19.1. Finally, the landing wing (Fig.4.4(d)), has an incidence distribution that is similar

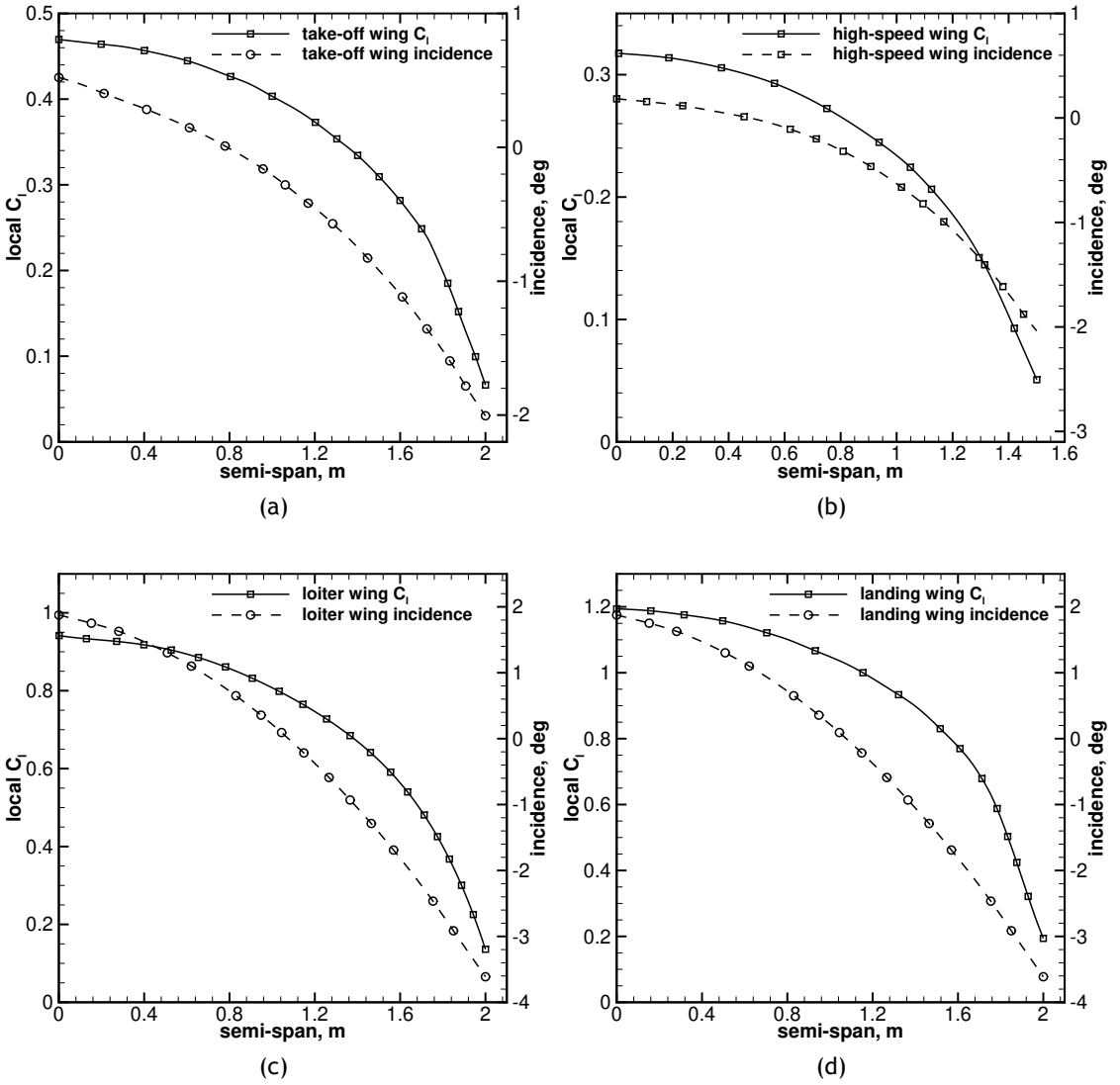

Figure 4.4: C_l and incidence distribution of the designed wings for: (a) takeoff, (b) high speed dash, (c) loiter and (d) landing.

to the loiter wing, since only one wing was designed for the two phases. The design angle of attack is higher (6.37°), due to the higher design lift coefficient and the respective lift-to-drag ratio is 15.84.

4.4.3.2 Off-design Conditions

For each baseline wing, the off-design performance was analysed with SOLAR/TAU running an AOA sequence from -2° to 18°. Both $C_L - \alpha$ and $C_D - \alpha$ curves were computed and are shown superimposed in Fig.4.5. Additionally, the design lift and drag coefficients are shown in the same figure.

Regarding the takeoff wing (Fig.4.5(a)), the $C_L - \alpha$ curve shows that the wing stalls at approximately 17.5° and the maximum lift coefficient is 1.42. The maximum lift-to-drag ratio is 22 at an AOA of 3°. The high speed baseline wing (Fig.4.5(b)) has a lower maximum lift coefficient (1.29). The wing stall is observed around 17°. The maximum L/D is 19 at an AOA

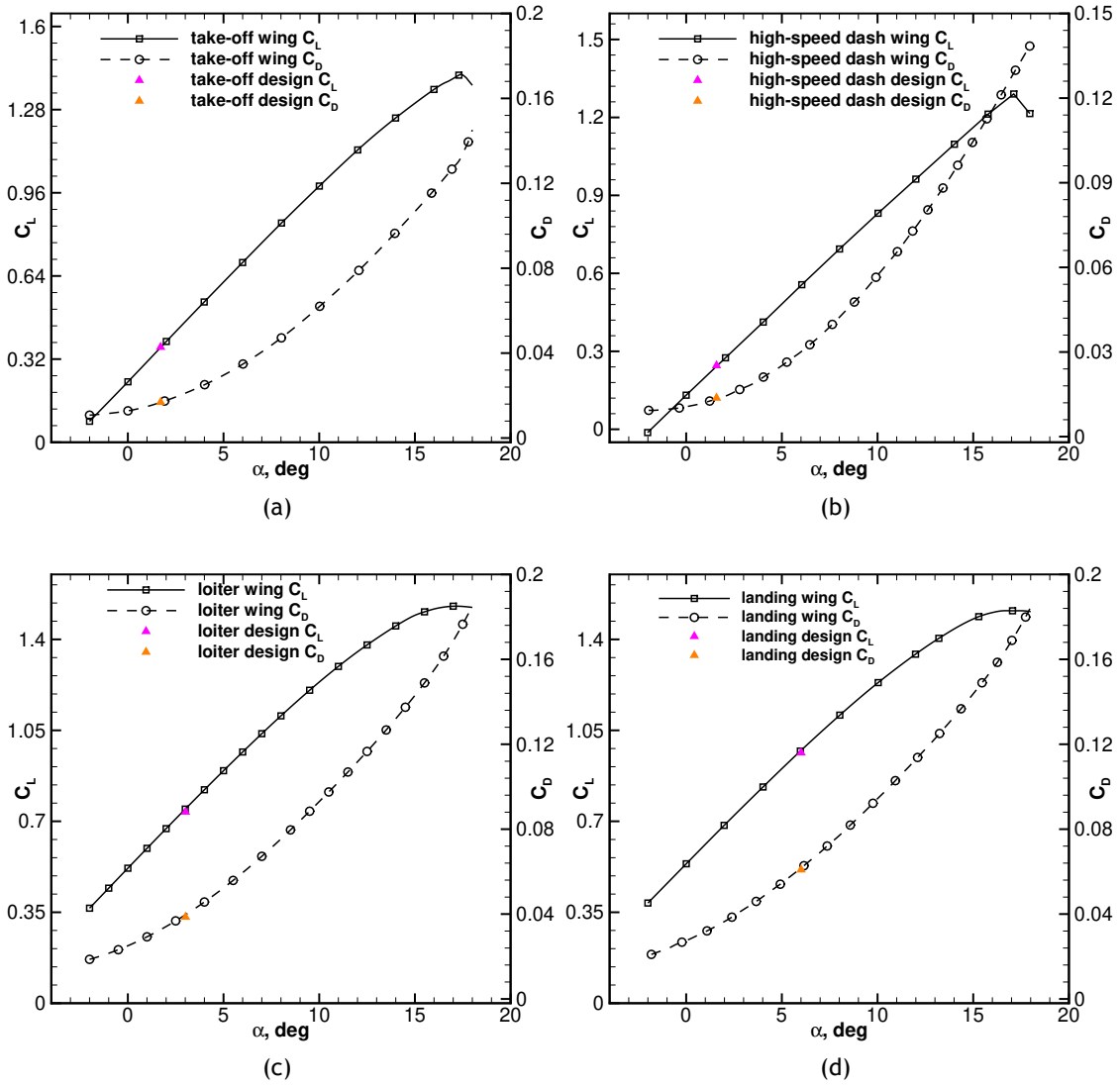

Figure 4.5: $C_L - \alpha$ and $C_D - \alpha$ curves of the designed wings for: (a) takeoff, (b) high speed dash, (c) loiter and (d) landing.

of 3°. The loiter baseline wing, whose curves are shown in Fig.4.5(c), shows a similar wing-stall angle of 17° and a higher maximum lift coefficient of 1.53. The maximum L/D is 20.73 at an AOA of -0.5°. Finally, the landing wing curves, seen in Fig.4.5(d), show the wing stall at approximately 16.5° and a maximum lift coefficient of 1.51. The maximum lift-to-drag ratio is 19.5 at 0.7° AOA. The loiter and landing baseline wings whilst sharing the same geometry, the Reynolds number is lower in the case of the landing wing. This translates in a lower $C_{L,max}$, lower stall AOA and reduced lift-to-drag ratio.

4.5 Wing-box Concept

The morphing wing-box concept arises from the intersection between the geometry changes needed to morph between the different baseline wings and the modularity requirements to facilitate LE and TE development. In more detail, the considered morphing capabilities and

requirements which drove the wing-box concept design are:

1. Wingspan extension: wingspan can vary from a minimum of 3.2 m (80% of the maximum wingspan) to a maximum of 4 m. For just one wing, the above corresponds to a minimum value of 1.6 m to a maximum value of 2 m;

2. Camber morphing: camber morphing is an intentional variation of the camber of the wing section from root to tip. The camber variation is achieved by leading and trailing edge morphing surfaces;

3. Modularity: the wing-box is the core structure of the wing which supports the majority of the bending and torsion loads. The LE and TE surfaces are added to the front and to the rear of the wing-box, respectively, in a manner that does not incur in aerodynamic penalties. The mechanisms, including structure, actuators and wiring, required for the telescopic motion are placed inside the wing-box. The mechanisms of the LE and TE morphing surfaces are placed inside their own structures.

The last requirement facilitated the development of each of the three mechanisms and also made the integration of all parts easier. Also, according to the required shape changes (span, camber and twist), it was possible to divide the wing cross section into three parts: LE surface, wing-box and TE surface. Each part contains its own actuation system within its bounds, such that the telescopic motion mechanism is placed inside the wing-box without restrictions. As mentioned before, in order to guarantee that all the actuation mechanisms can be accommodated inside the wing bounds, a minimum aerofoil thickness of 10% was specified.

Based on the reference wing designs purposely obtained for each of the four different flight conditions and the described design requirements, a morphing concept was proposed. Figure 4.6 illustrates the general wing concept in a schematic form, showing both extended (4.6(a)) and retracted (4.6(b)) configurations.

This concept consists of a two element telescopic wing containing variable camber leading and trailing edges, starting next to the fuselage and extending spanwise up to a region where the moving element of the wing, providing span variation, retracts into. The nomenclature adopted in the previous chapters is maintained. Thus, the fixed element of the telescopic wing-box is called inboard fixed wing (IFW) and the telescopic element of the wing-box is called outboard moving wing (OMW).

Since the most predominant flight phase of the mission is the loiter, the NACA 6510 aerofoil was selected for the fixed cross-section parts of the wing. The other two aerofoils shapes were obtained by decambering the LE and TE devices in the 900 mm length from the fuselage. In this concept, the NACA 0010 aerofoil is used at the wing tip to reduce the local lift coefficient and, consequently, the induced drag produced by the wing with the NACA 6510 aerofoil. A 200 mm distance from the tip was then adopted to transition the NACA 0010 aerofoil at the tip to a inward offset aerofoil obtained from the NACA 6510 aerofoil of the telescopic element. The fully retracted semi-span is 1.6 m with a fully extended semi-span of 2 m, providing 0.4 m of semi-span variation.

By comparing the three aerofoils resulting from the wing shape optimization it was decided to define a rigid wing-box starting at 30% of the chord and extending to 70% of the chord using the NACA 6510 aerofoil as reference because all aerofoils' thicknesses at those positions are the same. Based on this idea, the wing-box made of a composite sandwich skin with em-

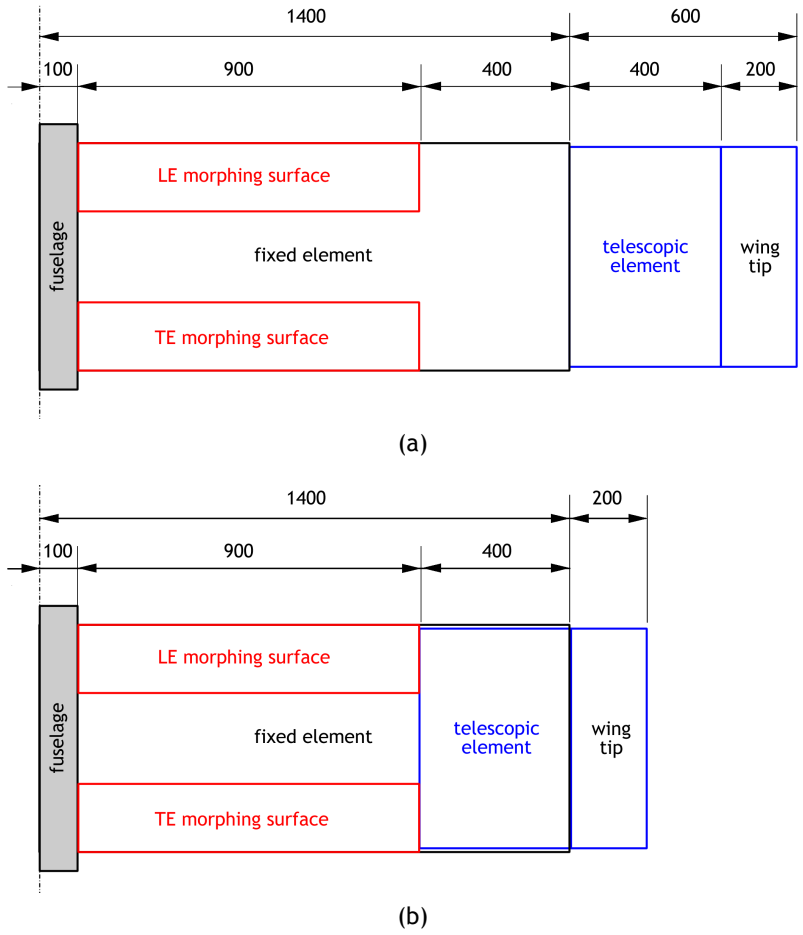

Figure 4.6: CHANGE morphing wing concept in planform view (dimensions in mm): (a) extended configuration and (b) retracted configuration.

bedded spar caps in the corners is shown in Fig.4.7. The wing-box is built in two pieces: the wing-box of the IFW and the wing-box of the OMW which fits and slides inside the inboard fixed part. The webs (vertical elements of the wing-box) of the IFW do not extend its full span. Instead, they are interrupted at 1 m from its root to allow the OMW to retract into the IFW. When fully extended, the OMW wing-box extends towards the wing root to a position 150 mm inboard of the outboard position of the variable camber devices to guarantee all loads from the OMW are properly transmitted to the IFW wing-box. The wing-box is made of only three materials: carbon fibre fabric with epoxy for the faces of the sandwich; PVC foam (Airex® C70.90) for the core of the sandwich; and pultruded unidirectional carbon fibre with epoxy for the spar caps.

Attached to the beginning of the outboard wing-box is a servomotor actuator, which moves with the OMW and actuates it using a rack and pinion transmission. Figure 4.8 clarifies all the components positioning, as well as the adopted actuator methodology.

In order to ensure geometrical compatibility between the IFW and OMW, the aerofoil of the sliding portion was built as a inward offset from the fixed portion aerofoil geometry. This offset is necessary to account for the sandwich skin thickness. This leads to a slightly different geometry of the local aerofoil when compared with the original NACA 6510. The original NACA 6510 aerofoil and its modified version are shown in Fig.4.9. In this figure, the original aerofoil is shown in a solid line and the modified aerofoil in a dashed line. The original NACA 6510 aerofoil

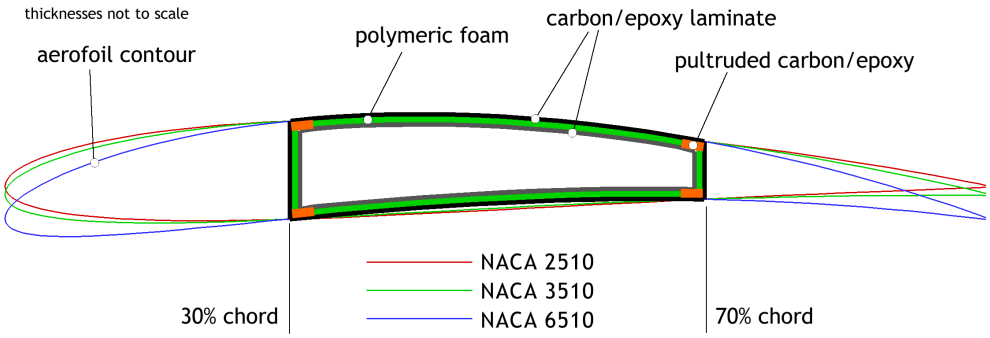

Figure 4.7: CHANGE wing-box section concept.

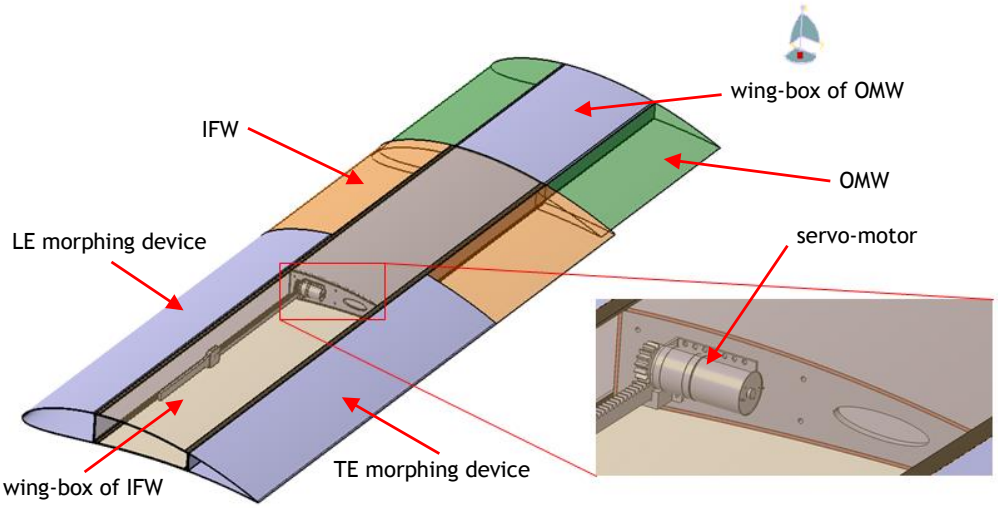

Figure 4.8: CHANGE morphing wing conceptual CAD design, illustrating the main structural parts, as well as actuation mechanism main components and its positioning.

has a thickness ratio of 10% and a relative camber of 6%. The modified aerofoil has slightly reduced thickness and camber, being 9.58% and 5.94%, respectively. Owing to the inward offset of the modified NACA 6510 aerofoil the local chord length of the OMW was reduced to 578 mm from the initial 600 mm.

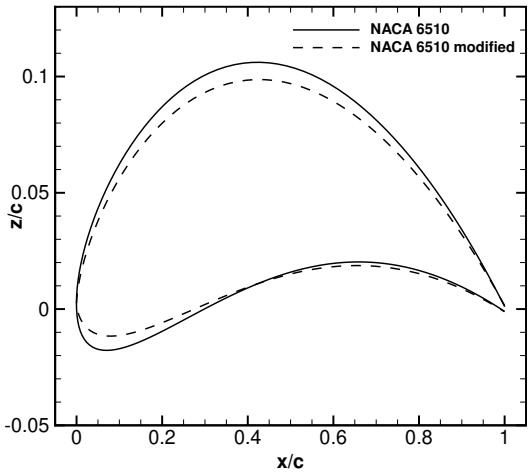

Figure 4.9: Morphing wing-box IFW and OMW aerofoils comparison.

4.6 Wing-box Structural Design

This section presents the results of the sizing of the wing-box structure subjected to bending and torsion resulting from the aerodynamic loads of the four main design conditions considered in the project: takeoff, loiter, dash and landing. The aim of this design is to produce a wing-box that provides the necessary strength and stiffness for all mission phases, within the bounds of the morphing specifications.

The IFW semi-span of 1.4 m shown in Fig.4.6 resulted from the requirements that a semi-span variation of 0.4 m and an aerofoil transition length of 0.2 m at the tip were necessary. This implies that the semi-span length when the wing is fully retracted is 1.6 m. Initially, the tip was only 0.1 m long giving the wing a semi-span of 1.5 m in the retracted configuration. That modification was implemented near the end of the detailed design of the wing thus, the results in the following sections corresponding to the dash wing configuration were obtained for a semi-span of 1.5 m.

4.6.1 Design Loads

Design loads were estimated with the use of the V-n diagram as specified in EASA's Certification Specifications for Very Light Aeroplanes, CS-VLA [148]. This diagram allows to obtain the symmetrical load factor envelope for any given wing configuration as a function of speed. It was assumed that the maximum and minimum manoeuvre load factors in any wing configuration are +3 and -1.5, respectively. The wing aerodynamic data used to compute the load factors were obtained using the off-design performance described in section 4.4. All wing configurations have a mean chord of 0.6 m. The cruise speed for the fully extended wing was assumed to be the already defined takeoff speed. It was also assumed that the minimum lift coefficient (maximum negative value of C_L) was half the maximum lift coefficient. The data required to construct the V-n diagrams are presented in Table 4.3.

Table 4.3: Required data to compute the V-n diagrams.

Wing configuration	Wing area, m^2	$C_{L,max}$	$C_{L,min}$	C_{L_α}, rad^{-1}	Design cruise speed, m/s
Takeoff	2.4	1.415	-0.708	4.368	21.1
High speed Dash	1.8	1.290	-0.645	4.033	30.6
Loiter	2.4	1.528	-0.764	4.256	21.1
Landing	2.4	1.510	-0.755	4.141	21.1

Four V-n diagrams were calculated, one for each of the main flight phases. Figure 4.10 shows the V-n diagram for each flight phase superimposed.

Each diagram is composed of the manoeuvre envelope and the gust envelope. As stated before, the aerofoils used for the takeoff, loiter, dash and landing were the NACA 3510, the NACA 6510, the NACA 2510 and the NACA 6510, respectively. In all cases the wing is fully extended but for the dash case. The critical envelope in every case turned out to be the gust envelope. The obtained four diagrams were superimposed and it was observed that, for the fully extended wing, the critical envelope is that of the loiter case. The dash envelope shows

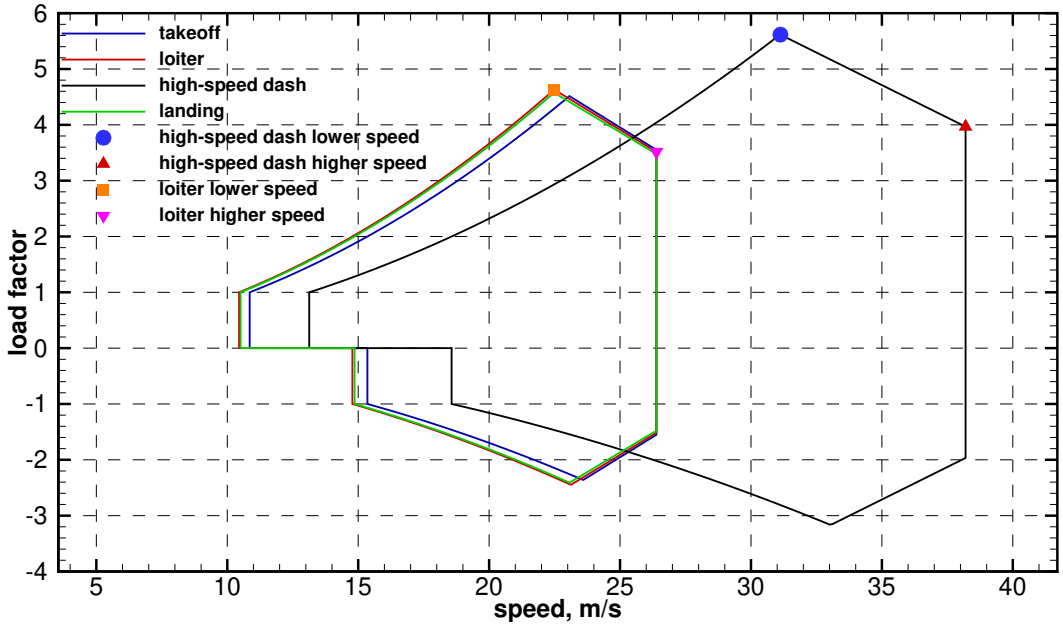

Figure 4.10: V-n diagrams for each of the four flight phases.

higher speeds and load factors and must also be considered in the wing structure sizing because, even though the wingspan is shorter, the resulting bending moment may be higher. For those two diagrams the positive limit load points were extracted, considering a low speed, high load factor and high AOA case and a high speed, high load factor and low AOA case. Therefore, four critical structural sizing points were identified using the V-n diagram. Referring to Fig.4.10, the loiter wing configuration critical cases are highlighted using a square (lower speed) and gradient (higher speed) symbol, and the high speed dash wing configuration, using a circle (lower speed) and a delta (higher speed) symbol.

From the values of speed and load factor, the lift coefficients were calculated. Then, from the $C_L - \alpha$ curves (from section 4.4), the corresponding AOA was obtained and subsequently, drag coefficient and pitching moment coefficient. Note that, due to the unavailability of $C_M - \alpha$ curves, this coefficient was estimated using two-dimensional aerofoil analysis using XFOIL [121]. Finally, lift, drag and pitching moment were calculated for the given speed and wing area. These values are summarized in Table 4.4. Because the negative load factors are much lower than the positive ones those were not used in the wing-box sizing.

Table 4.4: Load cases for wing-box sizing.

	Loiter wing configuration		Dash wing configuration	
	low speed	high speed	low speed	high speed
Speed, m/s	22.5	26.4	31.1	38.2
Load factor	4.63	3.51	5.62	3.97
Lift coefficient	1.529	0.842	1.289	0.605
Drag coefficient	0.17	0.048	0.14	0.035
Angle of attack, deg	17	4.33	17	6.59
Moment coefficient	-0.17	-0.185	-0.02	-0.06
Lift, N	1134.7	861.7	1376.6	972.6
Drag, N	126.2	49.1	149.5	56.3
Pitching moment, N·m	-75.7	-113.6	-12.8	-57.90

Since lift and drag are perpendicular and parallel, respectively, to the free stream direction, they were rotated by the AOA to give vertical and horizontal components, perpendicular and parallel to the wing chord line, respectively. These forces are shown in Table 4.5.

Table 4.5: Loads for wing-box sizing.

	Loiter wing configuration		Dash wing configuration	
	low speed	high speed	low speed	high speed
Vertical load, N	1122.0	862.9	1355.4	972.6
Horizontal load, N	-211.1	-16.1	-283.2	-55.7
Torsion moment, N·m	-75.7	-113.6	-12.8	-57.9

The wing-box sizing was performed based on the loads shown in Table 4.5. It was assumed that the wing-box alone takes all loads resulting from the aerodynamic forces and moments. Other loads, such as structure and systems' weight and any contributions from actuators, were not taken into consideration at this stage. However, the weight of the wing-box itself was considered. The lift distribution shape was determined using the in-design $C_l - b$ curves (presented in section 4.4). The appropriate baseline wings (high speed or loiter) curves were approximated using a fifth order polynomial fitting and then scaled to account for different total lift forces. The lift distributions along the wingspan were used assuming that the shape of the distribution is not affected by the AOA of the wing. Both drag and pitching moment distributions were assumed uniform along the wingspan. Since the wing operates at different AOA, the lift and drag force were rotated to produce a vertical force perpendicular to the wing chord and a horizontal force parallel to the wing chord. The distributions of these forces along the span are represented in Fig.4.11. Clearly, the low speed cases present the higher loads and will result in higher bending and shear forces although the torsion moments have smaller values.

In order to better represent the load distributions along the chord, the initial force system composed of one vertical force, F_V, and one horizontal force, F_H, applied at 25% of the wing chord, and a torsional moment, M, applied at this same location was substituted by two vertical forces, $F_{V,1}$ and $F_{V,2}$, applied at the fore and aft wing-box webs, respectively, and four horizontal forces applied at each spar cap corner, $F_H/4$, as shown in Fig.4.12.

From the force and moment equilibrium, forces $F_{V,1}$ and $F_{V,2}$ are found to be

$$F_{V,1} = F_V + \frac{M + 0.05cF_V}{0.4c} \tag{4.3}$$

$$F_{V,2} = -\frac{M + 0.05cF_V}{0.4c} \tag{4.4}$$

Note that the derived equations were obtained for ratios of the fore and aft spar positions to the chord length of the morphing wing-box of 0.3 and 0.7, respectively. The resultant equivalent forces values are presented in Table 4.6.

The fore vertical load was distributed along the front web of the wing-box, the aft vertical force was distributed along the rear web of the wing-box and the horizontal force was equally distributed by the four spar caps. The equivalent force distributions were calculated from the load distributions of Fig.4.11 multiplied by a safety factor of 1.5.

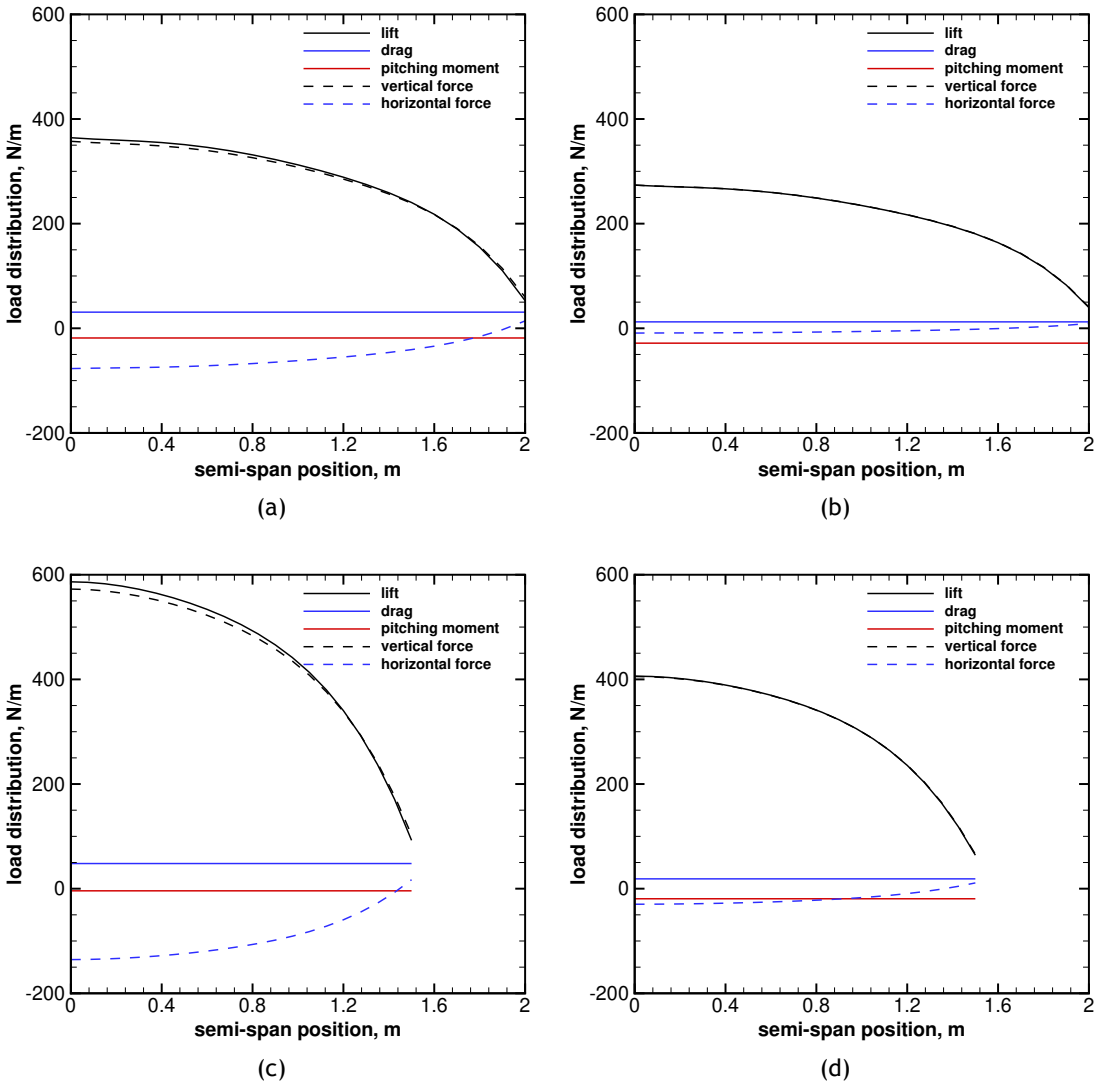

Figure 4.11: Load and moment distributions for: (a) loiter wing configuration at low speed, (b) loiter wing configuration at high speed, (c) dash wing configuration at low speed and (d) dash configuration at high speed.

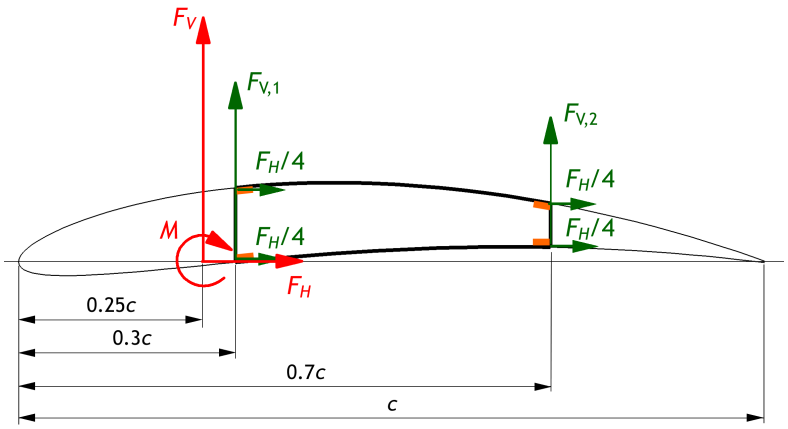

Figure 4.12: Equivalent force system for wing-box sizing (F_V is the vertical force, F_H the horizontal force and M the pitching moment).

Table 4.6: Equivalent loads used in the wing-box sizing.

	Loiter wing configuration		Dash wing configuration	
	low speed	high speed	low speed	high speed
Fore vertical load $F_{V,1}$, N	999.4	422.4	1698.9	914.7
Aft vertical load $F_{V,2}$, N	683.6	872.0	334.2	544.2
Horizontal load F_H, N	-316.6	-24.1	-424.8	-83.5

4.6.2 Materials

As stated before, the wing-box is made of only three materials: carbon-fibre fabric with epoxy for the faces of the sandwich; PVC foam (Airex® C70.90) for the core of the sandwich; and pultruded unidirectional carbon-fibre with epoxy for the spar caps (vDijk high-strength pultrusions). Material properties of the PVC foam and pultruded unidirectional carbon-fibre were obtained from the manufacturer's datasheet [127, 128]. The properties of the sandwich faces were assumed to be for a hand lay-up procedure with vacuum curing and its properties were determined (elastic moduli and ultimate tensile strength) in Chapter 2 (2.5.2).

The properties of these materials are presented in Table 4.7. The pultruded carbon fibre and woven carbon/epoxy were formulated as orthotropic materials and the PVC foam was considered to be an isotropic material. Note that subscripts 1 and 2 denote the direction of the fibre and perpendicular to the fibre, respectively (where applicable), and direction 3 denotes the out-of-plane or interlaminar direction, which was assumed to have the same properties as the perpendicular direction (where applicable).

Table 4.7: Material properties used in the wing-box sizing.

Property	Woven carbon/epoxy	Pultruded carbon/epoxy	Airex® C70.90
ρ, kg/m^3	1500	1600	100
E_1, GPa	46	105	0.084
E_2, GPa	46	7.5	-
E_3, GPa	46	7.5	-
G_{12}, GPa	3.25	3.75	0.040
G_{23}, GPa	3.25	3.75	-
ν_{12}	0.1	0.3	0.05
ν_{23}	0.1	0.3	-
F_{tu1}, MPa	600	1500	2.7
F_{tu2}, MPa	600	50	-
F_{tu3}, MPa	600	50	-
F_{cu1}, MPa	570	1200	2
F_{cu2}, MPa	570	250	-
F_{cu3}, MPa	570	250	-
S_{12}, MPa	90	70	1.7
S_{23}, MPa	90	70	-

4.6.3 Finite Element Model

The analyses of the wing-box for the four design conditions: extended wing at low speed, extended wing at high speed, retracted wing at low speed and retracted wing at high speed,

were performed using ANSYS® Structural APDL [132] with shell elements. An APDL script was written to handle geometry creation, material definition, section properties, meshing, analysis and post-processing.

The objective of the structural sizing was to minimize the weight of the wing-box, subjected to a maximum tip deflection of 0.05 m, a maximum wingtip angle of 5°, maintaining all stresses below the ultimate stresses of the materials and the inverse of *Tsai-Wu* strength ratio [149] below unity to avoid failure. The carbon-fibre reinforced polymer skins were oriented at an angle of $\pm 45°$. It was also assumed that the thickness of a single carbon/epoxy layer is 0.12 mm. All loads were multiplied by a safety factor of 1.5.

Elements SHELL181 were used to discretize the IFW. The sandwich skin was modelled with three layers built as offset surfaces from the aerofoil contour according to their own thickness. These three layers constitute the carbon/epoxy faces and foam core. In the locations of the embedded spar, the foam layer was replaced with rectangular cross-section unidirectional pultruded carbon/epoxy rectangular profiles. Likewise, the OMW was discretized using the same approach. The SHELL181 element is suitable for analysing thin to moderately-thick shell structures. It is a four-node element with six degrees of freedom at each node: three translations in the orthogonal axes directions, and rotations about those axes. This type of element is well-suited for linear, large rotation, and/or large strain nonlinear applications. Additionally, the change in shell thickness is taken into account in nonlinear analyses.

The peculiar structure used in the variable-span wing-box, required the use of contact elements, in order to correctly model the interface. The contact in the overlap surface between the IFW and the OMW was modelled with a shell to shell contact using TARGE170 (target element for 3D geometries) and CONTA173 (contact element for 3D shells without mid side nodes). Since the distinction between the contact and target surfaces was not clear in the interface, a symmetric contact (or "two-pass contact") was used. In this type of contact, each surface is designated to be both a target and a contact surface. Then, two sets of contact pairs between the contacting surfaces are generated. The symmetric contact is less efficient than an asymmetric one, due to the increased model complexity. However, in this particular situation this type of contact had to be used to reduce penetration between contact surfaces. In the performed structural sizing, the behaviour of the contact elements was standard, in order to capture the flexible nature of the contact interface.

The wing-box was considered to be built-in near the root vicinity. Additionally, the centre portion of the inner most rib of the OMW was constrained along the spanwise direction to simulate the constraint imposed by the rack and pinion actuator mechanism and thus avoid outward sliding of the OMW.

4.6.4 Mesh Convergence Study

A convergence analysis was carried out to assess the sensitivity of the maximum tip deflection and rotation as functions of the number of elements used to construct the FEM. Several meshes were created and a static analysis was performed using the "loiter higher speed" loading case and geometry. During this study, the contact between the IFW and OMW of the wing-box was considered to be standard (i.e. flexible). The refinement of the mesh was done by changing the elements size (in both chordwise and spanwise direction) in the finite element script. Figure

4.13 shows the convergence of the maximum wing-box tip deflection and rotation for several grids.

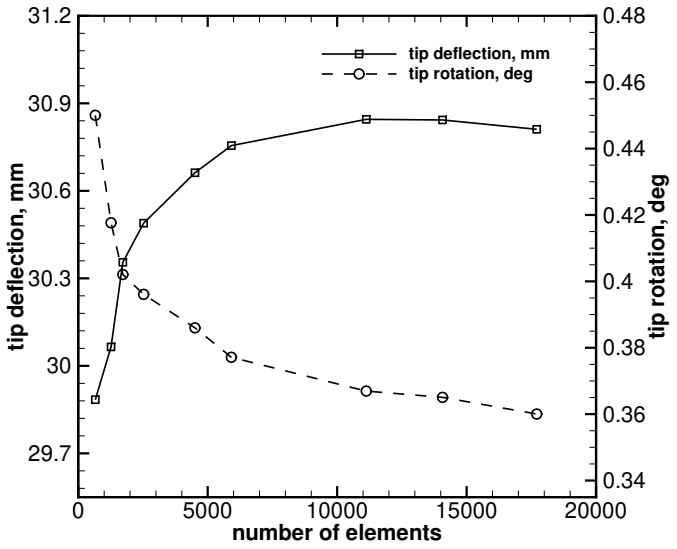

Figure 4.13: Morphing wing-box maximum tip vertical deflection and rotation obtained using different numbers of elements.

Observing Fig.4.13, an asymptotic convergence with increasing number of elements is visible. It is possible to conclude that the solution is for practical reasons converged for a grid with about 11000 elements. In fact, the tip deflection and rotation converges very rapidly until 11000 elements. Therefore, the FEM with approximately 11000 elements was selected for the following analysis.

4.6.5 Deflection and Stress Results

FEM analyses of the four cases given in Table 4.4 with the loads given in Table 4.6 distributed according to Fig.4.11 were performed. Figure 4.14 shows the displacements and Table 4.8 summarizes the maximum values of displacements and *Tsai-Wu* failure criterion for each case.

Table 4.8: Summary of the deflection and failure criterion results, for the various studied conditions.

	Loiter wing configuration		Dash wing configuration	
	low speed	high speed	low speed	high speed
Tip deflection, mm	40.4	31	27.7	18.9
Tip deflection to semi-span ratio	0.0202	0.0155	0.0185	0.0126
Tip rotation, deg	0.31	-0.36	0.6	0.16
Inverse of *Tsai-Wu* (IFW)	0.32	0.25	0.34	0.22
Inverse of *Tsai-Wu* (OMW)	1.12	0.85	1.05	0.72

From Fig.4.14, it is possible to see a displacement distribution which smoothly increases from root (on the left hand side) to tip. In every case, maximum displacements are relatively small compared with the wingspan. Also the twist is quite small. Due to the relative magnitude of the fore web and aft web vertical loads the wing-box twists nose up in all cases except for the

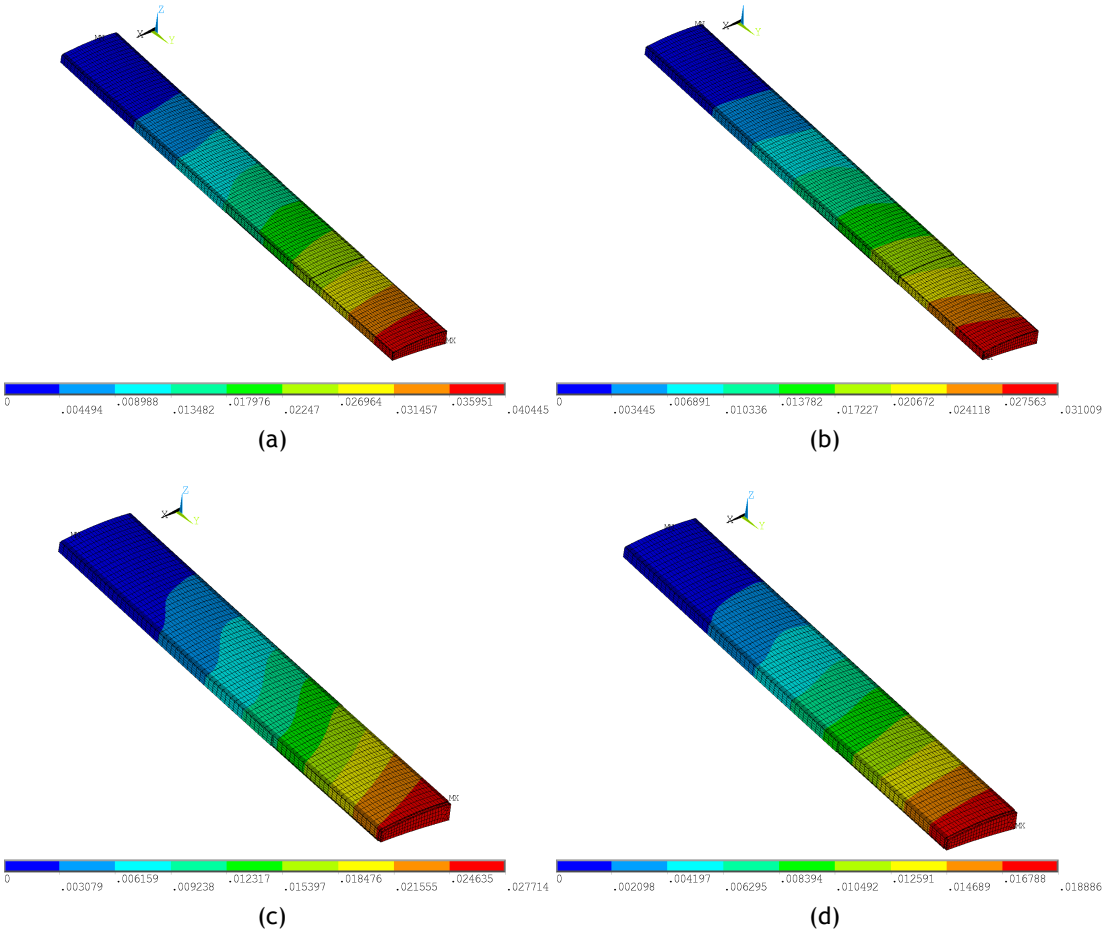

Figure 4.14: Wing-box displacements under design loads: (a) loiter wing configuration at low speed, (b) loiter wing configuration at high speed, (c) dash wing configuration at low speed and (d) dash configuration at high speed (displacements in m).

loiter wing configuration at low speed. This is explained by the higher aft vertical load relative to the fore vertical load of this case as seen in Table 4.6.

In the loiter wing configuration at low speed (Fig.4.14(a)), the displacement reaches a maximum of 40.4 mm. The tip displacement is relatively low, being only 1% of the span. This situation is necessary to allow an even slide of the two wing components. In fact, if the tip displacement were too large, the wing-box mechanism could eventually jam, compromising system integrity and functionality. Maximum twist appears at the wingtip and is also relatively small with a value of 0.31°. This indicates that the wing-box has high torsional stiffness, which will facilitate TE and LE morphing mechanisms integration. In the loiter wing configuration at high speed (Fig.4.14(b)), the tip displacement is inferior to the low speed loiter configuration case with a maximum value of 31 mm (a 25% reduction). Maximum twist appears also at the wingtip, being -0.36°. In the dash wing configuration at low speed (Fig.4.14(c)), the tip displacement is inferior to both loiter configuration conditions, being the maximum value about 28 mm. Maximum twist appears at the wingtip and has a value of 0.6°. In the dash wing configuration at high speed (Fig.4.14(d)), the tip displacement is the smallest of all studied conditions, being about 19 mm. Maximum twist takes place at the wingtip with a value of 0.16°.

Even though the dash wing configuration withstands higher loads, the loiter wing configuration undergoes larger tip displacements, even if comparing the tip displacement divided by

the corresponding configuration's wing semi-span, as seen in Table 4.8. This is a direct result of the larger wingspan of the loiter wing configuration (4 m) which is 33% larger than that of the dash wing configuration (3 m).

In Fig.4.15 the inverse of *Tsai-Wu* strength ratio criterion of the two sections of the wing-box for the loiter wing configuration at low speed is shown for the various material layers: outer sandwich laminate, sandwich core and inner sandwich laminate.

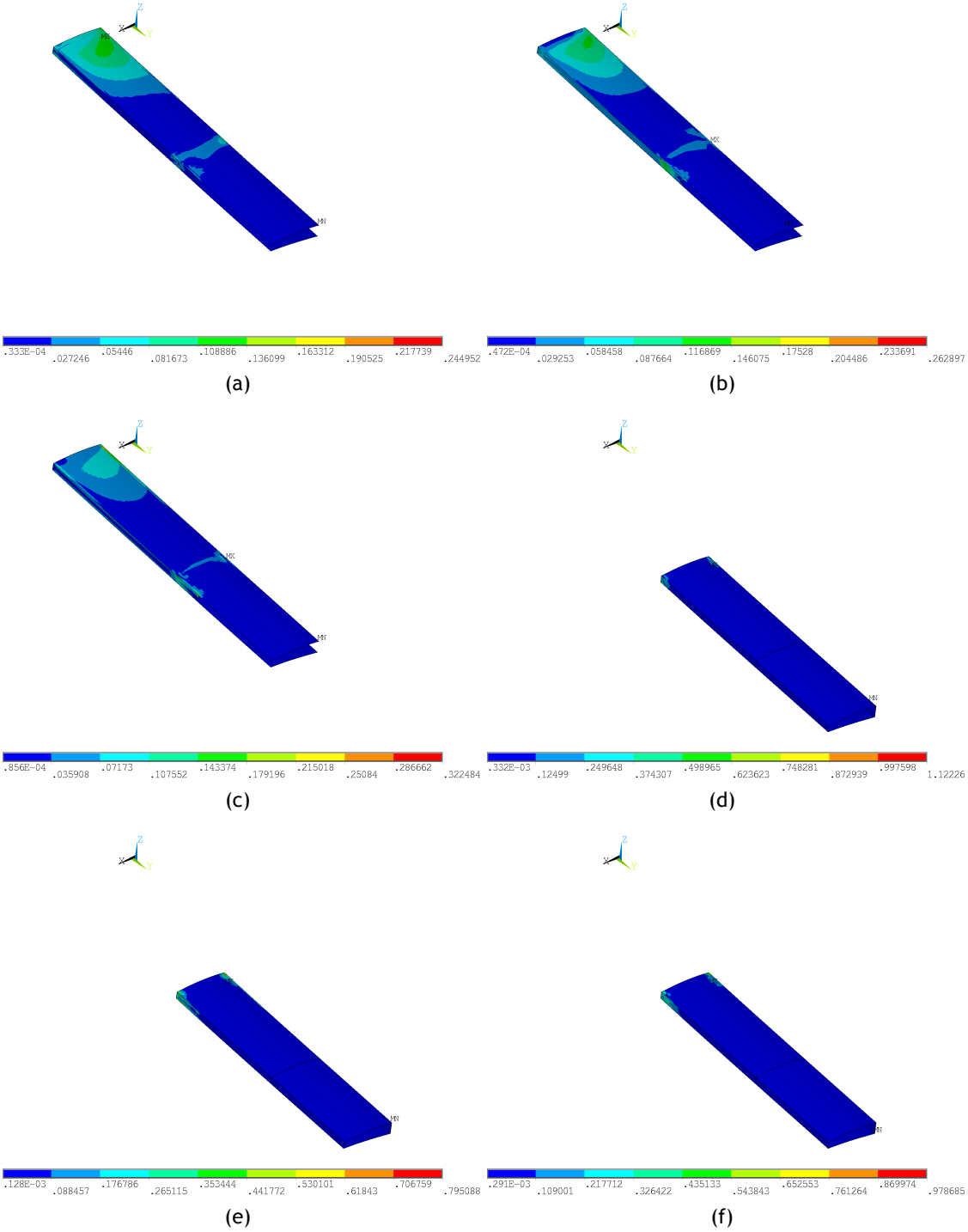

Figure 4.15: Inverse of *Tsai-Wu* strength ratio for the loiter wing configuration at low speed: (a) outer sandwich laminate of IFW, (b) sandwich core of IFW, (c) inner sandwich laminate of IFW, (d) outer sandwich laminate of OMW, (e) sandwich core of OMW and (f) inner sandwich laminate of OMW.

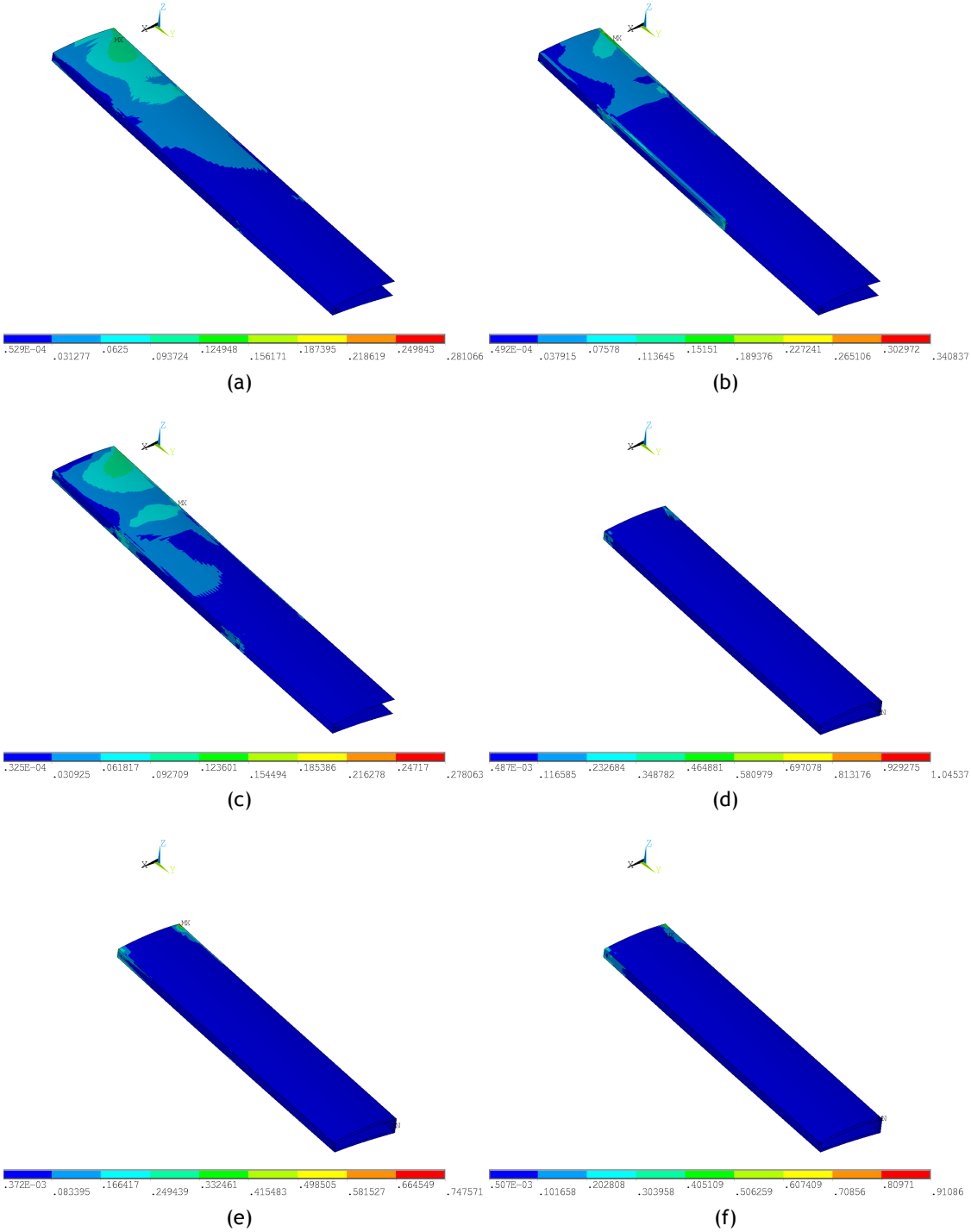

Figure 4.16: Inverse of *Tsai-Wu* strength ratio for the dash wing configuration at low speed: (a) outer sandwich laminate of IFW, (b) sandwich core of IFW, (c) inner sandwich laminate of IFW, (d) outer sandwich laminate of OMW, (e) sandwich core of OMW and (f) inner sandwich laminate of OMW.

The loiter wing configuration at high speed presents lower values of the *Tsai-Wu* criterion and this parameter's distribution is similar to the low speed case, thus, it is not shown. Regarding the IFW (Fig.4.15(a) to 4.15(c)), it is possible to conclude that the fixed wing-box is relatively oversized since the failure criterion never exceeds 0.32. As expected the more stressed areas are located near the end of the wing-box web (at 1 m from root) since this region is supporting the outboard moving portion. The generalized lightly loaded structure results from the fact that

the minimum thickness allowed in the composite laminate is 0.12 mm. With respect to the OMW (Fig.4.15(d) to 4.15(f)), very similar conclusions can be drawn. Again, the more stressed areas are in the contact region between the two wing elements. The maximum inverse of *Tsai-Wu* strength ratio is 1.12 in a localized small area in the outer carbon-epoxy layer near the root of the OMW (smaller than 2 mm^2). In the loiter wing configuration at high speed, the more stressed areas of the IFW are located near the end of the wing box web, as in the previous case. However, the failure criterion is now lower than the previous case and does not exceed 0.25. Regarding the moving portion of the wing-box, very similar conclusions can be drawn. Again, the more stressed areas are in the contact region between the two wing elements. Unlike the previous case study, the maximum value of the failure criterion never exceeds unity, being about 0.85 in the outer carbon-epoxy layer at the root of the OMW.

The inverse of *Tsai-Wu* strength ratio of the two sections of the wing-box for the dash wing configuration at low speed is shown in Fig.4.16. The dash wing configuration at high speed has similar inverse of *Tsai-Wu* strength ratio distributions but with smaller values, thus is not shown. Observing the fixed portion of the wing-box (Fig.4.16(a) to 4.16(c)), it is immediately visible that unlike in the configuration for loiter, the stress concentration near the end of the wing-box web disappeared owing to the OMW being fully retracted. Therefore the area that supports the load is greatly increased and the local bending moments are reduced due to the reduced wing span. Regarding the OMW (Fig.4.16(d) to 4.16(f)), one can conclude that the loading is mainly transferred through the IFW and because of this the loading in the former component is greatly reduced. However, when under load, the IFW reduces its section by a small percentage and that causes a squishing effect on the OMW. In the dash wing configuration at high speed the situation is very similar to the previous condition: the stress concentration near the end of the wing-box web disappeared. Concerning the OMW, the inverse of *Tsai-Wu* strength ratio is well below unity, being the maximum value 0.72.

From the above results it is clear that the wing-box has the required strength and stiffness. In some very small regions the stress intensity is quite high but this can be corrected by using localized reinforcements. The high stiffness is obtained because the minimum laminate thickness assumed is 0.12 mm for practical reasons. This fact also influences the mass of the component. On the other hand, this high stiffness favours the good functioning of the telescopic wing-box because it prevents increased friction between the inside of the IFW and the outside of the OMW that could result due to bending and twisting under load.

4.6.6 Final Design

In summary, the final wing-box sections have the dimensions and materials shown in Table 4.9 and Fig.4.17.

Table 4.9: Wing-box component dimensions and materials for IFW and OMW (dimensions in mm).

Component		Material	IFW dimensions	OMW dimensions
Spar cap	-	pultruded carbon/epoxy	11×2	5×2
Vertical sandwich	skins laminate	woven carbon/epoxy	0.12	0.12
	core	Airex® C70.90	2	2
Horizontal sandwich	skins laminate	woven carbon/epoxy	0.24	0.12
	core	Airex® C70.90	3	2

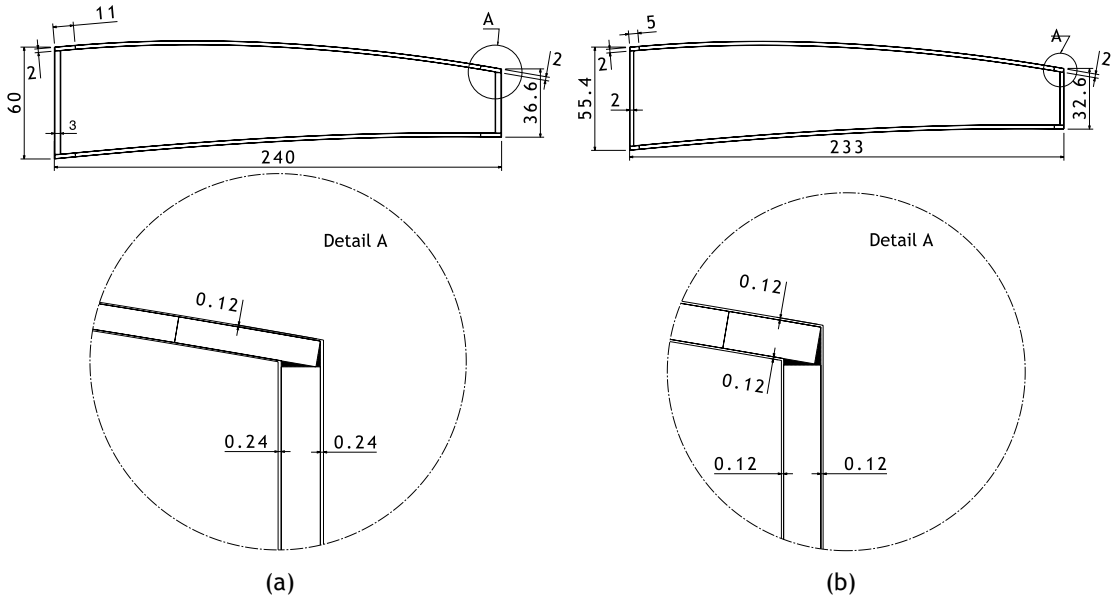

Figure 4.17: Wing-box cross-sections showing structural elements' dimensions (in mm): (a) IFW and (b) OMW.

Figure 4.18 shows CAD models of the variable-span wing-box in (a) retracted configuration, in (b) extended configuration and (c) a side by side comparison of the IFW and OMW.

In the illustrations seen in Fig.4.18, the leading and trailing edge devices and wingtip are not shown for clarity. It is possible to observe the almost seamless interface between the two portions of the telescopic wing and also the very small gap that was created using the current approach. In fact, the discontinuity between the two parts is directly related to the IFW skin thickness. Therefore, minimizing the latter not only helps to minimize the wing-box weight, but also reduces the gap, provided structural strength and stiffness are maintained. Internal ribs were placed at particular wing sections to provide support for the actuation mechanism or to increase skin stiffness in sections of the OMW with the full aerofoil contour. The spanwise double lines observed in Fig.4.18 represent the pultruded carbon spar caps of the wing-boxes which run continuously along the component. The chordwise double lines in the outboard part of the IFW represent unidirectional carbon/epoxy reinforcements inside the sandwich necessary to give the full aerofoil section the necessary stiffness since this portion of the wing does not contain any wing-box webs. These reinforcements were interrupted at the spar caps positions.

Figure 4.19(a) shows the IFW with the outer shell removed. Hence, the PVC foam and unidirectional carbon reinforcements are exposed. It is important to note the unidirectional reinforcements in the chordwise direction at the beginning and at the end of the profiled wing-box. They are important to guarantee the aerofoil shape is maintained under load, since this wing portion is hollow, and consequently has no internal support. The longitudinal pultruded carbon spar caps run uninterrupted from root to tip. The unidirectional chordwise carbon reinforcements are interrupted at the spar caps positions. These may be built during the manufacturing of the sandwich skins by placing various layers of unidirectional carbon filaments impregnated with epoxy resin until they complete the 2 mm thickness of the foam core. Figure 4.19(b) is similar to Fig.4.19(a), with the exception that the unidirectional reinforcements are hidden.

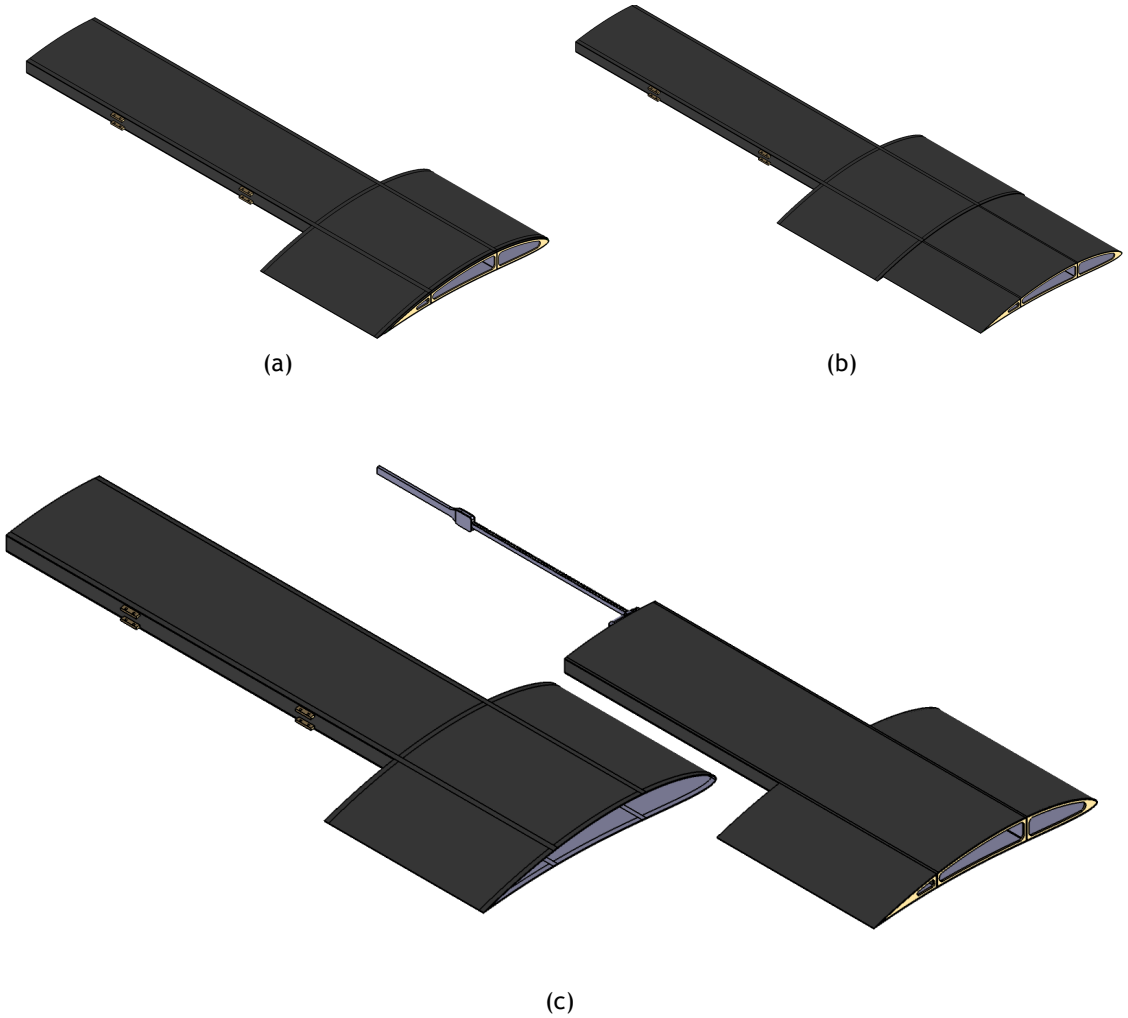

Figure 4.18: Variable-span wing-box in: (a) retracted configuration, (b) extended configuration and (c) IFW and OMW side by side comparison (wing tip not shown).

Therefore, it is possible to see the portion of the PVC foam that needs to be removed to accommodate the reinforcements. In Fig.4.19(c) the reinforcement ribs placed inside the IFW are visible. The rib shown on the left is responsible for supporting the actuation rack (and thus anchoring the actuation system) and the ribs on the right are used to reinforce the skin and close the gap near the tip of the morphing leading edge and trailing edge devices. Both ribs are made from birch plywood.

Figure 4.20(a) shows the OMW wing-box with the outer shell removed. Therefore, the PVC foam and unidirectional reinforcements become visible. Contrary to the IFW (see Fig.4.19(a)), the OMW does not have the unidirectional reinforcements in the chordwise direction, since there are ribs and spar webs inside this component to provide the adequate support. Figure 4.20(b) is similar to Fig.4.20(a), since only the unidirectional reinforcements are hidden. It is possible to see the portion of the PVC foam that needs to be removed to create the slots for the pultruded carbon spar caps. Figure 4.20(c) shows the reinforcement ribs placed inside the OMW. The rib shown on the left is responsible for supporting the actuation mechanism (and thus allowing the whole group to be assembled separately). The ribs in the centre and on the right are used to reinforce and close the section gap near the OMW leading and trailing edge root and tip, respectively. Similar to the IFW, all ribs are made from birch plywood.

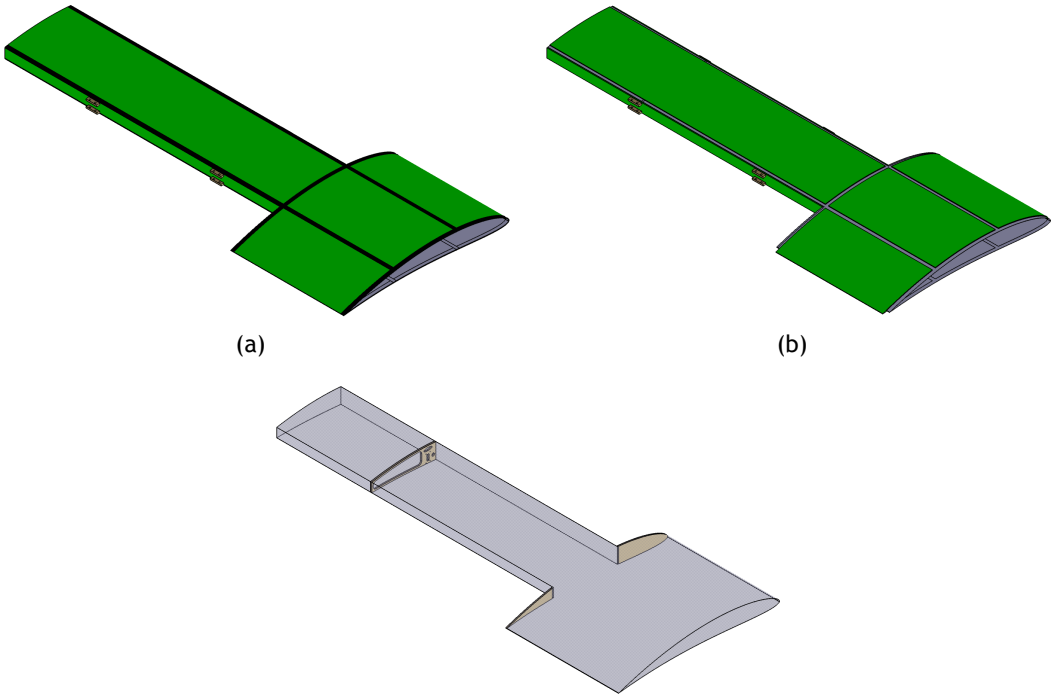

Figure 4.19: IFW internal structure view: (a) outer shell hidden, showing the foam and unidirectional reinforcements, (b) outer shell and unidirectional reinforcements hidden, showing the slots in the foam and (c) outer shell, unidirectional reinforcements and foam hidden and transparent inner shell, showing the internal reinforcement ribs.

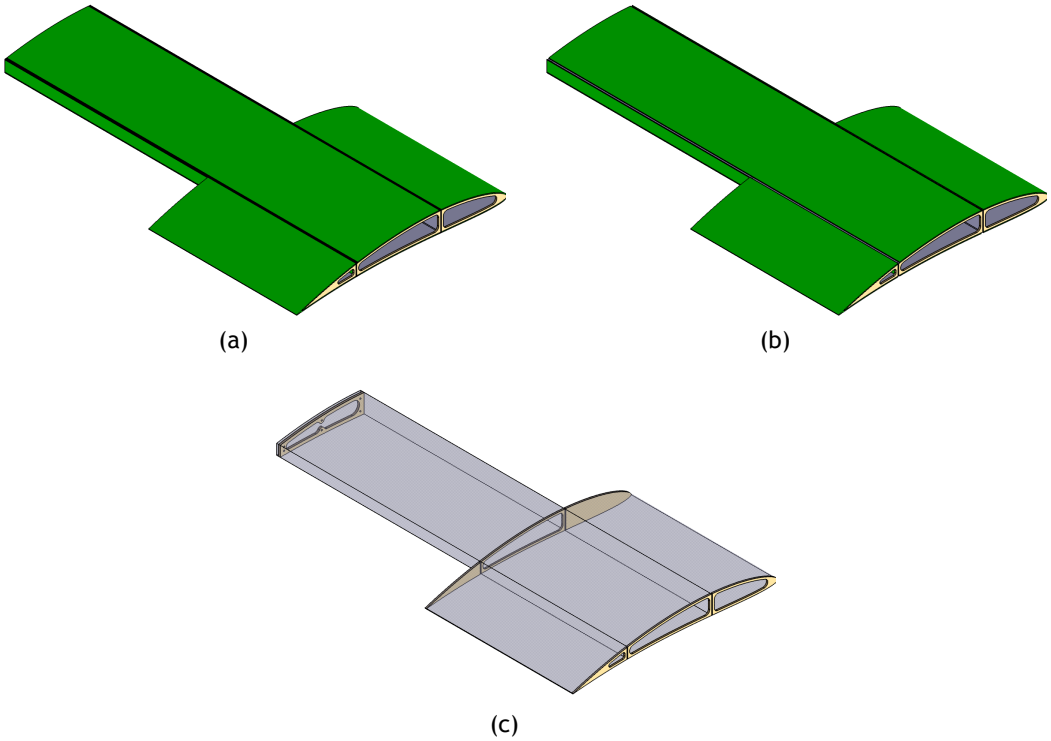

Figure 4.20: OMW internal structure view: (a) outer shell hidden, showing the foam and unidirectional reinforcements, (b) outer shell and unidirectional reinforcements hidden, showing the slots in the foam and (c) outer shell, unidirectional reinforcements and foam hidden and transparent inner shell, showing the internal reinforcement ribs (wing tip not shown).

4.7 Wing-box Prototype

After structural sizing, a prototype of the wing-box structure was built. The main purpose of the prototype was to define a suitable manufacturing procedure and to allow the pursuit of ground testing. Additionally, it aided the development, integration and characterization of the actuation mechanism.

4.7.1 Prototype Construction

The built prototype has the full size cross-section model and replicates the entire designed structure of the IFW and OMW wing-boxes, but it has only a spanwise length of 0.608 m. Due to material availability at the time of manufacturing, a sandwich core thickness of 3 mm was used instead of the original design thickness of 2 mm, though the material was the same.

It was decided to manufacture the wing-box in two parts, upper and lower, divided at mid web position, in order to facilitate the building procedure. A total of four moulds were manufactured, corresponding to the IFW and OMW upper and lower halves. The moulds were milled from high density polyurethane blocks (SikaBlock® M700). A three axis CNC router was used to machine the polyurethane blocks and produce the negative moulds. After the machining process, the moulds were hand sanded using increasingly fine wet abrasive paper, until 2000 grit was reached, in order to remove any milling imperfections and ensure high surface smoothness. Then, a release agent, Easy-Lease [150] from EasyComposites was applied in order to seal the mould surface and avoid the epoxy resin to adhere to the mould surface.

The sandwich skins with embedded spar caps, that constitute each wing half, were manufactured in one-shot using the hand-layup technique and were vacuum bag cured at room temperature. The epoxy resin and hardener used was the Sika® Biresin CR122 and CH122-3[151], respectively. This combination allows a resin potlife of 90 minutes, well suited for the complex hand-layup procedure required to build the wing-box halves. The carbon-fibre fabric used has a surface density of 90 g/m^2 (dry) and is a plain weave (carbon fibre with 50% warp 1K HS and 50% weft 1K HS). The pultruded CFRP rectangular profiles are manufactured by *vDijk Pultrusion Products* (DPP). Figure 4.21(a) shows one wing-box half after the vacuum being applied and Fig.4.21(b) after removing all the vacuum bagging tooling.

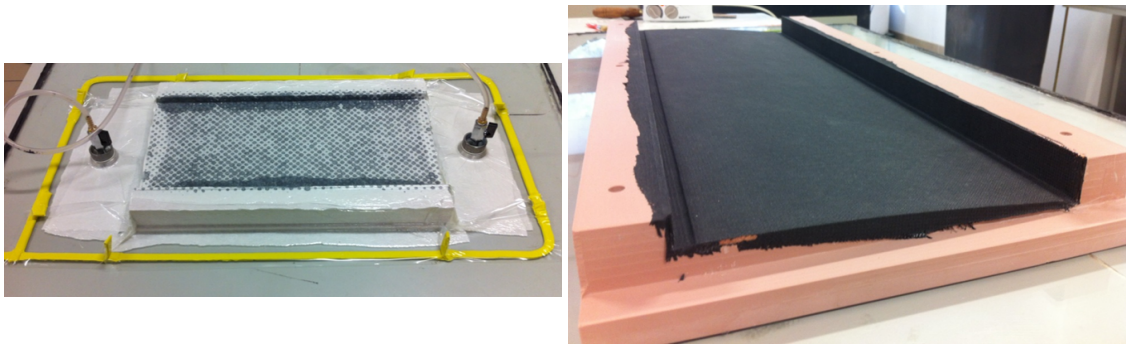

(a) (b)

Figure 4.21: Prototype manufacturing showing the wing-box half: (a) after applying vacuum and (b) after removing all the vacuum bagging tooling.

After curing, the two wing-box halves were bonded together using epoxy glue along the webs. The bonded interface was reinforced with two carbon/epoxy laminated layers, one inside and another outside of each wing-box web. Effectively, the two wing-box halves become a single part after manufacturing. Figure 4.22 shows the wing-box after the bonding process.

(a) (b)

Figure 4.22: Wing-box prototype manufacturing: (a) OMW with the halves glued together and (b) IFW and OMW side by side.

4.7.1.1 Lessons Learned

Some key conclusions were extracted from the prototype construction. On one hand, good geometric accuracy needs to be achieved in order to allow seamless fitting between the fixed and moving wing-boxes and to achieve the required aerodynamic performance. On the other hand, bonding areas should be avoided near the wing-box corners to guarantee the correct shear load transfer around the corners of the wing-box where the spar caps are inserted.

Due to the sliding nature of the OMW, tolerances in the overlap region are critical. It is expectable that some thickness variations during manufacturing of the IFW occur. Therefore, the following manufacturing sequence is recommended: build the IFW mould and then manufacture the IFW; then, measurements should be taken from the already made IFW to gather information to update IFW and OMW drawings (if needed) to reflect any slight differences in shape and dimensions; after this process, the OMW mould can be machined and only then this component is built. This procedure ensures correct tolerances with minimal effort.

To reduce the sliding friction between the IFW and OMW, the prototype has thin polytetrafluoroethylene (PTFE) linear bearings bonded to the inner corners of the IFW and to the outer corners of the OMW, as shown in Fig.4.23(b). However, the installation of such linear bearings proved challenging. Thus, in the final design a thin self adhesive PTFE film (3M® PTFE Extruded Tape 5491) was wrapped around the wing-box of the OMW and the linear guides were no longer used.

4.7.2 Actuation System

The actuation system was fully contained inside the wing-box thus avoiding any interference with other components and enabling the modularity of the morphing wing design. Figure 4.23 illustrates the system. The mechanism is composed by a pinion and rack system actuated by a custom developed servo-actuation system. Contrary to the previous developed actuation system, this one was mounted on a plywood rib attached to the OMW skin, moving with the latter. This was possible in the present prototype (and not in the previous one) owing to the extra available space in the wing, due to its larger chord. The rack was connected near the IFW root, using a plywood rib, allowing the servomotor to push/pull the OMW in the spanwise direction.

The custom developed servo actuation system is composed by three main elements: a geared brushed DC motor, a *Pololu Jrk 21v3* motor controller and a 10 turn 5 kΩ potentiometer.

The gearmotor consists of a high-power, 6 V brushed DC motor combined with a 98.78:1 metal spur gearbox. The gearmotor is cylindrical, with a diameter of 25 mm. It is capable of delivering a stall torque of 1.13 N·m and has a no-load rotational speed of 97 RPM, at 6 V. This motor was selected due to its small diameter, facilitating the integration in the small available space.

The *Pololu Jrk 21v3* motor controller is a highly configurable brushed DC motor controller that supports four interface modes: USB, logic-level serial, analogue voltage, and PWM. The controller can be used with feedback for closed-loop speed or position control, or it can be used without feedback as an open-loop speed control. In the current application the controller was used in closed-loop. The position feedback of the wing was achieved using a 10 turn 5 kΩ potentiometer, that is electrically connected to the motor controller board and mechanically connected to the wing rack. The wing position was controlled using a PWM signal, generated using common radio-modelling control systems. The signal is injected in the motor controller board that ensures the wing extends or retracts to the desired wingspan configuration.

In order to keep the weight low, the pinion and the rack were fabricated using an oil filled nylon, *Ertalon LFX*. This material is especially suitable for this type of application because of its low density, yet sufficient rigidity and low friction coefficient. Since the proposed mechanism was only intended to perform wingspan variations (and not roll manoeuvres through wingspan asymmetric variation), the pinion was designed so that the OMW actuation speed was about 100 mm/s. This calculation resulted in a pinion with a reference diameter of 20 mm, for a no-load condition (97 RPM). The maximum available force to move the OMW is 113 N. A modulus of 1.25 was chosen, since it offers a good compromise between the number of teeth that ensures a smooth torque transfer and manufacturing simplicity. The actuation pinion, feedback gear and rack were manufactured to specification using a three axis CNC router.

Figure 4.23 shows the OMW 4 mm birch plywood rib to which the DC gearmotor, the motor controller and the feedback potentiometer were installed. The rib can be easily detached from the OMW by removing six screws, greatly simplifying the maintenance of the actuation components.

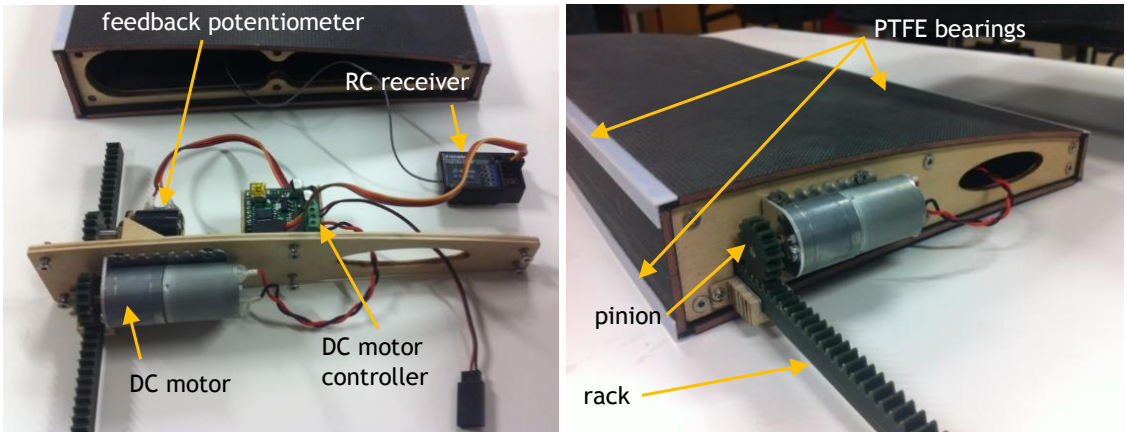

(a) (b)

Figure 4.23: Detailed view of the actuation system: (a) assembled and (b) disassembled.

4.7.3 Mass of Telescopic Wing-box Concept

From the telescopic wing-box prototype and implemented actuation system, the mass of the telescopic wing concept was estimated. Table 4.10 illustrates the mass breakdown of the components that constitute the prototype. The structural components and the actuation system components mass are separated in sub-assemblies to highlight its individual contribution to the overall mass.

Table 4.10: Detailed mass breakdown of one wing-box with telescopic actuation system.

Sub-assembly	Components	Mass, kg
Structure	Inboard wing-box	0.980
	Outboard wing-box	0.621
	PTFE bearings	0.136
	Supporting ribs	0.040
	Subtotal	1.780 (87%)
Actuation System	Pinion	0.003
	Rack	0.043
	DC motor	0.096
	DC motor controller	0.009
	Feedback potentiometer	0.023
	Cabling	0.096
	Subtotal	0.270 (13%)
	Total mass	2.05

The mass of the actuation mechanism is 0.27 kg which represents 13% of the total mass. On the other hand, the structural components represent 87% of the total telescopic wing-box mass, which is approximately 2.1 kg. In this prototype, due to material availability, a core thickness of 3 mm was used in the skin sandwiches instead of the 2 mm initially envisaged. Therefore, the structural mass may be slightly overestimated. The total mass of two fully functional morphing wing-boxes (left and right) without the LE and TE morphing devices would be around 4.2 kg.

4.8 Wing-box Prototype Ground Testing

The developed wing-box prototype was ground tested to ensure system functionality under load. Both structural testing and actuation system testing were performed on the prototype.

4.8.1 Structural Static Testing

The structural static testing was performed in order to verify the stiffness and strength of the wing-box. The testing was carried out in a jig specially developed for the telescopic wing-box. Structural strength and stiffness were verified by applying equivalent vertical loads at the tip, measuring its deflection and comparing with the numerical predictions.

4.8.1.1 Wing Loads

To build the shear and bending moment diagrams, polynomial approximations of the lift distributions were made to obtain the lift distribution as a function of the position along the wing's semi-span. Drag and pitching moment distributions were assumed constant along the span as described in section 4.6. These distributions were replaced by an equivalent force distribution system made up of a vertical force distribution (perpendicular to wing chord) and a horizontal force distribution (parallel to wing chord) applied to the fore and aft webs of the wing-box, at 30% and 70% of the chord, respectively. Figure 4.24(a) shows the calculated distributed forces for various load factors (1.5, 2.5, and 3.5). These loads are representative of the fully extended span since this configuration was found to correspond to the most critical one. Figure 4.24(b) shows the shear force diagram for load factors of 1.5 to 3.5, calculated from the analytical integration of the curves of Fig.4.24(a). Figure 4.24(c) shows the corresponding bending moment diagrams calculated from the analytical integration of the shear force.

4.8.1.2 Experimental Setup

A jig made of rectangular steel tubes was built to provide support for the wing-box prototype and various instrumentation components. The jig structure was sized for both strength and stiffness.

The wing-box prototype was clamped at the root and loaded at the tip, at a distance of 0.608 m from the root, with two forces that produce the same bending moment and shear force at the root as given by the load diagrams of Fig.4.24. The loading was increased or decreased by tightening or untightening the two nuts connected to the structure on the top of the jig, which forced the threaded rods to move up or down. The loads were transferred to the prototype by two pairs of rod end bearings. Each pair is constituted by a rod end bearing and a studded rod end bearing. These ball bearings prevent any moment to be transmitted from the threaded rods to the wing-box. The loads were applied at the wing-box structure near the wing-box webs. A load transfer rib was placed at the tip position to allow for the loads to be correctly transferred to the wing-box prototype. To guarantee that the plywood rib did not move laterally due to wing-box deflection during load application, two plywood strips were bonded onto the upper

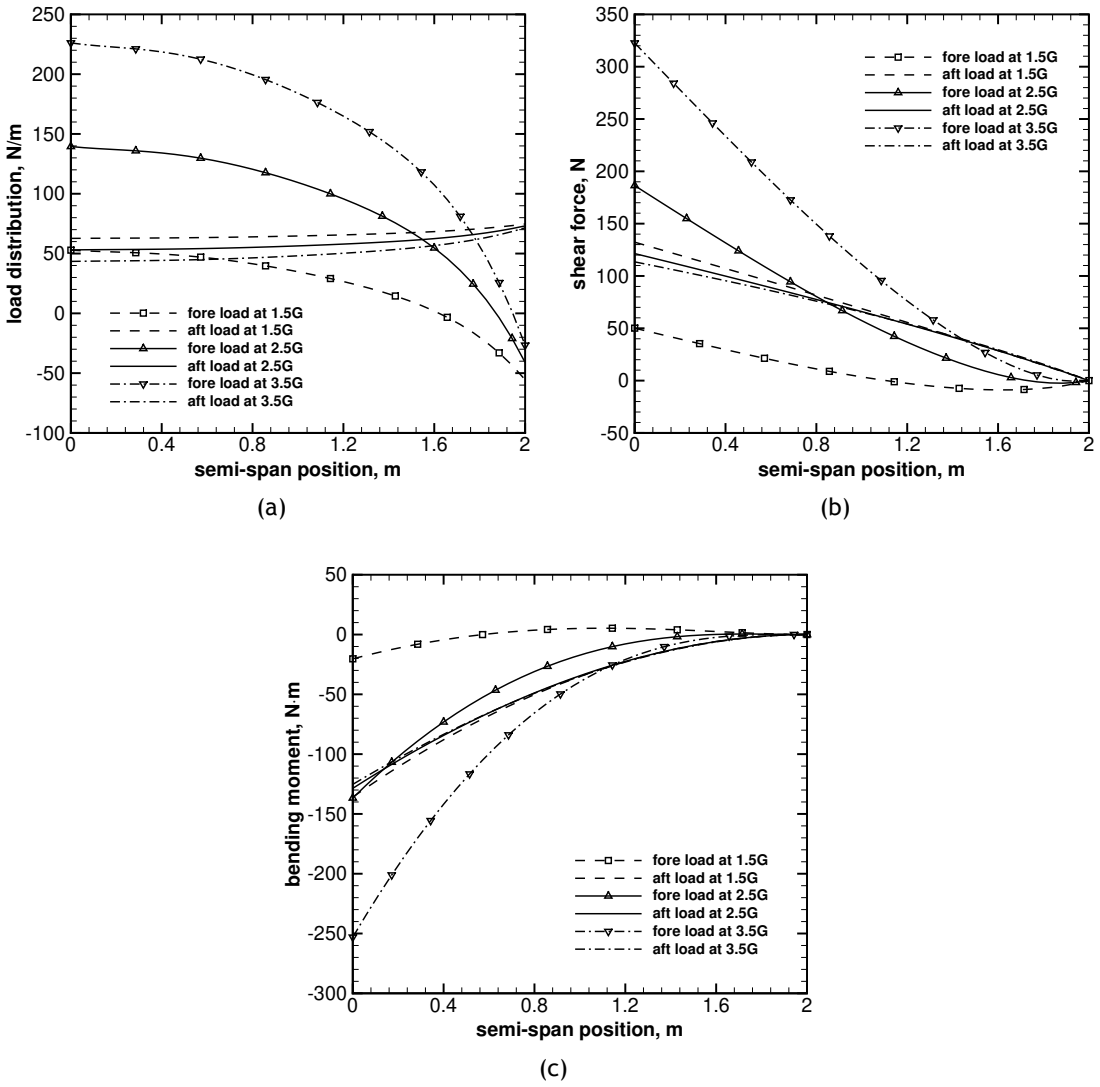

Figure 4.24: Fore and aft load distributions for three load factors: (a) equivalent loads, (b) shear force, and (c) bending moment.

and lower surfaces of the tip section, as seen in Fig.4.25. The load transfer rib, the two pairs of rod end bearings and the load cells are clearly seen in Fig.4.25.

The applied loading was monitored using two load cells Vishay® Model 616 [152]. Figure 4.26(a) shows the load cells used. The load cells were excited and conditioned using a National Instruments® PXI strain gauge signal conditioner [153]. PXI is a rugged PC-based platform for measurement and automation systems. PXI combines PCI electrical-bus features with a modular and expandable design. The applied forces can then be monitored using the LabVIEW® software [154], through a graphical and text interface. Figure 4.26(b) shows the PXI chassis with the strain-gauge conditioner, used to collect the load cell data and, consequently, apply the correct loading.

A comparator gauge dial and a graduated ruler were used to measure the displacements resulting from the fore and aft loads applied at the wing-box prototype. Figure 4.26(c) shows the comparator and the ruler used in the experimental setup.

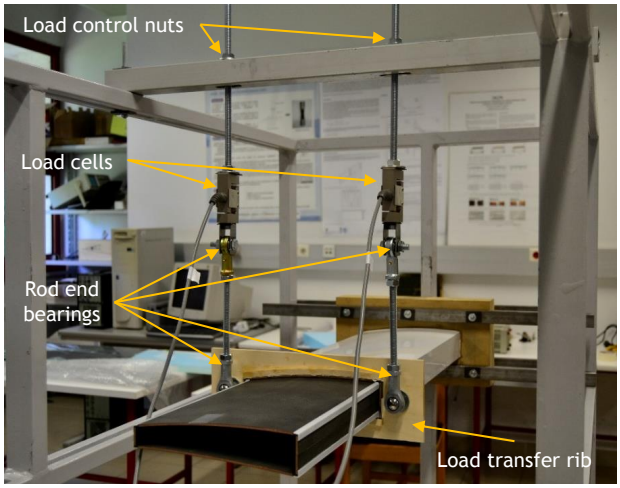

Figure 4.25: Experimental setup used to perform the wing-box static testing.

(a) (b) (c)

Figure 4.26: Components used for data acquisition in the experimental tests: (a) load cell, (b) data acquisition system and (c) graduated ruler and comparator gauge dial.

4.8.1.3 Results

The values of the bending moment at the wing root were recalculated for the position in which they were applied at the wing-box during the experimental test. Table 4.11 summarizes the loads applied at each position. The maximum applied load factor was 3.5, due to safety reasons, i.e., risk of damaging the wing-box's prototype.

Table 4.11: Fore and aft loads applied at the tip of the wing-box prototype.

load factor	fore load, N	aft load, N
1.5	50	132
2.5	186	116
3.5	323	101

Figure 4.27 demonstrates the values collected with the experimental tests representing the maximum deflection according to different load factors for fore and aft loads. Regarding the experimental tests' results, it was expected that the deflection increases, for the fore and rear loading, with increasing load factors. It is possible to see, from the shear force and bending moment diagrams, that the fore and aft loadings increase with increasing load factors and, as expected, this was reflected on the corresponding variation of the displacements.

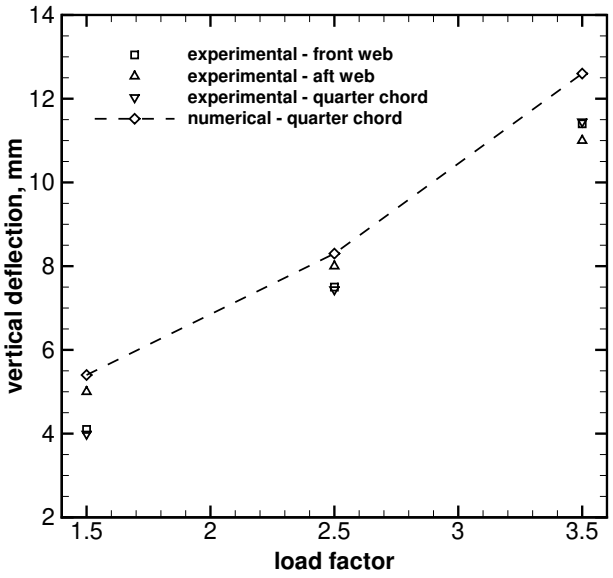

Figure 4.27: Numerical and experimental deflection results at a position of 0.608 m from the wing-box root.

Comparing the numerical model's results with the prototype experimental tests' results, the values are in good agreement. For a load factor of 3.5, the numerical displacement at a position of 0.608 m from the wing root, which is where the loads are applied at the experimental prototype, is around 11.4 mm. This value is close to the obtained numerical result of 12.6 mm. Analysing the vertical deflections for load factors of 1.5 and 2.5, the numerical model's displacements are around 5.4 mm and 8.3 mm, respectively, while in the experimental tests displacements of 4.1 mm and 7.5 mm were registered for the same load factors. The slight increased stiffness observed in the wing-box prototype relative to the numerical model is related to the thicker sandwich core foam used in the manufacturing of the prototype. In fact, due to availability of foam sheets at the time of manufacturing, a foam core thickness of 3 mm was used instead of the initially intended 2 mm.

During these tests, no permanent displacements were observed, since after unloading, the structure returned to its non-deformed state. From these results, it was confirmed that the sizing of the wing-box was correct, according to the operational requirements of the wing.

4.8.2 Actuation System Tests

A series of tests were performed to characterize the newly developed actuation system. The emphasis was on the actuation speed, energy requirements and durability of the electromechanical components.

4.8.2.1 Testing Methodology

Actuation Speed and Energy

This set of tests aimed at measuring the telescopic wing-box speed and energy consumption with varying load factor. To simulate the increasing load factor, the wing-box was loaded

in such a way that the OMW can slide unrestricted inside the IFW during the actuation sequence. For this reason, instead of loading the OMW with a distributed loading, an equivalent concentrated force was placed at the wingtip. This force was calculated so that its moment at the OMW/IFW interface was the same as that of the normal load distribution.

The wing-box prototype was powered using a power-supply in order to guarantee a stable voltage to the controller. A software was developed in C# programming language to control the wing-box and, simultaneously, register the position, voltage and current. This software interfaces with the *Jrk* motor controller using the *Pololu* USB software development kit. It allows the user to configure the intended span variation and the number of cycles to be performed. The former was particularly important, since it allowed averaging to be performed across a number of extension retraction cycles during the post-processing of the data. The data was recorded with a frequency of 60 Hz. Figure 4.29 shows a screenshot of the developed software and Fig.4.28 shows the complete testing assembly.

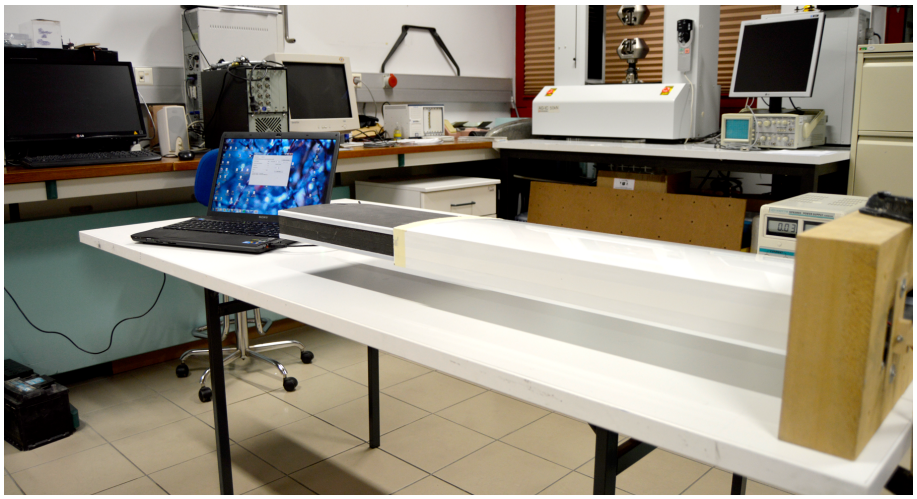

Figure 4.28: Experimental test assembly used in the determination of the actuation speed and specific energy, showing the computer with controlling and recording software and power source.

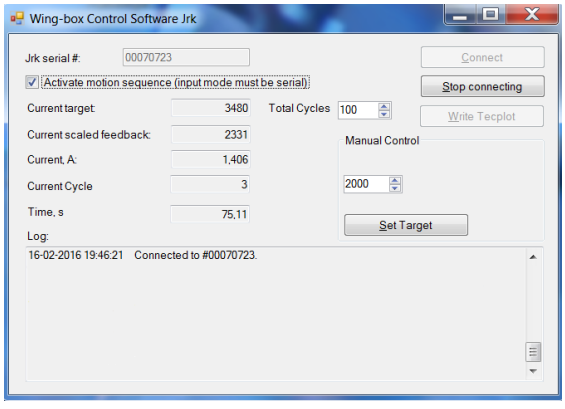

Figure 4.29: Screenshot of the software developed to control the wing-box and record all the data of interest.

The recorded data was later post-processed to compute the instantaneous power, actuation speed and energy. The actuation speed was computed by differentiating the spanwise

position with respect to time. Thus

$$V_{act,wb} = \frac{dy}{dt} \tag{4.5}$$

The energy was computed by integrating power (current $\times$ voltage) over the time necessary to complete an extension or retraction. Thus

$$E_{act,wb} = \int_{t_i}^{t_f} P(t)\, dt \tag{4.6}$$

The derivative and the integral were evaluated numerically using a second order central derivative and Simpson's rule, respectively. The specific actuation energy can be readily computed by diving the energy needed to complete an extension or retraction by the respective displacement. This metric expresses the energy required to actuate the system per unitary length.

Durability Tests

In order to guarantee reliable operation during the test flights, the actuation mechanism was subjected to stress cyclic tests. The testing methodology considered 1000 cycles of extension/retraction to suffice, since it is not planned to perform roll control using asymmetric span deployment. Therefore, considering the proposed mission profile (see section 4.3.2), only two complete extension/retraction cycles are expected to take place during the entire flight.

In more detail, the testing procedure consisted of a qualitative and quantitative assessment. The purpose of qualitative evaluation was to ensure that the overall system's functionality was maintained. In the quantitative testing, the main purpose was to find any evidence of wear or premature failure. Several parameters were evaluated: electric motor shaft for axial slack, rack and pinion for teeth wear, and sliding rails for thickness reduction (which would increase the wing-box slack).

4.8.2.2 Results

Actuation Speed and Energy

Figure 4.30 shows the actuation system speed in cm/s and the specific actuation energy in J/cm, as functions of the load factor.

Observing Fig.4.30, it is possible to see that the energy required to actuate the system increases with the load factor. Contrarily, the actuation speed reduces as the load factor is augmented. This was already expected, since increasing the load factor increases the friction force between wing parts and hence the servomotor has more difficulty in overcoming the increased force. The reduction in the servomotor speed is explained given the torque-speed (RPM) curve. In fact, as the motor increases RPM, its torque reduces. Therefore, as the friction force increases, more torque is necessary to keep the OMW moving and, consequently, the DC-motor is forced to reduce speed.

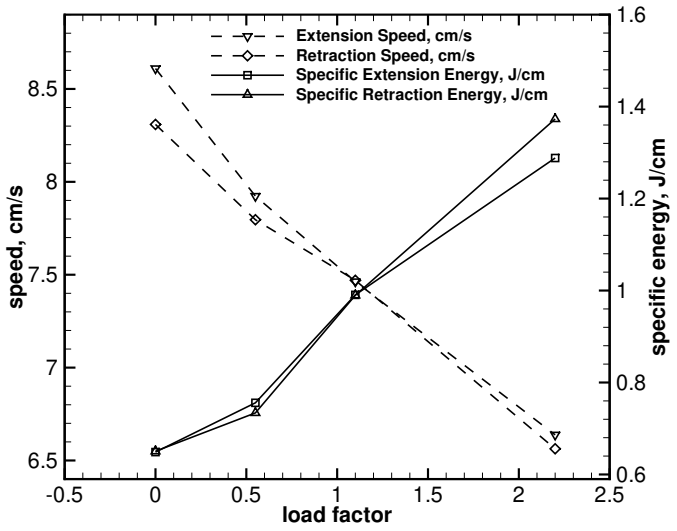

Figure 4.30: Actuation energy and speed results of the wing-box with varying load factor.

Notice that, at the 0G condition, the actuation speed was around 8.5 cm/s, which is lower than the design speed of 10 cm/s. This was due to the fact that the system was powered with 5 V, instead of the nominal 6 V and in a less degree due to the no load friction between the outboard and inboard wing-box.

The total energy required to perform an extension/retraction cycle varied from 65 J/cycle (0.018 Wh/cycle), at no load condition, to 120 J/cycle (0.033 Wh/cycle), at the higher tested load factor (value of 2.2).

Durability Tests

The durability testing was performed for a total of 1000 cycles. It was verified that system's functionality remained normal during those 1000 cycles. It was not possible to identify any type of wear or tear on the rack, pinion or PTFE linear bearings. Regarding the electric motor, there was an increase in the radial play of the shaft, due to some wear of the sleeve bushing that supports it. After the total number of cycles the radial play increased by 0.15 mm, being 0.2 mm. However, this did not cause any problems during the actuation of the VSW. This effect could be mitigated by using an additional support to the gearmotor axle.

The performed testing emphasized the advantage of using mechanical components made with oil filled nylon. In fact, since those components have the lubricant in their composition matrix, there is no need for external lubrication, which translates into a virtually maintenance free drive train.

4.9 Full-sized Morphing Wing

The full sized morphing wing was built by the CHANGE consortium, in order to pursue ground and flight testing. Most notably, two tests are described in the following sections: wind tunnel testing and RPAS flight testing.

The different partners of the CHANGE consortium investigated two LE and two TE morphing concepts. Each morphing concept has its own auxiliary spar, that serves to support the skins, ribs and actuators of the particular concept. In order to allow a quick and easy change of the LE/TE devices, a "quick to change" interface was developed. The interface was based on flanges bonded to the wing-box fore and aft webs. The auxiliary spar can then be screwed to the flanges. In that way, different concepts can be quickly integrated. Figure 4.31 shows a schematic of the complete full-scale CHANGE morphing wing, highlighting the positions of the LE and TE devices, as well as the span changing portion.

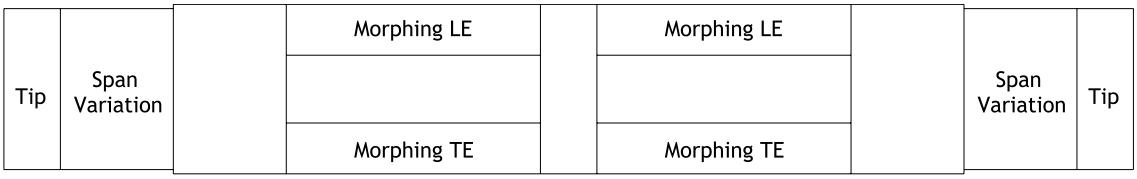

Figure 4.31: Planform schematic view of the complete full-scale CHANGE morphing wing.

4.9.1 Leading and Trailing Edge Morphing Devices

As mentioned before, the consortium investigated different leading and trailing edge morphing devices. In the following paragraphs, these concepts are described succinctly.

The first considered LE concept was developed by DLR (and abbreviated DLR-LE) and is based on the application of a compliant mechanism. The objective of the morphing device was to change from the shape of the high speed wing, that uses a NACA 2510, to the loiter wing shape, that uses a NACA 6510. Therefore, the aim of such concept was to provide the ability to morph between two different aerofoils. Geometric analysis of the aerofoils concluded that they could not be morphed into each other, by solely using a camber variation strategy. Hence, a skin tailoring was implemented to achieve compliance between the two shapes. This optimization delivers the skin thickness at evenly distributed positions around the LE, a stringer position and the deflection at the stringer position. A kinematic actuator was designed using topology optimization. The actuator was manufactured using fused deposition modelling. The load originating the shape change was introduced via an omega stringer and the complete solution was connected to the wing via an auxiliary spar. Figure 4.32(a) shows a cross-sectional view of the LE device. A more detailed description of the LE can be found in [56].

The second LE/TE solution was developed by TU Delft (and abbreviated TUD-LE/TE) and is based on combined twist and camber morphing. This concept was applied to the LE and also to the TE. By cutting the wing skin at both the LE and TE, near the wing-box spar, a slot was obtained, which allows the skin to be actuated. The skin was actuated in the chordwise direction and since freedom of movement exists in the spanwise direction, a combination of twist and camber morphing can then be obtained. Activating two actuators at different span positions with equal displacements results in camber, while differential actuation between the two actuators results in twist. The LE actuation is based on servo-actuators and a sliding mechanism supported by a ball linkage system. In the case of the TE, the sliding mechanism chosen used a straight guide system, due to lack of space (height) for ball linkages. Figures 4.32(b) and 4.32(c) show a CAD view of the described concepts. More information about this concept can be found in [57].

Regarding the trailing edge (TE), two concepts were proposed, studied and designed, as mentioned before. The first one was already described in the previous paragraph, since it is based on the same principle of the combined camber and twist morphing.

The other TE concept was developed by METU (METU-TE) and is based on a hybrid compliant/composite TE. By applying actuation at appropriate proportions to both upper and lower parts of the composite part of the hybrid control surface, camber change was achieved. Since the composite part is much stiffer than the compliant part, the latter stretches, whereas the composite part undergoes a nearly rigid body translation and rotation. By deforming upper and lower compliant parts differentially the upward or downward deflection of the control surface and, hence, the camber change of the wing, can be achieved. Figure 4.32(d) shows a CAD view of the concept, being the different skin parts identified. More information about this concept can be found in [155, 156].

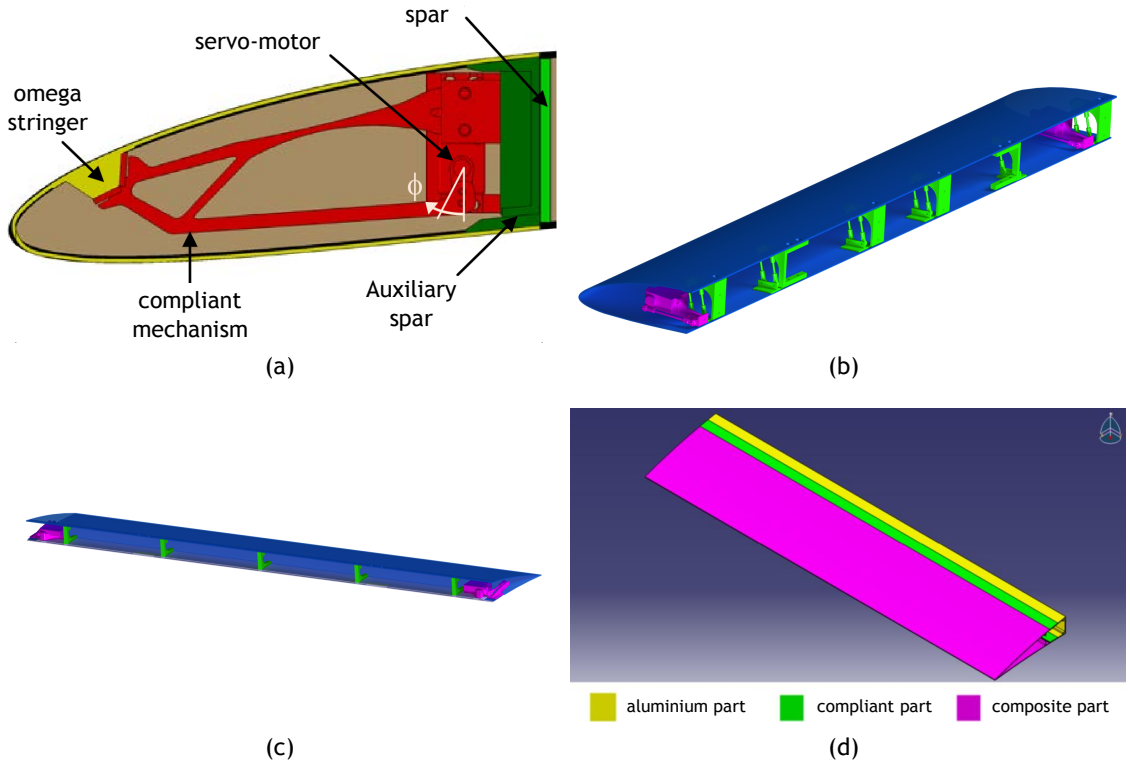

Figure 4.32: Leading and trailing edge morphing devices: (a) DLR trailing edge concept [56], (b) TU Delft leading and (c) trailing edge concepts [57], and (d) METU trailing edge concept [155, 156].

4.9.2 Wind Tunnel Testing

A wind tunnel testing campaign was carried out on the prototype wing to investigate the performance of the different morphing concepts and provide validation data for the CHANGE morphing assessment software. The wind tunnel testing was carried out at the Open Jet Facility of the Technological University of Delft. It is a closed circuit, open jet wind tunnel with an octagonal cross-section of 2.85 m$\times$2.85 m, and an airspeed of up to 28 m/s at ISA conditions.

The wind tunnel model consisted of four components, as highlighted in Fig.4.33: 1) the rigid wing that was used to mount the morphing mechanisms onto, 2) the LE morphing mech-

anism, 3) the TE morphing mechanism, and 4) the wing extension. The LE and TE morphing mechanisms can morph between a NACA 6510 and a NACA 2510, and the wing extension allowed for a wingspan of 1.60 m in the retracted configuration and 2.0 m in the extended configuration.

The wing was tested at two speeds, 15 m/s to resemble the loiter and landing phases (with maximum wingspan) and 28 m/s to resemble the high speed phase (with minimum wingspan). Five different AOAs, between -5° and 10° , were studied in different morphed and unmorphed configurations using the TUD-LE and TUD-TE and the DLR-LE morphing mechanisms, for camber and twist morphing. Note that for technical reasons the METU-TE was not tested.

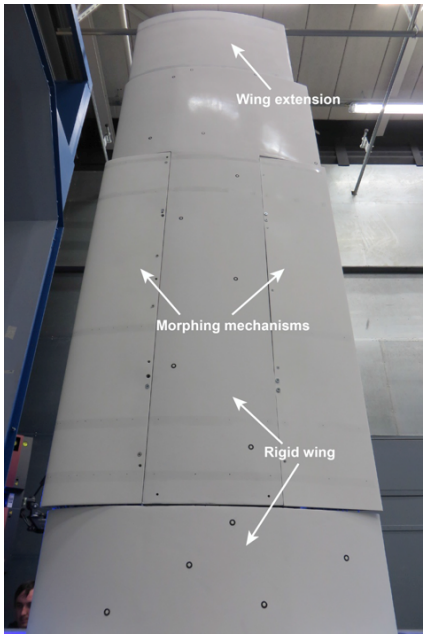

Figure 4.33: Full sized morphing wing prototype installed in the wind tunnel, highlighting its significant parts (photograph courtesy of the Technological University of Delft).

During the wind tunnel campaign, aerodynamic forces and moments were measured using a six component balance. The aerodynamic surface pressures were measured at 8 spanwise locations and up to 23 chordwise locations using pressure taps, and the wing deflections were measured using a 3D digital image correlation system. The pressure taps were connected to several *MEAS* ESP-HD pressure scanners, whose data was collected using the *MEAS* DTC Initium acquisition system. A total of 184 pressure taps were used in the wing prototype. The wing deflection measurements were carried out using an optical measurement system GOM® ATOS, based on fringe projection. The wing was marked with reference points and the system was used to scan the wing surface from different perspectives. Undeformed and deformed wing shape measurements were performed for the low speed condition (15 m/s). More information about the methodology can be found in [157].

No transient measurements were performed. Therefore, the mechanisms were driven to the commanded positions and then, when steady-state flow regime was achieved, the aerodynamic and deformations measurements were performed. The aerodynamic forces and moments and the static pressure data collected from the experiment showed that a similar trend exists between the experimental data and the numerical data computed by ARA. Regarding the deformation measurements, it was concluded that only the TUD-LE was capable of reaching the

required target shape in the wind tunnel measurement. Therefore, further investigation of the other concepts is required to identify what needs to be improved to guarantee that the correct target shape is achieved. Therefore, the TUD-LE concept was preferred to proceed to the flight testing. Nevertheless, the morphing wing was capable of withstanding the aerodynamic load and, consequently, the structural integrity was maintained.

4.9.3 Flight Testing

The final experimental activity in the CHANGE project consisted on the concept validation using flight testing. TEKEVER was responsible to perform the flight testing. The aim of the flight tests was to demonstrate the feasibility of using a morphing wing that combines multiple morphing mechanisms. The wind tunnel wing was adapted and another wing was manufactured and installed in TEKEVER's DR5 RPAS. The RPAS was already presented in section 4.3.1. Note that the second manufactured wing was a fixed rectangular wing with a plain flap. Thus, the flight testing was conducted with one morphing wing (right wing) and a conventional fixed wing (left wing). The morphing wing used the TUD-LE and TUD-TE.

During the wing manufacturing process TEKEVER adjusted the DR5's power-plant to comply with the increased weight and increased power consumption of the morphing configuration. Figure 4.34 illustrates the DR5 RPAS platform with the CHANGE morphing wing installed, before the flight testing and demonstration activities.

Figure 4.34: TEKEVER DR5 RPAS ready for flight testing (photograph courtesy of TEKEVER).

The platform was flown in RC mode in an aerodrome authorized for this type of operations. In addition to demonstrating the capability to morph multiple areas of the wing in flight, the flight served also to perform a qualitative assessment of the handling qualities of the morphing RPAS. This information is useful for future work and to gain insights into the possible future adoption of CHANGE technologies.

Due to lack of regulation for RPAS flight in non-segregated European airspace, the CHANGE flights took place in an authorized segregated airspace. Furthermore, the runway used was authorized for use by RC planes. All flights took place under Visual Meteorological Conditions (VMC). Regarding the flight plan, actions included non-standard circuits (i.e. right-hand circuits) on the active runway (pointing approximately to 310°). In particular, each flight test consisted in a takeoff, right-hand crosswind leg, right-hand down-wing leg, right-hand base leg, final leg

and then landing.

Flights were executed at a cruise airspeed of 55 km/h. During these flights, a single wing with morphing capabilities was used to validate the developed system. There was no instrumentation in the RPAS. Therefore, the focus of the flight was on demonstrating the feasibility of flying the complete morphing wing and also on the pilot handling qualities assessment. Figure 4.35 shows the TEKEVER DR5 RPAS flying with one CHANGE morphing wing.

(a)

(b)

Figure 4.35: TEKEVER DR5 RPAS flying with one morphing wing during: (a) takeoff and (b) landing (photograph courtesy of TEKEVER).

The handling qualities of the vehicle were assessed using the *Cooper-Harper* rating scale for aircraft controllability. This scale ranges from 1 to 10, with 1 indicating the best handling characteristics and 10 the worst. The pilot compared the flight performance with and without the morphing wing and concluded that the pitch and yaw-axis were good behaved and that roll-axis exhibited some deficiencies, requiring extensive pilot compensation. Overall, the RPAS was rated a 6 in the referred rating scale. Additionally, they concluded that the actuation of the morphing mechanisms was not sufficient to control the bank angle of the RPAS. Notice that the RPAS flew with only one morphing wing. This was not a desirable configuration and it negatively affected the flight testing results.

4.10 Concluding Remarks

Under the CHANGE project a morphing wing concept was required to achieve at least three types of shape changes, namely, span, camber and twist, in order to adapt its performance to different flight conditions of a RPAS. To respond to that requirements, a telescopic wing-box

concept was proposed and developed to allow span variations through an actuation mechanism contained within its bounds and to receive third party leading and trailing edge morphing devices.

The telescopic wing-box concept underwent several phases during its development process, including structural layout definition, finite element structural analysis, prototype manufacturing, structural loading tests and actuation mechanism tests. The selected materials and structural layout and the performed structural analyses led to a functional design, in terms of span actuation, and a lightweight structure with adequate strength and stiffness. Testing of the wing-box prototype validated both the structure performance and the actuation mechanism capability and durability. The structural static testing showed similar trends, when compared with the numerical predictions, which indicated the correctness of the numerical predictions and building process. The actuation mechanism was characterized in terms of actuation speed and specific energy consumption and it was concluded that it functioned within its designed specifications. Durability testing showed that the system outperformed the specifications and was capable of reliable functioning for at least 1000 extension/retraction cycles. Manufacturing techniques assessment for the single cell sandwich skin wing-box were also possible along with the prototype development, as well as detailed mass predictions of the full-scale wing model.

A full-scale morphing wing using the developed modular concept was successfully build by the consortium and the leading and trailing edge concepts from the different partners were integrated in a single wing. The concepts were validated using wind tunnel testing and flight testing. The wind tunnel testing confirmed that the morphing wing was capable of withstanding the aerodynamic loading. Hence, structural integrity was maintained in all studied situations. The concept validation using flight testing was carried by TEKEVER and showed that the span changing wing-box modular concept works reliably. Unfortunately, the flight testing campaign was not sufficiently detailed, which severely limited the conclusions that could be extracted. Additionally, only qualitative assessment was performed, which is highly subjective and prone to error. No flight data was recorded and a comparison flight with a baseline wing was not executed. This would have been of utmost importance to create a benchmark flight whose morphing wing could be compared to.

Chapter 5

Variable-span Wing Mass Model

5.1 Chapter Overview

In the past chapters the idealization, design, building, ground and flight testing of two telescopic VSWs was described in detail. The work performed so far clarified, without doubt, that variable-span morphing wings are promising and feasible methodologies, in terms of extending aircraft flight envelope and/or increasing performance. The previous chapter showed that different morphing technologies may coexist in the same wing. The studies of the previous chapters also highlighted that morphing concepts present an undesired mass increase due to their inherent complexity, both in the load carrying structure and in the actuation system responsible to perform morphing. This can potentially limit or even negate any performance benefits, depending on the intended flight mission and/or aeroplane type.

As discussed in section 1.3 of chapter 1, simple and sufficiently accurate mass prediction methods for designing morphing wings at the conceptual design phases are rare. Therefore, the benefits that one morphing strategy can offer over another or even over a conventional fixed wing are thus quite difficult to assess without resorting to detailed time consuming FEM, normally only performed at the detailed design phase. Consequently, this chapter is devoted to the derivation of a mass prediction model of telescopic wings.

A VSW concept with a trailing edge device is considered, being a middle ground between the work from chapters 2/3 and 4. In fact, the morphing wing-box from the previous chapter, integrated leading and trailing edge devices, whereas the VSW considered here only integrates a trailing edge device. The first step to derive the mass model was to determine the structural mass of the proposed concept for different geometrical and inertial parameters, such as wingspan, wing chord, span variation ratio, flap chord ratio and aeroplane weight. A minimum mass optimization problem with stiffness and strength constraints was implemented and solved for a sufficient number of combinations of the wing parameters, being the design variables, structural thicknesses and widths. A parametric structural FEM of the wing was built in APDL and solved in ANSYS®. Concurrently, the same study was performed for a conventional fixed wing. Using the computed data, mass and mass ratio functions were created by fitting multivariable polynomials: fixed wing mass, VSW mass and VSW to fixed wing mass ratio. The latter was used to ascertain the mass penalization of the adopted morphing concept. Additionally, the effects of various VSW design parameters in the structural mass were inferred and synthesized.

Based on the developed VSW to fixed wing mass ratio polynomial, the mass prediction model was developed. It was created using an existing conventional mass model, which was corrected using the newly developed polynomial approximation. Later, the contributions of the actuation system and the adaptative flap were added. The model was then applied to a telescopic morphing wing, being the mass results compared with the actual mass to ascertain its applicability and accuracy.

One must add that, the performed study is integrated in a new VSW design to be applied in the next generation RPAS: Olharapo 3. This RPAS, similarly to the previous Olharapo 2, is able to use either a VSW or a fixed wing when performing typical missions. The wing designed to the mentioned RPAS served as a reference to the parametric study.

5.2 Olharapo 3

Olharapo 3 is the successor of Olharapo 2. It shares the same features that were important to the success of the previous test flight campaigns, namely, high wing positioning and H-tail configuration. The wingspan has increased to 3.1 m and it is heavier than its predecessor, to allow higher payload, being the MTOW 150 N. The higher payload is important to allow more and better instrumentation and also to allow more batteries to extend the flight time. The wing is composed by a rectangular centre portion and tapered wing tip sections. The tapered portion of the wing starts at a semi-span of 0.6 m (x_{kink}), being the sweep angle ($\Lambda_{LE,kink}$) 9°. The aerodynamic chord (c_a) is 0.284 m, being the root and tip chords, 0.33 m and 0.18 m, respectively. The propulsion system is, again, a pusher type but the electric motor is now installed at the end of the tail boom, meaning that no transmission shaft is used. This increases propulsion system efficiency, as well as, reducing weight and complexity. The main specifications of Olharapo 3 are identified in Table 5.1 and Fig.5.1 shows a preliminary CAD design of the RPAS.

Table 5.1: Main specifications of Olharapo 3 RPAS platform fitted with a fixed wing.

Parameters	Values
MTOW	150 N
b	3.1 m
x_{kink}	0.6 m
Λ_{LE}	0°
$\Lambda_{LE,kink}$	9°
c_a	0.284 m
c_{root}	0.33 m
c_{tip}	0.18 m
Electric motor	Scorpion SII-4025-520 KV
Power source	LiPo 6s2p 24 Ah

Figure 5.1: Preliminary CAD design of Olharapo 3 RPAS.

As mentioned in the brief introduction to the chapter, the VSW that is object of study in this chapter, is to be integrated in Olharapo 3. Therefore, the described platform serves as basis to the current study.

5.3 Variable-span Wing Concept

Similarly to the variable-span wing-box, the morphing wing herein presented relies on a telescopic wing. In this manner, the layout of the VSW concept is based on a hollow IFW that is attached to the fuselage, inside of which an OMW slides actuated by an electromechanical mechanism. This concept consists of a two element rectangular telescopic wing containing a variable camber TE that starts next to the fuselage and extends in the spanwise direction up to the region where the moving element of the wing retracts into. The VSW does not possess ailerons, allowing for structural simplicity and improved aerodynamic performance. Rolling moments could be effectively controlled by asymmetrical wingspan variation.

The shape and size of the VSW reference design was obtained through an in-house computational constrained aerodynamic shape optimization code, aimed at determining the wing mean chord and span values that minimize its drag for the specified mission profile. A detailed description of the aerodynamic optimization procedure is given in [158]. Along with the optimization procedure, two geometrically compatible aerofoils were provided in a way that the OMW slides inside the IFW. The method employed to geometrically offset the aerofoils and determine its aerodynamic performance is fully explained in [159].

The aerofoil was specifically designed for the VSW with the purpose of achieving proper fitting between wing sections and higher overall aerodynamic performance. The new aerofoil, the UBI-03-012 and its modified version are shown in Fig.5.2. In this figure, the original aerofoil is shown in a solid line and the modified aerofoil in a dashed line. The original UBI-03-012 aerofoil has a thickness ratio of 10% and a relative camber of 5%. The modified aerofoil has slightly reduced thickness and camber, being 9.2% and 3%, respectively.

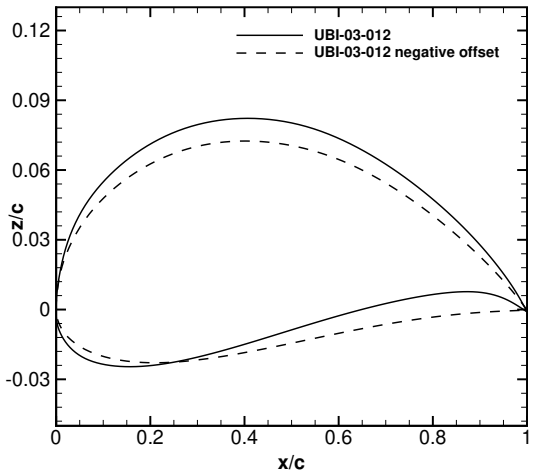

Figure 5.2: Variable-span wing IFW and OMW aerofoils comparison.

Figure 5.3 shows a planform conceptual view of the VSW, where the main planform parameter names are identified for easier description. The new VSW has some differentiating factors, namely the use of a canted wingtip and a morphing flap. The wingtip is intended to provide additional lateral-directional stability. In fact, it creates an effective dihedral angle, without changing the telescopic sections of the wing, thus, decreasing the structural and actuation system complexity that would result from non-flat wing sections. Additionally, the wingtip increases the overall aerodynamic efficiency. Finally, the addition of the morphing

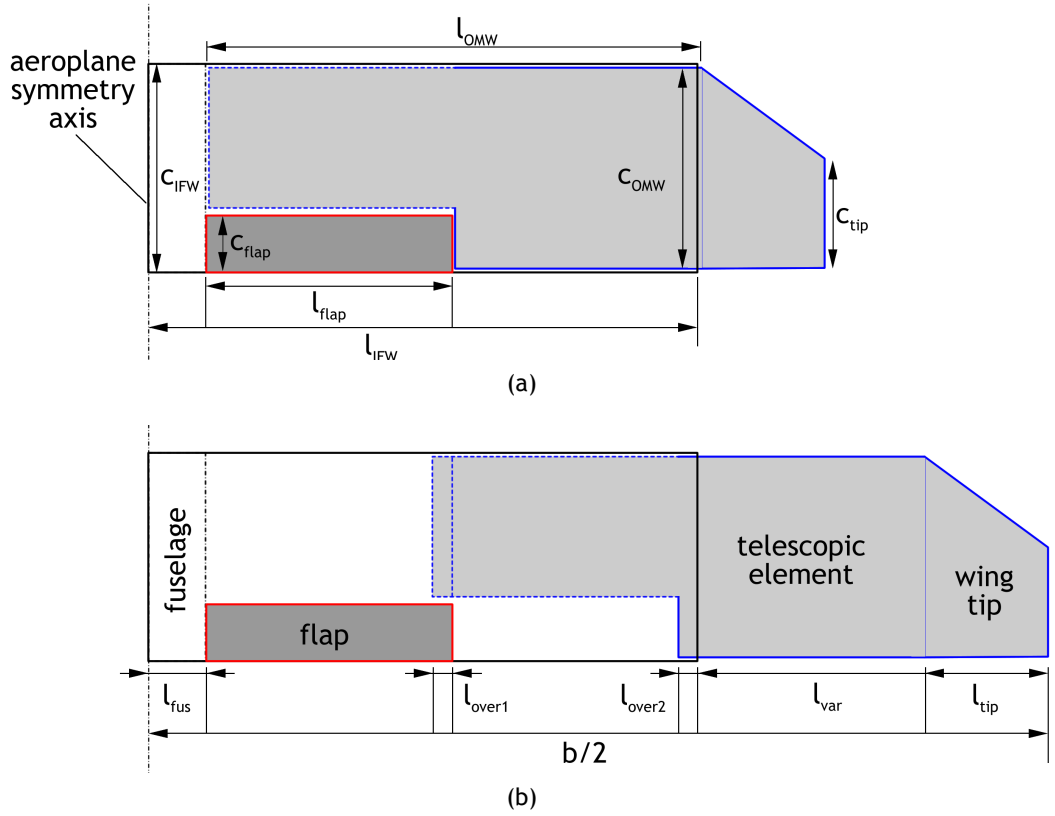

Figure 5.3: Variable-span wing conceptual planform view: (a) fully retracted configuration and (b) fully extended configuration, with geometrical wing parameters names identified.

flap enables camber changes, resulting in an increase in lift-to-drag ratio at different flight lift coefficients.

Both IFW and OMW wing panels have the design constraint of keeping chord and aerofoil geometry constants along each panel span, enabling proper fitting and support of the OMW. Observing Fig.5.3 one can see that the IFW length is denoted by l_{IFW}, the OMW length by l_{OMW}, the tip length by l_{tip} and the flap length by l_{flap}. The l_{var} parameter refers to the span length that is variable as a result of the movement of the OMW. There are two regions of contact that aid the load transfer from the OMW to the IFW: l_{over1} and l_{over2}. The former is the innermost region and is responsible for carrying the majority of the bending and torsional moment of the OMW. The latter corresponds to the outermost contact region, being responsible for providing stability in the chordwise direction. There is an additional length parameter that takes into account the fuselage length, called l_{fus}. Finally, IFW, OMW, flap and tip chords are designated as c_{IFW}, c_{OMW}, c_{flap} and c_{tip}, respectively.

5.3.1 Structural Concept and Materials

In principle, morphing wings tend to be heavier than conventional fixed wings due to increased structural and actuation complexity. Therefore, the structure should be designed and materials selected in such a way that sufficiently light wing components are attained. This facilitates integration into a realistic application while maintaining rigidity to carry flight loads. Therefore, the VSW uses a semi-monocoque structural concept, which consists in a stressed skin construction that carry shear loads, reinforced by multiple spars to carry bending and torsion

moments.

Figure 5.4 shows a schematic of the IFW and OMW wing sections, where the main sectional parameters are identified to facilitate the description.

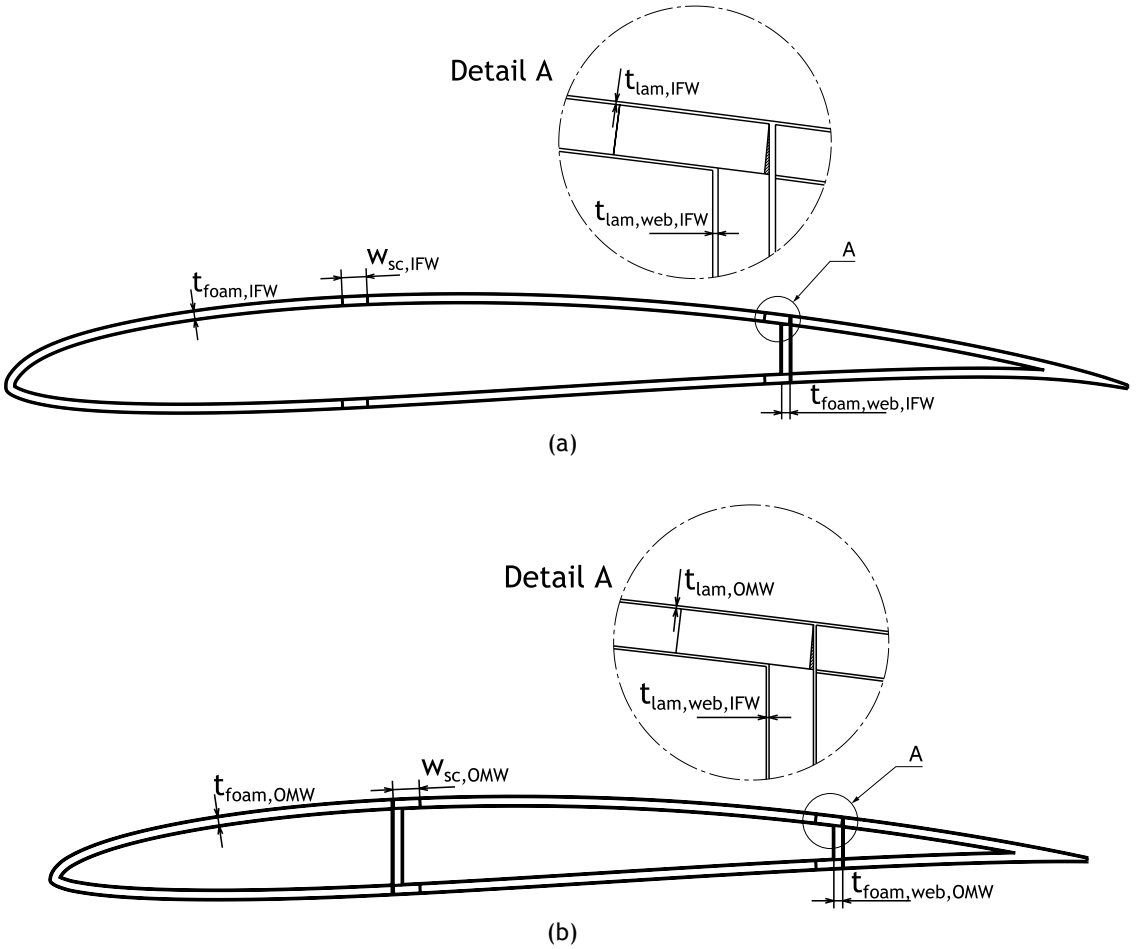

Figure 5.4: VSW cross-section view with sectional parameters names identified: (a) inboard fixed wing section and (b) outboard moving wing section.

Observing Fig.5.4, it is visible that both sections are composed by a composite sandwich made up with a foam core and two plies of bidirectional laminated carbon-epoxy composite. The fibres of the laminate are orientated at an angle of $\pm 45^{\circ}$. The four unidirectional pultruded carbon-epoxy composite spar caps are integrated into the skin, two in the upper surface and the other two in the lower surface. The two frontal spar caps are located in the thicker aerofoil section (30% of the local chord), while the two rear spar caps are located at a chord ratio dictated by the flap chord (c_{flap}).

Looking at the IFW section (Fig.5.4(a)), only one web (vertical element of the wing-box) is visible and it does not extend the full length. Instead, it is interrupted at the end of the flap position ($l_{fus} + l_{flap}$) from its root, in order to allow the OMW to retract into the IFW. Due to this constraint, no internal ribs can be used. Therefore, chordwise reinforcements made with unidirectional laminated carbon-epoxy composite are applied in three critical sections: beginning/end of the flap and IFW tip.

In Fig.5.4(b) it can be seen that the OMW has two webs. They extend from the component's root to the end of the rectangular portion (beginning of wing tip). Similar to the IFW,

the two frontal spar caps and webs are located in the thicker aerofoil section (30% of the local chord), while the two rear spar caps and webs are located in a chord ratio dictated by the flap chord (c_{flap}). There are no chordwise reinforcements in the OMW, since four internal ribs are used: OMW root and l_{over2} location, end of the rectangular portion and end of wingtip.

Several sectional parameters are identified in Fig.5.4: t_{lam} and $t_{lam,web}$ denote the laminate thicknesses of the skin contour and web; t_{foam} and $t_{foam,web}$ denote the foam core thicknesses of the skin contour and web; and w_{sc} denotes the width of the spar caps. The subscripts IFW and OMW are added to the mentioned terminology, in order to differentiate the parameters of the former and latter sections.

Similarly to the wing-box presented in chapter 4 (see section 4.5), the variable-span wing is made with three materials: carbon-fibre fabric with epoxy for the faces of the sandwich; PVC foam (Airex® C70.90) for the core of the sandwich and internal ribs; and pultruded unidirectional carbon-fibre with epoxy for the spar caps (vDijk high-strength pultrusions). These materials are identical to the ones used in the previous chapter. Therefore, its properties can be consulted in Table 4.7 (section 4.6).

5.4 Parametric Study Methodology

The most common approach to developing fixed-wing mass predictions is centred on the idea that a large database of wing masses and their associated geometry already exists through previous developed aircraft. Direct application of the above approach is not possible for morphing wing components because an adequate set of aircraft data does not exist. The approach used here is to develop a wing mass database and develop an equation that approximates this database. Using a Design of Experiments (DOE) to define a set of morphing wings with various shapes, representative FEMs were developed for each wing in the database and then sized to give a corresponding mass estimate. These data can then be approximated using an appropriate basis equation using a least squares regression technique resulting in the morphing wing mass equation. Only the structural mass was considered here, being the actuation system and flap mass added, later in the chapter, during the complete mass model derivation. The various aspects of this procedure are described in detail in the following sections.

The VSW presented in detail in the previous section serves as a basis to perform the parametric study with a double purpose. On one hand, it allows the study of the influence of a set of geometrical and inertial parameters on the structural mass of the VSW. On the other hand, as already mentioned, it allows the creation of the mass database, needed to create the approximation to predict the structural mass of the VSW. A total of five parameters were selected to perform the study. These are

1. b - wingspan in fully extended configuration;
2. c_{IFW} - inboard fixed wing chord;
3. $\bar{l}_{var}$ - wing variable-span ratio (with respect to semi-span);
4. $\bar{c}_{flap}$ - flap chord ratio (with respect to c_{IFW});
5. W - aeroplane MTOW.

The first four mentioned parameters are called the wing geometrical base parameters, since all the other wing dimensions are derived from them. Parameters one and two are illustrated in Fig.5.3. Parameters three and four, $\bar{l}_{var}$ and $\bar{c}_{flap}$, are nondimensionalized versions of l_{var} and c_{flap}, using the semi-span and the IFW chord, respectively. The fifth mentioned parameter, the aeroplane MTOW, W, was included in order to size the wings with different loading conditions, being used to compute the maximum load factor, using the CS-VLA regulation (described later).

For each set of parameters a minimum mass optimization problem with stiffness and strength constraints was implemented and solved, being the design variables structural thicknesses and widths. The optimization and structural FEM of the wing were developed in ANSYS® APDL.

5.4.1 Optimization

The optimization was carried out for each wing configuration, with the purpose of minimizing wing mass and, at the same time, ensure that each wing supports the prescribed loading. ANSYS® Mechanical APDL internal optimization facilities were used to carry out the optimization. The first order method was used, since it is the most accurate method available [160]. This method of optimization computes and uses derivative information. The constrained problem statement is transformed into an unconstrained one via penalty functions. Derivatives are formed for the objective function and the state variable penalty functions, using central finite differences, leading to a search direction in the design space. Various steepest descent and conjugate direction searches are performed during each iteration until convergence is reached. Each iteration is composed of multiple subiterations that include search direction and gradient computations [160].

The design variables adopted in the current study were: IFW and OMW laminate thicknesses, $t_{lam,IFW}$ and $t_{lam,OMW}$, and IFW and OMW spar cap widths, $w_{sc,IFW}$ and $w_{sc,OMW}$ (see Fig.5.4). Maximum bounds of laminate thicknesses were chosen based on the limitation of the thin shell element derivation assumptions, since shells elements can not have a radius of curvature to thickness ratio ≤ 0.5. The maximum spar cap widths were dictated by geometric constraints, i.e., maximum width that avoids mutual intersection. In the IFW, this is a function of the local and flap chord. In the OMW, it is only a function of the local chord.

Three constraint functions were adopted: maximum tip deflection and rotation, and ratio of elements that display failure. The tip deflection, w_{tip}, was limited to 2.5% of the span and the tip rotation, θ_{tip}, to be between -0.6 and 0.6°. These constraints were necessary to allow an even slide of the two wing components. In fact, if the tip displacement or rotation were too large, the VSW mechanism could eventually jam, compromising system integrity and functionality. These bounds were derived from past experience, namely the analyses performed in the past chapter (section 4.6). Additionally, a failure criterion constraint was used to detect structural failure of the wing. The inverse of *Tsai-Wu* strength ratio index failure criterion was used. In the current implementation, the ratio of the failed elements, $\overline{SR}_{TW}$, was imposed to be less than 0.1% of the total number of elements, rather than imposing that all elements do not display failure. This is due to the possibility of existing small areas with failed elements, that could be easily solved using local reinforcements. Since the current study is appropriate for the conceptual design phases, these small areas should not drive the overall design.

Summarizing, the optimization problem can be written as

$$
\begin{aligned}
\text{Minimize:} \quad & m_{wing} = f(w_{sc,IFW}, t_{lam,IFW}, w_{sc,OMW}, t_{lam,OMW}) \\
\text{Subjected to:} \quad & w_{sc,IFW,min} < w_{sc,IFW} < w_{sc,IFW,max} \\
& w_{sc,OMW,min} < w_{sc,OMW} < w_{sc,OMW,max} \\
& t_{lam,IFW,min} < t_{lam,IFW} < t_{lam,IFW,max} \\
& t_{lam,OMW,min} < t_{lam,OMW} < t_{lam,OMW,max} \\
& w_{tip} < 0.025\, b \\
& |\theta_{tip}| < 0.6^{\circ} \\
& \overline{SR}_{TW} < 0.001
\end{aligned}
\tag{5.1}
$$

Figure 5.5 summarizes the general flow of steps in the developed parametric design script.

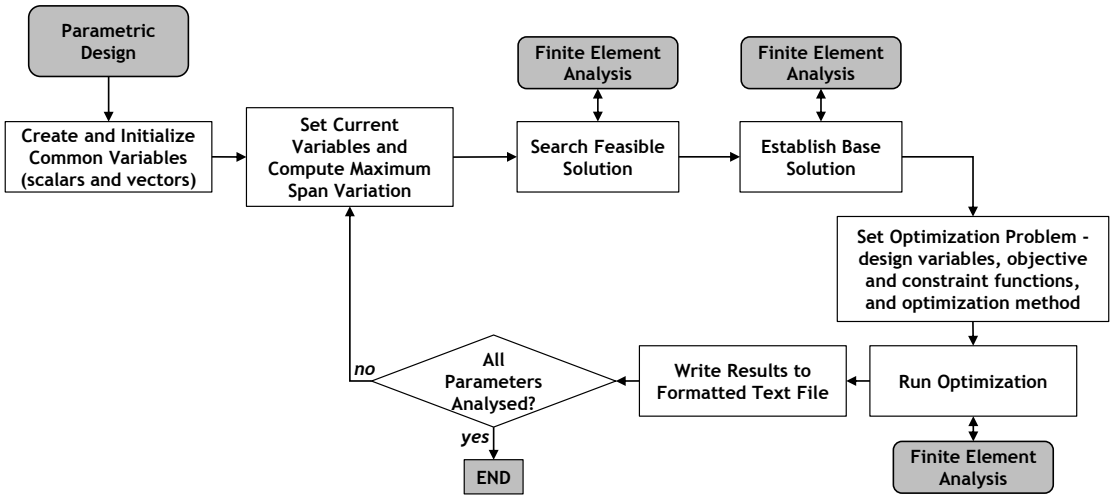

Figure 5.5: Parametric design script flowchart.

5.4.2 Finite Element Analysis

The numerical model of the VSW wing was developed using the ANSYS® Parametric Design Language (APDL) [132] with shell elements according to the base geometrical variables and design variables. The APDL script handles geometry creation, material definition, section properties, meshing, analysis and post-processing. The developed script allows the computation of a static solution (deformations, rotations and stresses) using small deformations. Due to computational resource optimization, SHELL281 element was used to discretize the surfaces. The SHELL281 element is an eight-node element suitable for analysing thin to moderately-thick shell structures. It has a total of six degrees of freedom at each node: translations in the x, y and z directions, and rotations about the x, y and z-axes. The element is well-suited for linear, large rotation, and/or large strain nonlinear applications.

The IFW sandwich skin was modelled with three layers built as offset surfaces from the aerofoil contour according to their own thickness. These three layers constitute the carbon/epoxy faces and foam core. In the locations of the embedded spar, the foam layer was

replaced with rectangular cross-section unidirectional pultruded carbon/epoxy rods. Likewise, the OMW was discretized using the same approach.

The peculiar structure used by the VSW, required the use of contact elements, in order to correctly model the interface. The contact in the overlapping surfaces between the IFW and the OMW was modelled with a shell to shell contact using TARGE170 (target element for 3D geometries surfaces) and CONTA174 (contact element for 3D shells with mid side nodes). The contact elements were added to the l_{over1} and l_{over2} regions. In order to reduce computational cost, an asymmetric contact was created. In this type of contact, one surface is designated to be the target and the other a contact surface. Then, one contact pair is created between surfaces. Contrary, in the symmetric contact both surfaces are designated as target and contact, which requires the creation of two contact pairs. Consequently, the asymmetric contact is more efficient than the symmetric contact. The contact elements' behaviour was chosen to be bonded, in order to reduce the computation cost of each analysis. However, an increase in the local stiffness is to be expected, which has the effect of underestimating the wing deformations. The bonded contact uses a Multipoint Constraint (MPC) formulation. MPC connection uses rigid constraint equations between the elements on the contact and target faces to model the bonded connection. The connection locations are determined using the contact element pinball radius and then the contact elements are replaced with internal constraint equations.

The performed solution was a static analysis, without large deflections and using the MPC based contact interface. Given these characteristics, the solution was linear, greatly expediting the computation. This allowed a reduced computation time for each static analysis, greatly reducing the optimization time and increasing the robustness of the analysis. Additionally, it increased the optimization stability, since it eliminated the possibility for unconverged solutions. It should be added that since a symmetric wing planform was assumed, only half of the wing was modelled. Figure 5.6 summarizes the general structure of the developed FEM script.

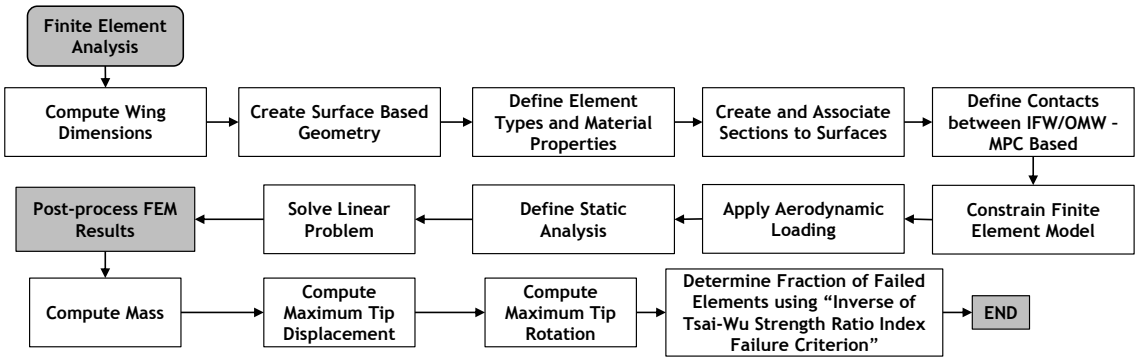

Figure 5.6: Finite element model flowchart.

5.4.3 Polynomial Fitting

Several basis functions can be used to approximate the mass of the wings in study. In the literature, the most popular functions are: full quadratic polynomial and conventional wing

mass equation. The general form of such equations are given by

$$m(\{X_{1:n}\}) = a_0 + \sum_{i=1}^{n} a_i X_i + \sum_{i=1}^{n} \sum_{j=i}^{n} a_{ij} X_i X_j \tag{5.2}$$

$$m(\{X_{1:n}\}) = a_0 + \prod_{i=1}^{n} X_i^{a_i} \tag{5.3}$$

where, $\{X_i\}$ represents one of the n parameters within the DOE and a_{ij} represent the unknown coefficients in each of the mass equations. On one hand, the quadratic approximation captures both linear and quadratic terms and tends to provide a good approximation when the design set displays moderate deviations from linear behaviour. Therefore, it can approximate the wing mass if a non-linear relationship of the wing mass parameters is verified. On the other hand, the conventional wing mass equation form is the product of monotonically varying wing parameters. The wing mass models given in many aircraft design references have this basic form. The second order polynomial allows a better study of the effect on the wing mass produced by each individual parameter, since both linear and two level interaction relationships between parameters could be identified. Therefore, given the latter requirement, the quadratic polynomial was chosen.

A total of two structural mass and one mass ratio equations were developed: fixed wing mass, VSW mass and VSW to fixed wing mass ratio. Multivariate polynomials were then created, $m_{str,fw}$, $m_{str,VSW}$ and $\overline{m}_{str,VSW/fixed}$ being a function of the wing parameters in the following form

$$m_{str,fw} = f(b, c_{IFW}, \bar{c}_{flap}, W) \tag{5.4}$$

$$m_{str,VSW} = f(b, c_{IFW}, \bar{l}_{var}, \bar{c}_{flap}, W) \tag{5.5}$$

$$\overline{m}_{str,VSW/fw} = f(b, c_{IFW}, \bar{l}_{var}, \bar{c}_{flap}, W) \tag{5.6}$$

where, Eqs.(5.4), (5.5) and (5.6) are functions of the already mentioned parametric study parameters, with the exception of the first (fixed wing polynomial) that does not have variable-span ratio. Notice that Eq.(5.6) is not a mass equation since it represents the ratio of VSW mass to fixed wing mass, thus being a non-dimensional quantity.

A mathematical algorithm was applied to find the unknown polynomial coefficients. The chosen method is based on an extension to the Granger causality test, called ERR-causality, and was developed by Zhao et al.[161]. The Granger causality test complies with simplicity requirements and is a common method suited for both linear and nonlinear regression that detects causality. However, it does not account for latent confounding effects and does not capture instantaneous and nonlinear causal relationships [162]. The extension is a causality nonparametric detection method that comprises an orthogonal least squares algorithm, uses a nonlinear system identification and produces an error reduction ratio-causality (ERR-causality). The ERR-causality test can be used to detect and track causal relationships between two signals. A detailed description of the method can be found in [161]. The main advantage of the ERR test is that it can be applied to nonlinear multivariate systems. Furthermore, with the ERR-causality method it is possible to organize the polynomial terms, in respect to its significance to the overall solution. Therefore, the complete polynomial model does not have to be used to provide a correct polynomial approximation, making it a more powerful and robust causality detection method. The minimum number of significant terms that adequately fit the dataset is

evaluated by calculating the Sum of Error Reduction Ratio (SERR) values. Using this metric, the final simplified polynomial can be obtained, by screening the terms that have lower influence in the dependent variable and eliminating them.

The resulting polynomials were evaluated using goodness of fitting parameters, such as the coefficient of determination, R^2, maximum relative error, maximum absolute error and Root Mean Squared Error (RMSE). The R^2 correlates the computed data with the predicted data by a square of the sample correlation coefficient, where values near to one indicate a good fit. RMSE is a fit standard error for regression and estimates the standard deviation of each data component. A detailed explanation of such parameters for error analysis is given in [163].

After computing the polynomial, it was important to visually validate the results by plotting the representation of the resulting polynomials with the data points overlaid for comparison reasons. These plots facilitated final considerations to be taken about the trends of each parameter on the wing mass. The five independent variables describe a hypersurface with a six-dimensional representation. As this is not possible to plot, the polynomial approximations were reduced to several polynomials with only two independent variables.

The polynomials coefficients were computed using a computer software developed by Zhao el al.[161], using C++ and Matlab. The polynomials were later post-processed using an in-house developed FORTRAN software. The structure of the developed software is shown in Fig.5.7.

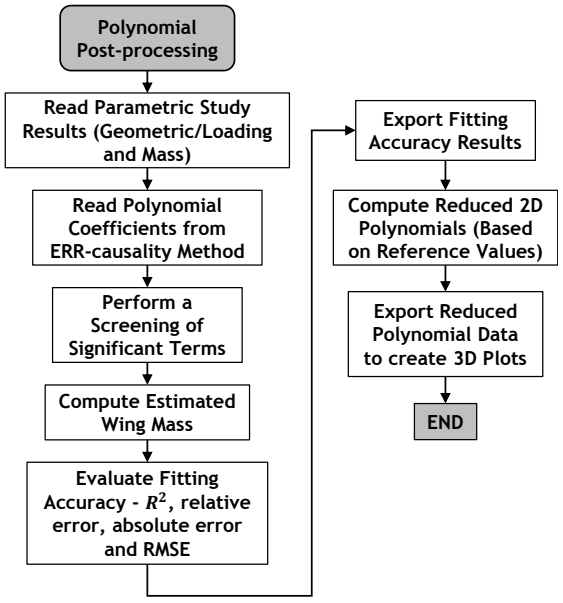

Figure 5.7: Polynomial approximation post-processing flowchart.

The post-processing software illustrated in Fig.5.7 was used to compute polynomials errors, perform the screening of significant terms and perform the polynomial reduction to effectively create the three-dimensional plots. The first step is to read the data computed in the parametric study, in order to have the data to evaluate the polynomials. The next step is to read the polynomial coefficients computed using the ERR-causality software. Afterwards, a screening of the significant terms is performed, in order to reduce the number of polynomial terms. The fitting accuracy metrics are calculated using the input mass data and the estimated mass data from the polynomial approximations. As referred before, the used metrics are the

coefficient of determination, R^2, maximum relative and absolute errors and RMSE. Finally, the polynomials are reduced to functions of two independent variables.

5.4.4 Loading

The design load cases are important to determine realistic sizes of the wing's structural components. These load cases are usually defined by the corner points of the V-n diagram. Ideally, the wing structure would be optimized with respect to all expected loading and operating conditions. However, this results in an extremely large number of loading conditions. Considering that the wing mass equation being developed here is to be used for the initial design phases only, selecting only the critical loading condition should suffice to demonstrate the approach.

In general terms, the morphing aircraft is expected to perform a long-endurance loiter, followed by an high speed. The morphing wing would have a high aspect ratio during loiter to reduce induced drag. During dash, the wing would have a low aspect ratio. Thus, the maximum speed of the dash wing is significantly higher than that of the loiter wing. Therefore, each configuration of the morphing wing has its own V-n diagram and, consequently, each configuration has its own set of design loads.

To extract the different design loads, the reference baseline VSW was analysed in three wing configurations: maximum, intermediate and minimum span. For each configuration, a manoeuvre and a gust V-n diagrams were computed, using the EASA's Certification Specifications for Very Light Aeroplanes, CS-VLA [148] and the RPAS specifications. From each V-n diagram the critical design points were extracted, considering bending loadings, i.e., maximum load factor.

For aeroplanes with low wing loading (W/S), the gust envelope is critical [164]. Therefore, the maximum load factor of the gust diagram was used as design point. The next paragraphs explain in more detail the rational behind this methodology. Figure 5.8 shows a schematic of the positive portion of the V-n diagram, where the gust diagram is critical.

Observing Fig.5.8, three distinct curves can be seen: cruise speed gust, dive speed gust and maximum lift coefficient. A total of four important speeds are also identified: design cruise speed, V_C, design dive speed, V_D, stall speed, V_{stall}, and design speed, V_{design}.

Referring to CS-VLA regulation, the design cruise speed, V_C, and the dive speed, V_D, are computed using the following equations

$$V_C = V_{C,min} = 2.4\sqrt{W/S} \tag{5.7}$$

$$V_D = V_{D,min} = 1.25 V_C \tag{5.8}$$

being, W the aircraft weight and S the wing area. Analysing Eq.(5.7), one concludes that cruise speed is a function of the wing loading.

The cruise and dive gust curves are computed, as functions of speed, according to the

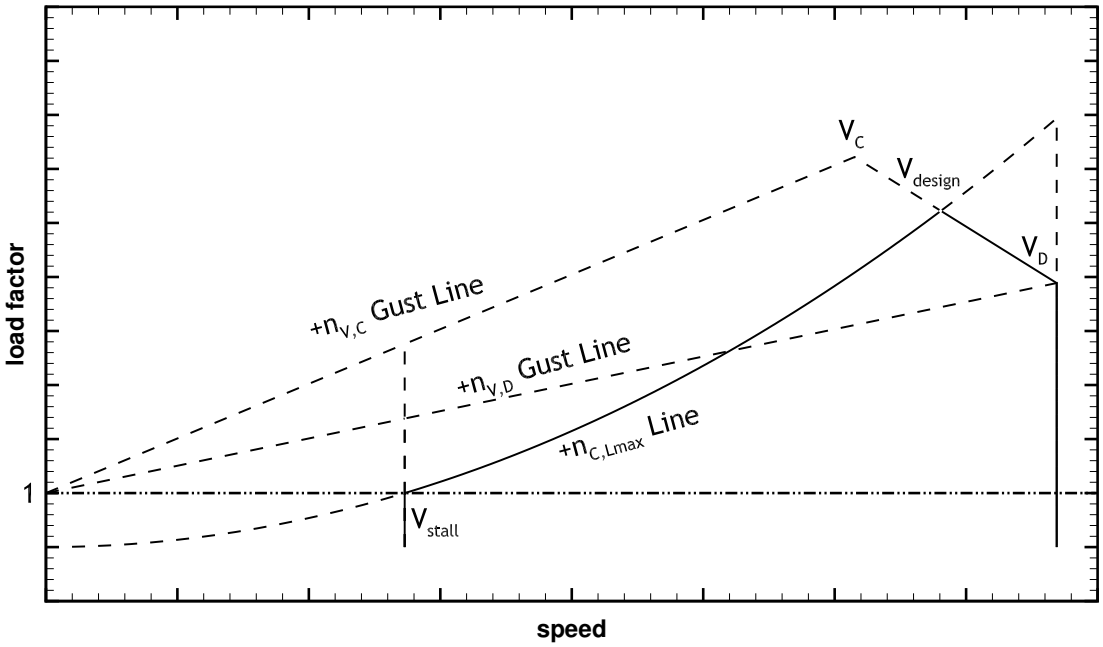

Figure 5.8: Schematic of the positive portion of the V-n diagram, where the gust diagram is critical.

CS-VLA regulation, using the following equations

$$n_{V_C} = 1 + \frac{\rho_{air}\, V\, C_{L_\alpha}\, K_g\, V_{g,C}}{2W/S} \tag{5.9}$$

$$n_{V_D} = 1 + \frac{\rho_{air}\, V\, C_{L_\alpha}\, K_g\, V_{g,D}}{2W/S} \tag{5.10}$$

where K_g is the gust alleviation factor, C_{L_α} is the wing lift curve slope, $V_{g,C}$ and $V_{g,D}$ are the gust vertical speeds in cruise and dive conditions, respectively. Note that the gust vertical speeds are constant values (given in CS-VLA). The gust alleviation factor and the aeroplane mass ratio, μ_g are introduced to correct for dynamic effects in the aircraft pitching and vertical motion and the time lag during which lift is building. They are computed from

$$K_g = 0.88\,\frac{\mu_g}{5.3+\mu_g} \quad \text{with} \quad \mu_g = \frac{2W}{\rho_{air}\, c_{IFW}\, C_{L_\alpha} S} \tag{5.11}$$

The lift curve slope is estimated from the aerofoil lift curve slope, considering an inviscid, incompressible flow over a wing with general planform [16]. Thus

$$C_{L_\alpha} = \frac{C_{l_\alpha}}{1 + C_{l_\alpha}/(\pi\, AR)(1+\tau)} \tag{5.12}$$

where, C_{l_α} is the aerofoil lift curve slope, AR is the wing aspect ratio and τ is a function of the wing planform. In the current work, although the wing planform is not elliptic, the lift distribution is assumed to have an elliptic shape. Therefore, τ can be neglected.

The stall load factor is computed using the definition of lift for maximum lift coefficient. Thus

$$n_{C_{L,max}} = \frac{0.5\,\rho_{air}\, V^2\, S\, C_{L,max}}{W} \tag{5.13}$$

From Fig.5.8, one can see that, for low speeds, the $n_{C_{L,max}}$ curve is the limiting load factor. When the cruise speed is reached, the load factor reduces linearly between the two gust curves. The maximum gust load factor speed is found in the intersection between n_{V_C} and n_{V_D} curves and $n_{C_{L,max}}$ curves, denoted by V_{design}. Therefore

$$n_{V_C} + \frac{n_{V_D} - n_{V_C}}{V_D - V_C}(V_{design} - V_C) = \frac{0.5\,\rho_{air}\,V_{design}^2\,S\,C_{L,max}}{W} \tag{5.14}$$

Solving Eq.(5.14) for V_{design}, yields the speed for the maximum gust load factor.

The design load factor can now be determined by substituting the computed speed in the load factor for the maximum lift coefficient. Thus

$$n_{design} = \frac{0.5\,\rho_{air}\,V_{design}^2\,S\,C_{L,max}}{W} \tag{5.15}$$

After computation of the design load factor, the design lift force can be readily computed from

$$L_{design} = n_{design} W \tag{5.16}$$

Drag and pitching moment can now be computed. The drag was determined using the lift-to-drag ratio of the baseline wing. This quantity was corrected using the aspect ratio, if a different wing is considered. Therefore

$$D_{design} = \frac{L_{design}}{(L/D)_{blw}\,AR/AR_{blw}} \tag{5.17}$$

where, $(L/D)_{blw}$ and AR_{blw} are the lift-to-drag ratio and aspect ratio of the baseline wing, respectively.

The pitching moment is computed from the baseline wing pitching moment coefficient and the design speed. Thus

$$M_{design} = 0.5\,\rho_{air}\,V_{design}^2\,S\,c_{IFW}\,C_{M,blw} \tag{5.18}$$

being $C_{M,blw}$ the pitching moment coefficient of the baseline wing. The pitching moment coefficient used is an average value in the studied range of lift coefficients of the baseline wing. It was assumed constant for all studied wing configurations.

The lift was considered to have an elliptic distribution, applied along the span at 25% chord position. Both drag and pitching moment distributions were assumed uniform along the wingspan. Lift and drag forces are perpendicular and parallel, respectively, to the free stream direction. However, since the effect of the AOA was not considered, they are assumed to be perpendicular and parallel to the wing chord line, respectively. Therefore, lift force is the vertical force, F_V, and the drag force is the horizontal force, F_H.

Finally, in order to better represent the load distributions along the chord, the initial force system of one vertical and horizontal force, applied at 25% of the wing chord, and a torsion moment about this same point, was substituted by two vertical forces applied at the fore and aft wing-box webs and four horizontal forces applied at each spar cap corner, as shown in Fig.5.9.

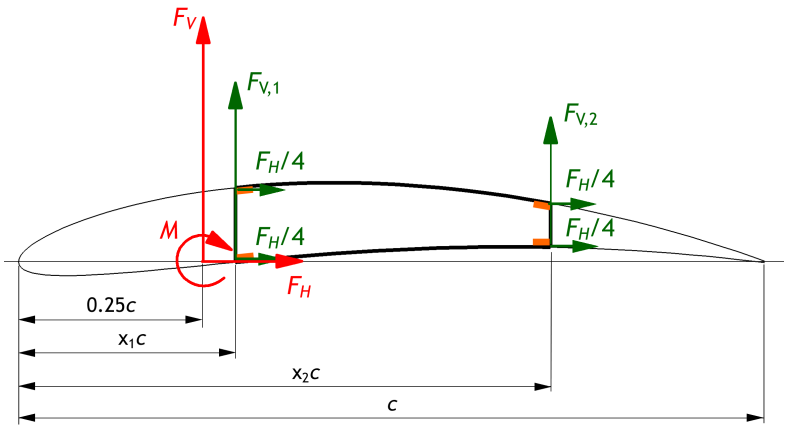

Figure 5.9: Equivalent force system of the VSW parametric study (F_V is the vertical force, F_H the horizontal force and M the pitching moment).

From the force and moment equilibrium, forces $F_{V,1}$ and $F_{V,2}$ are found to be

$$F_{V,1} = F_V - \frac{M - 0.25cF_V + \overline{x}_1 cF_V}{c(\overline{x}_1 - \overline{x}_2)} \tag{5.19}$$

$$F_{V,2} = \frac{M - 0.25cF_V + \overline{x}_1 cF_V}{c(\overline{x}_1 - \overline{x}_2)} \tag{5.20}$$

where, $\overline{x}_1$ and $\overline{x}_2$ are the ratios of the fore and aft spar positions to the chord length of the VSW. In the studied case, the fore ratio is 0.3 and the aft ratio is dependent on the flap chord $(1 - \overline{c}_{flap})$.

The fore vertical load was distributed along the frontal web of the wing, the aft vertical force was distributed along the rear web of the wing and the horizontal force was equally distributed by the four spar caps.

5.4.5 Geometric Scaling

In the parametric study, different wing geometric configurations were used. Thus, there was a need to create geometric mathematical relations between the different used parameters. In order to perform the scaling, a baseline or reference wing was used. As previously mentioned, the baseline wing corresponds to the dimensions and weight of the Olharapo 3 VSW and its dimensions are designated using the subscript *blw*, where "bl" stands for baseline and "w" to wing. The geometric scaling can be divided into spanwise, chordwise and sectional parameters. As the names implies, the former denotes parameters in the spanwise direction and the second in the chordwise direction. The latter denotes mathematical relations of the section thicknesses and widths.

5.4.5.1 Spanwise Formulas

In the spanwise scaling, the important input parameters are the wingspan, b, and the variable-span ratio, $\bar{l}_{var}$. The innermost overlap between the IFW and OMW, l_{over1} is scaled using the OMW exposed area (moving part) and tip area, as well as the y centroid of the same sections. In fact, with increasing l_{var} the bending moment in the contact surface location

increases and section centroid location moves away from the wing's root. Consequently, l_{over1} needs to increase to allow a smooth load transfer. The derived mathematical relation is given by

$$l_{over1} = \frac{l_{over1,blw}}{A_{var+tip,blw}\,\overline{y}_{var+tip,blw}} A_{var+tip}\,\overline{y}_{var+tip} \tag{5.21}$$

where, $A_{var+tip}$ is the area of the moving portion of the OMW plus the tip area and $\overline{y}_{var+tip}$ is the y section centroid of the moving portion of the OMW plus the tip. Note that the variable-span length, l_{var}, is directly computed from the semi-span and variable-span ratio. Thus

$$l_{var} = 0.5\,b\,\bar{l}_{var} \tag{5.22}$$

The tip length, l_{tip} is computed using a linear scaling relative to the span. Therefore

$$l_{tip} = l_{tip,blw}\,\frac{b}{b_{blw}} \tag{5.23}$$

Finally, the IFW length, l_{IFW}, OMW length, l_{OMW} and flap length, l_{flap} can be readily computed by careful analysis of Fig.5.3. Thus

$$l_{IFW} = 0.5\,b - l_{var} - l_{tip} \tag{5.24}$$

$$l_{OMW} = 2\,l_{var} + l_{over1} + l_{over2} \tag{5.25}$$

$$l_{flap} = l_{var} + l_{over1} \tag{5.26}$$

5.4.5.2 Chordwise Formulas

In the chordwise scaling, the fundamental parameter inputs are the IFW chord, c_{IFW} and the flap chord ratio, $\bar{c}_{flap}$. The flap chord can be readily computed using the flap chord ratio and the IFW chord. Hence

$$c_{flap} = \bar{c}_{flap}\,c_{IFW} \tag{5.27}$$

Both OMW chord, c_{OMW} and tip chord, c_{tip} are computed by linearly scaling the reference value relative to the IFW chord. Therefore

$$c_{OMW} = c_{OMW,blw}\,\frac{c_{IFW}}{c_{IFW,blw}} \tag{5.28}$$

$$c_{tip} = c_{tip,blw}\,\frac{c_{IFW}}{c_{IFW,blw}} \tag{5.29}$$

The aerofoil geometry is fixed (section 5.3) and, consequently, curvature, aerofoil thickness-to-chord ratio and LE radius, are all constant in the studied wing configurations.

5.4.5.3 Cross-section Formulas

IFW and OMW sections are composed of different structural elements, whose nomenclature as been previously elucidated in Fig.5.4 (section 5.3). All sectional parameters are

either constant or derived from the wing design variables: laminate thicknesses and spar caps widths. IFW web laminate thickness, $t_{lam,web,IFW}$, is considered to be twice the skin laminate thickness, $t_{lam,IFW}$, and the OMW web laminate thickness, $t_{lam,web,OMW}$ is considered to be equal to $t_{lam,OMW}$. Thus

$$t_{lam,web,IFW} = 2\, t_{lam,IFW} \tag{5.30}$$

$$t_{lam,web,OMW} = t_{lam,OMW} \tag{5.31}$$

The IFW skin foam thickness, $t_{foam,IFW}$, and the web foam thickness, $t_{foam,web,IFW}$, does not change throughout the parametric study. The same is valid for the OMW sections ($t_{foam,OMW}$ and $t_{foam,web,OMW}$).

5.4.6 Fixed Wing Reference Design

The fixed wing reference design was used to gauge the mass increase when considering the structural methodology of the VSW. In order to be comparable, the fixed wing has similar planform dimensions and cross-sections. However, the variable span ratio is zero, i.e., no outer moving wing. Due to the fact that the fixed wing was used as a reference, a more complex skin optimization layout was developed. In particular, the fixed wing skin was divided into four different regions, in order to allow the laminate thicknesses to vary along the span. However, the spar cap width was still kept constant in the spanwise direction, i.e., the spar caps remain rectangular. Therefore, a total of five design variables were used: four skin laminate thicknesses and one spar cap width. Figure 5.10 shows a model of the fixed wing, where the different optimization skin laminate areas were coloured to aid its identification.

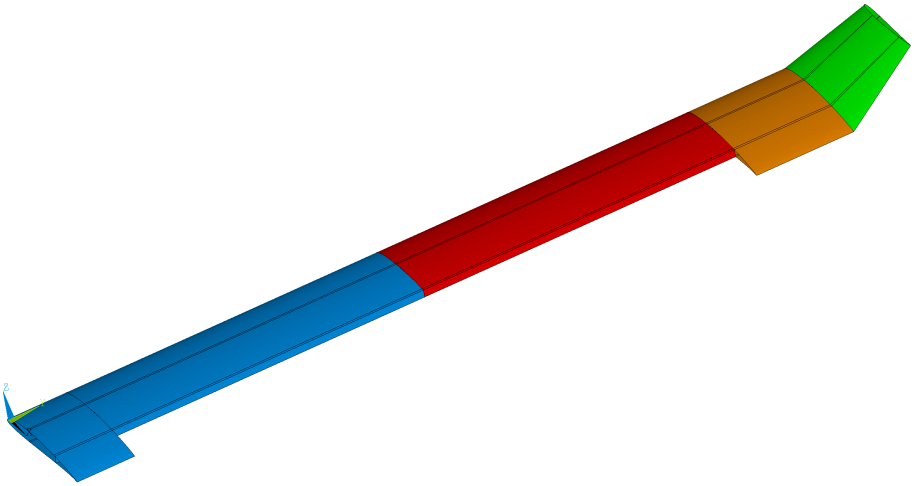

Figure 5.10: Fixed wing model with coloured sections, identifying the different skin laminate optimization areas.

5.5 Parametric Study Results

As presented in previous sections, the chosen design parameters are: wingspan, b, IFW wing chord, c_{IFW}, variable-span ratio, $\bar{l}_{var}$, flap chord ratio, $\bar{c}_{flap}$, and aeroplane MTOW, W.

For each input parameter the selected values are presented in Table 5.2.

Table 5.2: Parameter values used to create the design of experiments (baseline wing values in bold).

b, m				$[2.665$	$\mathbf{3.554}$	$4.442]$
c_{IFW}, m				$[\mathbf{0.257}$	0.321	$0.386]$
$\bar{l}_{var}$	$[0$	0.05	0.1	0.2	$(\bar{l}_{var,max}+0.2)/2.0$	$\boldsymbol{\bar{l}_{var,max}}]$
$\bar{c}_{flap}$				$[\mathbf{0.3}$	$0.4]$	
W, N				$[120$	$\mathbf{150}$	$180]$

In Table 5.2 the bold values correspond to the baseline wing dimensions and weight. As can be inferred from the same table, three values of span, IFW chord and aeroplane weight were selected. The values of span and weight were computed considering a ± 25% variation centred in the baseline wing reference values. The minimum value of the IFW chord was set to the reference, in order to avoid unrealistic aspect ratios. The other values were considered to be 1.25 and 1.5 times higher than the baseline. In what concerns $\bar{l}_{var}$ parameter, a total of six values were selected: the zero value corresponds to the conventional wing configuration and the $\bar{l}_{var,max}$ corresponds to the maximum variable-span ratio. The latter is a function of the span and the interface between the IFW and OMW (l_{over1}). Note that the baseline wing uses the larger variable-span ratio. Regarding $\bar{c}_{flap}$ parameter, only a higher value than the VSW reference value was added, in order to reduce the computational time. The parameters in study (independent variables) were used to create the wings to be optimized in ANSYS®, by using sequential repetitions of unique parameters combinations.

There are some geometrical and cross-section dimensions that were kept constant throughout the study. Table 5.3 summarizes these constant geometrical and cross-section dimensions. As described in section 5.4.5 some dimensions were scaled using the baseline wing dimensions. These reference values are presented in Table 5.4.

Table 5.3: Parametric study constant geometrical and cross-section dimensions.

Geometric		Cross-section	
l_{fus}	0.12 m	$t_{foam,IFW}$	2 mm
l_{over2}	0.025 m	$t_{foam,web,IFW}$	3 mm
Γ_{tip}	57°	$t_{foam,OMW}$	2 mm
		$t_{foam,web,OMW}$	2 mm

Table 5.4: Baseline wing geometrical parameters used in scaling.

Parameter	Value
$l_{over1,blw}$	0.125 m
$l_{tip,blw}$	0.157 m
$c_{OMW,blw}$	0.234 m
$c_{tip,blw}$	0.18 m

In the next sections, the results of the parametric study are presented. Since the parametric study is composed of a large dataset (324 parameter combinations), only a case study is shown using the baseline wing. The complete parametric study results are available in tabular form in Appendix A. Later in this section, the polynomial approximations for each studied case are analysed and the interaction between the parameters asserted.

5.5.1 Design Loading Analysis

According to what was introduced, a single reference wing was studied and loading values for different wings were generalized based on CS-VLA regulation gust loading. As stated previously, Olharapo 3's MTOW is 150 N and the morphing wing has a chord of 0.257 m, a span of 3.554 m in the fully extended configuration and a span of 3.104 m in the fully retracted configuration. Therefore, the span variation to semi-span ratio is 0.25.

Design loads were estimated with the use of the V-n diagram as specified in EASA's CS-VLA [148]. This diagram allows to obtain the symmetrical load factor envelope for any given wing configuration as a function of speed. It was assumed that the maximum and minimum manoeuvre load factors in any wing configuration are +3 and -1.5, respectively. Each diagram is composed of a manoeuvre envelope and a gust envelope. The gust speeds for the cruise, $V_{g,C}$, and dive, $V_{g,D}$, conditions are 15.24 m/s and 7.62 m/s, respectively. The cruise speed was computed using Eq.(5.7) and the wing lift coefficients curve slopes using Eq.(5.12). The aerofoil lift curve slope was estimated using XFOIL [121]. It was assumed that the minimum wing lift coefficient is half the maximum wing lift coefficient. The maximum lift coefficient, $C_{L,max}$, was assumed to be the same for all wings due to the Reynolds number and aerofoil similarity among the three wing configurations. This coefficient, along with lift-to-drag ratio and moment coefficient were estimated based on an aerodynamic analysis using VLM performed in XFLR5. The data required to construct the V-n diagrams is summarized in Table 5.5.

Table 5.5: Required data to compute the V-n diagrams.

Wing configuration	Wing area, m^2	$C_{L,max}$	$C_{L,min}$	C_{L_α}, rad^{-1}	Design cruise speed, m/s
Maximum Span	0.913	1.44	-0.72	5.062	30.76
Intermediate Span	0.798	1.44	-0.72	4.978	32.91
Minimum Span	0.682	1.44	-0.72	4.870	35.59

A total of three V-n diagrams were calculated, one for each wing configuration. Figure 5.11 shows the V-n diagram for each wing configuration superimposed. Referring to Fig.5.11, the critical case for the maximum, intermediate and minimum span wings is highlighted using a circle, a delta and a square symbol, respectively. Because the negative load factors are much lower than the positive ones those are not considered. The critical envelope in every case is, as expected, the gust envelope. Observing the three diagrams superimposed, the critical envelope is that of the fully extended wing, since it presents the higher load factor. The referred point corresponds to the speed and load factor computed with Eqs.(5.14) and (5.15), respectively. Therefore, in the parametric study maximum span configurations were used in all studied cases.

The presented analysis was generalized for all wing configurations and the lift, drag and pitching moment were calculated for the given speed, wing area and aeroplane weight, using Eqs.(5.16), (5.17) and (5.18), respectively. Recalling Eq.(5.17), the drag is computed by scaling the lift-to-drag ratio of the baseline, $(L/D)_{blw}$. A value of 32.6 was used. Regarding the pitching moment, C_M, a constant value of -0.15 was used for all the studied wings. The aerodynamic reference values are summarized in Table 5.6, whereas the loading values for all wing configurations and aeroplane MTOWs are summarized in Table A.1, in Appendix A.

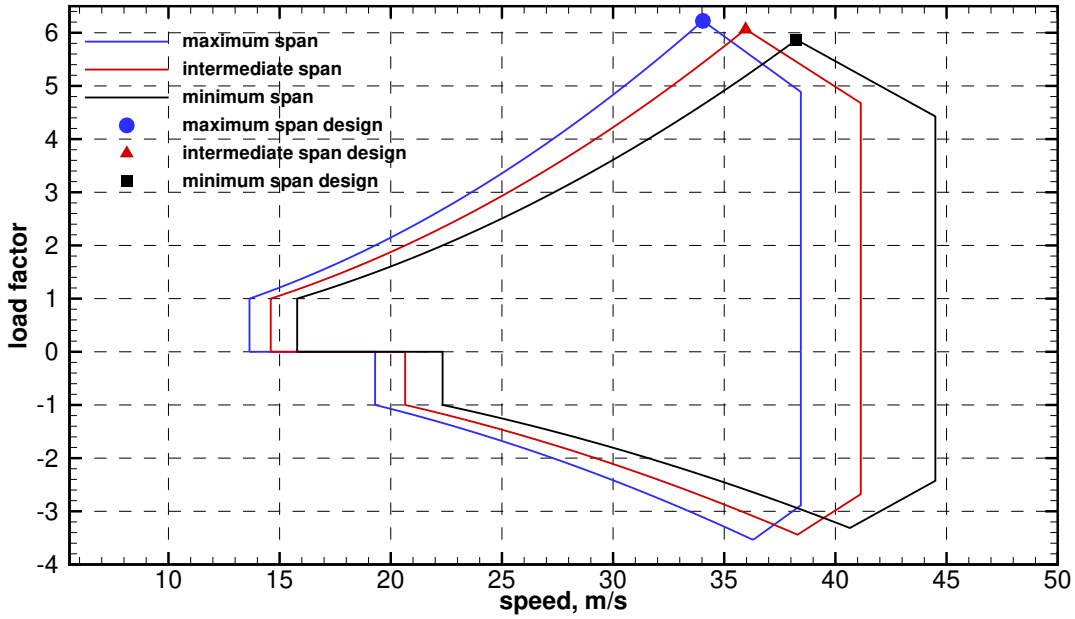

Figure 5.11: V-n diagrams for each wing configuration.

Table 5.6: Baseline wing aerodynamic scaling parameters.

Parameter	Value
$(L/D)_{blw}$	32.6
$C_{M,blw}$	-0.15

Since the effect of AOA was neglected, lift and drag are already the vertical and horizontal forces, respectively. The vertical force and pitching moment were moved to the spar web fore and aft positions using Eqs.(5.19) and (5.20), respectively. Finally, the horizontal force was divided by the four spar cap corners.

5.5.2 Baseline Wing Mesh Convergence Study

A convergence analysis of the finite element model of the baseline wing was carried out to assess the sensitivity of the maximum tip displacement and rotation as functions of the element number in the mesh. Several meshes were created and a static analysis was performed with the loading distributed along the span. Figure 5.12 shows the convergence of the maximum wing tip deflection and rotation for several mesh sizes.

Observing Fig.5.12, it is visible that the tip rotation shows a larger variation until 4000 elements, after which the variation is small. The tip deflection shows a more gradual convergence, showing, however, a reduction of the slope for 10000 elements. Thus, it is possible to conclude that the solution is stabilized for a grid with about 10000 elements.

It should be highlighted that, due to the nature of the parametric study, wing geometry changes depending on input parameters. Therefore, the mesh has to be updated. To avoid the time consuming process of performing a mesh study for each geometric configuration, the relative spacing between elements was kept constant across all FEM analysis. The resultant baseline wing FEM can be seen in Fig.5.13.

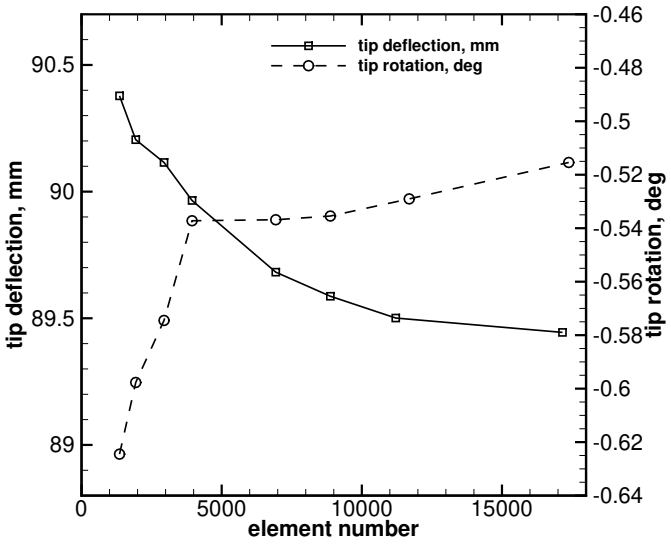

Figure 5.12: Baseline wing maximum tip deflection and rotation obtained using different numbers of elements.

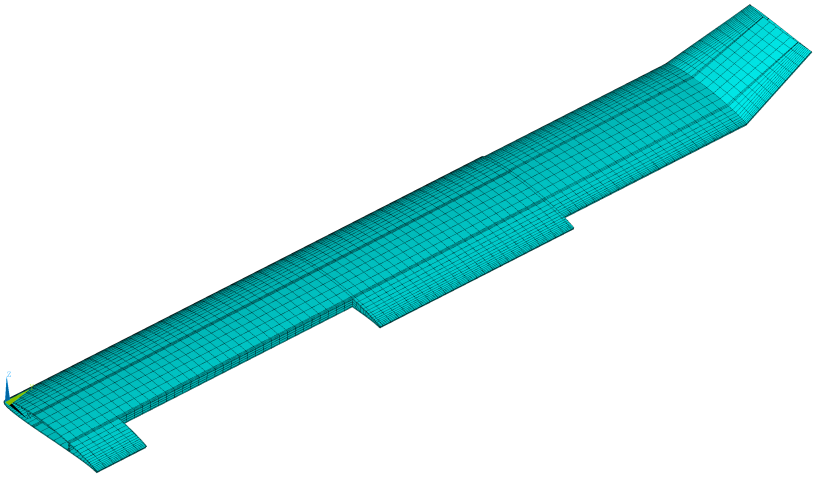

Figure 5.13: Finite element model of the complete baseline wing.

5.5.3 Baseline Wing Optimization and Analysis

The focus of this section is to assess the functionality and correctness of the FEM and optimization scripts developed in ANSYS® APDL. To achieve this, the baseline wing underwent structural optimization and subsequent structural analysis of the optimized structure.

Since a prototype of the baseline wing is planned to be built and installed in Olharapo 3, one should take in consideration the minimum bounds of the design variables. Regarding the skin laminate, the minimum acceptable value is 0.12 mm, corresponding to a layer of 185 g/m^2 plain weave carbon/epoxy. Therefore, both $t_{lam,IFW}$ and $t_{lam,OMW}$ minimum optimization bounds were set to this value. The spar widths minimum bounds were selected based on standard available sections from vDijk high-strength pultrusions [128]. Consulting the list, one concludes that the minimum available section is 2 mm$\times$0.4 mm, being this value used as limit to $w_{sc,IFW}$ and $w_{sc,OMW}$.

Using the above considerations, the optimization was run with the baseline wing specific-

ations. In Table 5.7 one can see the initial and final values of the design variables and of the objective and constraint functions; and in Fig.5.14 the variation of the same variables throughout the design sets. The initial values of the design variables were selected so that the wing had sufficient stiffness to guarantee a feasible solution, i.e., all constrains were fulfilled.

Table 5.7: Baseline wing design variables, and objective and constraint functions initial and final values.

	$w_{sc,IFW}$, mm	$t_{lam,IFW}$, mm	$w_{sc,OMW}$, mm	$t_{lam,OMW}$, mm	m_{wing}, kg	w_{tip}, m	θ_{tip}, deg	$\overline{SR}_{TW}$, %
Initial	50.0	0.48	40.0	0.13	2.54	0.028	-0.09	0.0073
Final	21.7	0.12	0.8	0.12	1.00	0.088	-0.36	0.0113

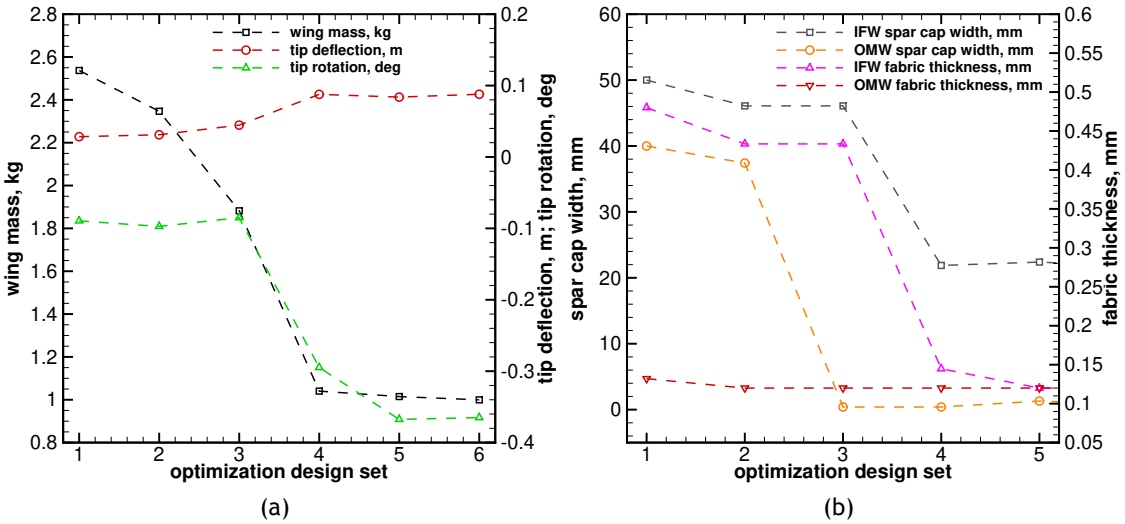

Figure 5.14: Baseline wing optimization design: (a) objective/constraint variables and (b) design variables.

Observing Fig.5.14, one can see that the wing mass was significantly reduced from 2.54 kg to 1 kg, indicating that the optimization started with design variables that were relatively far from the optimum. This can be confirmed from the constraint variables, w_{tip} and θ_{tip}, that are 0.028 m and -0.09° in the first set and 0.088 m and -0.36° in the final set. The upper bound of the tip deflection (0.088 m or 0.025 b) was reached, whereas the lower bound of the tip rotation -0.6° was not achieved. The latter happened since the skin laminates resist the majority of the torsion loading and they were limited by building requirements. This indicates that a thinner laminate could further lower the mass. On the other hand, the spar caps resist the majority of the bending loading and due to their higher design space, the tip deflection constraint was reached. Regarding the wing strength, it was not problematic since the $\overline{SR}_{TW}$ is not near the constraint value of 0.1%, being nearly ten times lower.

Using the optimized fabric thickness and spar cap widths, the wing was analysed in FEM. Wing surface plots of the vertical displacements and failure criterion were obtained to perform a detailed analysis. The former can be seen in Fig.5.15. The referred figure shows a displacement distribution which smoothly increases from root (on the left hand side) to tip. The displacement reaches a maximum of 0.088 m at the wing tip, being around 2.5% of the span. As expected, the maximum twist appears at the wing tip. Due to the relative magnitude of the fore web

and aft web vertical loads the VSW demonstrates a positive twist. It should be noticed that, as discussed in the previous paragraph, both tip deflection and rotation satisfy the imposed optimization constrains (<2.5% of span and between ± 0.6°).

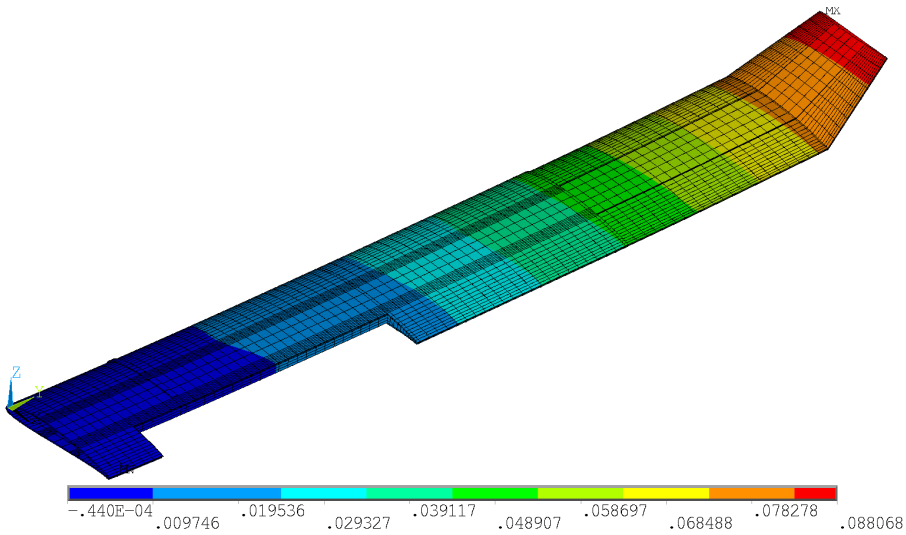

Figure 5.15: Vertical displacements of the optimized baseline VSW (displacements in m).

Figure 5.16 shows the inverse of *Tsai-Wu* strength ratio criterion of the baseline VSW, for the various material layers: outer sandwich laminate, sandwich core (foam and pultruded carbon/epoxy) and inner sandwich laminate.

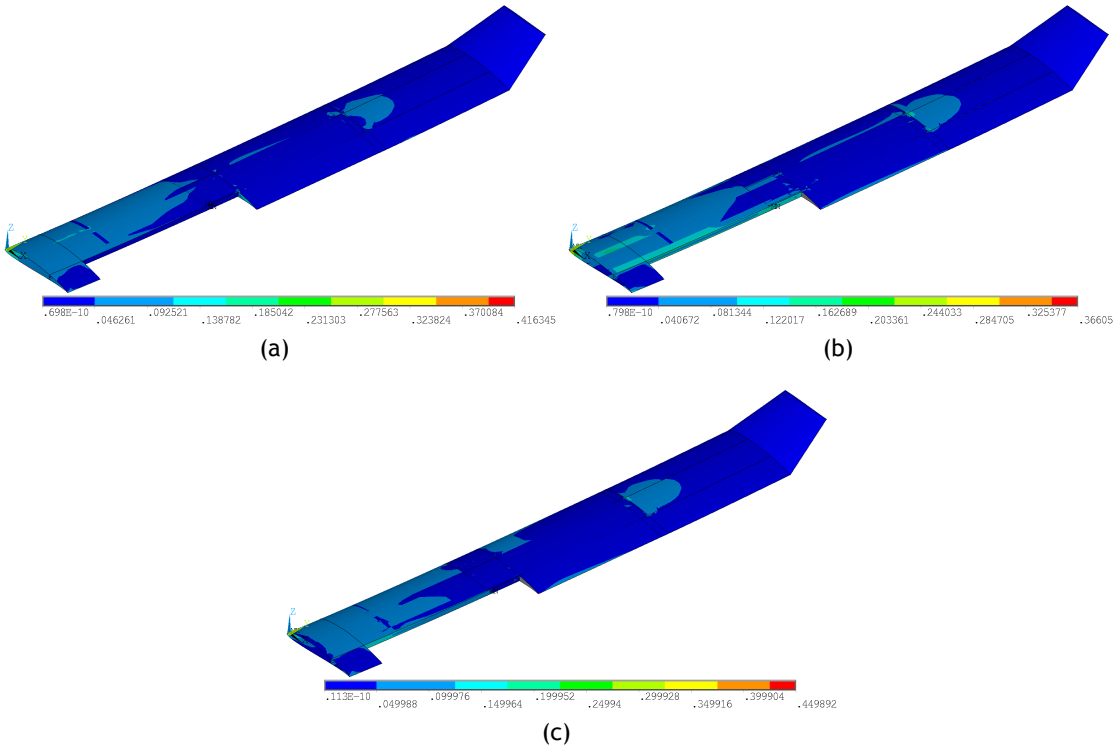

Figure 5.16: Inverse of *Tsai-Wu* strength ratio of the optimized baseline VSW: (a) outer sandwich laminate, (b) sandwich core (foam and pultruded carbon/epoxy) and (c) inner sandwich laminate.

Observing Fig.5.16, it is possible to conclude that both IFW and OMW are oversized since

the failure criterion never exceeds unity, being about 0.45 near the wing root. The more stressed areas of the IFW are located near the root and in the region of l_{over1} contact zone. In particular, the maximum failure criterion near the root area was to be expected since it is there that the maximum bending moment is present, along with the flap discontinuity, that creates a stress concentration. Regarding the moving portion of the VSW, one can see that it is relatively oversized, as evidenced by the even lower failure criterion. The more stressed areas are seen in the end of the second contact region (l_{over2}) between the two wing elements, being more pronounced in the location of the spar caps.

In conclusion, the generalized lightly loaded structure results from the fact that the minimum thicknesses allowed in the skin composite laminate were 0.12 mm, specially in the OMW, where the loads are much lower. It should be added that the use of bonded contact formulation reduced the accuracy of stress predictions near the contact zones. In fact, in the l_{over1} and l_{over2} areas the surfaces are bonded and no stress concentration can be identified due to the normal pressure effects. In the previous chapter (section 4.6.5), the use of a standard contact formulation clearly identified those zones with stress concentrations near the contact region.

5.5.4 Parameter Influence and Mass Estimation

The nonlinear ERR-Causality method was used to derive multivariable second order polynomials to predict wing mass and wing mass penalty. A total of three polynomials were computed: reference fixed-wing, VSW and VSW to fixed wing ratio. The latter effectively gives VSW mass penalty and was calculated to predict the increment in mass of a VSW, when compared with a fixed wing of the same dimensions and structural concept.

The used approximation method includes an arrangement of the significant terms from higher to lower significance. It is expected that using higher number of terms, the polynomial fitting precision would increase. However, in the present study a synthetic and accurate polynomial equation is desired, since it simplifies its use. Therefore, the equations should be as short and simple as possible. To simplify the polynomials a study of the SERR was performed. The variation of SERR was computed with increasing number of terms, until the variation was lower than a predetermined factor, called the convergence stopping criterion, being, in the current study, 0.1%. A higher value could be used to further simplify the polynomial. On the contrary, a lower value could be used to increase the fitting accuracy. A SERR value equal to 100% would stand for an ideal regression where there is a perfect relationship between the computed and the predicted data.

After computation of the polynomials, the influence of each parameter can be determined by a careful analysis of the obtained equations. Note that, the independent variables of the polynomials were considered as the difference between a given parameter and its average over the design space. Additional three-dimensional plots were produced to perform a graphical exploration of the most significant parameter interactions. The analysis of each polynomial approximation is performed in the following sections.

5.5.4.1 Fixed Wing

Table 5.8 shows the SERR study of the fixed wing polynomial. One can infer that SERR increases with increasing number of terms and that its variation is not linear. This is due to the different significance of each term. The convergence occurs for 12 terms, since $\triangle$SERR decreases below the convergence stopping criterion of 0.1% (0.04%). The increment in precision in the next set is 0.02%, being also below the convergence stopping criterion. It is important to analyse at least a further term, since the variation of SERR can occur in a lightly dampened oscillatory behaviour. The resulting SERR gives 99.72% of the solution, being close to 100%, which indicates that the strength of association between the variables is high and the method is adequate to fit the data. Note that with the complete polynomial, the SERR is 99.74%, thus, very little (<0.2%) would be gained by adding more terms.

Table 5.8: Fixed wing polynomial SERR calculated for different number of terms (convergence shown in bold).

	1	2	3	4	5	6	7	8
SERR	78.36%	86.16%	91.60%	94.45%	96.52%	98.13%	98.48%	98.76%
$\triangle$SERR		9.95%	6.32%	3.11%	2.19%	1.67%	0.35%	0.29%

9	10	11	**12**	13
99.01%	99.52%	99.68%	**99.72%**	99.74%
0.26%	0.51%	0.16%	**0.04%**	0.02%

Error metrics of the polynomial fitting were assessed and are shown in Table 5.9. The data in the table confirms that the second order polynomial produces an adequate fit of the data. The maximum relative error is below 10% and the maximum absolute error is below 0.050 kg, which is a low value, considering that the minimum computed wing mass is 0.259 kg.

Table 5.9: Fixed wing polynomial goodness of fit parameters.

Max. absolute error, kg	Max. relative error	RMSE, kg
0.048	0.098	0.0157

A visual validation of the approximation was performed by overlapping actual and predicted data and by plotting the actual data against the predicted data with error bounds. The former is presented in Fig.5.17(a) and the latter in Fig.5.17(b). Regarding Fig.5.17(a), one can see that some data points near the data peaks are not accurately represented. Thus, the maximum absolute error is certainly found in those places. Observing Fig.5.17(b), it is seen that the majority of the data points are in the neighbourhood of the $x = y$ line, being only three data points near the $\pm$ 10% error lines, thus validating visually the suitability of the employed method.

The resultant polynomial can be seen in Eq.(5.32). The terms are organized in decreasing

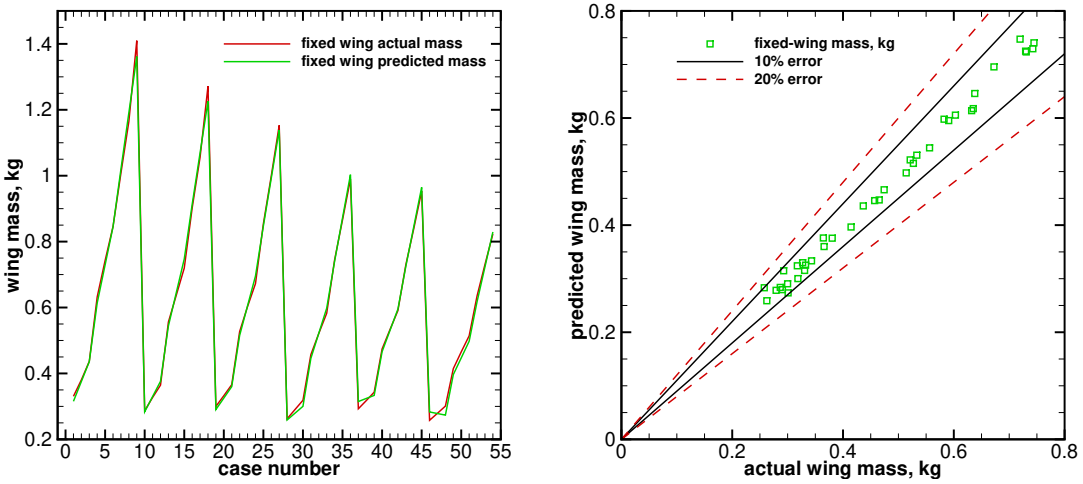

Figure 5.17: Data fitting assessment of the fixed wing polynomial: (a) actual and predicted data overlapped and (b) actual mass plotted against predicted mass with error bounds.

order of significance, facilitating the identification of the most significant ones.

$$\begin{aligned} m_{str,fw} &= f(b, c_{IFW}, \bar{c}_{flap}, W) \\ &= 0.3546\,(b-3.554) - 1.5466\,(c_{IFW}-0.321) + 0.002768\,(W-150) \\ &\quad -1.2893\,(b-3.554)(c_{IFW}-0.321) - 0.8358\,(\bar{c}_{flap}-0.35) + 0.002076\,(b-3.554)(W-150) \\ &\quad -0.01322\,(c_{IFW}-0.321)(W-150) - 0.4256\,(b-3.554)(\bar{c}_{flap} + 0.06819\,(b-3.554)^2 \\ &\quad -22.007\,(\bar{c}_{flap}-0.35)^2 + 5.9577\,(c_{IFW}-0.321)^2 - 0.00469\,(W-150)(\bar{c}_{flap}-0.35) + 0.6186 \end{aligned} \tag{5.32}$$

In Eq.(5.32), the parameter $(b-3.554)$ in the first term represents the difference between the given span and the average of the spans given in Table 5.2. The other terms follow a similar reasoning. Analysing the referred equation, one may acknowledge that span and chord (first and second terms) have the higher significance, accounting for 86.16% of the total significance. The high influence of b and c_{IFW} in the wing mass was already expected. In fact, a higher aspect ratio (higher span and/or lower chord) have the effect of increasing the root bending moment, demanding extra structural mass to comply with the structural constraints. The aeroplane weight is also important since wing loading is increased and, consequently, root bending moment increases. The additional linear parameter, flap chord ratio appears to be inversely correlated with wing mass. Therefore, an increase in flap chord, reduces the wing mass. However, caution should be taken, since the actual flap mass was not included in the study.

In order to visually analyse the interaction of parameters, three-dimensional plots were produced. Only the two most significant interactions are presented: span $\times$ IFW chord and span $\times$ weight. The data computed using the parametric study and the data approximated by the nonlinear regression are overlapped and illustrated in the form of scatter and surface plots, respectively. Figure 5.18 illustrates the three-dimensional plots of span and chord for the three weights, with constant flap chord ratio, and Fig.5.19 the three-dimensional plots of span and weight for the three studied chords, with constant flap chord ratio.

Observing Figs.5.18(a) to (c), one can verify an increase in mass with increasing span and decreasing chord. Increasing span, augments root bending moment, while lowering the chord

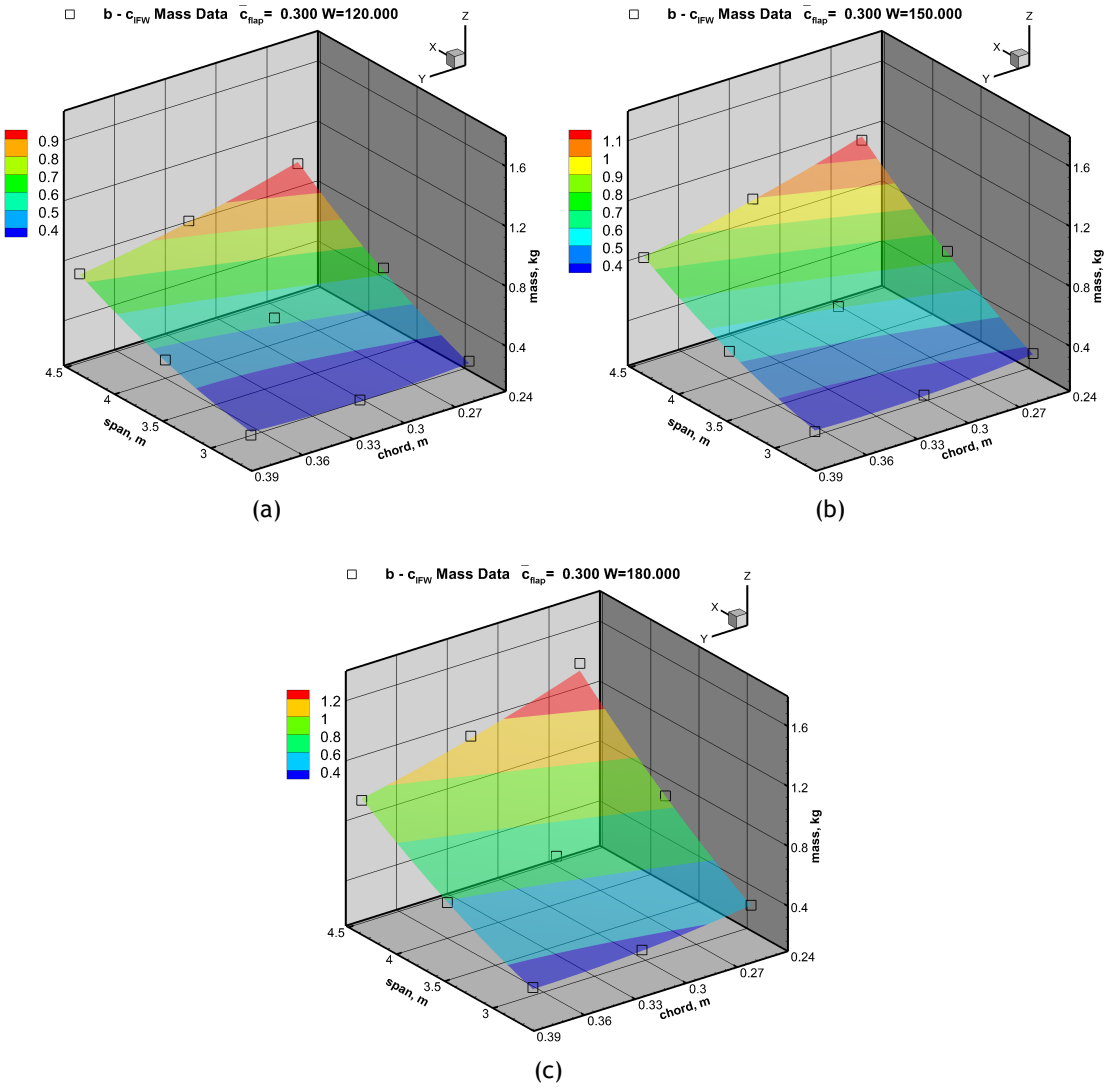

Figure 5.18: Fixed wing mass predictions and actual data points as functions of span and chord for the three studied weighs ($\bar{c}_{flap} = 0.3$): (a) 120 N, (b) 150 N and (c) 180 N.

reduces the section inertia, requiring more structural material, to achieve the same stiffness and strength. The trends are similar for the three aeroplanes weights, but the magnitudes vary considerably, as expected. In fact, for the lower aeroplane weight, the maximum wing mass is 1.03 kg, whereas for the higher weight, the maximum mass is 1.37 kg. However, the minimum wing mass is approximately similar for the three MTOWs, occurring for minimum span and maximum chord. The minimum mass varies between 0.332 kg and 0.376 kg.

Looking at Figs.5.19(a) to (c), one can see the same trend for all figures: increasing span and MTOW increases wing mass. The span increase has more impact in the wing mass than the MTOW variation, as indicated by the higher slope of the former. Maximum mass occurs for the smaller chord (Fig.5.19(a)), being 1.37 kg. As in the previous analysed figures, the minimum mass is approximately similar irrespective of the chord, varying between 0.335 kg and 0.363 kg, but occurs for minimum MTOW and span. One should also add that the variation is nearly linear, as evidenced by the near planar surfaces.

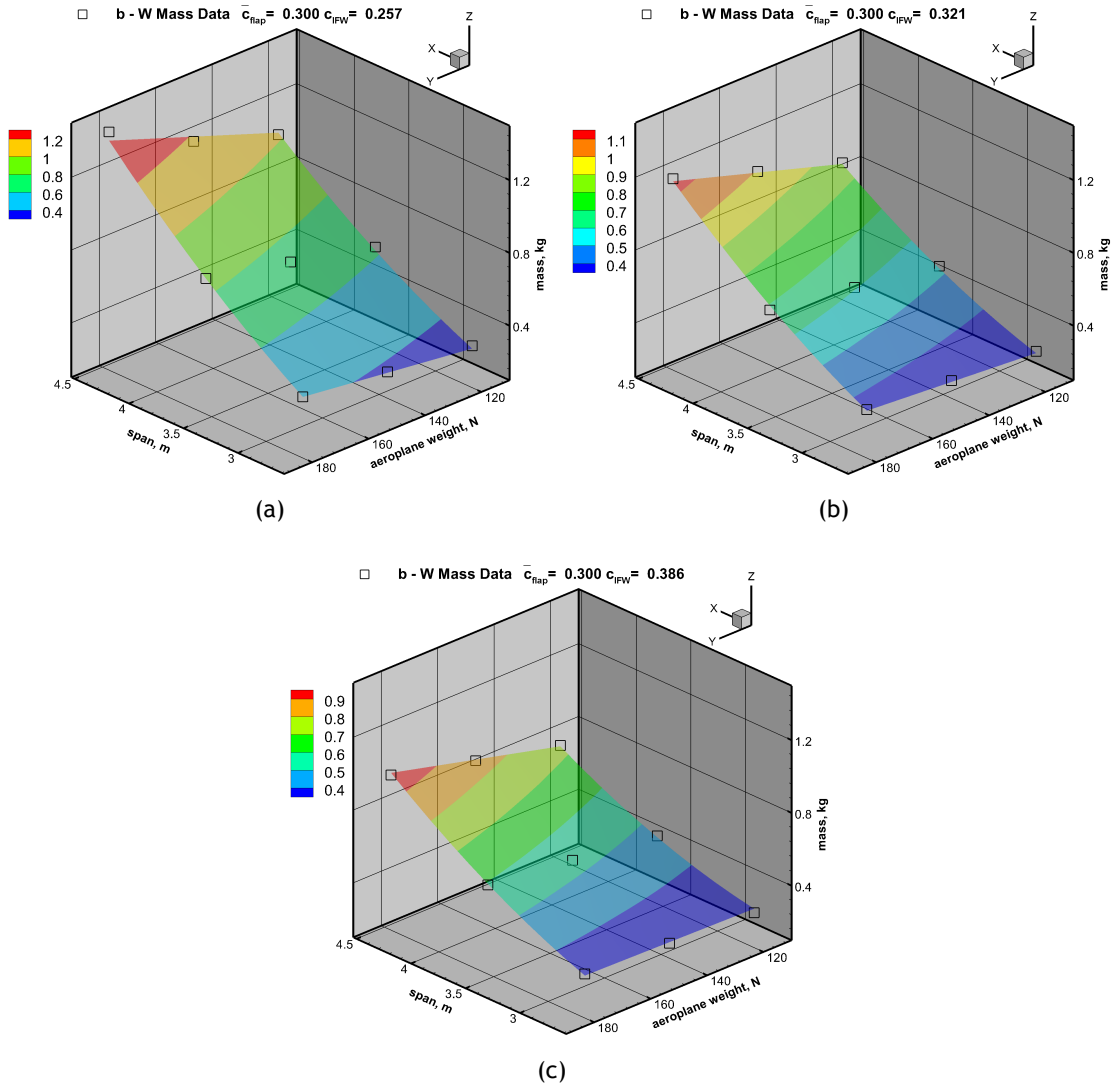

Figure 5.19: Fixed wing mass predictions and actual data points as functions of span and weight for the three studied wing chords ($\bar{c}_{flap} = 0.3$): (a) 0.257 m, (b) 0.321 m and (c) 0.386 m.

5.5.4.2 Variable-span Wing

Table 5.10 shows the SERR study of the VSW polynomial. Analysing the table, one can see that the convergence occurs for 13 terms, since ΔSERR decreases below the convergence stopping criterion of 0.1% (0.09%). The increment in precision in the next set is 0.06%, being also below the convergence stopping criterion. The resulting SERR with 13 terms gives 99.41% of the solution (total is 99.58%). As in the fixed wing polynomial, the resulting SERR value is close to 100%, which indicates that the strength of association between the variables is high and the method is adequate to fit the data.

Additional error metrics of the polynomial fitting were assessed, being shown in Table 5.11. By analysing the referred table, it becomes clear that the polynomial produces an adequate fit of the data. The maximum relative error is below 12%. The maximum absolute error is approximately 0.14 kg, which is a relatively high value. However, the RMSE error is only 0.023 kg, which indicates that the majority of the data points have a significantly lower value. To corroborate the previous statement, a visual validation was performed, using a plot that

Table 5.10: VSW polynomial SERR calculated for different number of terms (convergence shown in bold).

	1	2	3	4	5	6	7	8
SERR	80.72%	85.80%	90.15%	93.92%	95.81%	97.10%	97.45%	97.79%
ΔSERR		6.29%	5.07%	4.19%	2.01%	1.35%	0.36%	0.35%

9	10	11	12	**13**	14
98.47%	98.84%	99.11%	99.33%	**99.41%**	99.47%
0.70%	0.37%	0.27%	0.23%	**0.08%**	0.06%

overlaps the actual and predicted data and by plotting the actual data against the predicted data with error bounds. The former is presented in Fig.5.20(a) and the latter in Fig.5.20(b).

Table 5.11: VSW polynomial goodness of fit parameters.

Max. absolute error, kg	Max. relative error	RMSE, kg
0.139	0.119	0.0227

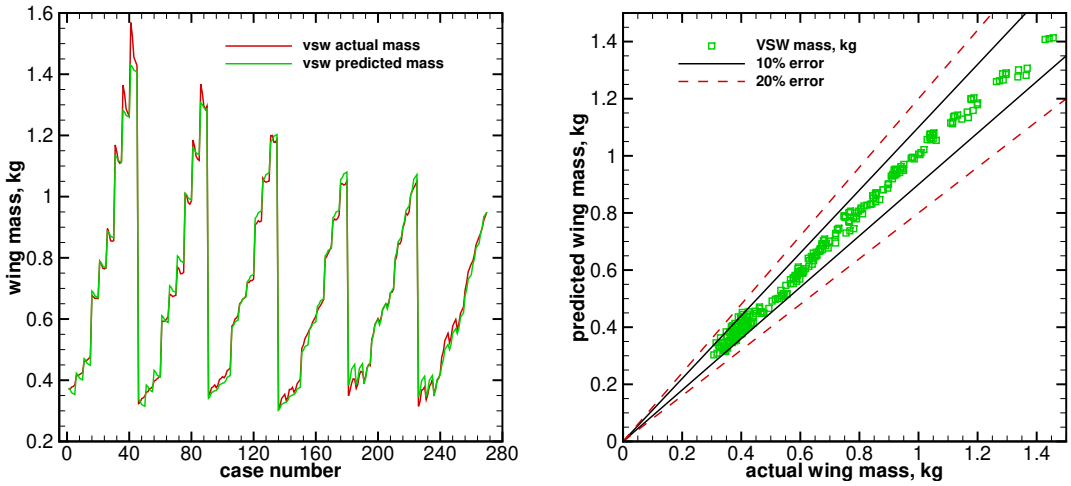

Figure 5.20: Data fitting assessment of the VSW polynomial approximation: (a) actual and predicted data overlapped and (b) actual mass plotted against predicted mass with error bounds.

In Fig.5.20(a), one can see that some data points near the data peaks are not accurately approximated. Probably this contributes to the higher maximum absolute and relative error. However, the majority of the data is well approximated, as can be seen in Fig.5.20(b). It can be observed that most points are in the neighbourhood of the $x = y$ line, being the majority of the data points effectively inside the $\pm$ 10% error lines.

The resultant polynomial is presented in Eq.(5.33). As in the previous polynomial, the

terms are organized in decreasing order of significance.

$$
\begin{aligned}
m_{str,VSW} &= f(b, c_{IFW}, \bar{l}_{var}, \bar{c}_{flap}, W) \\
&= 0.3632\,(b - 3.554) - 1.2557\,(c_{IFW} - 0.321) \\
&\quad + 0.002496\,(W - 150) - 1.4998\,(b - 3.554)(c_{IFW} - 0.321) - 0.8066\,(\bar{c}_{flap} - 0.35) \\
&\quad + 0.001875\,(b - 3.554)(W - 150) - 0.4752\,(b - 3.554)(\bar{c}_{flap} - 0.35) + 0.07991\,(b - 3.554)^2 \\
&\quad - 28.002\,(\bar{c}_{flap} - 0.35)^2 + 9.1823\,(c_{IFW} - 0.321)^2 - 0.01185\,(c_{IFW} - 0.321)(W - 150) \\
&\quad + 3.5632\,(c_{IFW} - 0.321)(\bar{l}_{var} - 0.153) - 1.0233\,(\bar{l}_{var} - 0.153) + 0.6893
\end{aligned}
\tag{5.33}
$$

Analysing Eq.(5.33) it is possible to conclude that the presented polynomial is similar to the fixed wing polynomial (Eq.(5.32)). The high influence of wingspan, weight and IFW chord on the wing mass is verified, both in linear and non-linear contributions. Interestingly, the variable-span ratio has a small contribution to the overall solution (0.3%). This is somewhat intriguing and is probably explained by the larger contribution of the other parameters, which effectively mask the effect of span change. This also indicates that the morphing interface is more complicated than anticipated and that the structural duplication, resulting from the IFW/OMW interface, could not be as significant as expected. Thus, further considerations about the influence of span change have to be deferred to the VSW to fixed wing ratio polynomial. The flap chord ratio is again inversely correlated with wing mass. However, as in the fixed wing case, caution should be taken, since the actual flap mass was not included in this study.

Similarly to the previous studied case, three-dimensional plots were produced to aid the visualization of the interaction between parameters. The most significant interaction is presented, being span $\times$ IFW chord. To aid the comprehension of the impact of the variable-span ratio, span is plotted against the latter. The data computed in the parametric study and the data approximated using the nonlinear regression are overlapped and illustrated in the form of scatter and surface plots, respectively. Figure 5.21 illustrates the three-dimensional plots of span and chord for two extreme variable-span ratios, with constant flap chord ratio and weight, and Fig.5.22 the three-dimensional plots of span and variable-span ratio for the three studied IFW chords, with the remaining parameters constant.

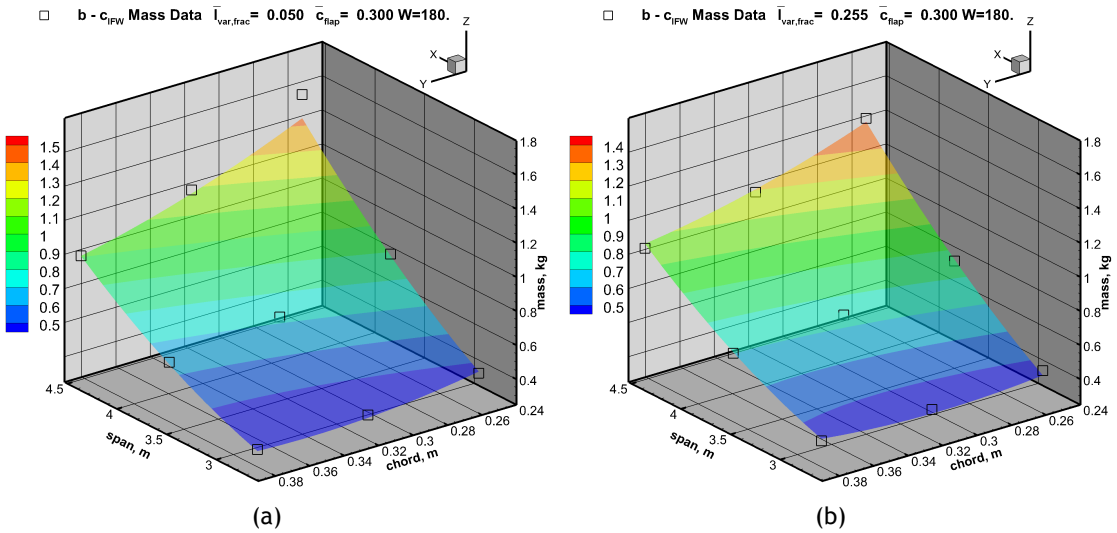

Figure 5.21: VSW mass predictions and actual data points as functions of span and IFW chord for two variable-span ratios ($\bar{c}_{flap} = 0.3$ and $W = 180$ N): (a) 0.05 and (b) 0.255.

Observing Figs.5.21(a) and (b), it is possible to see that the increase of the variable-span ratio causes a small decrease in the wing mass. The two figures show the same trends: the increase in span and the decrease in chord increases the wing mass. However, the span effect is slightly more pronounced than the chord effect. Additionally, the chord effect is more pronounced for higher span values. Therefore, higher mass occurs for maximum span and minimum wing chord. The maximum wing mass is 1.429 kg and 1.407 kg for the lower and higher variable-span ratios, respectively.

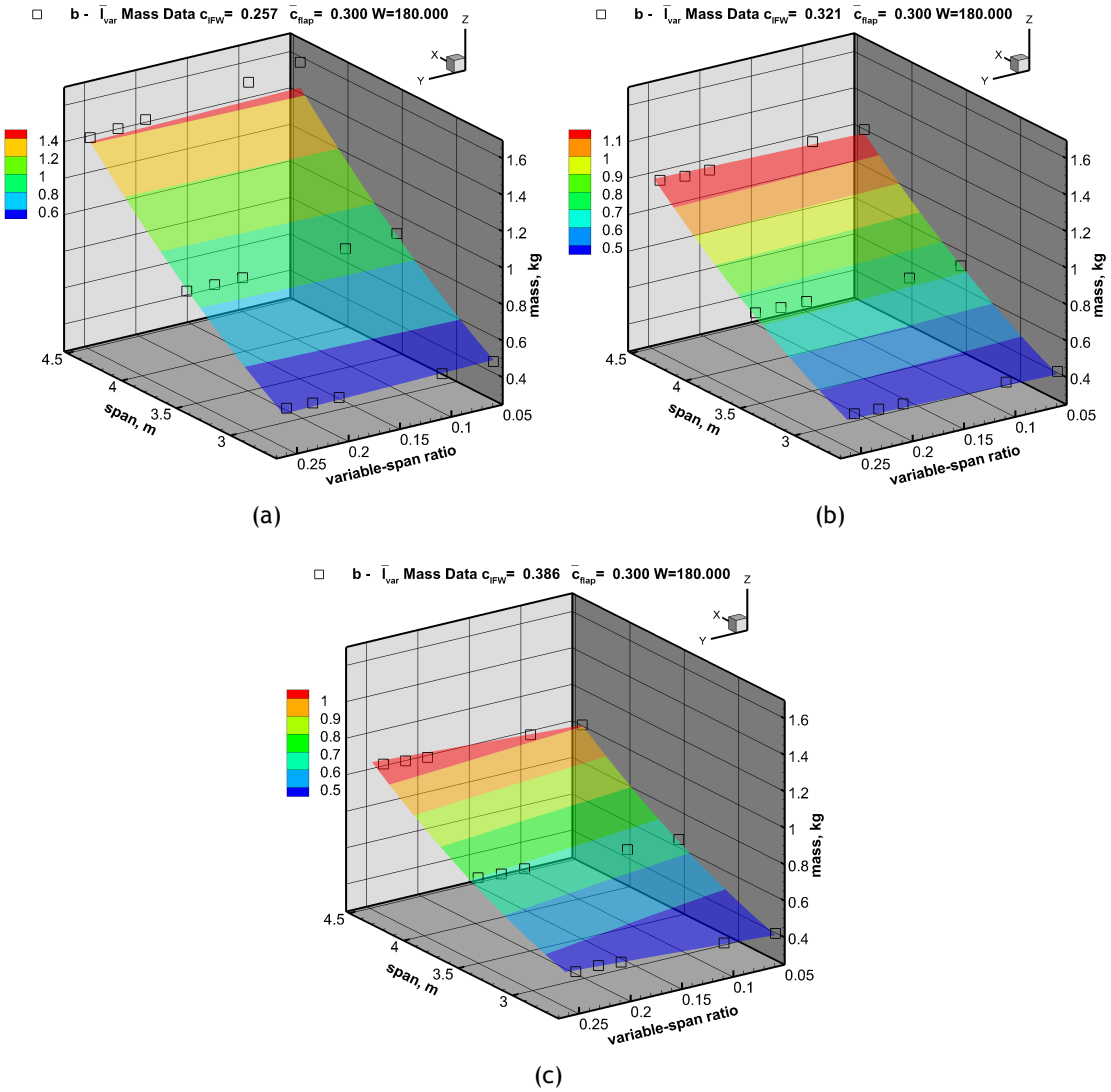

Figure 5.22: VSW mass predictions and actual data points as functions of span and variable-span ratio for the three studied IFW chords ($\bar{c}_{flap} = 0.3$ and $W = 180$ N): (a) 0.257 m, (b) 0.321 m and (c) 0.386 m.

Figures 5.22(a) to (c) show that the increase in chord causes a decrease in wing mass. The span has the highest influence on the wing mass, with the mass increasing with span. As anticipated from the polynomial analysis, the influence of the variable-span ratio is almost negligible, as evidenced by the near horizontal surfaces, in the variable-span ratio axis. Despite this, the lower chord shows a small mass reduction with increasing variable-span ratio, whereas the higher chord shows a mass increase. Therefore, the trend inverts between these two chords, being the slope nearly zero for the intermediate one (Fig.5.22(b)). This could be explained by the available area to transfer the loading between the IFW/OMW: the lower chord has less area

and the larger chord has more area. It should be added that, the higher wing mass is visible for the maximum span, minimum variable-span ratio and minimum chord. The maximum wing mass reaches 1.429 kg for the smaller chord and 1.005 kg for the larger chord.

5.5.4.3 Variable-span Wing Mass Ratio

Similar to the previous polynomials, a SERR study was performed. Table 5.12 shows the SERR study of the VSW to fixed wing polynomial. Analysing the table, one can see that convergence occurs for 16 terms with a $\triangle$SERR of 0.07%. The resulting SERR with 16 terms corresponds to 97.41% of the solution, being the maximum SERR 97.46%. Contrary to the fixed wing and VSW polynomials, the resulting SERR value is not as close to 100%. In fact, in the previous polynomials, the SERR was greater than 99% and in the current case barely exceeds 97.4%.

Table 5.12: VSW to fixed wing ratio polynomial SERR variation for different number of terms (convergence shown in bold).

	1	2	3	4	5	6	7	8
SERR	29.81%	58.84%	65.81%	72.66%	79.72%	85.83%	89.65%	91.96%
$\triangle$SERR		97.39%	11.84%	10.42%	9.71%	7.67%	4.45%	2.57%

9	10	11	12	13	14	15	**16**	17
92.88%	94.54%	95.20%	95.77%	96.36%	96.88%	97.34%	**97.41%**	97.44%
1.00%	1.78%	0.70%	0.60%	0.61%	0.54%	0.48%	**0.07%**	0.027%

Additional error metrics of the polynomial fitting were assessed and are shown in Table 5.13. Analysing the referred table, it is evident that the approximation has sufficient accuracy. The maximum relative error is below 5% and RMSE error is 0.016, which indicates that the majority of the data points have significantly lower error values.

Table 5.13: VSW to fixed wing ratio polynomial goodness of fit parameters.

Max. absolute error	Max. relative error	RMSE
0.0536	0.0485	0.0163

Similar to the previous studied polynomials, a visual validation was performed. Figure 5.23(a) presents the actual and predicted data overlapped and Fig.5.23(b) the actual data plotted against the predicted data with error bounds. Observing Fig.5.23(a), one can see that some data points near the data peaks are not accurately approximated, specially for reduced mass ratios. This effect was already observed in the previous polynomials. However, the majority of the data is well approximated, as can be seen in Fig.5.23(b), since most data points are in the neighbourhood of the $x = y$ line. In fact, the relative error is considerable lower than in the previous polynomials.

The resultant polynomial is presented in Eq.(5.34). Again, the terms are organized in

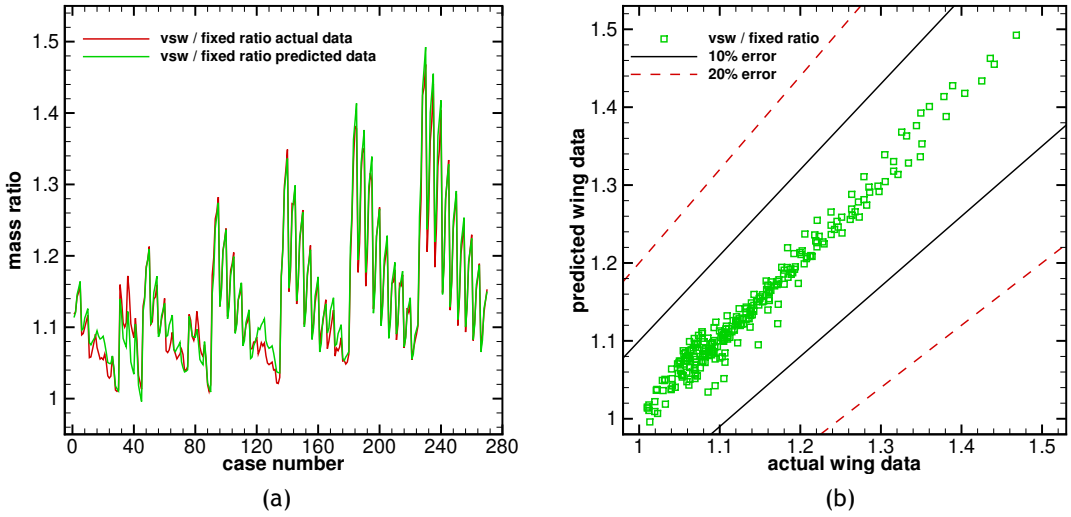

Figure 5.23: Data fitting accuracy of the VSW to fixed wing mass ratio: (a) actual and predicted data overlapped and (b) actual mass ratio plotted against predicted mass ratio with error bounds.

decreasing order of significance.

$$
\begin{aligned}
m_{str,VSW/fw} = f(b, c_{IFW}, \bar{l}_{var}, \bar{c}_{flap}, W) &= -0.06964\,(b-3.554) \\
&+ 0.9585\,(c_{IFW}-0.321) - 0.6468\,(b-3.554)(c_{IFW}-0.321) \\
&+ 0.3507\,(\bar{l}_{var}-0.153) + 6.1716\,(c_{IFW}-0.321)(\bar{l}_{var}-0.153) \\
&- 0.0009336\,(W-150) - 0.3275\,(b-3.554)(\bar{l}_{var}-0.153) + 0.2809\,(\bar{c}_{flap}-0.35) \\
&+ 0.0400\,(b-3.554)^2 + 3.8598\,(c_{IFW}-0.321)^2 + 1.8603\,(\bar{l}_{var}-0.153)\bar{c}_{flap} \\
&+ 2.6966\,(c_{IFW}-0.321)(\bar{c}_{flap}-0.35) - 0.1838\,(b-3.554)(\bar{c}_{flap}-0.35) \\
&- 0.003389\,(\bar{l}_{var}-0.153)(W-150) + 0.7316\,(\bar{l}_{var}-0.153)^2 + 1.1066
\end{aligned}
\tag{5.34}
$$

Analysing Eq.(5.34) it is possible to see that, again, span and chord have the higher effect, both with linear and non-linear contributions. However, contrary to the previous polynomial, the variable-span ratio has now a significant contribution appearing has a linear parameter and also combined with chord. This corroborates the fact that the other parameters were effectively masking the effect of the span variation ratio. The impact of the latter is complex, being the three-dimensional plots crucial to interpret the influence between parameters. Two interactions are presented: span $\times$ IFW chord and span $\times$ variable-span ratio. Figure 5.24 illustrates the three-dimensional plots of span and IFW chord for four variable-span ratios, with constant flap chord ratio and aeroplane weight, and Fig.5.25 the three-dimensional plots of span and variable-span ratio for the three studied IFW chords, with constant flap chord ratio and aeroplane weight.

Figure 5.24(a) to (d) demonstrates an interesting and complex influence of span and chord. Different trends are visible for the four variable-span ratios. Among the four variable-span ratios, the mass prediction surface appears to rotate along a diagonal line that crosses the minimum span and maximum chord points, in the sense of increasing the maximum mass penalty, while keeping the minimum approximately constant. Thus, higher mass penalties occur for minimum span and maximum chord. On the other hand, for each span ratio appears to exist a combination of span and chord that minimizes the mass penalty of the morphing wing. For $\bar{l}_{var} = 0.05$, the minimum occurs for an intermediate chord and span, whereas for $\bar{l}_{var} = 0.255$,

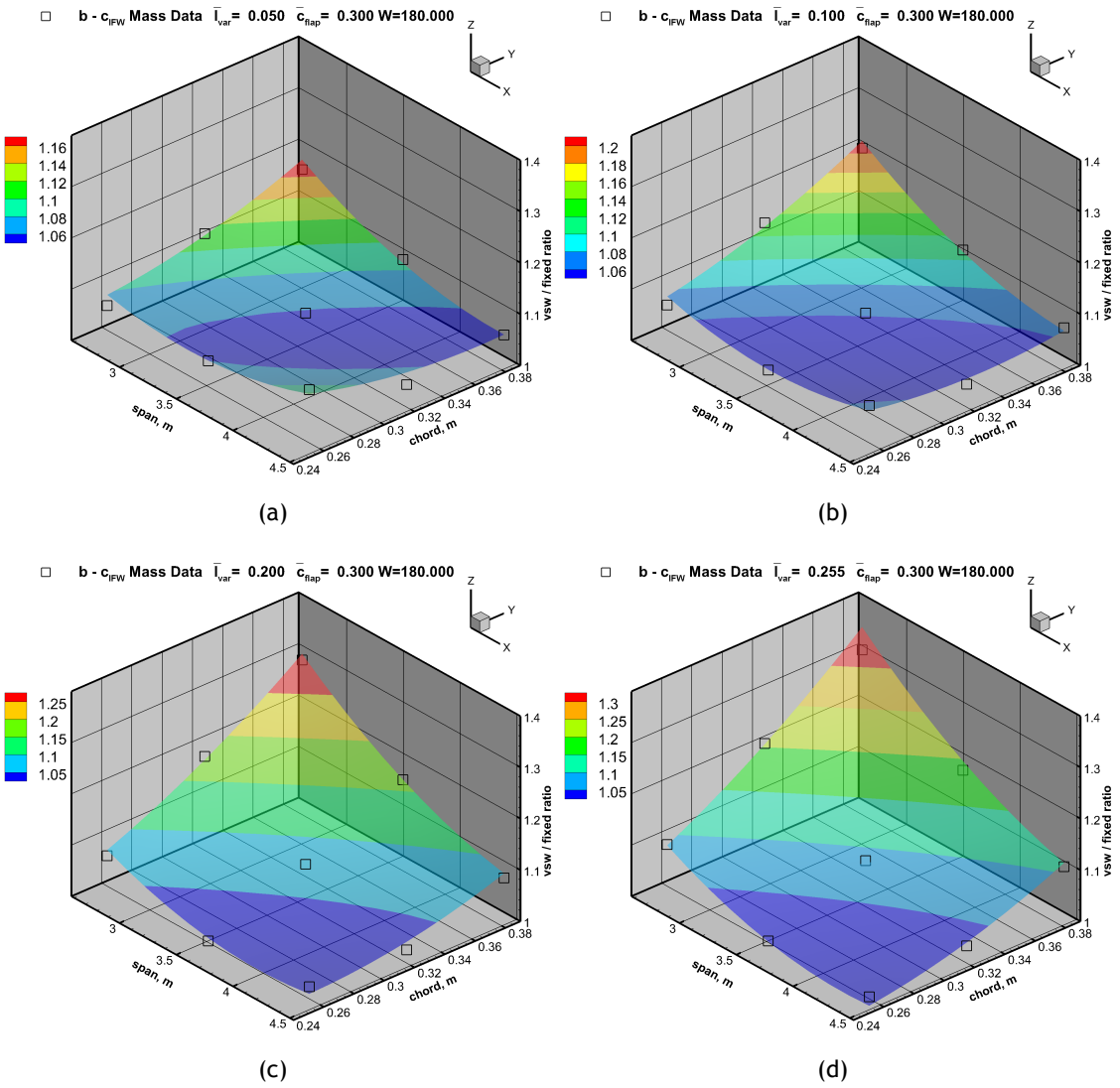

Figure 5.24: VSW to fixed wing ratio mass predictions and actual data points as functions of span and IFW chord for four variable-span ratios ($\bar{c}_{flap} = 0.3$ and $W = 180$ N): (a) 0.05, (b) 0.1, (c) 0.2 and (d) 0.255.

maximum span and minimum chord grants the minimum mass penalty. The maximum penalty reaches 1.177 for the lower variable-span ratio and 1.350 for the higher variable-span ratio.

Observing Fig.5.25(a) until (c), one can see distinct trends for the three chords. The lower chord has two peaks of higher mass penalty for minimum span and maximum variable-span ratio and vice-versa. In the second chord, only one peak exists and is more marked, occurring for minimum span and maximum $\bar{l}_{var}$. In the higher studied chord (Fig.5.25(c)), the latter effect is even more marked, being the mass penalty 1.350. In fact, a rotation of the surfaces about the maximum span, minimum variable-span ratio diagonal is observed. Therefore, it is not a straightforward task to conclude which variable-span ratio minimizes the mass penalty for a given span and chord. However, the plots show that for a given span and chord, there is a $\bar{l}_{var}$ that minimizes the mass penalty of using the VSW. The maximum penalty reaches 1.104 for the smaller chord.

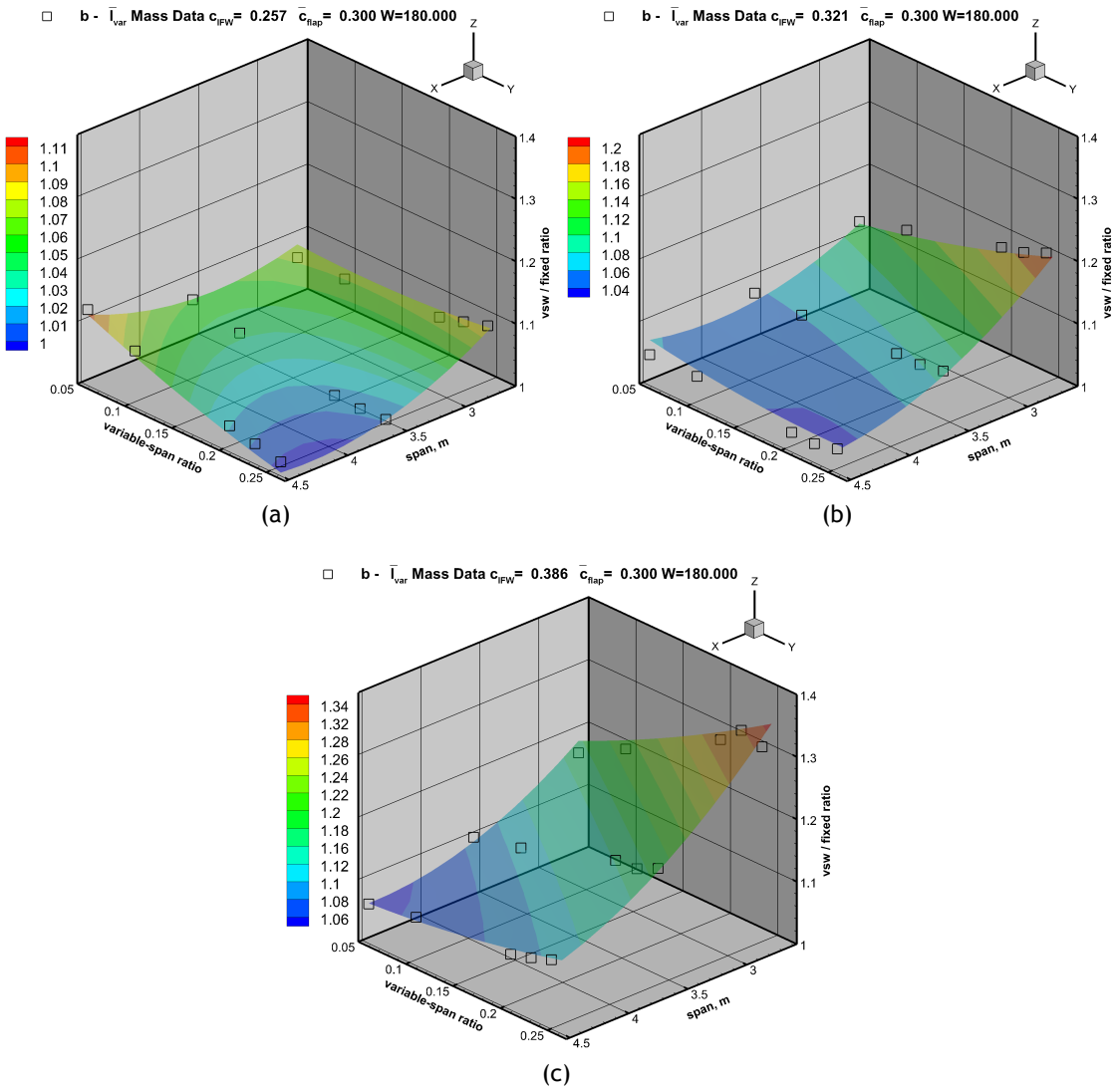

Figure 5.25: VSW to fixed wing ratio mass predictions and actual data points as functions of span and variable-span ratio for the three studied IFW chords ($\bar{c}_{flap} = 0.3$ and $W = 180$ N): (a) 0.257 m, (b) 0.321 m and (c) 0.386 m.

5.6 Wing Mass Prediction Model

In the previous section, the structural mass of a fixed wing and a VSW has been computed. Based on those data points, the ratio of the two wing masses were computed to effectively create a polynomial of VSW to fixed wing mass ratio, which predicts the mass increase of using the VSW. Thus, the objective of the current work is to use the latter to correct an existing mass model. This is a desirable endeavour, since a designer that has access to a mass model that is already validated, can use this approach to correct it, if considering a span changing morphing approach. Therefore, the polynomial approximation is used to correct an existing fixed wing mass model. Usually, semi-empirical mass models already include the actuation system mass in the full equation. Since the developed polynomial only considers the structural mass increment, the system's mass should be subtracted. Later, the contribution of the flap and actuation system

masses can be added. Thus

$$m_{VSW} = \overline{m}_{str,VSW/fw}(m_{fw} - m_{sys,fw}) + m_{flap} + m_{act,sys} \tag{5.35}$$

where m_{VSW} is the complete wing mass, $\overline{m}_{str,VSW/fw}$ is the fixed wing to VSW mass ratio polynomial (obtained from Eq.(5.34)), $m_{sys,fw}$ is the system's mass of the fixed wing, m_{flap} is the flap mass, and $m_{act,sys}$ is the span actuation system mass. Notice that the first term effectively gives the structural mass of the VSW, $m_{str,VSW}$. The polynomial of Eq.(5.34) can be simplified into the following polynomial

$$\begin{aligned} m_{str,VSW/fw} = f(b, c_{IFW}, \bar{l}_{var}, \bar{c}_{flap}, W) = &-0.0318b - 1.10797c_{IFW} \\ &- 0.64679bc_{IFW} - 0.83412\bar{l}_{var} + 6.1716c_{IFW}\bar{l}_{var} - 0.0004168W \\ &- 0.32748b\bar{l}_{var} - 0.21589\bar{c}_{flap} + 0.0400b^2 + 3.8598c_{IFW}^2 + 1.8603\bar{l}_{var}\bar{c}_{flap} \\ &+ 2.6966c_{IFW}\bar{c}_{flap} - 0.1838b\bar{c}_{flap} - 0.003389\bar{l}_{var}W + 0.73159\bar{l}_{var}^2 + 1.4376 \end{aligned} \tag{5.36}$$

In the next sections, the flap mass (m_{flap}) and the span actuation system mass ($m_{act,sys}$) prediction models development is presented.

5.6.1 Flap Mass Prediction Model

In the current approach, the flap mass model was developed considering either a simple shell with no actuation or an adaptative flap. Thus, flap mass can be divided in two contributions

$$m_{flap} = m_{str,flap} + m_{act,flap} \tag{5.37}$$

where, $m_{str,flap}$ is the structural mass and $m_{act,flap}$ the actuation system mass. To estimate the former, a flap area ratio is used to correct the structural mass. Thus

$$m_{str,flap} = k_{flap}\,\frac{S_{flap}}{S_{VSW}}\,m_{str,VSW} \tag{5.38}$$

with k_{flap} equal to 1 if using a simple shell with no actuation, and greater than 1 if an adaptative flap is used. The flap area is given by

$$S_{flap} = c_{IFW}\,\bar{c}_{flap}\,l_{flap} \tag{5.39}$$

The adaptative flap actuation mass can be estimated using the following equation

$$m_{act,flap} = \Omega_{act,flap}\,S_{flap} \tag{5.40}$$

being $\Omega_{flap,act}$ the flap actuation system mass density. This parameter has a typical value of 1.9 kg/m^2 when considering conventional actuation [57]. For other actuator types it is difficult to estimate, given the high variability of actuation systems methodologies.

5.6.2 Actuation System Mass Prediction Model

The actuation system mass was derived using a semi-empirical approach. Data from the suppliers and informed guesses were merged together to derive a realistic prediction. The mass of the actuation system can be subdivided in the following contributions

$$m_{act,VSW} = 2\left(m_{motor} + m_{rack} + m_{others}\right) \tag{5.41}$$

where m_{motor} is the gear-motor and actuation pinion mass, m_{rack} is the rack mass and m_{others} is a term that accounts for brackets, mounting ribs, motor controller, additional gearing and cabling. The actuation system components can be installed in a centre bay, or in the OMW root, moving together with the latter. This impacts the amount of cabling and rack lengths and, thus, should be taken in consideration. To account for this, m_{rack} and m_{others} mass terms have two different equations. The whole equation is multiplied by two to account for the need of two sets of actuators.

In the VSW, span variation can be used for performance or for performance and roll control. In the latter, the speed requirements are higher and thus, more powerful motors are needed, which translates into a higher actuation system mass. To account for this, a binary value was introduced, $k_{act,type}$, being 0 for performance only and 1 for performance and roll control.

The gear-motor mass was estimated by analysing a database of geared DC motors available in [165, 166]. Two motor series were considered: 25D and 37D. For each series various gear ratios are available, being the mass variation small (<4 g). Therefore, for the performance scenario the motor mass is the 25D series average mass and for performance and roll control it is corrected for the mass of 37D series. Thus

$$m_{motor} = 0.1 + 0.12\, k_{act,type} + 0.02 \tag{5.42}$$

where, 0.1 kg is the mass of the 25D DC gear-motor, 0.12 kg is the mass difference between motor series and 0.02 kg is the pinion mass.

The rack mass is proportional to the variable-span length. The $k_{act,type}$ is used to account for the increased mass, necessary to avoid buckling during the higher accelerations, when the system is used to perform roll control. Thus

$$m_{rack} = 1.1\; 0.102\, b\,(1 - \bar{l}_{var})\,(1 + 0.1\frac{b}{3} + 0.25\, k_{act,type}) \tag{5.43}$$

$$m_{rack} = 1.1\; 0.102\, b\,\bar{l}_{var}\,(1 + 0.1\frac{b}{3} + 0.25\, k_{act,type}) \tag{5.44}$$

where, 0.102 kg/m corresponds to the rack mass per metre, being computed based on a standard section of 6 mm $\times$ 15 mm made with Ertalon LFX. This standard section was sized for a wingspan of 3 m, being corrected with a term proportional to $0.1b/3$. The factor 1.1 accounts for the extra rack length needed for fixtures and feedback. This value is increased by 25% if roll control is to be performed, due to higher force transmission. Equation (5.43) is used when the actuation system is installed in a central bay and Eq.(5.44) when installed in the OMW's root.

Finally, the m_{others} mass contribution was added to account for brackets, mounting ribs,

motor controller, feedback potentiometer and respective gear and cabling. Thus

$$m_{others} = 0.1 \tag{5.45}$$

$$m_{others} = 0.1 + 0.03\, b\, (1 - \bar{l}_{var}) \tag{5.46}$$

where, Eq.(5.45) is used for centre mounted system, being independent of the geometric parameters and Eq.(5.46) for OMW mounted system. In the latter, an extra term is added that accounts for the necessity to add cable from the fuselage to the OMW. The constant 0.03 kg/m corresponds to the cabling mass per metre.

5.7 Wing Mass Prediction Model - Case Study

The VSW mass model developed in the previous section is now applied to the VSW presented in chapter 2, in order to provide a case study. Recalling the mass model equation (illustrated in Eq.(5.35)), one concludes that a fixed wing mass model is needed. In the present work, an adapted version of the general aviation wing mass model from [124] was used. This equation accounts for structural and actuation systems mass and has the following form

$$m_{fw} = 0.0465\, S^{0.758} \left(\frac{AR}{\cos^2 \Lambda}\right)^{0.6} \lambda^{0.04} \left(\frac{100\, t/c}{\cos \Lambda}\right)^{-0.3} (n_{design} W)^{0.49} \tag{5.47}$$

where, λ is the taper ratio and Λ is the wing sweep.

Due to the fact that Eq.(5.47) accounts for both structural and systems weights, the latter contribution, $m_{sys,fw}$, has to be subtracted. Previous built conventional wings of RPASs in the same weight class were analysed and it was found that the actuation system mass accounts for approximately 12.5% of the total wing mass. Therefore, this value was used to correct the fixed wing mass.

The VSW has the geometrical and inertial characteristics presented in Table 5.14. These are important to feed the fixed wing model and the polynomial approximation.

Table 5.14: Geometrical and inertial parameters of the first VSW prototype.

b, m	c_{IFW}, m	$\bar{l}_{var}$	$\bar{c}_{flap}$	W, N	t/c	n_{design}	λ	Λ, deg
2.5	0.265	0.45	0	60	0.1	6	1	0

Since the actuation system is located in a central bay, its mass is estimated using Eqs.(5.42), (5.43) and (5.45). Additionally, the actuation system is used to perform roll control and, thus, $k_{act,type}$ is 1. On the other hand, the VSW does not have a flap and because of this the flap mass model was not used.

Table 5.15 summarizes the results of the mass prediction model along with the actual wing weights, to facilitate comparison. The VSW actual weights were extracted from Table 2.7 (chapter 2).

Observing Table 5.15, one can see that the VSW mass model provides a good approximation, exhibiting an error below 10%. In particular, the actuation system approximation overestimates the mass with an error below 3%, being the main error source the rack mass

Table 5.15: Mass model predictions and actual prototype weights.

Component	Predicted mass, kg	Actual mass, kg	Error, %
m_{motor}	0.480	0.490	
m_{rack}	0.206	0.171	
m_{others}	0.100	0.106	
$m_{act,VSW}$	0.786	0.767	2.4%
$m_{str,VSW}$	1.198	1.079	11.0%
m_{VSW}	1.983	1.846	7.4%

approximation. This is interesting, since the first VSW have racks made with aluminium, which were expected to be heavier. The structural mass of the VSW demonstrated the higher error, being 11%, but is nevertheless an acceptable approximation.

5.8 Concluding Remarks

In this chapter, the derivation of a mass model of a VSW with an adaptive flap was described. This model was created by using an existing conventional wing mass model, corrected using a polynomial approximation that estimates the mass increase of using a VSW.

Mass and mass ratio functions were created by fitting multivariable polynomials: fixed wing mass, VSW mass and VSW to fixed wing mass ratio. The polynomial approximations were derived based on a parametric study, which analysed the impact of wingspan, wing chord, span variation ratio, flap chord ratio and aeroplane weight. Then, a minimum mass optimization problem was developed in ANSYS® with stiffness and strength constraints, being the design variables structural thicknesses and widths. A parametric structural FEM was built to allow the structural analyses to be performed. The study was done for a conventional fixed wing and the VSW, which were then combined to ascertain the VSW mass increment, i.e., the mass penalization of the adopted morphing concept. The polynomials were found to produce good approximations of the wing mass. Additionally, the effects of various VSW design parameters in the structural mass were inferred and synthesized. On one hand, it was found that span and chord have the highest impact in the wing mass. On the other hand, the VSW to fixed wing mass ratio proved that the influence of span variation ratio in the wing mass is more complex than anticipated. In fact, it was found that the mass increase does not grow proportionally with span variation ratio and that, for each combination of span and chord, there exists a span variation ratio that minimizes the mass penalty.

Based on the VSW to fixed wing ratio polynomial and the contributions of the actuation system and the adaptative flap, a mass model was derived. In order to ascertain its accuracy, a case study was performed, using the original VSW (described in chapter 2) as reference. A satisfactory mass estimation was observed, with errors below 10%.

The work presented showed that the conceptual idea behind the development of the morphing wing mass equation is relatively straightforward. However, the implementation of the overall process revealed some complex areas, namely the one related with the sizing loads. The CS-VLA regulation was used to derive credible loads. However, these are only applicable for low wing loading aeroplanes and in the speed range of the regulation (Ma<0.3).

Chapter 6

Conclusions and Recommendations

6.1 Executive Summary

A fully functional VSW system was developed covering areas from aerodynamic optimization and structural design, to composite prototyping manufacturing and actuator and structural testing. In the aerodynamic design optimization it was found that, at low speeds, the original fixed wing has slightly better performance than the VSW, due to the performance reduction of the modified aerofoil, the higher relative thickness ratio of the IFW aerofoil and the increase in vehicle's weight. However, for speeds higher than 25 m/s the performance trend was inverted, since the retraction of the OMW occurs, which reduced the wing area and consequently the total wing drag. To aid the structural design a FEM was created in a commercial software and the effect of the interface between the IFW and the OMW was studied in detail. Static aerodynamic loading conditions were analysed for various load factors, which proved that the VSW structure can withstand the flight loads. Additionally, an aeroelastic study was performed, focusing on the flutter critical speed estimation. It was concluded that the effect of rigidity loss in the interface between the IFW and the OMW, has a negative impact on the critical flutter speed. Nevertheless, the flutter speed was outside the flight speed envelope required for Olharapo RPAS. A full-scale prototype was built to allow the pursuit of several ground tests. The wing was built using composite materials and an electro-mechanical actuation mechanism was developed using an aluminium rack and pinion system driven by two servomotors. The ground evaluation focused on the structural elements and the actuation system. The static bending testing demonstrated that the wing can withstand loads up to 4.5G at its maximum wingspan configuration. The actuation system testing revealed that the deployment time was low (1.8 s for the 0G condition). The system efficiency testing determined that the maximum efficiency is around 51% for the 0G load case and decreases to about 27% at the 4G condition.

Following the ground testing of the VSW, it was concluded that it was suitable to be installed on Olharapo 2H RPAS airframe for in-flight testing. The airframe changes necessary to fit the VSW and the instrumentation for evaluating the VSW in-flight were described. Two sets of flight tests were done: aerodynamic and energy characterization. The former aimed at determining the lift-to-drag ratio for different airspeeds and the latter was performed to measure the propulsive and manoeuvring energy when performing a given mission, which was chosen in such a way that the multi-role capability of the VSW could be exercised. In the aerodynamic testing, in-flight evaluation of the RPAS fitted with the VSW demonstrated full flight capability and showed improvements produced by the VSW over a conventional fixed wing for speeds above cruise speed. At low speeds, the original wing has slightly better performance than the VSW. The performance trend was inverted beyond approximately 19 m/s, where the fully retracted VSW was better than the conventional wing. At this airspeed the L/D exceeds the one of the conventional wing. The benefit continued to increase, being the VSW in minimum span configuration 35% better than the original fixed wing at 30 m/s. In the other performed

test, it was concluded that the VSW fitted RPAS has less overall energy consumption despite the increased vehicle's weight. The energy reduction occurred only in the high-speed condition but was so marked that it offset the increase in energy during takeoff, climb and loiter phases.

Based on the knowledge gained from designing, building and flight testing the above mentioned VSW, a new telescopic wing concept that allows the integration of other morphing strategies was developed. In fact, it was identified that the geometric compatibility between IFW/OMW, severely limits the hardware integration near the wing root and creates a barrier to the integration of other moving surfaces. The new morphing wing was developed within the CHANGE project. The capabilities adopted for this wing were span change, and LE and TE camber changes. A modular design philosophy was adopted, such that the individual systems could be separately developed and then integrated. The modular design was based on a wing-box like structure. The structure was sized for strength and stiffness using FEM, based on flight loads derived from the mission requirements. The development of a partial span, full-sized cross-section prototype allowed the validation of the structural performance and actuation mechanism capability and durability. The structural static testing showed similar trends, when compared with the numerical predictions, which indicated the correctness of numerical predictions and building methods. The actuation mechanism was characterized in terms of actuation speed and specific energy consumption and it was concluded that it functioned within its designed specifications. Durability testing showed that the system outperforms the specifications and was capable of reliable functioning for at least 1000 extension/retraction cycles. A full-wing prototype was built by the consortium and the LE and TE concepts from the different partners were integrated in a single wing. The concept was validated using wind tunnel and flight testing. The wind tunnel testing confirmed system functionality under load. Hence, structural integrity was maintained in all studied situations. The flight testing was carried out by TEKEVER and showed that the modular concept worked reliably. However, the flight testing campaign was not sufficiently detailed, which severely limited the conclusions that could be extracted, since no flight data was recorded and a comparison flight with a baseline wing was not executed.

The work in the last chapter was performed to create a mass model of a VSW with a TE device, located in the IFW near the wing root. The performed work tries to eliminate a lacuna, due to the virtual non-existence of accurate mass prediction methods for designing morphing wings at the conceptual design phases. The model was created by using an existing conventional wing mass model, corrected using a newly developed polynomial approximation that estimates the mass increase of using a VSW. Mass and mass ratio functions were created by fitting multivariable polynomials: fixed wing mass, VSW mass and VSW to fixed wing mass ratio. The polynomial approximations were derived based on a parametric study, which analysed the impact of wingspan, wing chord, span variation ratio, flap chord ratio and aeroplane weight. A minimum mass optimization problem with stiffness and strength constraints was implemented and solved for a sufficient number of combinations of the wing parameters, being the design variables structural thicknesses and widths. A parametric FEM of the wing was built in APDL and solved in ANSYS®. The study was done for a conventional fixed wing and the VSW, which were then combined to ascertain the VSW mass increment, i.e, the mass penalization of the adopted morphing concept. The polynomials were found to produce good approximations of the wing mass. Additionally, the effects of the various VSW design parameters in the structural mass were inferred and synthesized. On one hand, it was found that the span and chord had the highest impact in the wing mass. On the other hand, the VSW to fixed wing mass ratio proved that the influence of span variation ratio in the wing mass is more complex than anticipated. In fact, it

was found that the mass increase does not grow proportionally with span variation ratio and that for each combination of span and chord, exists a span variation ratio that minimizes the mass penalty. The VSW to fixed wing ratio function was then used to derive the mass model. Equations to estimate flap mass and span variation actuation system were developed, using semi-empirical information. In order to ascertain the accuracy of the model, a case study was done, using the original VSW (presented in chapter 2) as reference. Satisfactory mass estimation results were observed, with errors below 10%. Although the mass model results were encouraging, more case studies are necessary to prove its applicability over a wide range of VSWs.

To summarize all the work performed, one can say that VSW concepts are able to achieve considerable geometry changes, which in turn translates into considerable aerodynamic gains, despite the increased weight. They influence all aspects of the wing design, from the structural side to the actuation mechanisms. The adopted concept, a telescopic wing, has numerous advantages related with simplicity and system reliability. In fact, the sliding nature of the adopted design facilitates modelling when compared with concepts that require the use of elastomeric skins, keeping actuation forces sufficiently low to use lightweight servo actuators, especially when the contact surfaces are protected with a low friction film or paint. Actually, concepts that use elastomeric skins noticeably require higher actuation force (needed to strain the skin) and are prone to rupture due to cyclic loads (strain/unstrain) and also perforations due to impacts. Additionally, these concepts suffer from out-of-pane displacements that disrupt the aerodynamic surface, potentially negating any performance benefits. Nevertheless, the telescopic concept has some disadvantages. On one hand, there are some aerodynamic issues arising due to the lack of geometric independence of IFW and OMW, i.e., the aerofoils depend on each other to guarantee compatibility. On the other hand, a weight increase is to be expected due to IFW and OMW sliding inside each other and, consequently, skin duplications. This structural mass increase could easily offset the possible advantages that the adaptive wing can provide. As seen from the studies performed, the mass penalties were important for the RPASs under consideration. A mass penalty on the CHANGE wing structure of 22% represents a mass penalty on the whole aircraft (with a takeoff mass of 25 kg) of around 3.5%. Further mass penalties may arise from the actuation mechanisms. In the presented telescopic wing-box concept, the span extension mechanism accounted for 13% of wing mass, not considering LE and TE morphing devices. The first VSW concept, from which the CHANGE wing concept evolved, brings further insight to the mass problem. Unlike the CHANGE wing, it does not possess LE or TE surfaces but was required to perform roll control by asymmetrical span actuation, rendering the power of the actuation system comparatively higher. In this case, the actuation mechanism (including mechanism supporting structure) accounted for almost 30% of the wing's total mass, mainly due to the actuation speed requirement that led to heavier actuators. In this design, the overall wing mass penalty relative to a fixed wing was 42%, representing a penalty on the 6 kg RPAS of 10% of its takeoff mass. The parametric study tried to summarize the mass penalties of such concepts, being successful at demonstrating that the mass penalty is not straightforward and that a careful selection of span, chord and variable-span ratio can minimize the weight increase.

6.2 Original Contributions

It is clear from the conclusions above that the main objectives of the work were accomplished. Following is a summary of the main original contributions found in this document:

- Effective and viable telescopic wing: the studies performed on the VSW successfully proved its feasibility, from an operational point of view, and demonstrated that performance gains can be achieved. The wing structure proved to be airworthy and the actuation system showed fast and effective actuation. Two prototypes were built and bench tested, and one prototype was thoroughly flight tested, including the quantification of the performance gains relative to a conventional wing. Therefore, the current work significantly contributed to increasing the TRL of the span changing technologies.
- Systematization of structural methodologies and building procedures: the work proposed structural methodologies and building procedures that could be used as a foundation to build other morphing wings.
- Automated and fully parametric structural model analysis procedure (using ANSYS® APDL): throughout the work, parametric FEM models were developed to perform structural analysis (static and modal) of VSWs. These results were compared to those obtained with full-scale prototype models, showing very good agreement. As far as the author is aware, these parametric models are unique in the literature.
- Comprehensive and systematic study of the effects of five aircraft parameters in the structural mass of telescopic wings: the analyses of as many parameters as possible in a single study dramatically increases the possibilities of discerning correlations between different parameters that may prove valuable to reduce the mass penalty of span changing wings.
- Derivation of multivariable polynomial approximations, used to create a mass model of VSWs: it is of special interest the VSW to fixed wing mass ratio polynomial, that was used to derive the mass model. The use of the latter polynomial to correct an existing conventional mass model is desirable, since it allows existing validated models to be used. Additionally, the mass model derivation constituted a significant step towards the adaptation of VSWs in the near future, since it helps to predict, during the initial phases of the design process, if morphing wings are justifiable in the particular scenario, given the mass increase.

6.3 Future Work and Recommendations

The work presented in this thesis explored the feasibility of VSWs, as well as methods to predict the mass of such concepts. In this way, the future work and recommendations are essentially divided in the concepts themselves and in the mass prediction model. A third section is included to add some final considerations about the work.

6.3.1 Variable-span Wing Concepts

Much effort was dedicated to the idealization of the VSW design, with an emphasis on practicability, since flight testing was an objective from the beginning of the project. However,

the work is far from complete. The developed instrumented morphing RPAS allows a myriad of different flight tests to be performed. Probably the most significant could be the roll control study using asymmetric deployment of the VSW. In fact, flight tests demonstrated the feasibility of such approach, but, a formal study was not performed. This study should encompass the roll rate determination for various airspeeds and span variations, and a comparison with the conventional wing ailerons. Conclusion about the vehicle's latero-directional stability and span variation speed requirements should also be derived. The latter would provide an unique insight about the speed requirements of the span changing actuation system, in order to guarantee the controllability and stability of the RPAS.

One other aspect that could be addressed is the VSW actuation system, since it is one of the main contributors to the mass and energy requirements increase. On one hand, bench testing of the first prototype (section 2.7.2 of chapter 2) revealed low actuator efficiency. Several factors contributed to this, but probably the most significant were the thermal losses in the brushed DC motors. Therefore, coreless DC motor based servomotor architectures should be explored in the future, since these show efficiencies greater than 90%. On the other hand, in the second prototype, better materials were used to reduced the mechanical components' mass, along with a lighter servomotor system. However, further investigation could be done to identify other solutions to reduce the actuation system mass.

6.3.2 Mass Prediction Model

In the last chapter of the thesis, a mass model was derived, using FEM simulations coupled to a first order gradient based optimization, to ensure minimum mass of the wing configurations. The influence of span variation in the wing mass proved to be more complex than anticipated. The developed parametric model involved a detailed formulation of the wing interfaces and scaling. However, two aspects could have clouded the mass predictions. The first aspect is related with the use of the bonded contact formulation in the IFW/OMW interface. This slightly increased the local stiffness, and consequently could have underestimated the mass increment of the span changing wings. The other aspect is associated with the exclusion of large deflections effects. Due to the low tip displacements, it is unlikely that large deflection effects could significantly change the results. However, unstable geometries (i.e. buckling) could be identified with large displacements, and go unnoticed using a linear formulation. In other words, some high AR wings could be feasible using a linear theory and proved to be problematic, when including large deflection effects. For the previous reasons, these aspects should be addressed in the future.

One other aspect that could be enhanced is the optimization algorithm employed. The first order optimization method used, has been shown to yield reasonable results for engineering problems and is significantly faster than heuristic methods. However, it could be less accurate than the latter and is prone to entrapment in local minima. Therefore, interfacing to an external optimizer should be investigated, given that the developed FEM scripts are completely independent, i.e., can be treated as a "black box".

Other issue that was identified is related with the parametric study parameters minimum and maximum bounds. In fact, parameter bounds should be extended to encompass a larger design space, in order to extend the applicability of the mass model and, consequently, facilitate the comparison with other VSWs.

Additional work should also be performed to add other parameters to the parametric study, and more importantly, to the mass model. For example, the aerofoil thickness (t/c) could be added to account for its influence in structural mass, since thinner aerofoils reduce section inertia, contributing to an increased structural mass.

One final aspect that could be enhanced is the morphing flap mass predictions. In fact, as seen in the first chapter, various adaptative flap concepts exist, using conventional, shape-memory alloy or piezoelectric actuation. Thus, a large variation of the prototypes' mass exist. Further work should be done to synthesize this variation, greatly facilitating mass predictions.

6.3.3 Final Considerations

All the work described in this document was performed with low speed RPASs in mind. Therefore, some remarks regarding the scalability to General Aviation (GA) and Commercial Aviation (CA) aircraft should be made.

A GA aircraft in CS-VLA class is typically a low-subsonic aircraft with its expected maximum Mach number (Ma) of around 0.25 to 0.30. In terms of aerodynamics this is still in the same flow regime (incompressible) as the RPASs that were studied. When considering CA aircraft (CS-23 or CS-25), simple similitude and scaling approaches are not applicable because the cruise speed is around a Ma of 0.85 to 0.90, being considerably higher than the speed of the studied RPASs. This not only increases the magnitudes of aerodynamic forces and moments, but completely changes the flow regime. These aspects were not considered in the design, so an extrapolation of the information gathered is not possible for the case of CA.

In the VSW, to avoid excessive friction or mechanism locking, the wing displacements have to be kept low. Hence a high rigidity wing is necessary, which is, in some degree, contrary to the philosophy used to size GA or CA wing structures. In fact, recent wing designs heavily use composite material with increasingly vertical wing tip displacements (up to 13% of the wingspan). This flexibility also allows other effects to be explored, like dihedral effect due to wing bending, for example. One other aspect that should be considered is related to internal space availability. As a matter of fact, depending on the variable-span variation ratio, more space is needed for the wing movement and, hence, less space is available to install other systems or fuel tanks. This in turn would increase fuel tanks fitting complexity or, in the worst case, would reduce the amount of fuel the aircraft can carry and, consequently, reducing its range.

To sum up the last two paragraphs, the fact is that some challenges would have to be solved to make variable-span wings work on commercial aviation. However, RPASs are perfect scale demonstrators, being the ideal platforms to make that possible in the next decades.

Bibliography

[1] Sarkar, A. 'Evolving Green Aviation Transport System: A Hoilistic Approah to Sustainable Green Market Development'. In: *American Journal of Climate Change* 1.3 (2012), pp. 164–180. ISSN: 2167-9495. DOI: 10.4236/ajcc.2012.13014 (cit. on p. 1).

[2] Kroo, I. 'Innovations in Aeronautics'. In: *42nd AIAA Aerospace Sciences Meeting and Exhibit*. Aerospace Sciences Meetings. Reno, Nevada, USA: American Institute of Aeronautics and Astronautics, Jan. 2004. DOI: doi:10.2514/6.2004-1 (cit. on pp. 1, 2).

[3] The Editors of Encyclopædia Britannica. *Metamorphosis*. 7th Aug. 2009. URL: https://www.britannica.com/science/metamorphosis (Retrieved 02/04/2017) (cit. on p. 2).

[4] Sofla, A., Meguid, S., Tan, K. and Yeo, W. 'Shape morphing of aircraft wing: Status and challenges'. In: *Materials & Design* 31.3 (2010), pp. 1284–1292. ISSN: 0261-3069. DOI: 10.1016/j.matdes.2009.09.011 (cit. on pp. 2, 24).

[5] Weisshaar, T. A. 'Morphing Aircraft Technology - New Shapes for Aircraft Design'. In: *RTO-MP-AVT-141 - NATO Research and Technology Organisation Applied Vehicle Technology Panel Specialists, Meeting on Multifunctional Structures/Integration of Sensors and Antennas*. Vilnius, Lithuania, Oct. 2006, pp. 1.1–1.20 (cit. on pp. 2, 22).

[6] McGowan, A., Vicroy, D., Busan, R. and Hahn, A. 'Perspectives on highly adaptable or morphing aircraft'. In: *NATO RTO AVT-168 Symposium*. Évora, Portugal, Apr. 2009, pp. 1.1–1.14 (cit. on p. 2).

[7] Seigler, T. M. 'Dynamics and control of morphing aircraft'. PhD thesis. Virginia, USA: Virginia Polytechnic Institute and State University, Aug. 2005. URL: http://hdl.handle.net/10919/28681 (cit. on p. 2).

[8] Pendleton, E. 'Back to the Future-How Active Aeroelastic Wings are a Return to Aviation's Beginnings and a Small Stepto Future Bird-Like Wings'. In: *RTO AVT Symposium on Active Control Technology for Enhanced Performance Operational Capabilities of Military Aircraft, Land Vehicles, and Sea Vehicles*. Braunschweig, Germany, May 2000, pp. 3.1–3.6 (cit. on pp. 2, 25).

[9] Joshi, S. P., Tidwell, Z., Crossley, W. and Ramakrishnan, S. 'Comparison of Morphing Wing Strategies Based Upon Aircraft Performance Impacts'. In: *45th AIAA/ASME/ASCE/AHS/ASC Structures Structural Dynamics Materials Conference*. Vol. 2. Palm Springs, California, 2004, pp. 1–7. ISBN: 978-1-62410-079-6. DOI: 10.2514/6.2004-1722 (cit. on p. 3).

[10] Skillen, M. and Crossley, W. 'Developing Morphing Wing Weight Predictors with Emphasis on the Actuating Mechanism'. In: *47th AIAA/ASME/ASCE/AHS/ASC Structures, Structural Dynamics, and Materials Conference*. Structures, Structural Dynamics, and Materials and Co-located Conferences. Newport, Rhode Island, USA: American Institute of Aeronautics and Astronautics, May 2006. DOI: 10.2514/6.2006-2042 (cit. on pp. 4, 31, 32).

[11] Breuker, R. D. and Werter, N. 'On the Importance of Morphing Deformation Scheduling for Actuation Force and Energy'. In: *Aerospace* 3.4 (2016). ISSN: 2226-4310. DOI: 10.3390/aerospace3040041 (cit. on p. 4).

[12] Reich, G. and Sanders, B. 'Introduction to Morphing Aircraft Research'. In: *Journal of Aircraft* 44.4 (July 2007), pp. 1059–1059. ISSN: 0021-8669. DOI: 10.2514/1.28287 (cit. on p. 4).

[13] Gamboa, P. 'Multidisciplinary Design Optimization of Morphing Aircraft'. PhD thesis. Covilhã, Portugal: Departamento de Ciências Aeroespaciais, Universidade da Beira Interior, Dec. 2007 (cit. on pp. 4, 42).

[14] Vasista, S., Tong, L. and Wong, K. C. 'Realization of Morphing Wings: A Multidisciplinary Challenge'. In: *Journal of Aircraft* 49.1 (Jan. 2012), pp. 11–28. ISSN: 0021-8669. DOI: 10.2514/1.C031060 (cit. on p. 4).

[15] Barbarino, S., Bilgen, O., Ajaj, R. M., Friswell, M. I. and Inman, D. J. 'A Review of Morphing Aircraft'. In: *Journal of Intelligent Material Systems and Structures* 22.9 (2011), pp. 823–877. DOI: 10.1177/1045389X11414084 (cit. on pp. 4, 5).

[16] Anderson Jr., J. D. *Fundamentals of Aerodynamics*. 5th ed. McGraw-Hill Education, 2010. ISBN: 978-0073398105 (cit. on pp. 5, 22, 23, 25, 28, 161).

[17] Heinze, E. P. A. 'Increasing the Speed Range & The Makhonine Way'. In: *Flight* XXIV.20 (May 1932), pp. 417–418 (cit. on p. 6).

[18] Simons, M. *Sailplanes 1965-2000*. 2nd ed. pp. 58-61. Königswinter: EQIP Werbung & Verlag GmbH, 2005. ISBN: 3-9808838-1-7 (cit. on pp. 6, 7).

[19] Gevers, D. E. *Multi-Purpose Aircraft*. United States Patents Office, Patent No. 5,645,250. July 1997. URL: https://patentscope.wipo.int/search/en/detail.jsf?docId=US38717265 (cit. on p. 6).

[20] Arrison, L., Birocco, K., Gaylord, C., Herndon, B., Manion, K. and Metheny, M. *2002-2003 AE/ME Morphing Wing Design*. Blacksburg, Virginia, USA: Virginia Tech, 2003 (cit. on pp. 6, 7).

[21] Malewicki, D. J. *Aerovisions Inc., UMAAV*. 2004. URL: http://www.canosoarus.com/05UMAAV/UMAAV01.htm (Retrieved 02/04/2017) (cit. on p. 7).

[22] Blondeau, J., Richeson, J. and Pines, D. 'Design of a Morphing Aspect Ratio Wing Using an Inflatable Telescoping Spar'. In: *44th AIAA/ASME/ASCE/AHS/ASC Structures, Structural Dynamics, and Materials Conference*. Structures, Structural Dynamics, and Materials and Co-located Conferences. American Institute of Aeronautics and Astronautics, Apr. 2003. DOI: 10.2514/6.2003-1718 (cit. on pp. 7, 8).

[23] Blondeau, J. and Pines, D. 'Design and Testing of a Pneumatic Telescopic Wing for Unmanned Aerial Vehicles'. In: *Journal of Aircraft* 44 (2007), pp. 1088–1099. ISSN: 0021-8669. DOI: 10.2514/1.22205 (cit. on p. 8).

[24] Neal, D., Good, M., Johnston, C., Robertshaw, H., Mason, W. and Inman, D. 'Design and Wind-Tunnel Analysis of a Fully Adaptive Aircraft Configuration'. In: *45th AIAA/ASME/ASCE/AHS/ASC Structures, Structural Dynamics, and Materials and Co-located Conferences*. Palm Springs, California, USA: American Institute of Aeronautics and Astronautics, Apr. 2004. DOI: 10.2514/6.2004-1727 (cit. on pp. 8, 24).

[25] Neal, D., Farmer, J. and Inman, D. 'Development of a Morphing Aircraft Model for Wind Tunnel Experimentation'. In: *47th AIAA/ASME/ASCE/AHS/ASC Structures, Structural Dynamics, and Materials and Co-located Conferences*. Newport, Rhode Island, USA: American Institute of Aeronautics and Astronautics, May 2006. DOI: 10.2514/6.2006-2141 (cit. on pp. 8, 9, 24).

[26] Stern, M. M. and Cohen, E. 'VAST AUAV (Variable Airspeed Telescoping Additive Unmanned Air Vehicle)'. In: *Rapid 2013 Conference and Exposition, Including 3D Imaging*. Pittsburgh, PA: SME, June 2013 (cit. on pp. 8, 9).

[27] Joo, J. J., Sanders, B., Johnson, T. and Frecker, M. I. 'Optimal actuator location within a morphing wing scissor mechanism configuration'. In: *Proc. SPIE*. Vol. 6166. 2006, pp. 24–35. DOI: 10.1117/12.658830 (cit. on p. 9).

[28] Bharti, S., Frecker, M., Lesieutre, G. and Browne, J. 'Tendon actuated cellular mechanisms for morphing aircraft wing'. In: *Modeling, Signal Processing, and Control for Smart Structures 2007*. Vol. 6523. Apr. 2007, pp. 6523–6523-13. DOI: 10.1117/12.715855 (cit. on p. 9).

[29] Johnson, T., Frecker, M., Abdalla, M., Gurdal, Z. and Lindner, D. 'Nonlinear Analysis and Optimization of Diamond Cell Morphing Wings'. In: *Journal of Intelligent Material Systems and Structures* 20.7 (2009), pp. 815–824. DOI: 10.1177/1045389X08098098 (cit. on p. 9).

[30] Ajaj, R. M., Saavedra Flores, E. I., Friswell, M. I., Allegri, G., Woods, B. K. S., Isikveren, A. T. and Dettmer, W. G. 'The Zigzag wingbox for a span morphing wing'. In: *Aerospace Science and Technology* 28 (2013), pp. 364–375. ISSN: 12709638. DOI: 10.1016/j.ast.2012.12.002 (cit. on p. 10).

[31] Gamboa, P., Aleixo, P., Vale, J., Lau, F. and Suleman, A. 'Design and Testing of a Morphing Wing for an Experimental UAV'. In: *Platform Innovations and System Integration for Unmanned Air, Land and Sea Vehicles (AVT-SCI Joint Symposium - RTO-MP-AVT-146)*. Neuilly-sur-Seine, France, May 2007, pp. 17.1–17.30 (cit. on pp. 10, 11).

[32] Gamboa, P., Vale, J., Lau, F. J. P. and Suleman, A. 'Optimization of a Morphing Wing Based on Coupled Aerodynamic and Structural Constraints'. In: *AIAA Journal* 47.9 (2009), pp. 2087–2104. DOI: 10.2514/1.39016 (cit. on pp. 11, 23).

[33] Vocke III, R. D., Kothera, C. S., Woods, B. K., Bubert, E. A. and Wereley, N. M. *One Dimensional Morphing Structures for Advanced Aircraft, Recent Advances in Aircraft Technology*. Ramesh K. Agarwal (Ed.), InTech, Feb. 2012. ISBN: 978-953-51-0150-5. DOI: 10.5772/37333 (cit. on p. 11).

[34] Woods, B. K. and Friswell, M. I. 'The Adaptive Aspect Ratio morphing wing: Design concept and low fidelity skin optimization'. In: *Aerospace Science and Technology* 42 (2015), pp. 209–217. ISSN: 1270-9638. DOI: 10.1016/j.ast.2015.01.012 (cit. on pp. 11, 12).

[35] Cadogan, D., Graham, W. and Smith, T. 'Inflatable and rigidizable wings for unmanned aerial vehicles'. In: *2nd AIAA "Unmanned Unlimited" Conf. and Workshop & Exhibit*. Vol. 6630. InfotechAerospace Conferences. San Diego, California, USA: American Institute of Aeronautics and Astronautics, Sept. 2003. DOI: 10.2514/6.2003-6630 (cit. on pp. 12, 13).

[36] Cadogan, D., Smith, T., Uhelsky, F. and Mackusick, M. 'Morphing Inflatable Wing Development for Compact Package Unmanned Aerial Vehicles'. In: *45th AIAA/ASME/ASCE/AHS/ASC Structures, Structural Dynamics and Materials Conference*. Structures, Structural Dynamics, and Materials and Co-located Conferences. Palm Springs, California, USA: American Institute of Aeronautics and Astronautics, Apr. 2004. DOI: 10.2514/6.2004-1807 (cit. on p. 12).

[37] Cadogan, D., Scarborough, S., Gleeson, D., Dixit, A., Jacob, J. and Simpson, A. 'Recent Development and Test of Inflatable Wings'. In: *47th AIAA/ASME/ASCE/AHS/ASC Structures, Structural Dynamics and Materials Conference*. Structures, Structural Dynamics, and Materials and Co-located Conferences. Newport, Rhode Island, USA: American Institute of Aeronautics and Astronautics, May 2006. DOI: 10.2514/6.2006-2139 (cit. on pp. 12, 13).

[38] Bae, J. S., Seigler, T. M. and Inman, D. J. 'Aerodynamic and Static Aeroelastic Characteristics of a Variable-Span Morphing Wing'. In: *Journal of Aircraft* 42 (2005), pp. 528–534. ISSN: 0021-8669. DOI: 10.2514/1.4397 (cit. on p. 12).

[39] Vale, J., Leite, A., Lau, F. and Suleman, A. 'Aero-Structural Optimization and Performance Evaluation of a Morphing Wing with Variable Span and Camber'. In: *Journal of Intelligent Material Systems and Structures* 22.10 (2011), pp. 1057–1073. DOI: 10.1177/1045389X11416031 (cit. on p. 13).

[40] Leylek, E. and Costello, M. 'Benefits of Autonomous Morphing Aircraft in Loiter and Attack Missions'. In: *AIAA Atmospheric Flight Mechanics Conference*. Guidance, Navigation, and Control and Co-located Conferences. Toronto, Ontario, Canada: American Institute of Aeronautics and Astronautics, Aug. 2010. DOI: 10.2514/6.2010-7507 (cit. on p. 13).

[41] Lesieutre, G., Browne, J. and Frecker, M. 'Scaling of Performance, Weight, and Actuation of a 2-D Compliant Cellular Frame Structure for a Morphing Wing'. In: *Journal of Intelligent Material Systems and Structures* 22.10 (2011), pp. 979–986. DOI: 10.1177/1045389X11412641 (cit. on p. 13).

[42] Ajaj, R., Friswell, M., Saavedra Flores, E., Little, O. and Isikveren, A. 'Span Morphing: A Conceptual Design Study'. In: *53rd AIAA/ASME/ASCE/AHS/ASC Structures, Structural Dynamics and Materials Conference*. Structures, Structural Dynamics, and Materials and Co-located Conferences. American Institute of Aeronautics and Astronautics, Apr. 2012. DOI: 10.2514/6.2012-1510 (cit. on p. 14).

[43] Kryvokhatko, I. S. and Sukhov, V. V. 'Experimental Investigation of Aerodynamic Performance of a Small UAV With a Telescopic Wing'. In: *2013 IEEE 2nd International Conference Actual Problems of Unmanned Air Vehicles Developments Proceedings (APUAVD)*. Oct. 2013, pp. 17–20. DOI: 10.1109/APUAVD.2013.6705272 (cit. on pp. 14, 98, 104).

[44] Beaverstock, C. S., Fincham, J., Friswell, M. I., Ajaj, R. M., De Breuker, R. and Werter, N. 'Effect of Symmetric & Asymmetric Span Morphing on Flight Dynamics'. In: *AIAA Atmospheric Flight Mechanics Conference*. AIAA SciTech Forum. National Harbor, Maryland, USA: American Institute of Aeronautics and Astronautics, Jan. 2014. DOI: 10.2514/6.2014-0545 (cit. on p. 14).

[45] Beaverstock, C. S., Woods, B. K. S., Fincham, J. H. S.-M. and Friswell, M. I. 'Performance Comparison between Optimised Camber and Span for a Morphing Wing'. In: *Aerospace* 2.3 (2015), pp. 524–554. ISSN: 2226-4310. DOI: 10.3390/aerospace2030524 (cit. on p. 15).

[46] Spillman, J. J. 'The use of variable camber to reduce drag, weight and costs of transport aircraft'. In: *The Aeronautical Journal (1968)* 96.951 (1992), pp. 1–9 (cit. on p. 15).

[47] Ricci, S. and Terraneo, M. 'Conceptual Design of an Adaptive Wing for a Three-surfaces Airplane'. In: *46th AIAA/ASME/ASCE/AHS/ASC Structures, Structural Dynamics and Materials Conference*. Structures, Structural Dynamics, and Materials and Co-located Conferences. Austin, Texas, USA: American Institute of Aeronautics and Astronautics, Apr. 2005. DOI: 10.2514/6.2005-1959 (cit. on pp. 15, 16).

[48] Kota, S., Osborn, R., Ervin, G., Maric, D., Flick, P. and Paul, D. ‘Mission Adaptive Compliant Wing - Design, Fabrication and Flight Test’. In: *NATO RTO AVT-168 Symposium*. Évora, Portugal, Apr. 2009, pp. 18.1–18.19. DOI: 10.14339/RTO-MP-AVT-168-18-pdf (cit. on p. 16).

[49] Center, A. F. R. *NASA Successfully Tests Shape-Changing Wing for Next Generation Aviation*. 2015. URL: https://www.nasa.gov/press-release/nasa-successfully-tests-shape-changing-wing-for-next-generation-aviation (Retrieved 02/04/2017) (cit. on pp. 16, 17).

[50] Sahin, M., Sakarya, E., Ünlüsoy, L., Insuyu, E. T., Özgen, S., Seber, G. and Yaman, Y. ‘Design, Analysis and Experimental Modal Testing of a Mission Adaptive Wing of an Unmanned Aerial Vehicle’. In: *UVW2010, International Unmanned Vehicle Workshop*. Turkish Air Force Academy, Istanbul, Turkey, June 2010, pp. 52–56 (cit. on pp. 16, 17).

[51] Woods, B. K. S. and Friswell, M. I. ‘Preliminary Investigation of a Fishbone Active Camber Concept’. In: *Volume 2: Mechanics and Behavior of Active Materials; Integrated System Design and Implementation; Bio-Inspired Materials and Systems; Energy Harvesting*. Stone Mountain, Georgia, USA, Sept. 2012, pp. 555–563. ISBN: 978-0-7918-4510-3. DOI: 10.1115/SMASIS2012-8058 (cit. on pp. 16, 17).

[52] Gaspari, A. D. and Ricci, S. ‘A Two-Level Approach for the Optimal Design of Morphing Wings Based on Compliant Structures’. In: *Journal of Intelligent Material Systems and Structures* 22.10 (2011), pp. 1091–1111. DOI: 10.1177/1045389X11409081 (cit. on pp. 17, 18).

[53] Gaspari, A. D., Ricci, S. and Riccobene, L. ‘Design, Manufacturing and Wind Tunnel Validation of an Active Camber Morphing Wing Based on Compliant Structures’. In: *Proceedings of ICAST 2014*. 2014, pp. 1–12 (cit. on p. 17).

[54] Gaspari, A. D., Ricci, S., Travaglini, L., Cavagna, L., Antunes, A., Odaguil, F. and Lima, G. ‘Active Camber Morphing Wings Based on Compliant Structures: an Aeroelastic Assessment’. In: *23rd AIAA/AHS Adaptive Structures Conference*. AIAA SciTech Forum. Kissimmee, Florida, USA: American Institute of Aeronautics and Astronautics, Jan. 2015. DOI: 10.2514/6.2015-1054 (cit. on p. 17).

[55] Ricci, S., De Gaspari, A. and Riccobene, L. ‘Design, Manufacturing and Wind Tunnel Test of a Morphing Wing Based on Compliant Structures’. In: *24th AIAA/AHS Adaptive Structures Conference*. AIAA SciTech Forum. San Diego, California, USA: American Institute of Aeronautics and Astronautics, Jan. 2016. DOI: 10.2514/6.2016-1316 (cit. on p. 17).

[56] Radestock, M., Riemenschneider, J., Monner, H. P. and Rose, M. ‘Experimental Investigation of a Compliant Mechanism for a UAV Leading Edge’. In: *Proceedings of the 7th ECCOMAS Thematic Conference on Smart Structures and Materials*. Ponta Delgada, Azores, July 2015 (cit. on pp. 18, 143, 144).

[57] Werter, N., Sodja, J., Spirlet, G. and Breuker, R. D. ‘Design and Experiments of a Warp Induced Camber and Twist Morphing Leading and Trailing Edge Device’. In: *24th AIAA/AHS Adaptive Structures Conference*. AIAA SciTech. San Diego, California: American Institute of Aeronautics and Astronautics, Jan. 2016. DOI: 10.2514/6.2016-0315 (cit. on pp. 18, 143, 144, 184).

[58] Pecora, R., Amoroso, F., Magnifico, M., Dimino, I. and Concilio, A. 'KRISTINA: Kinematic rib-based structural system for innovative adaptive trailing edge'. In: *Proc. SPIE 9801, Industrial and Commercial Applications of Smart Structures Technologies*. Las Vegas, Nevada, USA, Mar. 2016, pp. 9801–9801-11. DOI: 10.1117/12.2218516 (cit. on p. 18).

[59] Koreanschi, A., Gabor, O. S., Acotto, J., Brianchon, G., Portier, G., Botez, R. M., Mamou, M. and Mebarki, Y. 'Optimization and design of an aircraft's morphing wing-tip demonstrator for drag reduction at low speed, Part I - Aerodynamic optimization using genetic, bee colony and gradient descent algorithms'. In: *Chinese Journal of Aeronautics* 30.1 (2017), pp. 149–163. ISSN: 1000-9361. DOI: 10.1016/j.cja.2016.12.013 (cit. on p. 19).

[60] Koreanschi, A., Gabor, O. S., Acotto, J., Brianchon, G., Portier, G., Botez, R. M., Mamou, M. and Mebarki, Y. 'Optimization and design of an aircraft's morphing wing-tip demonstrator for drag reduction at low speeds, Part {II} - Experimental validation using Infra-Red transition measurement from Wind Tunnel tests'. In: *Chinese Journal of Aeronautics* 30.1 (2017), pp. 164–174. ISSN: 1000-9361. DOI: 10.1016/j.cja.2016.12.018 (cit. on p. 19).

[61] Qiu, J. and Ji, H. 'Research on applications of piezoelectric materials in smart structures'. In: *Frontiers of Mechanical Engineering* 6.1 (2011), pp. 99–117. ISSN: 1673-3592. DOI: 10.1007/s11465-011-0212-4 (cit. on p. 19).

[62] Barrett, R., McMurtry, R., Vos, R., Tiso, P. and Breuker, R. D. 'Post-buckled precompressed piezoelectric flight control actuator design, development and demonstration'. In: *Smart Materials and Structures* 15.5 (2006), p. 1323 (cit. on p. 19).

[63] Vos, R., Breuker, R. D., Barrett, R. M. and Tiso, P. 'Morphing Wing Flight Control Via Postbuckled Precompressed Piezoelectric Actuators'. In: *Journal of Aircraft* 44.4 (July 2007), pp. 1060–1068. ISSN: 0021-8669. DOI: 10.2514/1.21292 (cit. on p. 19).

[64] Bilgen, O., Kochersberger, K. B. and Inman, D. J. 'Macro-fiber composite actuators for a swept wing unmanned aircraft'. In: *The Aeronautical Journal* 113.1144 (2009), pp. 385–395. DOI: 10.1017/S0001924000003055 (cit. on p. 20).

[65] Paradies, R. and Ciresa, P. 'Active wing design with integrated flight control using piezoelectric macro fiber composites'. In: *Smart Materials and Structures* 18.3 (2009), p. 035010. DOI: 10.1088/0964-1726/18/3/035010 (cit. on p. 20).

[66] Bilgen, O., Butt, L. M., Day, S. R., Sossi, C. A., Weaver, J. P., Wolek, A., Mason, W. H. and Inman, D. J. 'A novel unmanned aircraft with solid-state control surfaces: Analysis and flight demonstration'. In: *Journal of Intelligent Material Systems and Structures* 24.2 (2013), pp. 147–167. DOI: 10.1177/1045389X12459592 (cit. on p. 20).

[67] Jani, J. M., Leary, M., Subic, A. and Gibson, M. A. 'A review of shape memory alloy research, applications and opportunities'. In: *Materials & Design (1980-2015)* 56 (2014), pp. 1078–1113. ISSN: 0261-3069. DOI: 10.1016/j.matdes.2013.11.084 (cit. on p. 20).

[68] Elzey, D. M., Sofla, A. Y. N. and Wadley, H. N. G. 'A bio-inspired high-authority actuator for shape morphing structures'. In: *Proc. SPIE*. Vol. 5053. 2003, pp. 92–100. DOI: 10.1117/12.484745 (cit. on p. 20).

[69] Alasty, A., Alemohammad, S. H., Khiabani, R. and Khalighi, Y. 'Maneuverability Improvement for an Ultra Light Airplane Model Using Variable Shape Wing'. In: *AIAA Atmospheric Flight Mechanics Conference and Exhibit*. Guidance, Navigation, and Control and Co-located Conferences. Providence, Rhode Island, USA: American Institute of Aeronautics and Astronautics, Aug. 2004. DOI: 10.2514/6.2004-4831 (cit. on p. 21).

[70] Seow, A. K., Liu, Y. and Yeo, W. K. 'Shape Memory Alloy as Actuator to Deflect a Wing Flap'. In: *49th AIAA/ASME/ASCE/AHS/ASC Structures, Structural Dynamics, and Materials Conference, 16th AIAA/ASME/AHS Adaptive Structures Conference,10th AIAA Non-Deterministic Approaches Conference, 9th AIAA Gossamer Spacecraft Forum, 4th AIAA Multidisciplinary Design*. Structures, Structural Dynamics, and Materials and Co-located Conferences. Schaumburg, Illinois, USA: American Institute of Aeronautics and Astronautics, Apr. 2008. DOI: 10.2514/6.2008-1704 (cit. on p. 21).

[71] Abdullah, E., Bil, C. and Watkins, S. 'Application of Smart Materials for Adaptive Airfoil Shape Control'. In: *47th AIAA Aerospace Sciences Meeting including The New Horizons Forum and Aerospace Exposition*. Aerospace Sciences Meetings. Orlando, Florida, USA: American Institute of Aeronautics and Astronautics, Jan. 2009. DOI: 10.2514/6.2009-1359 (cit. on p. 21).

[72] Barbarino, S., Pecora, R., Lecce, L., Concilio, A., Ameduri, S. and Rosa, L. D. 'Airfoil Structural Morphing Based on S.M.A. Actuator Series: Numerical and Experimental Studies'. In: *Journal of Intelligent Material Systems and Structures* 22.10 (2011), pp. 987–1004. DOI: 10.1177/1045389X11416032 (cit. on pp. 21, 22).

[73] Pecora, R., Barbarino, S., Lecce, L. and Russo, S. 'Design and Functional Test of a Morphing High-Lift Device for a Regional Aircraft'. In: *Journal of Intelligent Material Systems and Structures* 22.10 (2011), pp. 1005–1023. DOI: 10.1177/1045389X11414083 (cit. on p. 22).

[74] Perkins, D., Reed, J. and Havens, E. 'Morphing Wing Structures for Loitering Air Vehicles'. In: *45th AIAA/ASME/ASCE/AHS/ASC Structures, Structural Dynamics, and Materials and Co-located Conferences*. Palm Springs, California, USA: American Institute of Aeronautics and Astronautics, Apr. 2004. DOI: 10.2514/6.2004-1888 (cit. on p. 22).

[75] Reed, J. L., Hemmelgarn, C. D., Pelley, B. M. and Havens, E. 'Adaptive wing structures'. In: *Proc. SPIE 5762, Smart Structures and Materials 2005: Industrial and Commercial Applications of Smart Structures Technologies*. Vol. 5762. San Diego, California, USA, May 2005, pp. 5762–5762-11. DOI: 10.1117/12.599922 (cit. on p. 23).

[76] Ricketts, R. H. and Doggett R. V., J. *Wind-tunnel experiments on divergence of forward-swept wings*. NASA-TP-1685, L-13549. Hampton, VA, USA: NASA Langley Research Center, Aug. 1980. URL: http://hdl.handle.net/2060/19800020786 (cit. on p. 23).

[77] Perry, R. 'Variable-sweep aircraft - A case history of multiple re-innovation'. In: *3rd Annual Meeting*. Annual Meeting. Boston, Massachusetts, USA: American Institute of Aeronautics and Astronautics, Nov. 1966. DOI: 10.2514/6.1966-983 (cit. on p. 23).

[78] Polhamus, E. and Hammond, A. *Aerodynamic Research Relative to Variable-Sweep Multimission Aircraft*. NASA N67-33072. Hampton, Virginia, United States of America: Langley Research Center, 1967 (cit. on p. 23).

[79] Bowman, J., Sanders, B., Cannon, B., Kudva, J., Joshi, S. and Weisshaar, T. 'Development of Next Generation Morphing Aircraft Structures'. In: *48th AIAA/ASME/ASCE/AHS/ASC Structures, Structural Dynamics, and Materials Conference*. Structures, Structural Dynamics, and Materials and Co-located Conferences. Honolulu, Hawaii, USA: American Institute of Aeronautics and Astronautics, Apr. 2007. DOI: 10.2514/6.2007-1730 (cit. on p. 24).

[80] Flanagan, J., Strutzenberg, R., Myers, R. and Rodrian, J. 'Development and Flight Testing of a Morphing Aircraft, the NextGen MFX-1'. In: *48th AIAA/ASME/ASCE/AHS/ASC Structures, Structural Dynamics, and Materials Conference*. Structures, Structural Dynamics, and Materials and Co-located Conferences. Honolulu, Hawaii, USA: American Institute of Aeronautics and Astronautics, Apr. 2007. DOI: 10.2514/6.2007-1707 (cit. on p. 24).

[81] Andersen, G., Cowan, D. and Piatak, D. 'Aeroelastic Modeling, Analysis and Testing of a Morphing Wing Structure'. In: *48th AIAA/ASME/ASCE/AHS/ASC Structures, Structural Dynamics, and Materials Conference*. Structures, Structural Dynamics, and Materials and Co-located Conferences. Honolulu, Hawaii, USA: American Institute of Aeronautics and Astronautics, Apr. 2007. DOI: 10.2514/6.2007-1734 (cit. on p. 24).

[82] Lentink, D., Muller, U. K., Stamhuis, E. J., Kat, R. de, Gestel, W. van, Veldhuis, L. L. M., Henningsson, P., Hedenstrom, A., Videler, J. J. and Leeuwen, J. L. van. 'How swifts control their glide performance with morphing wings'. In: *Nature* 446.7139 (Apr. 2007), pp. 1082–1085. ISSN: 0028-0836. DOI: 10.1038/nature05733 (cit. on p. 24).

[83] *Additional technical information on RoboSwift*. Team RoboSwift. Sept. 2008. URL: http://www.roboswift.nl/images/RoboSwift_Technical_Factsheet.pdf (cit. on pp. 24, 25).

[84] Di Luca, M., Mintchev, S., Heitz, G., Noca, F. and Floreano, D. 'Bioinspired morphing wings for extended flight envelope and roll control of small drones'. In: *Interface Focus* 7.1 (2016). ISSN: 2042-8898. DOI: 10.1098/rsfs.2016.0092 (cit. on pp. 24, 25).

[85] Miller, G. D. *Active Flexible Wing (AFW) Technology*. AFWAL-TR-87-3096. Los Angeles, CA, United States of America: Rockwell International North American Aircraft Operations, Feb. 1988. URL: http://www.dtic.mil/cgi-bin/GetTRDoc?Location=U2&doc=GetTRDoc.pdf&AD=ADB131204 (cit. on p. 26).

[86] Pendleton, E. W., Bessette, D., Field, P. B., Miller, G. D. and Griffin, K. E. 'Active Aeroelastic Wing Flight Research Program: Technical Program and Model Analytical Development'. In: *Journal of Aircraft* 37.4 (July 2000), pp. 554–561. DOI: 10.2514/2.2654 (cit. on p. 26).

[87] Wilson, J. 'Active Aeroelastic Wing: A New/Old Twist on Flight'. In: *Aerospace America* 40 (2002), pp. 34–37 (cit. on p. 26).

[88] Clarke, R., Allen, M., Dibley, R., Gera, J. and Hodgkinson, J. 'Flight Test of the F/A-18 Active Aeroelastic Wing Airplane'. In: *AIAA Atmospheric Flight Mechanics Conference and Exhibit*. Guidance, Navigation, and Control and Co-located Conferences. San Francisco, California, USA: American Institute of Aeronautics and Astronautics, Aug. 2005. DOI: 10.2514/6.2005-6316 (cit. on p. 26).

[89] Amprikidis, M. and Cooper, J. 'Experimental Validation of Wing Twist Control Using Adaptive Internal Structures'. In: *45th AIAA/ASME/ASCE/AHS/ASC Structures, Structural Dynamics and Materials Conference*. Structures, Structural Dynamics, and Materials and Co-located Conferences. Palm Springs, California, USA: American Institute of Aeronautics and Astronautics, Apr. 2004. DOI: 10.2514/6.2004-1884 (cit. on p. 26).

[90] Amprikidis, M. and Cooper, J. 'Development of Smart Spars for Active Aeroelastic Structures'. In: *44th AIAA/ASME/ASCE/AHS/ASC Structures, Structural Dynamics, and Materials Conference*. Structures, Structural Dynamics, and Materials and Co-located Conferences. Norfolk, Virginia, USA: American Institute of Aeronautics and Astronautics, Apr. 2003. DOI: 10.2514/6.2003-1799 (cit. on p. 26).

[91] Cooper, J. 'Adaptive Stiffness Structures for Air Vehicle Drag Reduction'. In: *Multifunctional Structures/Integration of Sensors and Antennas, Meeting Proceedings NATO RTO-MP-AVT-141 Symposium*. Neuilly-sur-Seine, France, 2006, pp. 15.1–15.12 (cit. on pp. 26, 27).

[92] Vos, R., Gurdal, Z. and Abdalla, M. 'Mechanism for Warp-Controlled Twist of a Morphing Wing'. In: *Journal of Aircraft* 47.2 (Mar. 2010), pp. 450–457. ISSN: 0021-8669. DOI: 10.2514/1.39328 (cit. on p. 26).

[93] Ajaj, R., Friswell, M., Dettmer, W., Isikveren, A. and Allegri, G. 'Conceptual Modeling of an Adaptive Torsion Wing Structure'. In: *52nd AIAA/ASME/ASCE/AHS/ASC Structures, Structural Dynamics and Materials Conference*. Structures, Structural Dynamics, and Materials and Co-located Conferences. Denver, Colorado, USA: American Institute of Aeronautics and Astronautics, Apr. 2011. DOI: 10.2514/6.2011-1883 (cit. on p. 27).

[94] Sahoo, D. and Cesnik, C. 'Roll Maneuver Control of UCAV Wing Using Anisotropic Piezoelectric Actuators'. In: *43rd AIAA/ASME/ASCE/AHS/ASC Structures, Structural Dynamics, and Materials Conference*. Structures, Structural Dynamics, and Materials and Co-located Conferences. Denver, Colorado, USA: American Institute of Aeronautics and Astronautics, Apr. 2002. DOI: 10.2514/6.2002-1720 (cit. on p. 27).

[95] Cesnik, C. and Brown, E. 'Active Warping Control of a Joined Wing/Tail Airplane Configuration'. In: *44th AIAA/ASME/ASCE/AHS/ASC Structures, Structural Dynamics, and Materials Conference*. Structures, Structural Dynamics, and Materials and Co-located Conferences. Norfolk, Virginia, USA: American Institute of Aeronautics and Astronautics, Apr. 2003. DOI: 10.2514/6.2003-1715 (cit. on p. 27).

[96] Detrick, M. and Washington, G. 'Modeling and Design of a Morphing Wing for Micro Unmanned Aerial Vehicles via Active Twist'. In: *48th AIAA/ASME/ASCE/AHS/ASC Structures, Structural Dynamics, and Materials Conference*. Structures, Structural Dynamics, and Materials and Co-located Conferences. Honolulu, Hawaii, USA: American Institute of Aeronautics and Astronautics, Apr. 2007. DOI: 10.2514/6.2007-1788 (cit. on p. 27).

[97] Barrett, R. M. 'Adaptive aerostructures: the first decade of flight on uninhabited aerial vehicles'. In: *Proc. SPIE*. Vol. 5388. San Diego, California, USA, 2004, pp. 190–201. DOI: 10.1117/12.536681 (cit. on p. 28).

[98] Sofla, A., Elzey, D. and Wadley, H. 'Two-way Antagonistic Shape Actuation Based on the One-way Shape Memory Effect'. In: *Journal of Intelligent Material Systems and Structures* 19.9 (2008), pp. 1017–1027. DOI: 10.1177/1045389X07083026 (cit. on p. 28).

[99] Lv, H., Leng, J. and Du, S. ‘A Survey of Adaptive Materials and Structures Research in China’. In: *50th AIAA/ASME/ASCE/AHS/ASC Structures, Structural Dynamics, and Materials Conference*. Structures, Structural Dynamics, and Materials and Co-located Conferences. American Institute of Aeronautics and Astronautics, Apr. 2009. DOI: 10.2514/6.2009-2389 (cit. on p. 28).

[100] Bye, D. and McClure, P. ‘Design of a Morphing Vehicle’. In: *48th AIAA/ASME/ASCE/AHS/ASC Structures, Structural Dynamics, and Materials Conference*. Structures, Structural Dynamics, and Materials and Co-located Conferences. Honolulu, Hawaii, USA: American Institute of Aeronautics and Astronautics, Apr. 2007. DOI: 10.2514/6.2007-1728 (cit. on p. 28).

[101] Skillen, M. D. and Crossley, W. A. *Modeling and Optimization for Morphing Wing Concept Generation II. Part 1; Morphing Wing Modeling and Structural Sizing Techniques*. NASA/CR-2008-214902/PT1. Hampton, Verginia, USA: NASA Langley Research Center, Feb. 2008. URL: http://hdl.handle.net/2060/20080009777 (cit. on pp. 28, 31).

[102] Love, M., Zink, P., Stroud, R., Bye, D., Rizk, S. and White, D. ‘Demonstration of Morphing Technology through Ground and Wind Tunnel Tests’. In: *48th AIAA/ASME/ASCE/AHS/ASC Structures, Structural Dynamics, and Materials Conference*. Structures, Structural Dynamics, and Materials and Co-located Conferences. Honolulu, Hawaii, USA: American Institute of Aeronautics and Astronautics, Apr. 2007. DOI: 10.2514/6.2007-1729 (cit. on pp. 28, 29).

[103] Ivanco, T., Scott, R., Love, M., Zink, S. and Weisshaar, T. ‘Validation of the Lockheed Martin Morphing Concept with Wind Tunnel Testing’. In: *48th AIAA/ASME/ASCE/AHS/ASC Structures, Structural Dynamics, and Materials Conference*. Structures, Structural Dynamics, and Materials and Co-located Conferences. Honolulu, Hawaii, USA: American Institute of Aeronautics and Astronautics, Apr. 2007. DOI: 10.2514/6.2007-2235 (cit. on p. 28).

[104] Shelton, A., Tomar, A., Prasad, J., Smith, M. and Komerath, N. ‘Active Multiple Winglets for Improved Unmanned-Aerial-Vehicle Performance’. In: *Journal of Aircraft* 43.1 (Jan. 2006), pp. 110–116. ISSN: 0021-8669. DOI: 10.2514/1.13987 (cit. on p. 28).

[105] Manzo, J. E. ‘Analysis and Design of a Hyper-Elliptical Cambered Span Morphing Aircraft Wing’. MSc thesis. Ithaca, New York, USA: Cornell University, June 2006. URL: http://hdl.handle.net/1813/3210 (cit. on pp. 28, 29).

[106] Bourdin, P., Gatto, A. and Friswell, M. I. ‘Aircraft Control via Variable Cant-Angle Winglets’. In: *Journal of Aircraft* 45.2 (Mar. 2008), pp. 414–423. ISSN: 0021-8669. DOI: 10.2514/1.27720 (cit. on p. 29).

[107] Bourdin, P., Gatto, A. and Friswell, M. I. ‘Performing co-ordinated turns with articulated wing-tips as multi-axis control effectors’. In: *The Aeronautical Journal* 114.1151 (2010), pp. 35–47. DOI: 10.1017/S0001924000003511 (cit. on pp. 29, 30).

[108] Falcão, L., Gomes, A. A. and Suleman, A. ‘Aero-structural Design Optimization of a Morphing Wingtip’. In: *Journal of Intelligent Material Systems and Structures* 22.10 (2011), pp. 1113–1124. DOI: 10.1177/1045389X11417652 (cit. on p. 29).

[109] Han, M. W., Rodrigue, H., Kim, H. I., Song, S. H. and Ahn, S. H. ‘Shape memory alloy/glass fiber woven composite for soft morphing winglets of unmanned aerial vehicles’. In: *Composite Structures* 140 (2016), pp. 202–212. ISSN: 0263-8223. DOI: 10.1016/j.compstruct.2015.12.051 (cit. on p. 30).

[110] Hannon, C., Agyepong, L., Toropov, V. and Querin, O. 'An Alternative View on Weight Estimation for the Aircraft Industry: Problems and MDO Solutions'. In: *12th AIAA/ISSMO Multidisciplinary Analysis and Optimization Conference*. Multidisciplinary Analysis Optimization Conferences. Victoria, British Columbia, Canada: American Institute of Aeronautics and Astronautics, Sept. 2008. DOI: 10.2514/6.2008-5877 (cit. on p. 30).

[111] Ajaj, R. M., Friswell, M. I., Smith, D. and Isikveren, A. T. 'A conceptual wing-box weight estimation model for transport aircraft'. In: *The Aeronautical Journal* 117.1191 (2013), pp. 533–551. DOI: 10.1017/S0001924000008174 (cit. on p. 31).

[112] Bindolino, G., Ghiringhelli, G., Ricci, S. and Terraneo, M. 'Multilevel Structural Optimization for Preliminary Wing-Box Weight Estimation'. In: *Journal of Aircraft* 47.2 (Mar. 2010), pp. 475–489. ISSN: 0021-8669. DOI: 10.2514/1.41552 (cit. on p. 31).

[113] Chambers, M. C., Ardema, M. D., Patron, A. P., Hahn, A. S., Miura, H. and Moore, M. D. *Analytical Fuselage and Wing Weight Estimation of Transport Aircraft*. Technical Memorandum 110392. Moffett Field, California, USA: NASA Ames Research Center, Apr. 1996. URL: https://ntrs.nasa.gov/archive/nasa/casi.ntrs.nasa.gov/19960025262.pdf (cit. on p. 31).

[114] Elham, A., Rocca, G. L. and Tooren, M. van. 'Development and implementation of an advanced, design-sensitive method for wing weight estimation'. In: *Aerospace Science and Technology* 29.1 (Aug. 2013), pp. 100–113. ISSN: 1270-9638. DOI: 10.1016/j.ast.2013.01.012 (cit. on p. 31).

[115] Andrews, S. A., Perez, R. E. and Wowk, D. 'Wing weight model for conceptual design of nonplanar configurations'. In: *Aerospace Science and Technology* 43 (June 2015), pp. 51–62. ISSN: 1270-9638. DOI: 10.1016/j.ast.2015.02.011 (cit. on p. 31).

[116] Jemitola, P. O., Monterzino, G. and Fielding, J. 'Wing mass estimation algorithm for medium range box wing aircraft'. In: *The Aeronautical Journal* 117.1189 (Mar. 2013), pp. 329–340. DOI: 10.1017/S0001924000008022 (cit. on p. 31).

[117] Kaufman, M., Balabanov, V., Giunta, A. A., Grossman, B., Mason, W. H., Burgee, S. L., Haftka, R. T. and Watson, L. T. 'Variable-complexity response surface approximations for wing structural weight in HSCT design'. In: *Computational Mechanics* 18.2 (1996), pp. 112–126. ISSN: 1432-0924. DOI: 10.1007/BF00350530 (cit. on p. 31).

[118] Frommer, J. and Crossley, W. 'Enabling Continuous Optimization for Sizing Morphing Aircraft Concepts'. In: *43rd AIAA Aerospace Sciences Meeting and Exhibit*. Aerospace Sciences Meetings. Reno, Nevada, USA: American Institute of Aeronautics and Astronautics, Jan. 2005. DOI: 10.2514/6.2005-816 (cit. on pp. 31, 32).

[119] Tigner, B., Meyer, M., Holden, M., Rawdon, B., Page, M., Watson, W. and Kroo, I. 'Test techniques for small-scale research aircraft'. In: *16th AIAA Applied Aerodynamics Conference*. Fluid Dynamics and Co-located Conferences. Albuquerque, New Mexico, USA: American Institute of Aeronautics and Astronautics, June 1998. DOI: 10.2514/6.1998-2726 (cit. on p. 32).

[120] Mestrinho, J., Gamboa, P. and Santos, P. 'Design Optimization of a Variable-Span Morphing Wing for a Small UAV'. In: *52nd AIAA/ASME/ASCE/AHS/ASC Structures, Structural Dynamics and Materials Conference*. Structures, Structural Dynamics, and Materials and Co-located Conferences. Denver, Colorado: American Institute of Aeronautics and Astronautics, Apr. 2011. DOI: 10.2514/6.2011-2025 (cit. on pp. 41, 44).

[121] Drela, M. *XFOIL 6.94 User Guide*. Massachusetts Institute of Technology & Astro Harold Youngren Aerocraft, Inc., Dec. 2001 (cit. on pp. 42, 119, 167).

[122] Katz, J. and Plotkin, A. *Low-Speed Aerodynamics*. Second. Cambridge University Press, 2001 (cit. on p. 42).

[123] Mukherjee, R., Gopalarathnam, A. and Kim, S. 'An Iterative Decambering Approach for Post-Stall Prediction of Wing Characteristics from Known Section Data'. In: *41st Aerospace Sciences Meeting and Exhibit*. Aerospace Sciences Meetings. Reno, Nevada, USA: American Institute of Aeronautics and Astronautics, Jan. 2003. DOI: 10.2514/6.2003-1097 (cit. on p. 42).

[124] Raymer, D. P. 'Chapter 15 - Weights'. In: *Aircraft Design: A Conceptual Approach*. Fifth. AIAA Education Series, AIAA, Aug. 2012, pp. 451–464. ISBN: 978-1-60086-911-2. DOI: 10.2514/4.869112 (cit. on pp. 42, 186).

[125] Zhou, J., Tits, A. and Lawrence, C. *User's Guide for FFSQP Version 3.7*. United States of America: Electrical Engineering Department and Institute for Systems Research, University of Maryland, Apr. 1997 (cit. on p. 42).

[126] Secanell, M. and Suleman, A. 'Numerical Evaluation of Optimization Algorithms for Low-Reynolds-Number Aerodynamic Shape Optimization'. In: *AIAA Journal* 43.10 (Oct. 2005), pp. 2262–2267. ISSN: 0001-1452. DOI: 10.2514/1.12563 (cit. on p. 42).

[127] *AIREX® C70 Universal Structural Foam*. GM-TDS-106. AIREX. July 2011. URL: http://www.airexbaltekbanova.com/airex-c70-pvc-foam.html (cit. on pp. 46, 122).

[128] *DPP high performance micro-pultrusion profiles - Specification sheet*. 13/06/2014. Van Dijk Pultrusion Products. June 2014. URL: http://www.dpp-pultrusion.com/wp-content/uploads/2012/12/DPP-specificationsheet-2014.pdf (cit. on pp. 46, 122, 169).

[129] Green, D. W., Winandy, J. E. and Kretschmann, D. E. 'Mechanical properties of wood'. In: *Wood handbook : wood as an engineering material*. USDA Forest Service, Forest Products Laboratory. General technical report FPL; GTR-113, 1999, pp. 4.1–4.45 (cit. on pp. 46, 47).

[130] ASTM Standard D3039/D3039M. 'Standard Test Method for Tensile Properties of Polymer Matrix Composite Materials'. In: *ASTM International* (2014). DOI: 10.1520/D3039_D3039M-14 (cit. on p. 46).

[131] Raymer, D. P. 'Chapter 14 - Structures and Loads'. In: *Aircraft Design: A Conceptual Approach*. Fifth. AIAA Education Series, AIAA, Aug. 2012, pp. 389–450. ISBN: 978-1-60086-911-2. DOI: 10.2514/4.869112 (cit. on p. 47).

[132] ANSYS. *Mechanical APDL Structural Analysis Guide*. Release 15.0. Canonsburg, PA, United States of America: ANSYS, Inc., Nov. 2013 (cit. on pp. 48, 123, 156).

[133] ANSYS. *Mechanical APDL Theory Reference*. Release 15.0. Canonsburg, PA, United States of America: ANSYS, Inc., Nov. 2013 (cit. on pp. 51, 55).

[134] Theodorsen, T. 'General Theory of Aerodynamic Instability and the Mechanism of Flutter'. In: *NACA Technical Report No. 496* (1934) (cit. on p. 53).

[135] Theodorsen, T. and Garrick, I. 'Mechanism of Flutter, A Theoretical and Experimental Investigation of the Flutter Problem'. In: *NACA Technical Report No. 685* (1940) (cit. on p. 53).

[136] Scanlan, R. and Rosenbaum, R. 'Outline of an Acceptable Method of Vibration and Flutter Analysis for a Conventional Airplane'. In: *Airframe and Equipment Engineering Report No. 43 and Aviation Safety Release No. 302* (1948) (cit. on pp. 53, 54).

[137] *SR 1500 - Epoxy laminating system*. 24/01/2014. Sicomin - Epoxy Systems. Jan. 2014. URL: http://www.sicomin.com/datasheets/product-pdf39.pdf (cit. on p. 61).

[138] Riseborough, P. *APM.Plane Extended Kalman Filter Navigation Overview and Tuning*. 2016. URL: http://ardupilot.org/dev/docs/extended-kalman-filter.html#extended-kalman-filter-navigation-overview-and-tuning (Retrieved 02/04/2017) (cit. on p. 79).

[139] Duke, E., Antoniewicz, R. and Krambeer, K. *Derivation and Definition of a Linear Aircraft Model*. Edwards, California, United States of America: Scientific and Technical Information Division of NASA, 1988 (cit. on pp. 87, 88).

[140] Etkin, B. and Reid, L. *Dynamics of Flight, Stability and Control*. Third. John Wiley & Sons, 1996 (cit. on p. 87).

[141] Silvestre, M., Morgado, J., Alves, P., Santos, P., Gamboa, P. and Páscoa, J. 'Propeller Performance Measurements at Low Reynolds Numbers'. In: *International Journal of Mechanics* 9.April (2015), pp. 154–166. ISSN: 1998-4448 (cit. on pp. 92, 93).

[142] Albuquerque, P. F., Gamboa, P. V. and Silvestre, M. A. 'Multidisciplinary and Multilevel Design Methodology of Unmanned Aerial Vehicles Using Enhanced Collaborative Optimization'. In: *International Journal of Mechanical, Aerospace, Industrial, Mechatronic and Manufacturing Engineering* 9.4 (2015), pp. 544–553. DOI: urn:dai:10.1999/1307-6892/18259 (cit. on p. 95).

[143] Yaman, Y. 'Combined morpHing Assessment software usiNG flight Envelope data and mission based morphing prototype wing development, CHANGE, an Overview Presentation'. In: *Proceedings of the 3rd International EASN Association Workshop on Aerostructures*. Milano, Italy, Oct. 2013 (cit. on pp. 106, 107).

[144] Ciarella, A., Hahn, M., Wong, P. and Peace, A. 'Comparison of Aerodynamic Design Methodologies for Morphing UAV Wings'. In: *Proceedings of the 7th Ankara International Aerospace Conference*. Ankara, Turkey, Sept. 2013 (cit. on p. 110).

[145] Ciarella, A., Tsotskas, C., Hahn, M., Werter, N., Breuker, R. D., Beaverstock, C., Friswell, M. I., Yang, Y., Özgen, S., Antoniadis, A., Drikakis, D. and Tsoutsanis, P. 'A Multi-Fidelity, Multi-Disciplinary Analysis and Optimization Framework for the Design of Morphing UAV Wing'. In: *16th AIAA/ISSMO Multidisciplinary Analysis and Optimization Conference*. AIAA Aviation. Dallas, Texas, USA: American Institute of Aeronautics and Astronautics, June 2015. DOI: 10.2514/6.2015-2326 (cit. on p. 110).

[146] Shaw, J. A., Stokes, S. and Lucking, M. A. 'The rapid and robust generation of efficient hybrid grids for rans simulations over complete aircraft'. In: *International Journal for Numerical Methods in Fluids* 43.6-7 (2003), pp. 785–821. ISSN: 1097-0363. DOI: 10.1002/fld.497 (cit. on p. 111).

[147] Schwamborn, D. and Gerhold, T. 'The DLR TAU-Code: Recent Applications in Research and Industry'. In: *European Conference on Computational Fluid Dynamics ECCOMAS CFD*. Egmond aan Zee, The Netherlands, Sept. 2006 (cit. on p. 111).

[148] *Certification Specifications for Very Light Aeroplanes CS-VLA*. Amendment 1. European Aviation Safety Agency, Mar. 2009 (cit. on pp. 118, 160, 167).

[149] Paepegem, W. V. and Degrieck, J. ‘Calculation of damage-dependent directional failure indices from the Tsai-Wu static failure criterion’. In: *Composites Science and Technology* 63.2 (2003), pp. 305–310. ISSN: 0266-3538. DOI: 10.1016/S0266-3538(02)00251-8 (cit. on p. 123).

[150] *Easy-Lease - chemical release agent*. 02/07/2015. Easy Composites. July 2015. URL: https://system.eu2.netsuite.com/core/media/media.nl?id=5279&c=3937524&h=8c69743215fbbd59bd6b&_xt=.pdf (cit. on p. 132).

[151] *Biresin CR122 - Composite resin system*. 06/2016. Sika - Tooling & Composites. June 2016. URL: http://deu.sika.com/dms/getdocument.get/b7489b0a-fdeb-3804-8820-699cc29b158c/Biresin_CR122_eng.pdf (cit. on p. 132).

[152] *Models 615 and 616 Tension Compression Load Cells*. 12066. Vishay Precision Group, Inc. Oct. 2016. URL: http://www.vishaypg.com/docs/12066/615-616.pdf (cit. on p. 137).

[153] *NI PXIe-4330/4331 User Manual*. 373029A-01. National Instruments Corporation. Apr. 2010. URL: www.ni.com/pdf/manuals/373029a.pdf (cit. on p. 137).

[154] *Software LabVIEW 2015 - Help*. 371361M-01. National Instruments Corporation. June 2015. URL: http://zone.ni.com/reference/en-XX/help/371361M-01/ (cit. on p. 137).

[155] Arslan, P., Kalkan, U., Tiras, H., Tunçöz, I. O., Yang, Y., Gürses, E., Sahin, M., Özgen, S. and Yaman, Y. ‘Structural Analysis of an Unconventional Hybrid Control Surface of a Morphing Wing’. In: *Proceedings of the 25th International Conference on Adaptive Structures and Technologies*. Hague, The Neatherlands, Jan. 2014 (cit. on p. 144).

[156] Yaman, Y., Tunçöz, I. O., Yang, Y., Arslan, P., Kalkan, U., Tiras, H., Gürses, E., Sahin, M. and Özgen, S. ‘Decamber Morphing Concepts by Using a Hybrid Trailing Edge Control Surface’. In: *Aerospace-Open Access Journal* 2.3 (2015), pp. 482–504. DOI: 10.3390/aerospace2030482 (cit. on p. 144).

[157] Radestock, M., Riemenschneider, J., Monner, H., Huxdorf, O., Werter, N. and Breuker, R. D. ‘Deformation measurement in the wind tunnel for an UAV leading edge with a morphing mechanism’. In: *30th Congress of the International Council of the Aeronautical Sciences*. Daejeon Convention Center (DCC), Daejeon, Korea, Sept. 2016 (cit. on p. 145).

[158] Albuquerque, P. F., Gamboa, P. V. and Silvestre, M. ‘Multidisciplinary and Multilevel Aircraft Design Methodology Using Enhanced Collaborative Optimization’. In: *16th AIAA/ISSMO Multidisciplinary Analysis and Optimization Conference*. Dallas, Texas: American Institute of Aeronautics and Astronautics, Jan. 2015. DOI: 10.2514/6.2015-2650 (cit. on p. 151).

[159] Sousa, D., Gamboa, P. V. and Melo, D. ‘Aerodynamic performance of aerofoils obtained from a geometric offset applied to a given initial aerofoil’. In: *Open Engineering* 6.1 (Dec. 2016). DOI: 10.1515/eng-2016-0098 (cit. on p. 151).

[160] ANSYS. *Mechanical APDL and Mechanical Applications Theory Reference*. Release 13.0. Canonsburg, PA, United States of America: ANSYS, Inc., Nov. 2010 (cit. on p. 155).

[161] Zhao, Y., Billings, S. A., Wei, H. and Sarrigiannis, P. G. ‘Tracking time-varying causality and directionality of information flow using an error reduction ratio test with applications to electroencephalography data.’ In: *Physical review. E, Statistical, nonlinear, and soft matter physics* 86.5 Pt 1 (Nov. 2012), p. 51919. ISSN: 1550-2376 (Electronic). DOI: 10.1103/PhysRevE.86.051919 (cit. on pp. 158, 159).

[162] Eichler, M. ‘Causal Inference in Time Series Analysis’. In: *Causality*. John Wiley & Sons, Ltd, 2012, pp. 327–354. ISBN: 9781119945710. DOI: 10.1002/9781119945710.ch22 (cit. on p. 158).

[163] Taylor, J. R. ‘Covariance and Correlation’. In: *Introduction to Error Analysis*. University Science Books, 1997, pp. 209–266. ISBN: 9780935702750 (cit. on p. 159).

[164] Torenbeek, E. ‘The Wing Structure and Its Weight’. In: *Advanced Aircraft Design*. John Wiley & Sons, 2013, pp. 319–362. ISBN: 9781118568101. DOI: 10.1002/9781118568101.ch11 (cit. on p. 160).

[165] Pololu Robotics & Electronics. *25D mm Metal DCGearmotors*. 2017. URL: https://www.pololu.com/category/115/25d-mm-metal-gearmotors (Retrieved 02/04/2017) (cit. on p. 185).

[166] Pololu Robotics & Electronics. *37D mm Metal DC Gearmotors*. 2017. URL: https://www.pololu.com/category/116/37d-mm-metal-gearmotors (Retrieved 02/04/2017) (cit. on p. 185).

Appendix A

Mass Study Parametric Analysis Results

A.1 Loading Conditions

Table A.1: Design lift and drag force and pitching moment used in the parametric study.

b	c	W	V_{design}	n_{design}	L_{design}	D_{design}	M_{design}
2.665	0.257	120	34.8	6.08	729.5	29.8	-16.3
	0.321		31.0	6.04	724.5	37.0	-20.4
	0.386		28.0	5.93	711.4	43.6	-24.5
3.554	0.257		30.9	6.40	768.3	23.6	-16.3
	0.321		27.4	6.30	756.5	29.0	-20.4
	0.386		24.7	6.14	736.4	33.9	-24.5
4.442	0.257		28.1	6.61	792.8	19.5	-16.3
	0.321		24.8	6.45	774.3	23.8	-20.4
	0.386		22.3	6.23	748.0	27.5	-24.5
2.665	0.257	150	38.2	5.87	880.9	36.0	-20.4
	0.321		34.2	5.87	880.8	45.0	-25.5
	0.386		31.0	5.80	870.5	53.4	-30.6
3.554	0.257		34.0	6.22	933.5	28.6	-20.4
	0.321		30.3	6.18	926.4	35.5	-25.5
	0.386		27.4	6.06	908.6	41.8	-30.6
4.442	0.257		31.0	6.45	968.1	23.8	-20.4
	0.321		27.5	6.36	953.9	29.3	-25.5
	0.386		24.8	6.19	929.0	34.2	-30.6
2.665	0.257	180	41.2	5.69	1024.8	41.9	-24.5
	0.321		36.9	5.72	1029.8	52.7	-30.6
	0.386		33.6	5.68	1022.8	62.8	-36.7
3.554	0.257		36.8	6.06	1091.0	33.5	-24.5
	0.321		32.9	6.05	1089.3	41.8	-30.6
	0.386		29.8	5.97	1074.6	49.4	-36.7
4.442	0.257		33.6	6.31	1136.0	27.9	-24.5
	0.321		29.9	6.26	1126.8	34.6	-30.6
	0.386		27.0	6.14	1104.3	40.7	-36.7

A.2 Fixed Wing

Table A.2: Parametric study fixed wing design variables and mass results.

Case	b, m	c_{IFW}, m	$\bar{c}_{flap}$	W, N	w_{sc}, mm	$t_{lam,1}$, mm	$t_{lam,2}$, mm	$t_{lam,3}$, mm	$t_{lam,4}$, mm	Mass, kg
1	2.665	0.257	0.3	120	9.603	0.065	0.026	0.008	0.001	0.331
2	2.665	0.257	0.3	150	11.044	0.085	0.041	0.015	0.008	0.380
3	2.665	0.257	0.3	180	12.482	0.123	0.040	0.008	0.041	0.437
4	3.554	0.257	0.3	120	17.075	0.099	0.043	0.014	0.001	0.632
5	3.554	0.257	0.3	150	20.430	0.136	0.049	0.015	0.001	0.743
6	3.554	0.257	0.3	180	23.365	0.166	0.063	0.024	0.002	0.846
7	4.442	0.257	0.3	120	25.102	0.167	0.087	0.026	0.028	1.008
8	4.442	0.257	0.3	150	32.005	0.169	0.092	0.041	0.001	1.164
9	4.442	0.257	0.3	180	36.538	0.193	0.105	0.310	0.002	1.410
10	2.665	0.257	0.4	120	8.375	0.054	0.023	0.003	0.001	0.287
11	2.665	0.257	0.4	150	10.030	0.065	0.037	0.005	0.001	0.327
12	2.665	0.257	0.4	180	11.557	0.085	0.036	0.008	0.001	0.365
13	3.554	0.257	0.4	120	14.505	0.097	0.046	0.007	0.007	0.556
14	3.554	0.257	0.4	150	17.984	0.109	0.047	0.011	0.002	0.638
15	3.554	0.257	0.4	180	20.959	0.130	0.050	0.018	0.001	0.720
16	4.442	0.257	0.4	120	22.968	0.138	0.061	0.012	0.002	0.902
17	4.442	0.257	0.4	150	28.250	0.146	0.085	0.019	0.001	1.056
18	4.442	0.257	0.4	180	32.073	0.215	0.072	0.171	0.002	1.272
19	2.665	0.321	0.3	120	6.706	0.040	0.014	0.002	0.001	0.300
20	2.665	0.321	0.3	150	7.980	0.047	0.020	0.008	0.002	0.332
21	2.665	0.321	0.3	180	9.328	0.059	0.024	0.005	0.002	0.366
22	3.554	0.321	0.3	120	11.848	0.060	0.021	0.003	0.001	0.527
23	3.554	0.321	0.3	150	14.544	0.072	0.027	0.006	0.001	0.603
24	3.554	0.321	0.3	180	16.729	0.079	0.042	0.012	0.001	0.672
25	4.442	0.321	0.3	120	18.158	0.075	0.037	0.007	0.001	0.854
26	4.442	0.321	0.3	150	22.035	0.101	0.043	0.011	0.002	1.000
27	4.442	0.321	0.3	180	25.227	0.134	0.055	0.018	0.004	1.153
28	2.665	0.321	0.4	120	5.714	0.033	0.013	0.002	0.001	0.262
29	2.665	0.321	0.4	150	6.973	0.038	0.021	0.002	0.001	0.291
30	2.665	0.321	0.4	180	8.097	0.050	0.021	0.002	0.001	0.319
31	3.554	0.321	0.4	120	10.161	0.051	0.019	0.002	0.002	0.457
32	3.554	0.321	0.4	150	12.516	0.061	0.026	0.003	0.001	0.521
33	3.554	0.321	0.4	180	14.489	0.073	0.034	0.006	0.001	0.582
34	4.442	0.321	0.4	120	15.733	0.073	0.029	0.003	0.001	0.745
35	4.442	0.321	0.4	150	19.159	0.087	0.041	0.008	0.001	0.866
36	4.442	0.321	0.4	180	22.408	0.112	0.047	0.009	0.002	0.990
37	2.665	0.386	0.3	120	5.076	0.022	0.012	0.001	0.001	0.293
38	2.665	0.386	0.3	150	6.087	0.029	0.014	0.001	0.001	0.318
39	2.665	0.386	0.3	180	7.052	0.035	0.018	0.002	0.002	0.343
40	3.554	0.386	0.3	120	8.566	0.036	0.014	0.002	0.002	0.474
41	3.554	0.386	0.3	150	10.579	0.044	0.019	0.002	0.002	0.533
42	3.554	0.386	0.3	180	12.444	0.052	0.025	0.003	0.001	0.591

Continued on next page

Table A.2 – continued from previous page

Case	b, m	c_{IFW}, m	$\overline{c}_{flap}$	W, N	w_{sc}, mm	$t_{lam,1}$, mm	$t_{lam,2}$, mm	$t_{lam,3}$, mm	$t_{lam,4}$, mm	Mass, kg
43	4.442	0.386	0.3	120	13.171	0.046	0.020	0.001	0.001	0.730
44	4.442	0.386	0.3	150	16.178	0.060	0.025	0.003	0.001	0.839
45	4.442	0.386	0.3	180	18.514	0.078	0.037	0.006	0.010	0.953
46	2.665	0.386	0.4	120	4.072	0.022	0.008	0.001	0.001	0.258
47	2.665	0.386	0.4	150	5.040	0.024	0.013	0.001	0.001	0.279
48	2.665	0.386	0.4	180	5.976	0.030	0.015	0.001	0.001	0.301
49	3.554	0.386	0.4	120	7.254	0.030	0.013	0.002	0.001	0.415
50	3.554	0.386	0.4	150	8.982	0.040	0.016	0.001	0.002	0.466
51	3.554	0.386	0.4	180	10.415	0.048	0.022	0.003	0.002	0.514
52	4.442	0.386	0.4	120	11.260	0.040	0.018	0.001	0.001	0.635
53	4.442	0.386	0.4	150	13.764	0.056	0.022	0.004	0.001	0.731
54	4.442	0.386	0.4	180	16.284	0.068	0.030	0.003	0.001	0.823

A.3 Variable-span Wing

Table A.3: Parametric study variable-span wing design variables and mass results.

Case	b, m	c_{IFW}, m	$\bar{l}_{var}$	$\bar{c}_{flap}$	W, N	$w_{sc,IFW}$, mm	$t_{lam,IFW}$, mm	$w_{sc,OMW}$, mm	$t_{lam,OMW}$, mm	Mass, kg
1	2.665	0.257	0.050	0.3	120	9.254	0.046	1.988	0.011	0.370
2	2.665	0.257	0.100	0.3	120	9.308	0.044	1.681	0.011	0.371
3	2.665	0.257	0.200	0.3	120	9.738	0.036	1.681	0.011	0.378
4	2.665	0.257	0.226	0.3	120	9.940	0.034	1.681	0.011	0.380
5	2.665	0.257	0.251	0.3	120	10.117	0.033	1.681	0.011	0.384
6	2.665	0.257	0.050	0.3	150	10.958	0.059	2.206	0.015	0.414
7	2.665	0.257	0.100	0.3	150	11.110	0.056	1.933	0.015	0.415
8	2.665	0.257	0.200	0.3	150	11.658	0.046	1.933	0.015	0.418
9	2.665	0.257	0.226	0.3	150	12.031	0.043	1.933	0.015	0.422
10	2.665	0.257	0.251	0.3	150	12.129	0.043	1.933	0.015	0.425
11	2.665	0.257	0.050	0.3	180	12.518	0.073	2.184	0.022	0.462
12	2.665	0.257	0.100	0.3	180	12.687	0.070	2.184	0.022	0.462
13	2.665	0.257	0.200	0.3	180	13.196	0.062	2.184	0.022	0.466
14	2.665	0.257	0.226	0.3	180	13.336	0.062	2.184	0.022	0.471
15	2.665	0.257	0.251	0.3	180	13.522	0.062	2.184	0.022	0.476
16	3.554	0.257	0.050	0.3	120	16.339	0.078	3.689	0.017	0.677
17	3.554	0.257	0.100	0.3	120	16.548	0.073	2.988	0.017	0.672
18	3.554	0.257	0.200	0.3	120	17.352	0.060	2.988	0.017	0.667
19	3.554	0.257	0.227	0.3	120	17.747	0.056	2.988	0.017	0.668
20	3.554	0.257	0.254	0.3	120	18.141	0.050	2.988	0.017	0.667
21	3.554	0.257	0.050	0.3	150	19.529	0.101	3.887	0.024	0.789
22	3.554	0.257	0.100	0.3	150	19.745	0.096	3.575	0.024	0.781
23	3.554	0.257	0.200	0.3	150	20.742	0.078	3.575	0.024	0.766
24	3.554	0.257	0.227	0.3	150	21.221	0.071	3.584	0.024	0.764
25	3.554	0.257	0.254	0.3	150	21.614	0.068	3.575	0.024	0.766
26	3.554	0.257	0.050	0.3	180	22.529	0.124	4.682	0.029	0.896
27	3.554	0.257	0.100	0.3	180	22.925	0.115	4.089	0.029	0.881
28	3.554	0.257	0.200	0.3	180	24.025	0.093	4.089	0.029	0.856
29	3.554	0.257	0.227	0.3	180	24.573	0.087	4.089	0.029	0.854
30	3.554	0.257	0.254	0.3	180	25.056	0.083	4.089	0.029	0.856
31	4.442	0.257	0.050	0.3	120	25.382	0.123	4.683	0.029	1.169
32	4.442	0.257	0.100	0.3	120	25.490	0.116	4.393	0.029	1.147
33	4.442	0.257	0.200	0.3	120	26.608	0.094	4.393	0.029	1.115
34	4.442	0.257	0.227	0.3	120	27.261	0.085	4.393	0.029	1.109
35	4.442	0.257	0.254	0.3	120	27.698	0.084	4.393	0.029	1.115
36	4.442	0.257	0.050	0.3	150	30.455	0.153	5.601	0.030	1.364
37	4.442	0.257	0.100	0.3	150	30.650	0.144	5.601	0.030	1.336
38	4.442	0.257	0.200	0.3	150	32.293	0.115	5.601	0.030	1.287
39	4.442	0.257	0.227	0.3	150	32.979	0.105	5.601	0.030	1.274
40	4.442	0.257	0.254	0.3	150	33.915	0.093	5.601	0.030	1.264
41	4.442	0.257	0.050	0.3	180	35.266	0.187	6.394	0.034	1.569
42	4.442	0.257	0.100	0.3	180	35.585	0.174	6.394	0.034	1.525

Continued on next page

Table A.3 – continued from previous page

Case	b, m	c_{IFW}, m	$\bar{l}_{var}$	$\bar{c}_{flap}$	W, N	$w_{sc,IFW}$, mm	$t_{lam,IFW}$, mm	$w_{sc,OMW}$, mm	$t_{lam,OMW}$, mm	Mass, kg
43	4.442	0.257	0.200	0.3	180	37.479	0.139	6.394	0.034	1.456
44	4.442	0.257	0.227	0.3	180	38.440	0.127	6.394	0.034	1.442
45	4.442	0.257	0.254	0.3	180	39.597	0.113	6.394	0.034	1.428
46	2.665	0.257	0.050	0.4	120	8.003	0.039	2.343	0.009	0.324
47	2.665	0.257	0.100	0.4	120	8.210	0.035	1.466	0.009	0.327
48	2.665	0.257	0.200	0.4	120	8.584	0.029	1.629	0.009	0.340
49	2.665	0.257	0.226	0.4	120	8.761	0.027	1.466	0.009	0.342
50	2.665	0.257	0.251	0.4	120	8.870	0.027	1.466	0.009	0.348
51	2.665	0.257	0.050	0.4	150	9.710	0.047	2.677	0.011	0.361
52	2.665	0.257	0.100	0.4	150	9.767	0.043	2.173	0.011	0.362
53	2.665	0.257	0.200	0.4	150	10.361	0.036	1.890	0.011	0.373
54	2.665	0.257	0.226	0.4	150	10.528	0.033	1.755	0.011	0.374
55	2.665	0.257	0.251	0.4	150	10.738	0.033	1.755	0.011	0.379
56	2.665	0.257	0.050	0.4	180	11.129	0.058	3.144	0.015	0.398
57	2.665	0.257	0.100	0.4	180	11.339	0.054	2.195	0.015	0.400
58	2.665	0.257	0.200	0.4	180	11.919	0.044	2.022	0.015	0.405
59	2.665	0.257	0.226	0.4	180	12.066	0.043	2.022	0.015	0.409
60	2.665	0.257	0.251	0.4	180	12.350	0.043	2.022	0.015	0.416
61	3.554	0.257	0.050	0.4	120	14.424	0.067	4.045	0.017	0.593
62	3.554	0.257	0.100	0.4	120	14.553	0.062	3.163	0.017	0.592
63	3.554	0.257	0.200	0.4	120	15.217	0.050	2.703	0.017	0.594
64	3.554	0.257	0.227	0.4	120	15.519	0.049	2.538	0.017	0.600
65	3.554	0.257	0.254	0.4	120	15.739	0.049	2.538	0.017	0.608
66	3.554	0.257	0.050	0.4	150	17.378	0.083	5.142	0.019	0.682
67	3.554	0.257	0.100	0.4	150	17.502	0.077	4.282	0.019	0.678
68	3.554	0.257	0.200	0.4	150	18.334	0.062	3.608	0.019	0.673
69	3.554	0.257	0.227	0.4	150	18.660	0.056	3.869	0.019	0.676
70	3.554	0.257	0.254	0.4	150	19.255	0.055	3.147	0.019	0.678
71	3.554	0.257	0.050	0.4	180	20.128	0.100	6.013	0.023	0.769
72	3.554	0.257	0.100	0.4	180	20.299	0.095	4.886	0.023	0.764
73	3.554	0.257	0.200	0.4	180	21.509	0.074	3.668	0.023	0.748
74	3.554	0.257	0.227	0.4	180	22.151	0.067	3.668	0.023	0.748
75	3.554	0.257	0.254	0.4	180	22.418	0.065	3.668	0.023	0.752
76	4.442	0.257	0.050	0.4	120	22.371	0.103	6.428	0.024	1.008
77	4.442	0.257	0.100	0.4	120	22.757	0.097	4.773	0.024	1.001
78	4.442	0.257	0.200	0.4	120	23.815	0.076	4.019	0.024	0.980
79	4.442	0.257	0.227	0.4	120	24.169	0.069	4.019	0.024	0.975
80	4.442	0.257	0.254	0.4	120	24.516	0.069	4.019	0.024	0.986
81	4.442	0.257	0.050	0.4	150	27.199	0.128	8.576	0.026	1.185
82	4.442	0.257	0.100	0.4	150	27.550	0.121	5.743	0.026	1.165
83	4.442	0.257	0.200	0.4	150	28.815	0.093	5.518	0.026	1.132
84	4.442	0.257	0.227	0.4	150	29.694	0.084	4.944	0.026	1.123
85	4.442	0.257	0.254	0.4	150	29.853	0.073	5.839	0.026	1.118
86	4.442	0.257	0.050	0.4	180	31.333	0.162	8.942	0.038	1.368
87	4.442	0.257	0.100	0.4	180	31.787	0.152	5.613	0.038	1.338
88	4.442	0.257	0.200	0.4	180	33.447	0.119	5.613	0.038	1.296

Continued on next page

Table A.3 – continued from previous page

Case	b, m	c_{IFW}, m	$\bar{l}_{var}$	$\bar{c}_{flap}$	W, N	$w_{sc,IFW}$, mm	$t_{lam,IFW}$, mm	$w_{sc,OMW}$, mm	$t_{lam,OMW}$, mm	Mass, kg
89	4.442	0.257	0.227	0.4	180	33.991	0.108	5.721	0.038	1.285
90	4.442	0.257	0.254	0.4	180	34.658	0.108	5.613	0.038	1.296
91	2.665	0.321	0.050	0.3	120	6.193	0.029	1.174	0.007	0.352
92	2.665	0.321	0.100	0.3	120	6.765	0.023	1.862	0.007	0.359
93	2.665	0.321	0.200	0.3	120	6.674	0.020	1.538	0.007	0.375
94	2.665	0.321	0.224	0.3	120	6.725	0.020	1.174	0.007	0.379
95	2.665	0.321	0.247	0.3	120	6.753	0.020	1.174	0.007	0.385
96	2.665	0.321	0.050	0.3	150	7.910	0.028	1.724	0.008	0.375
97	2.665	0.321	0.100	0.3	150	7.986	0.027	1.647	0.008	0.384
98	2.665	0.321	0.200	0.3	150	8.151	0.025	1.397	0.008	0.401
99	2.665	0.321	0.224	0.3	150	8.318	0.024	1.397	0.008	0.406
100	2.665	0.321	0.247	0.3	150	8.389	0.024	1.397	0.008	0.412
101	2.665	0.321	0.050	0.3	180	9.183	0.035	2.570	0.010	0.408
102	2.665	0.321	0.100	0.3	180	9.243	0.034	2.232	0.010	0.416
103	2.665	0.321	0.200	0.3	180	9.683	0.030	1.639	0.010	0.432
104	2.665	0.321	0.224	0.3	180	9.619	0.030	1.632	0.010	0.435
105	2.665	0.321	0.247	0.3	180	9.672	0.030	1.632	0.010	0.441
106	3.554	0.321	0.050	0.3	120	11.528	0.038	3.326	0.011	0.576
107	3.554	0.321	0.100	0.3	120	11.548	0.036	3.002	0.011	0.583
108	3.554	0.321	0.200	0.3	120	12.026	0.031	2.165	0.011	0.600
109	3.554	0.321	0.225	0.3	120	12.033	0.030	2.073	0.011	0.604
110	3.554	0.321	0.249	0.3	120	12.084	0.030	2.073	0.011	0.612
111	3.554	0.321	0.050	0.3	150	13.966	0.048	3.963	0.013	0.650
112	3.554	0.321	0.100	0.3	150	14.036	0.046	3.736	0.013	0.655
113	3.554	0.321	0.200	0.3	150	14.637	0.039	2.662	0.013	0.665
114	3.554	0.321	0.225	0.3	150	14.822	0.036	2.545	0.013	0.668
115	3.554	0.321	0.249	0.3	150	14.890	0.036	2.545	0.013	0.675
116	3.554	0.321	0.050	0.3	180	16.344	0.058	4.295	0.014	0.719
117	3.554	0.321	0.100	0.3	180	16.421	0.054	3.804	0.014	0.719
118	3.554	0.321	0.200	0.3	180	17.272	0.046	2.928	0.014	0.726
119	3.554	0.321	0.225	0.3	180	17.439	0.042	2.928	0.014	0.726
120	3.554	0.321	0.249	0.3	180	17.766	0.040	2.928	0.014	0.730
121	4.442	0.321	0.050	0.3	120	17.661	0.056	4.669	0.013	0.908
122	4.442	0.321	0.100	0.3	120	17.773	0.053	4.631	0.013	0.913
123	4.442	0.321	0.200	0.3	120	18.429	0.044	3.799	0.013	0.921
124	4.442	0.321	0.224	0.3	120	18.568	0.040	3.436	0.013	0.917
125	4.442	0.321	0.248	0.3	120	18.930	0.038	3.178	0.013	0.921
126	4.442	0.321	0.050	0.3	150	21.378	0.073	6.575	0.018	1.060
127	4.442	0.321	0.100	0.3	150	21.722	0.069	3.856	0.018	1.050
128	4.442	0.321	0.200	0.3	150	22.530	0.057	3.856	0.018	1.047
129	4.442	0.321	0.224	0.3	150	22.598	0.052	4.363	0.018	1.049
130	4.442	0.321	0.248	0.3	150	22.964	0.051	3.856	0.018	1.051
131	4.442	0.321	0.050	0.3	180	24.913	0.092	4.415	0.023	1.199
132	4.442	0.321	0.100	0.3	180	25.153	0.087	6.178	0.023	1.200
133	4.442	0.321	0.200	0.3	180	26.234	0.071	4.415	0.023	1.178
134	4.442	0.321	0.224	0.3	180	26.500	0.067	4.415	0.023	1.177

Continued on next page

Table A.3 – continued from previous page

Case	b, m	c_{IFW}, m	$\bar{l}_{var}$	$\bar{c}_{flap}$	W, N	$w_{sc,IFW}$, mm	$t_{lam,IFW}$, mm	$w_{sc,OMW}$, mm	$t_{lam,OMW}$, mm	Mass, kg
135	4.442	0.321	0.248	0.3	180	26.699	0.067	4.415	0.023	1.187
136	2.665	0.321	0.050	0.4	120	5.657	0.019	1.589	0.006	0.307
137	2.665	0.321	0.100	0.4	120	5.675	0.018	1.478	0.006	0.318
138	2.665	0.321	0.200	0.4	120	5.895	0.017	1.000	0.006	0.341
139	2.665	0.321	0.224	0.4	120	5.894	0.017	1.000	0.006	0.347
140	2.665	0.321	0.247	0.4	120	5.960	0.017	1.000	0.006	0.354
141	2.665	0.321	0.050	0.4	150	6.957	0.023	2.215	0.007	0.334
142	2.665	0.321	0.100	0.4	150	6.947	0.022	1.724	0.007	0.343
143	2.665	0.321	0.200	0.4	150	7.483	0.019	1.785	0.007	0.370
144	2.665	0.321	0.224	0.4	150	7.362	0.019	1.220	0.007	0.370
145	2.665	0.321	0.247	0.4	150	7.461	0.019	1.220	0.007	0.377
146	2.665	0.321	0.050	0.4	180	8.014	0.029	2.440	0.009	0.361
147	2.665	0.321	0.100	0.4	180	8.039	0.028	2.229	0.009	0.370
148	2.665	0.321	0.200	0.4	180	8.312	0.025	1.417	0.009	0.389
149	2.665	0.321	0.224	0.4	180	8.434	0.025	1.417	0.009	0.396
150	2.665	0.321	0.247	0.4	180	8.527	0.025	1.417	0.009	0.403
151	3.554	0.321	0.050	0.4	120	10.030	0.032	3.247	0.009	0.505
152	3.554	0.321	0.100	0.4	120	10.052	0.030	2.869	0.009	0.515
153	3.554	0.321	0.200	0.4	120	10.414	0.026	1.778	0.009	0.536
154	3.554	0.321	0.225	0.4	120	10.505	0.026	1.778	0.009	0.545
155	3.554	0.321	0.249	0.4	120	10.615	0.026	1.778	0.009	0.555
156	3.554	0.321	0.050	0.4	150	12.243	0.039	3.988	0.011	0.567
157	3.554	0.321	0.100	0.4	150	12.313	0.037	3.537	0.011	0.576
158	3.554	0.321	0.200	0.4	150	12.825	0.031	2.190	0.011	0.590
159	3.554	0.321	0.225	0.4	150	12.963	0.031	2.190	0.011	0.599
160	3.554	0.321	0.249	0.4	150	13.077	0.031	2.190	0.011	0.609
161	3.554	0.321	0.050	0.4	180	14.300	0.048	4.510	0.013	0.627
162	3.554	0.321	0.100	0.4	180	14.451	0.045	4.300	0.013	0.637
163	3.554	0.321	0.200	0.4	180	15.052	0.037	2.536	0.013	0.644
164	3.554	0.321	0.225	0.4	180	15.298	0.037	2.536	0.013	0.654
165	3.554	0.321	0.249	0.4	180	15.425	0.037	2.536	0.013	0.663
166	4.442	0.321	0.050	0.4	120	15.455	0.048	5.085	0.013	0.797
167	4.442	0.321	0.100	0.4	120	15.497	0.045	4.476	0.013	0.805
168	4.442	0.321	0.200	0.4	120	16.132	0.037	2.753	0.013	0.816
169	4.442	0.321	0.224	0.4	120	16.200	0.037	2.753	0.013	0.826
170	4.442	0.321	0.248	0.4	120	16.279	0.037	2.753	0.013	0.837
171	4.442	0.321	0.050	0.4	150	18.864	0.061	6.266	0.015	0.917
172	4.442	0.321	0.100	0.4	150	19.039	0.057	5.738	0.015	0.927
173	4.442	0.321	0.200	0.4	150	19.860	0.046	3.353	0.015	0.924
174	4.442	0.321	0.224	0.4	150	20.021	0.044	3.353	0.015	0.928
175	4.442	0.321	0.248	0.4	150	20.172	0.044	3.353	0.015	0.940
176	4.442	0.321	0.050	0.4	180	22.069	0.076	7.084	0.020	1.042
177	4.442	0.321	0.100	0.4	180	22.115	0.071	6.391	0.020	1.042
178	4.442	0.321	0.200	0.4	180	22.969	0.056	4.701	0.020	1.038
179	4.442	0.321	0.224	0.4	180	23.320	0.056	3.921	0.020	1.040
180	4.442	0.321	0.248	0.4	180	23.496	0.056	3.921	0.020	1.051

Continued on next page

Table A.3 – continued from previous page

Case	b, m	c_{IFW}, m	$\bar{l}_{var}$	$\bar{c}_{flap}$	W, N	$w_{sc,IFW}$, mm	$t_{lam,IFW}$, mm	$w_{sc,OMW}$, mm	$t_{lam,OMW}$, mm	Mass, kg
181	2.665	0.386	0.050	0.3	120	5.066	0.012	1.543	0.004	0.349
182	2.665	0.386	0.100	0.3	120	5.229	0.012	1.551	0.004	0.366
183	2.665	0.386	0.200	0.3	120	4.992	0.012	0.888	0.004	0.390
184	2.665	0.386	0.222	0.3	120	5.249	0.011	1.516	0.004	0.404
185	2.665	0.386	0.244	0.3	120	5.063	0.011	0.888	0.004	0.404
186	2.665	0.386	0.050	0.3	150	6.194	0.015	1.886	0.005	0.374
187	2.665	0.386	0.100	0.3	150	6.104	0.015	1.699	0.005	0.387
188	2.665	0.386	0.200	0.3	150	6.134	0.015	1.765	0.005	0.418
189	2.665	0.386	0.222	0.3	150	6.464	0.015	1.796	0.005	0.429
190	2.665	0.386	0.244	0.3	150	6.215	0.015	1.065	0.005	0.427
191	2.665	0.386	0.050	0.3	180	7.229	0.019	2.142	0.006	0.397
192	2.665	0.386	0.100	0.3	180	7.266	0.019	2.072	0.006	0.412
193	2.665	0.386	0.200	0.3	180	7.361	0.018	1.940	0.006	0.441
194	2.665	0.386	0.222	0.3	180	7.125	0.019	2.120	0.007	0.451
195	2.665	0.386	0.244	0.3	180	7.282	0.018	1.234	0.006	0.448
196	3.554	0.386	0.050	0.3	120	8.606	0.020	2.684	0.006	0.534
197	3.554	0.386	0.100	0.3	120	8.606	0.019	2.453	0.006	0.551
198	3.554	0.386	0.200	0.3	120	8.607	0.018	1.499	0.006	0.582
199	3.554	0.386	0.222	0.3	120	8.644	0.018	1.499	0.006	0.591
200	3.554	0.386	0.245	0.3	120	8.627	0.018	1.499	0.006	0.601
201	3.554	0.386	0.050	0.3	150	10.587	0.025	3.370	0.008	0.589
202	3.554	0.386	0.100	0.3	150	10.597	0.025	3.034	0.008	0.605
203	3.554	0.386	0.200	0.3	150	10.695	0.022	1.851	0.008	0.631
204	3.554	0.386	0.222	0.3	150	10.751	0.022	1.851	0.008	0.640
205	3.554	0.386	0.245	0.3	150	10.753	0.022	1.851	0.008	0.650
206	3.554	0.386	0.050	0.3	180	12.468	0.031	3.916	0.009	0.645
207	3.554	0.386	0.100	0.3	180	12.404	0.030	3.509	0.009	0.656
208	3.554	0.386	0.200	0.3	180	12.543	0.027	3.045	0.009	0.686
209	3.554	0.386	0.222	0.3	180	12.760	0.026	2.178	0.009	0.687
210	3.554	0.386	0.245	0.3	180	12.787	0.026	2.178	0.009	0.697
211	4.442	0.386	0.050	0.3	120	12.888	0.029	4.200	0.008	0.790
212	4.442	0.386	0.100	0.3	120	12.939	0.027	3.839	0.008	0.806
213	4.442	0.386	0.200	0.3	120	13.145	0.024	3.318	0.008	0.847
214	4.442	0.386	0.222	0.3	120	13.273	0.023	2.305	0.008	0.845
215	4.442	0.386	0.243	0.3	120	13.244	0.023	2.305	0.008	0.856
216	4.442	0.386	0.050	0.3	150	15.934	0.038	5.128	0.011	0.898
217	4.442	0.386	0.100	0.3	150	15.973	0.036	4.671	0.011	0.912
218	4.442	0.386	0.200	0.3	150	16.214	0.031	4.049	0.011	0.945
219	4.442	0.386	0.222	0.3	150	16.392	0.030	2.831	0.011	0.940
220	4.442	0.386	0.243	0.3	150	16.318	0.030	2.831	0.011	0.950
221	4.442	0.386	0.050	0.3	180	18.703	0.047	5.821	0.014	1.005
222	4.442	0.386	0.100	0.3	180	18.822	0.045	5.491	0.014	1.018
223	4.442	0.386	0.200	0.3	180	19.263	0.039	3.240	0.014	1.029
224	4.442	0.386	0.222	0.3	180	19.249	0.039	3.240	0.014	1.038
225	4.442	0.386	0.243	0.3	180	19.283	0.039	3.240	0.014	1.050
226	2.665	0.386	0.050	0.4	120	4.222	0.011	0.713	0.004	0.315

Continued on next page

Table A.3 – continued from previous page

Case	b, m	c_{IFW}, m	$\bar{l}_{var}$	$\bar{c}_{flap}$	W, N	$w_{sc,IFW}$, mm	$t_{lam,IFW}$, mm	$w_{sc,OMW}$, mm	$t_{lam,OMW}$, mm	Mass, kg
227	2.665	0.386	0.100	0.4	120	4.186	0.011	0.713	0.004	0.330
228	2.665	0.386	0.200	0.4	120	4.314	0.011	1.261	0.004	0.367
229	2.665	0.386	0.222	0.4	120	4.225	0.011	0.713	0.004	0.370
230	2.665	0.386	0.244	0.4	120	4.264	0.011	0.713	0.004	0.379
231	2.665	0.386	0.050	0.4	150	5.394	0.013	1.623	0.004	0.337
232	2.665	0.386	0.100	0.4	150	5.427	0.013	1.572	0.004	0.353
233	2.665	0.386	0.200	0.4	150	5.361	0.012	0.882	0.004	0.380
234	2.665	0.386	0.222	0.4	150	5.469	0.012	0.882	0.004	0.388
235	2.665	0.386	0.244	0.4	150	5.469	0.012	1.608	0.004	0.402
236	2.665	0.386	0.050	0.4	180	6.298	0.016	1.932	0.005	0.356
237	2.665	0.386	0.100	0.4	180	6.347	0.016	1.832	0.005	0.373
238	2.665	0.386	0.200	0.4	180	6.259	0.015	1.046	0.005	0.399
239	2.665	0.386	0.222	0.4	180	6.351	0.015	1.046	0.005	0.406
240	2.665	0.386	0.244	0.4	180	6.355	0.015	1.887	0.006	0.422
241	3.554	0.386	0.050	0.4	120	7.572	0.016	2.381	0.005	0.476
242	3.554	0.386	0.100	0.4	120	7.521	0.016	2.124	0.005	0.494
243	3.554	0.386	0.200	0.4	120	7.593	0.015	1.269	0.005	0.530
244	3.554	0.386	0.222	0.4	120	7.634	0.015	1.269	0.005	0.541
245	3.554	0.386	0.245	0.4	120	7.717	0.015	1.269	0.005	0.553
246	3.554	0.386	0.050	0.4	150	9.164	0.022	2.966	0.007	0.523
247	3.554	0.386	0.100	0.4	150	9.234	0.021	2.699	0.007	0.541
248	3.554	0.386	0.200	0.4	150	9.338	0.020	1.572	0.007	0.576
249	3.554	0.386	0.222	0.4	150	9.440	0.020	1.572	0.007	0.588
250	3.554	0.386	0.245	0.4	150	9.429	0.020	1.572	0.007	0.598
251	3.554	0.386	0.050	0.4	180	10.767	0.026	3.401	0.008	0.567
252	3.554	0.386	0.100	0.4	180	10.807	0.025	3.235	0.008	0.586
253	3.554	0.386	0.200	0.4	180	11.066	0.024	1.823	0.008	0.618
254	3.554	0.386	0.222	0.4	180	11.142	0.024	1.823	0.008	0.629
255	3.554	0.386	0.245	0.4	180	11.201	0.024	1.823	0.009	0.640
256	4.442	0.386	0.050	0.4	120	11.296	0.024	3.721	0.007	0.694
257	4.442	0.386	0.100	0.4	120	11.465	0.023	3.624	0.007	0.719
258	4.442	0.386	0.200	0.4	120	11.662	0.020	1.971	0.007	0.755
259	4.442	0.386	0.222	0.4	120	11.696	0.020	1.971	0.007	0.768
260	4.442	0.386	0.243	0.4	120	11.720	0.020	1.971	0.007	0.781
261	4.442	0.386	0.050	0.4	150	13.990	0.032	4.582	0.010	0.790
262	4.442	0.386	0.100	0.4	150	14.056	0.030	4.410	0.010	0.811
263	4.442	0.386	0.200	0.4	150	14.253	0.028	2.409	0.010	0.842
264	4.442	0.386	0.222	0.4	150	14.288	0.028	2.409	0.010	0.855
265	4.442	0.386	0.243	0.4	150	14.358	0.028	2.409	0.010	0.869
266	4.442	0.386	0.050	0.4	180	16.542	0.040	5.406	0.012	0.880
267	4.442	0.386	0.100	0.4	180	16.599	0.037	5.156	0.012	0.897
268	4.442	0.386	0.200	0.4	180	16.868	0.034	2.850	0.012	0.922
269	4.442	0.386	0.222	0.4	180	16.997	0.034	2.850	0.012	0.936
270	4.442	0.386	0.243	0.4	180	17.049	0.034	2.850	0.012	0.949

Appendix B

Publications

B.1 Journals

1. Santos, P., Sousa, J., and Gamboa, P., "Variable-span wing development for improved flight performance", In: Journal of Intelligent Material Systems and Structures 28.8 (2017), pp. 961-978. http://journals.sagepub.com/doi/abs/10.1177/1045389X15595719

2. Silvestre, M.A.R., Morgado, J., Alves, P., Santos, P., Gamboa, P., Páscoa, J.C., "Propeller Performance Measurements at Low Reynolds Numbers", In: International Journal of Mechanics 9 (2015), pp. 154-166. www.naun.org/main/NAUN/mechanics/2015/a372003-136.pdf

B.2 Scientific Conferences

1. Santos, P., Sousa, D., Gamboa, P., Zhao, Y., "Effect of Design Parameters on the Structural Mass of a Telescopic Wing", 6th EASN International Conference, Porto, Portugal, 18-21 October, 2016.

2. Gamboa, P., Santos, P., "Telescopic Wing-Box for a Morphing Wing", 24th AIAA/AHS Adaptive Structures Conference, San Diego, California, 4-8 January 2016. https://arc.aiaa.org/doi/abs/10.2514/6.2016-0317

3. Santos, P.D., Gamboa, P.V., "Evaluation of Energy Required for Flight by a UAV Fitted with a Variable-Span Wing Performing a Given Mission Profile", AIAA Atmospheric Flight Mechanics Conference, Dallas, Texas, 22-26 June 2015. https://arc.aiaa.org/doi/abs/10.2514/6.2015-2391

4. Santos, P.D., Gamboa, P.V., "Developing Flight Testing Capabilities with Fixed-Wing Remotely Piloted Aircraft Systems", 3 EJIL - LAETA Young Researchers Meeting, ADAI, Coimbra, 7-8 May 2015.

5. Silvestre, M., Morgado, J, Alves, P., Santos, P., Gamboa, P., Páscoa, J., "Low Reynolds Number Propeller Performance Testing", 5th International Conference on Fluid Mechanics and Heat & Mass Transfer (FLUIDSHEAT14), Lisbon, Portugal, October 30 - November 1, 2014. www.wseas.us/e-library/conferences/2014/Florence/MECH/MECH-19.pdf

6. Santos, P.D.R., Sousa, J.V.R., Gamboa, P.V., "Telescopic Wing for Improved Flight Performance", Design, Modelling and Experiments of Advanced Structures and Systems – DeMEASS VI, Ede, the Netherlands, 26-28 May, 2014.

7. Sousa, J., Santos, P., Gamboa, P., "Control Systems for UAV Flight Testing", International Conference on Engineering ICEUBI2013 – Engineering for Economic Development, Covilhã,

Portugal, 27-29 November, 2013.

8. Gamboa, P., Santos, P., Silva, J., Santos, P.M.B., “Flutter Analysis of a Composite Variable-Span Wing”, 4th International Conference on Integrity, Reliability and Failure – IRF 2013, Funchal, Portugal, 23-27 June, 2013.
9. Santos, P., Gamboa, P., Santos, P.M.B., Silva, J., “Structural Design of a Composite Variable-Span Wing”, 4th International Conference on Integrity, Reliability and Failure – IRF 2013, Funchal, Portugal, 23-27 June, 2013.
10. Gamboa, P., Santos, P., Miguel, L., “Development of a Variable-Span Morphing Wing”, II LAETA Young Researchers Meeting, FEUP, Portugal, 10-11 April, 2012.